



The
University
Of
Sheffield.

Development of Advanced Imaging Based Diagnostics for Flame Studies

MISS YIRAN WANG

Combustion and Flow Diagnostics Research Group
Department of Mechanical Engineering

This thesis is submitted to the University of Sheffield for the degree of
Doctor of Philosophy, 2018

Declaration

The work presented in this thesis is that of the Author and has not been submitted for any other award or degree at the University of Sheffield or any other university or institution.

Acknowledgements

I would like to thank the many people, in many countries, who so generously contributed to my studies and life.

First of all, I would like to express my sincere gratitude to my supervisor, Professor Yang Zhang, for his continuous support, expertise, patient guidance, encouragement and advice throughout my four years of PhD study. He also supervised my undergraduate final year project and guided me into the combustion field. His guidance helped me during all of the research and writing of this thesis. He cared so much about my work, and he responded to my questions and queries promptly, although more than 100 students are under his guidance. His profound knowledge and ideas inspired my research and broadened my horizons. He offered many opportunities to me for academic conferences and internships. I could not have imagined having a better advisor and mentor for my studies.

I would like to thank my second supervisor, Professor Shuisheng He for his continuous support, patience, motivation, enthusiasm and advice for my research and life. I would like to thank Dr. Robert Woolley for his advice and modification of my paper, as well as the suggestion from the first-year viva.

I would also like to thank my colleagues in the Combustion research group; Hussain Saeed, Jiansheng Yang, Paco Carranza Ch, Zhen Ma, Halleh Mortazavi, Ahmad Faik, Lukai Zheng, Shuaida Ji, Songyang Yu, Hangxu Zhou, Houshi Jiang, Ahmad fuad Abdul rasid, Yufeng Lai, Xiao Wang and Muyi Pan for their support and cooperation in laboratory work and for making my time during my PhD very enjoyable.

I am also hugely appreciative of Dr. Jiansheng Yang for sharing his MATLAB programming expertise, and for his assistance with experiments. Without his help, I would have been able to conduct the experiments and process the data skillfully. I would like to thank Dr. Qian Wang for her continuous support for my research. Although she is in China, she always helped to solve my problems promptly. I am grateful to Dr. Chloe McDaid for her contribution to my thesis writing. My undergraduate final year project was under her guidance, which inspired my interest

in combustion studies.

I am so thankful to my boyfriend for his constant accompany. He has brought infinite happiness, comfort, support and love to me. He participated in all my experiments, although he is in an utterly different research area and he is very busy with his studies. He also contributed to my academic writing. He always encouraged me when I encountered obstacles. He takes good care of every aspect of me. He is the best boyfriend in the world. I could not imagine my life without him.

Finally, I would like to express the most profound gratitude to my parents for their love, comfort, encouragement and support for my life and studies. My parents are the most important people in my life. They kept me going and they taught me everything. Everything they have given me, I will always keep it inside. I love them forever.

Publications

Journals:

1. Y. Wang, L. Zheng, R. Woolley, Y. Zhang, Investigation of Ignition Process from Visible to Infrared by a High-speed Colour Camera, *Fuel*, vol. 185, pp. 500-507, 2016.
2. Y. Wang, Y. Zhang, Simultaneous High-speed Schlieren and Direct Imaging of Ignition Process with Digitally Enhanced Visualisation, *Energy Procedia*, Vol. 66, pp. 241-244, 2015.
3. H. Mortazavi, Y. Wang, Z. Ma, Y. Zhang, The Investigation of CO₂ Effect on the Characteristics of a Methane Diffusion Flame, *Experimental Thermal and Fluid Science*, vol. 92, pp. 97-102, 2018.

Conference papers:

1. Y. Wang, Y. Zhang, High-speed Schlieren and Direct Imaging of Ignition Process with Digitally Enhanced Visualisation, The 12th International Conference on Combustion & Energy Utilisation, Lancaster, UK, 2014.
2. Y. Wang, Z. Ma, Y. Zhang, Effects of Ignition Location on Soot and Species Formation through Tracking Flame Light Emission and Temperature, 26th ICDERS, Boston, MA, USA, 2017.
3. Q. Wang, J. Yang, Y. Wang, Y. Zhang, C. Zhao, Experimental Investigation of Co-flow Effect on Ignition Process of a Methane Jet Diffusion Flame, 25th ICDERS, Leeds, UK, 2015.
4. H. Mortazavi, Y. Wang, Z. Ma and Y. Zhang, The Investigation of CO₂ Effect on the Characteristics of Methane Diffusion Flame, 12th International Conference on Heat Transfer, Fluid Mechanics and Thermodynamics, At Costa del Sol, Spain, 2016 (awarded best paper).

Abstract

As flame light emission is correlated to flame colour appearance, a unique image post-processing method introduced in this thesis establishes a relationship between the multiple flame emission species (CH^* , C_2^* , soot and soot precursor) and their corresponding colour signal presences. This method implements simultaneous visualisation and investigation of flame emission from the visible to infrared spectrum using a single image. The captured flame images are converted from the 'Red, Green and Blue (RGB)' to the 'Hue, Saturation and Value (HSV)' colour model space. Multiple emission species can be differentiated from the captured images according to their specific ranges from the hue domain.

An infrared-emission-only region is found in between the visible flame chemiluminescence and yellow colour soot emission on the captured two-dimensional (2D) flame images. The water vapour, the carbon dioxide and the direct infrared light emission of polycyclic aromatic hydrocarbons (PAHs) are ruled out as the possible source of the detected infrared emission. However, the comparison with published data indicates that the captured infrared emission associated with soot precursor region, because it is found that the relative distribution of the captured infrared flame emission in both the co-flowing normal diffusion flames (NDFs) and inverse diffusion flames (IDFs) of our experiments coincide with the region of PAH resolved in the published laser experiment. The captured infrared is inferred from the direct infrared light emission of soot precursor which excludes PAHs. It may also attribute to the soot precursor which selectively scattering the soot infrared radiation. It is interesting to note that the ignition process starts with the development of a blue flame in the all of the case studies. Subsequently, the infrared soot precursor and visible yellow sooty flame simultaneously occur.

This thesis attempts to investigate the flame ignition and propagation characteristics by applying various experimental diagnostic techniques, which include direct high-speed imaging, schlieren imaging, stereo imaging and two-colour flame temperature measurement techniques. The results have indicated that the ignition location, CO_2 concentration and plate surface temperature have significant effects on the initial flame

propagation properties, flame temperature and soot formation in the impinging flame ignition process. The flame temperature is evaluated with the help of a modified two-colour method, by measuring glowing thin SiC fibres that are positioned in the flow field. It is evident that soot production is susceptible to ignition location from the stages of ignition to a stable flame condition, and so are the active chemical species such as CH^* and C_2^* . Enormous soot is accumulated during the ignition process when the flame is initiated from the nozzle exit. The increase of CO_2 concentration significantly inhibits the soot formation and reduces the flame temperature. The wall quenching phenomenon takes place in each case due to the cool plate effect. The increase of plate surface temperature shortens the time span from flame ignition to a steady state whilst suppressing the soot formation. Furthermore, the flame temperature will increase when the equivalence ratio approaches unity.

The absolute soot propagation velocity determination in three-dimensional (3D) space relies on the strength of the flame 3D reconstruction technique via the high-speed stereo imaging technique. The pixel correspondence issue between two sequential frames is resolved by the optical flow Lucas-Kanade algorithm. The correspondence of the 3D coordinate is obtained from its corresponding 2D mapping, thereby determining the instantaneous soot propagation speed. This method can also be utilised in wildfire studies.

Table of Contents

Declaration	ii
Acknowledgements	iii
Publications	v
Abstract	vi
Table of Contents	viii
Nomenclature	xii
List of Tables	xvi
List of Figures	xvii
Chapter 1 Introduction	1
1.1 Motivations	1
1.2 Aims and Objectives	3
1.2.1 Aims	3
1.2.2 Objectives.....	3
1.3 Thesis Outline	5
Chapter 2 Literature Review	6
2.1 Introduction	6
2.2 Flame classification.....	6
2.2.1 Diffusion and premixed flames	6
2.2.2 Laminar and turbulent diffusion flames	11
2.3 Flame Light Emission	15
2.3.1 Flame chemiluminescence	15
2.3.2 Blackbody radiation of soot	17
2.3.3 IR emission of water and carbon dioxide.....	22
2.3.4 IR emission of PAH.....	24
2.3.5 Ultraviolet emission of OH*	27
2.4. Flame Ignition and Propagation	28
2.4.1 Ignition definition	28
2.4.2. Ignition systems	28
2.4.3 Ignition location	31
2.4.4 Burning velocity and flame speed.....	32

2.5 Impinging Flames	32
2.5.1 Introduction	32
2.5.2 Impinging flame structure	33
2.5.3 Impinging flame patterns	34
2.5.4 Impact factors of impinging flames	37
2.6 Experimental Flame Imaging Diagnostic Techniques	38
2.6.1 Introduction	38
2.6.2 Schlieren imaging.....	39
2.6.3 Laser imaging.....	42
2.6.4 Digital flame colour discrimination methodology	44
2.6.5 Thermal imaging and thermal couples	47
2.6.6 Stereo imaging	48
2.7 Summary	53
Chapter 3 Simultaneous Multiple Light Emission Tracking by a Single Camera: Method and Algorithm	54
3.1 Introduction	54
3.2 Light Emission of Hydrocarbon Flames	55
3.3 Digital Flame Colour Discrimination Methodology	55
3.4 Flame Visualisation from the Infrared to Visible Spectrum via an Optimised Digital Imaging Processing Method.....	56
3.5 Algorithm of the Image Post-processing Technique	58
3.5.1 Conversion from RGB to HSV colour model.	58
3.5.2 Denoising the mask of the flame image.....	58
3.5.3 Conversion of images from the HSV to RGB model with selective enhancement of weak emission.....	60
3.6 Flame Chemiluminescence Measurement.....	60
3.7 Summary	62
Chapter 4 Simultaneous Multiple Light Emission Tracking by a Single Camera: Infrared Flame Emission Study.....	64
4.1 Introduction	64
4.2 Identification of Infrared Flame Emission	64
4.2.1 Identification of infrared emission via a stereo adapter and optical	

filters	64
4.2.2 Identification of infrared emission via a blackbody infrared calibrator and heated wire	67
4.3 Source of Captured Infrared Flame Emission.....	69
4.3.1 Combination of colouration of the blue and orange flames.....	69
4.3.2 Over-exposure of the sooty flame	70
4.3.3 Water and carbon dioxide.....	70
4.3.4 Blackbody radiation of low-temperature-soot	71
4.3.5 Soot Precursor	73
4.4 Multiple Light Emission Evolution in the Ignition Process of Fundamental Flame Models.....	78
4.4.1 Ignition process of a free jet propane non-premixed flame	78
4.4.2 Ignition process of co-flowing normal diffusion and inverse diffusion flames	80
4.4.3 Ignition process of a methane impinging flame	81
4.5 Summary	84
Chapter 5 Ignition Location Effect on Soot and Species Formation Using Simultaneous Multiple Light Emission Tracking and Schlieren Imaging	85
5.1 Introduction.....	85
5.2 Experimental Procedure	87
5.2.1 Experimental setup.....	87
5.2.2 Selective digital image enhancement technique	89
5.3 Results and Discussion.....	89
5.3.1 Sooty flame dominated ignition process	90
5.3.2 Blue flame dominated ignition process.....	99
5.3.3 Plate temperature effects on flame characteristics	103
5.4 Summary	105
Chapter 6 Effects of Ignition Location on Soot and Species Formation in the Impinging Configuration through Tracking Flame Light Emission and Temperature	106
6.1 Introduction.....	106
6.2 Two-colour Method.....	106
6.3 Experimental Procedure	108

6.3.1 Experimental setup.....	108
6.3.2 Flame temperature measurement	110
6.3.3 Selective digital image enhancement technique	111
6.4 Results and Discussion.....	111
6.5 Summary	117
Chapter 7 Co-Flow Effect on the Ignition Process	118
7.1 Introduction.....	118
7.2 Experimental Setup	118
7.3 Results and Discussion.....	120
7.3.1 Image processing method.....	120
7.3.2 Colour images analysis	126
7.3.3 Schlieren image analysis	130
7.4 Summary	132
Chapter 8 3D Flame Reconstruction and Flame Velocity Measurement	133
8.1. Background of the Stereo Imaging Technique	133
8.2 Stereo Imaging Procedure	134
8.2 3D Reconstruction of Flame	136
8.3 Flame Velocity Measurement.....	139
8.3.1 Pixel intensity threshold and geometry	139
8.3.2 Optical flow estimation: Lucas-Kanade method.....	143
8.3.3 Comparison of two methods	149
8.4 Optical Flow of a Schlieren Image Sequence	150
8.5 Summary	151
Chapter 9 Conclusion and Future Work.....	152
9.1 Conclusion	152
9.2 Scope of Future Work	155
References	156

Nomenclature

Acronyms

1D	One-dimensional
2D	Two-dimensional
3D	Three-dimensional
BOS	Background Oriented Schlieren
CCD	Charge Coupled Device
CFD	Computational Fluid Dynamics
CMOS	Complimentary metal-oxide-semiconductor
CT	Computed Tomography
DFCD	Digital Flame Colour Discrimination
DNS	Direct Numerical Simulation
EGR	Exhaust Gas Recirculation
FGR	Flue Gas Recirculation
fps	Frames per second
H.O.T	Higher order terms
HSV	Hue, Saturation, Value
IDF	Inverse diffusion flame
LES	Large Eddy Simulation
NASA	The National Aeronautics and Space Administration
NDF	Normal diffusion flame
PAH	Polycyclic Aromatic Hydrocarbon
PIV	Particle Image Velocimetry
PLII	Planar Laser-induced Incandescence
PLIF	Planar Laser-induced Fluorescence
RGB	Red, Green, Blue
RMS	Root Mean Squared
UIBs	Unidentified Infrared Bands

Abbreviations

CI engine	Compression-ignition engine
DCM	Dichloromethane
DPIV	Digital image particle velocimetry
emf	Thermo Electromotive Force
FPIV	Film recording image velocimetry
IC engine	Internal combustion engines
IR	Infrared
Le	Lewis number
Re	Reynolds number
SI engine	Spark-ignition engine
SiC	Silicon carbide
UV	Ultraviolet
VIS	Visible

Greek

α	Thermal diffusivity
$\alpha_{A,B}$	Seebeck coefficient
λ	Wavelength
μ	Dynamic viscosity
ρ	Density
ϕ	Equivalence ratio

Symbols

b	Wien's displacement constant
c	Speed of light in a vacuum
C	Gas concentration
c_f	Specific heat capacity
d	Mass diffusivity

d_q	Quenching distance
e	Photon energy
E_s	Seebeck voltage
ϵ_λ	Spectral emissivity
f	Frequency of the radiation
f_v^*	Depletion reservoir for the soot growth
h	Planck's constant
h_f	Height of the flame
k	Thermal conductivity
k_s	Surface specific rate
m	Mass flow
M	Molecular mass
Pr	Prandtl number
q	Heat release every single mole of combustion
Sc	Schmidt number
S_l	Laminar flame velocity
S_t	Turbulent flame velocity
S_u	Burning velocity
S_λ	Instrument factor
T	Temperature
u	Velocity
$\alpha_{A,B}$	Seebeck coefficient

Chemical symbols

C_2	Excited-state C_2
C_3H_8	Propane
CH	Methylidyne radical
CH^*	Excited-state CH
CH_4	Methane

CO	Carbon Monoxide
CO ₂	Carbon Dioxide
H ₂	Hydrogen
H ₂ O	Water
KBr	Potassium bromide
LiF	Lithium fluoride
N ₂	Nitrogen
NaCl	Sodium chloride
NO	Nitrous Oxide
NO _x	Nitrous oxides
O ₂	Oxygen
OH	Hydroxyl radicals
SO ₂	Sulfur Dioxide
SO ₃	Sulfur Trioxide

List of Tables

Table 2. 1 Assignments of infrared absorption peaks to functional groups.	26
Table 5. 1 CO ₂ flow conditions and corresponding camera (Photron SA4) settings in each case.....	88
Table 6. 1 SiC fibre thermal properties.	108
Table 6. 2 Test conditions.....	109
Table 7. 1 Flow conditions	119

List of Figures

Fig. 2. 1 The flame profiles with various air concentration.	8
Fig. 2. 2 Colour images of a methane flame with an increase in air concentration (Fijałkowski, 2011).	9
Fig. 2. 3 (a) The initial temperature effect on S_i ; 1: ethene/ air flame, 2: propane/ air flame, 3: methane/ air flame, (b) Hydrogen/ air premixed flame propagation speed under different T_0 (Turns, 2000).	10
Fig. 2. 4 (a) The laminar and turbulent premixed flames profiles for a Bunsen burner, (b) The relation between the flow rate of gas mixture, U_f , and height of the flame, h . (Lee, North and Santavicca, 1993).....	10
Fig. 2. 5 Structure of the candle flame (Roth, 2003).....	11
Fig. 2. 6 The radial cross-section of gas concentration and the temperature distribution of an ideal laminar jet diffusion flame (Irvin Glassman and Yetter, 2008).	12
Fig. 2. 7 The real flame front structure of a laminar diffusion flame (Irvin Glassman and Yetter, 2008).	13
Fig. 2. 8 (a) Images of a laminar and turbulent propane diffusion flame and (b) Turbulent ethylene jet diffusion flames with various Re (Muñiz and Mungal, 2001).	14
Fig. 2. 9 The relation between the flame height and Re (Molkov and Saffers, 2013).	14
Fig. 2. 10 The CH^* and C_2^* emission of a hydrocarbon flame (<i>Chemiluminescence</i> , 2005).	15
Fig. 2. 11 (a) Propane-air premixed flame image, (b) Flame CH^* emission with narrow band filter of 430 ± 4 nm and (c) Flame C_2^* emission with a narrow band filter of 576 ± 4 nm.....	16
Fig. 2. 12 Schematic of the soot formation mechanism.	17
Fig. 2. 13 Axial profiles of intensities of scattering and fluorescence at 90° for a laminar methane diffusion flame (Garo, Prado and Lahaye, 1990).	18
Fig. 2. 14 The formation of PAH (Richter and Howard, 2000).	18
Fig. 2. 15 Micrograph of soot aggregates (Tian <i>et al.</i> , 2007).....	19

Fig. 2. 16 The Planck emission of the soot particles (<i>Black body radiation and planck's radiation law</i> , 2017).	21
Fig. 2. 17 Image sequence of the ignition process of a methane diffusion flame with co-flow air.	21
Fig. 2. 18 Flame infrared emission measured with an NaCl prism. The upper curve was measured with wider slits than the lower (Plyler and Plyler, 1948).	22
Fig. 2. 19 Infrared emission of a Bunsen flame measured with a LiF prism (Plyler and Plyler, 1948).	23
Fig. 2. 20 Infrared emission of a Bunsen flame in the region of 12 μm to 24 μm measured with a KBr prism (Plyler and Plyler, 1948).	23
Fig. 2. 21 The comparison of flame spectra at different measurement positions (Lindecrantz, 2010).	24
Fig. 2. 22 Telescope image of the W5 star forming in the VIS and IR regions. The infrared emission is shown in red, which originates in PAHs (Administrator, 2016).	25
Fig. 2. 23 C-C and C-H vibrational modes (Ota, 2015).	25
Fig. 2. 24 The PAH emission spectrum of the Orion Bar from 3 μm to 20 μm (Els Peeters, 2002).	25
Fig. 2. 25 The infrared spectrum of the DCM-soluble material sample (Mckinnon, Meyer and Howard, 1996).	26
Fig. 2. 26 The OH spectrum in a lean premixed methane-air flame (Griebel, Siewert and Jansohn, 2007).	27
Fig. 2. 27 Zero-temperature-gradient of hot object ignition ($T_{w1} < T_{w2} < T_{w3} < T_{w4}$) (Yang, 1962).	29
Fig. 2. 28 (a) The relationship between the minimum ignition energy E_{min} and the electrode interval d , and (b) The relationship between the minimum ignition energy E_{min} and the equivalence ratio ϕ (Ballal and Lefebvre, 1979).	31
Fig. 2. 29 Structure of an impinging non-reacting jet (Chloe and Mcdaid, 2013).	33
Fig. 2. 30 Structure of an impinging reacting jet (Chloe and Mcdaid, 2013).	34
Fig. 2. 31 Eight typical flame patterns. The flames are captured under (a) 1/50 s shutter speed and (b) 1/4000 s shutter speed (Foat, Yap and Zhang, 2001).	35
Fig. 2. 32 A standard Z-configuration parallel-light schlieren system (Gnani <i>et al.</i> ,	

2015).	40
Fig. 2. 33 A typical BOS system using a digital CCD camera to focus a background image with random oriented points.	41
Fig. 2. 34 Schematic of a typical PIV imaging system.	42
Fig. 2. 35 Schematic of a typical PLIF system.	44
Fig. 2. 36 (a) The sakura photo displayed in the RGB colour model space; (b) The photo is separated into Red, Green and Blue channels, respectively (<i>Cherry Blossoms in Japan: All About Sakura and Hanami - LIVE JAPAN</i> , 2018).	45
Fig. 2. 37 (a) The RGB colour model space (Nishad and Manicka Chezian, 2013) and (b) the HSV colour model space (Cardani, 2001).	46
Fig. 2. 38 The hue value distribution of orange soot and flame chemiluminescence (CH^* and C_2^*) are from 0 to 80 degrees and 180 to 300 degrees respectively.	46
Fig. 2. 39 Optical illusions examples (<i>Fun Optical Illusions</i> , 2015).	48
Fig. 2. 40 (a) Single camera system. (b) Two-camera system. (Tombari <i>et al.</i> , 2008)	49
Fig. 2. 41 (a) Schematic of the epipolar constraint and (b) The stereo-camera system in a standard form. (Mattoccia, 2014)	50
Fig. 2. 42 (a) Schematic of the depth measurement and (b) Horopter in the stereo imaging system. (Mattoccia, 2013)	50
Fig. 2. 43 A pair of flame stereo images.	51
Fig. 2. 44 (a) Stereo adapter, (b) Structure of the stereo adapter and (c) Schematic of the stereo adapter function (Wang, 2009).	52
Fig. 2. 45 Time-resolved 3D structure reconstruction of an enhanced blue flame in the impinging configuration (Wang <i>et al.</i> , 2013).	53
Fig. 3. 1 Images of a propane non-premixed flame at 0.102 s after ignition: (a) The original image at a shutter speed of 1/2000 s; (b) the orange sooty flame region; (c) the chemiluminescence-induced blue flame which is enhanced 20 times; (d) the infrared soot emission which is enhanced 15 times; (e) the entire image after selective image enhancement and (f) the colour distribution histogram in hue space.	57
Fig. 3. 2 (a) The flame mask is composed of the blue pixels with hue values from 180 to 252 degrees, (b) The specific blue pixels whose intensity is larger than	

500, (c) The mask after the nonlinear digital filtering technique and (d) Small objects are removed from the binary image.	59
Fig. 3. 3 The 3×3 nonlinear digital filtering technique model.	59
Fig. 3. 4 The spectral sensitivity of the high-speed Photron SA4 camera (Yang, Ma and Zhang, 2015).	61
Fig. 4. 1 (a) An example of a captured synchronous flame image pair, (b) The processed synchronous image pair in black and white format and (c) The displacement of the left and right images.	65
Fig. 4. 2 The synchronous images of a propane partially premixed flame (a) without a filter and (b) with a visible wideband filter (385 – 725 nm wavelength) and their corresponding colour distribution histograms in hue space.....	66
Fig. 4. 3 The synchronous images of a propane diffusion flame with (a) an infrared filter (760 nm cut-on wavelength) and (b) a visible light filter (385 – 725 nm) and their corresponding colour distribution histograms in hue space.....	67
Fig. 4. 4 The processed synchronous image pair with (a) an infrared filter and (b) a visible light filter (385 – 725 nm) in black and white format. The number of pixels of the left and right images are 20814 and 15673 respectively. (c) The deviation between the synchronous images is 24.7 %.	67
Fig. 4. 5 (a)-(c) The emission of the calibrator captured by the high-speed camera and the corresponding colour distribution histograms in hue space at temperatures of 480 °C, 490 °C and 510 °C, respectively.	68
Fig. 4. 6 (a)-(c) The hot wire images captured by the high-speed camera and corresponding colour distribution histograms in the hue space at temperatures of 472 °C, 506 °C and 522 °C respectively.	69
Fig. 4. 7 Left: The captured image of a propane diffusion where the infrared emission is enhanced 15 times. Right: The colour distribution histogram in hue domain regarding the original captured image without enhancement.	70
Fig. 4. 8 Image sequence of the early stage of the ignition process of co-flowing methane flame.	70
Fig. 4. 9 The captured images of lean premixed flames of (a) propane/air and (b) methane/air at an equivalence ratio of 0.98 and their corresponding colour distribution histograms in hue space.	71

Fig. 4. 10 The black body radiation spectrum for temperatures between 300 K and 10,000 K in a log-log diagram (Tinetti, Encrenaz and Coustenis, 2013).....	72
Fig. 4. 11 (a) Ignition instance of (a) diffusion propane flame, (b) methane co-flow flame and (c) methane impinging flame.	73
Fig. 4. 12 (a) Direct imaging photo; (b) soot volume fraction from PLII; (c) superimposed PLIF images of OH and PAHs of a laminar propane co-flowing NDF (Xiong, Cha and Chung, 2015). Post-processed flame images of (d) methane and (e) propane co-flowing NDF at the steady state.	75
Fig. 4. 13 (a) Colour-map and (b) the visible colour image of ethylene-air IDFs with contours of peak time-averaged PLIF and PLII signals overlaid (Mikofski <i>et al.</i> , 2007). Post-processed image of propane-air IDFs flowing with (c) low and (d) high air velocities.	76
Fig. 4. 14 The transmission of the bandpass infrared filter (Winder, 2002).	77
Fig. 4. 15 Schematic of selective infrared scattering from soot precursor.	77
Fig. 4. 16 (a) The original and (b) selectively enhanced image sequences of the ignition process in a propane non-premixed flame with the corresponding number of pixels.....	79
Fig. 4. 17 The time-dependent number of pixels of the soot-induced orange flame, infrared soot precursor and the chemiluminescence-induced blue flame. Lines are provided to guide the eyes.....	79
Fig. 4. 18 (a) Original and post-processed image sequence of a methane-air co-flowing NDF ignition process and (b) Post-processed image sequence of a propane-air sooty co-flowing IDF ignition process.	81
Fig. 4. 19 (a) Post-processed image sequences. The infrared emission and blue flame are enhanced 30 times, (b) Time-dependent number of pixels of soot precursor, soot and chemiluminescence-induced blue flame emission and (c) Time-dependent colour-modelled CH^*/C_2^* of the blue flame region in an impinging methane flame.	83
Fig. 5. 1 Schematic of the experimental setup.	88
Fig. 5. 2 (a) Original image; 15 times enhancement of (b) Infrared flame emission and (c) Chemiluminescence-induced blue flame and (d) Image after selective image enhancement of the '6CH ₄ +3CO ₂ ' case 96 ms after ignition.....	89

Fig. 5. 3 The five selected ignition locations (top left) and the unburned fuel streams under different flow conditions.....	90
Fig. 5. 4 Simultaneous (a) Enhanced colour and (b) Schlieren image sequences of the ‘6CH ₄ ’ ignition process initiated at the ‘Nozzle’ location.....	91
Fig. 5. 5 Simultaneous (a) Enhanced colour and (b) Schlieren image sequences of the ‘6CH ₄ ’ ignition process initiated at the ‘Middle’ location.	92
Fig. 5. 6 Simultaneous (a) Enhanced colour and (b) Schlieren image sequences of the ‘6CH ₄ ’ ignition process initiated at the ‘Plate’ location.	92
Fig. 5. 7 Simultaneous (a) Enhanced colour and (b) Schlieren images sequences of the ‘6CH ₄ ’ ignition process initiated at the ‘Plate 25’ location.	93
Fig. 5. 8 Simultaneous (a) Enhanced colour and (b) Schlieren image sequences of the ‘6CH ₄ ’ ignition process initiated at the ‘Plate 50’ location.	93
Fig. 5. 9 Time-dependent (a) Number of pixels of infrared flame emission, (b) Number of pixels of the visible orange sooty flame, (c) Mean intensity of the visible sooty flame and (d) Colour-modelled CH*/C ₂ * of the chemiluminescence-induced blue flame, of the ‘6CH ₄ ’ cases.	95
Fig. 5. 10 Colour map of the colour-modelled CH*/C ₂ * ratio distribution for the ‘6CH ₄ Nozzle’ case and the images of the sooty flame emission in the visible and infrared spectra respectively of the ‘6CH ₄ Nozzle’ case, 120 ms after ignition.	96
Fig. 5. 11 Colour maps of the colour-modelled CH*/C ₂ * ratio distribution of the (a) ‘Nozzle’, (b) ‘Middle’, (c) ‘Plate’, (d) ‘Plate 25’ and (e) ‘Plate 50’ ‘6CH ₄ ’ cases.	97
Fig. 5. 12 (a) Enhanced colour and (b) Schlieren image sequences of the ‘6CH ₄ +4CO ₂ Middle’ ignition process captured simultaneously. The blue and infrared region are enhanced 15 times.	97
Fig. 5. 13 Time-dependent number of pixels of the infrared flame emission, the soot-induced orange flame and the blue/green intensity ratios of the chemiluminescence-induced blue flame of (a)-(c) the ‘6CH ₄ +3CO ₂ ’ and (d)-(f) the ‘6CH ₄ +4CO ₂ ’, respectively.	98
Fig. 5. 14 Image sequences of the ‘6CH ₄ +5CO ₂ ’ ignition process initiated at the (a-e) ‘Nozzle’, ‘Middle’, ‘Plate’, ‘Plate 25’ and ‘Plate 50’ locations, respectively. The	

blue flame and infrared emission colourations are enhanced 10 times.....	100
Fig. 5. 15 Time-dependent (a) Number of pixels of the infrared emission, (b) Number of pixels of the soot-induced orange flame and (c) Blue/green intensity ratios of the chemiluminescence-induced blue flame of the ‘6CH ₄ +5CO ₂ ’ flame.	101
Fig. 5. 16 Image sequences of the ‘6CH ₄ +8CO ₂ ’ ignition process initiated at the (a) ‘Middle’ and (b) ‘Plate 50’ locations, respectively. The blue flame and infrared emission colourations are enhanced ten times.	102
Fig. 5. 17 (a) Quantity and mean intensity of the soot emission with varying CO ₂ concentration and (b) Time taken until reaching a steady state with different CO ₂ concentrations.....	103
Fig. 5. 18 Schlieren images of the cold methane flow with the plate temperature 23 °C and 100 °C.	103
Fig. 5. 19 Time-dependent (a)-(c) Total number of pixels of infrared flame emission and orange soot emission and (d)-(f) CH*/C ₂ * ratio with different initial plate temperatures for the ‘6CH ₄ ’, the ‘6CH ₄ +3CO ₂ ’, and the ‘6CH ₄ +4CO ₂ ’ cases respectively. The flames are all initiated at the nozzle exit.....	104
Fig. 6. 1 The SiC bundle containing 500 ultra-thin filaments.....	107
Fig. 6. 2 Experimental setup.	108
Fig. 6. 3 (a) Stereo adaptor, (b) Stereo images pair. A 10-stop ND filter is applied on the left side and the right side directly images the flame without any filter. ...	110
Fig. 6. 4 Comparison between measured and reference temperature of calibration source.	110
Fig. 6. 5 (a) Image after selective image enhancement, (b) Visible soot emission, (c) Blue flame enhanced 10 times and (d) Infrared soot precursor emission enhanced 10 times.	111
Fig. 6. 6 Image sequences of the ‘Air 4’ ignition process initiated at the (a) ‘Nozzle’, (b) ‘Middle’ and (c) ‘Plate’ cases respectively.	113
Fig. 6. 7 Fibre L6 temperature evolution in the wall quenching process of the ‘Air 4’ cases ignited at the ‘Nozzle’, ‘Middle’ and ‘Plate’ locations.	113
Fig. 6. 8 Time-dependent number of pixels of (a) Soot-induced orange flame and (b) Infrared soot precursor and (c) colour-modelled CH*/C ₂ * ratios of the	

chemiluminescence-induced blue flame, of the ‘Air 4’ cases.....	114
Fig. 6. 9 Image sequences of the ignition process of (a) the ‘Air 8’, (b) ‘Air 10’ and (c) ‘Air 12’ cases. The flames are initiated at the nozzle exit.....	116
Fig. 6. 10 Time-dependent temperature variation of the L1, L2 and L3 fibres, ignited at nozzle in the ‘Air 8’ and ‘Air 10’ cases. ‘L’ and ‘R’ represent flame left and right sides of the respectively.....	117
Fig. 7. 1 (a) The schematic of the burner and (b) cross-sectional drawings of the burner (Chloe and Mcdaid, 2013).....	119
Fig. 7. 2 Schematic of the experimental setup.....	120
Fig. 7. 3 (a) The original image with 1/500 s shutter speed, (b) The chemiluminescence-induced bluish flame regime enhanced 25 times, (c) The infrared soot precursor enhanced 30 times and (d) The entire image after selective imaging enhancement.....	121
Fig. 7. 4 The schlieren and the enhanced image sequences of the ignition processes in the (a) ‘Pure methane’, (b) ‘Air 14’ and (c) ‘Air 75’ with the corresponding number of pixels.....	124
Fig. 7. 5 Histograms of the flame colour distribution evolution in the hue domain during the ignition processes of the (a) ‘Pure methane’, (b) ‘Air 14’ and (c) ‘Air 75’ cases.....	125
Fig. 7. 6 The time-dependent number of pixels of the soot-induced orange flame, infrared soot precursor and the chemiluminescence-induced blue flame of the (a)-(c) ‘Pure methane’, ‘Air 14’ and ‘Air 75’ flames respectively.....	127
Fig. 7. 7 The time-dependent mean intensities of the (a) Soot-induced orange flame and (b) Infrared emission regions and (c) Colour-modelled CH^*/C_2^* ratios of the chemiluminescence-induced blue flame.....	128
Fig. 7. 8 Comparisons of repeated attempts for the ‘Air 14’ flame: (a) Enhanced images, (b) Number of pixels, (c) and (d) Mean intensity of the soot and infrared emission respectively and (e) Measured CH^*/C_2^*	130
Fig. 7. 9 The cold fuel flow patterns at different co-flow air flow rates.....	130
Fig. 7. 10 (a) Illustration of the tip and bottom positions, (b) the tip position tracing with time and (c) the bottom position tracing with time at different air flow rates.....	131

Fig. 8. 1 (a) Overview of a stereo imaging procedure (Mattoccia, 2014) and (b) Stereo images pairs imaged from the angles of depression 30°, elevation 30°, right 30°, left 30° and in parallel to the camera.	134
Fig. 8. 2 The schematic of the rectification process. The stereo imaging is rectified to the standard form (Mattoccia, 2013).	135
Fig. 8. 3 3D coordinate measurement via triangulation (Tombari <i>et al.</i> , 2008).....	135
Fig. 8. 4 (a) The five calibrating locations based on the left view of the stereo imaging and (b) The epipolar between the left and right views.....	136
Fig. 8. 5 (a) The captured pool fire image and its corresponding (b) flame 3D reconstruction result. The blue circle marks the magnified region in Fig. 8.6.	137
Fig. 8. 6 (a) The time-dependent flame image sequence, (b) The 3D structure magnification of the blue circled region in Fig. 8.5 and (c) The time-dependent 3D flame structures.	138
Fig. 8. 7 The stereo image pair of the burner, enhanced 20 times.	138
Fig. 8. 8 The target region (b) is filtered from the local area marked in (a). (c) The centre of the target region.	139
Fig. 8. 9 (a) The path of the target region (blue circle), (b) The 3D movement of the target region and (c) The time-dependent velocity development of the target region.....	140
Fig. 8. 10 (a) The path of the target region (green circle), (b) The 3D movement of the target region and (c) The time-dependent velocity development of the target region.....	141
Fig. 8. 11 (a) The path of the target region (purple circle), (b) The 3D movement of the target region, and (c) The time-dependent velocity development of the target region.....	142
Fig. 8. 12 (a) The path of the target region (yellow circle), (b) The 3D movement of the target region and (c) The time-dependent velocity development of the target region.....	142
Fig. 8. 13 The optical flow of two sequential frames. The vector scales were enhanced 30 times.	143
Fig. 8. 14 The time-dependent vector field evolution of the flame images. The vector scales were enhanced 30 times.....	144

Fig. 8. 15 Schematic of the velocity measurement process.	146
Fig. 8. 16 The time-dependent 3D velocity vector field variation.	147
Fig. 8. 17 (a) The target regions marked by the blue circles on the flame image and (b) The velocity variation in the selective regions.	148
Fig. 8. 18 2D vector field based on different window sizes.....	149
Fig. 8. 19 The velocity measurement results of local regions with different window sizes.	149
Fig. 8. 20 The soot velocity variation of the target region measured by the (a) Pixel intensity threshold and (b) Optical flow methods.	150
Fig. 8. 21 Schlieren images processed by the optical flow method.	150

Chapter 1

Introduction

1.1 Motivations

Combustion is the main mechanism of energy utilisation. Based on the World Energy Resources report in 2015, 85.99% of the energy used by humans is derived from combustion (World Energy Council, 2016). Combustion is of great significance for domestic use. Electrical energy relies principally on combustion. In 2015, 40% of the electricity demand was supplied by coal combustion (World Energy Council, 2016). Most transportation relies on the combustion of petroleum products. With respect to industrial processes, combustion phenomena take place in the steel and metal smelting industry, heat treatment and some industrial burning devices, such as boilers, chemical fluid heaters, glass melting and solid drying (El-Mahallawy and Habik, 2002). Combustion also plays an important role in environmental protection, for instance, in waste incineration. On the other hand, engine emission waste needs to be strictly controlled, which contains unburnt hydrocarbons, nitrogen oxides (NO_x), carbon monoxide (CO), sulfur dioxide (SO₂) and sulfur trioxide (SO₃), as well as various forms of particulate matter (Lodgejr, 1996). Besides, wildfire and explosion disasters may take place if combustion gets out of control, which may result in the immeasurable casualties and property losses. Therefore, combustion investigation has great importance in industry and daily life.

The ignition of a flammable gas mixture is always accompanied by complicated chemical reactions and multiple parameter variations, such as temperature, pressure and flame propagation velocity. The investigation of ignition processes is highly desirable in many combustion devices, especially in internal combustion (IC) engines. Unlike the continuous combustion in a gas turbine where ignition will only affect the flame initiation, the combustion in the spark-ignition (SI) engine is critically dependent on certain ignition process, in particular ignition energy and location, because the inhomogeneous mixture of the fuel and air has to be ignited by a spark plug at a chosen location in each cycle. The combustion efficiency and the evolution

of the distribution of the air/fuel/products are strongly affected by the ignition location in a non-uniform and unsteady turbulent flow field. Laboratory studies often apply an impinging configuration to simulate the interaction between the flame and piston in the combustion chamber, aiming to understand its effect on the ignition process. Hence flame ignition, especially the effect of ignition location on impinging flames is intensively studied in this thesis.

Optical diagnostics are the primary approaches for the experimental flame laboratory study and industrial fire detection (Albers and Agrawal, 1999; Otsuka and Wolanski, 2001). Laser imaging is a non-intrusive measurements method, which can visualise the spatial and temporal flame evolution. Particle image velocimetry (PIV) provides the velocity information of the flow fields. Planar laser-induced fluorescence (PLIF) technique is applied to measure the species concentrations of hydroxyl radicals (OH) and methylidyne radical (CH) in the reaction zone and quantity of the pollutants, such as NO, CO and SO₂ (Kaminski *et al.*, 2000). Typical laser imaging systems can track only a single radical species. Research can track several radicals simultaneously with multiple charge-coupled device (CCD) cameras (Ahmed and Mastorakos, 2006a). The experimental setup and operation procedure are complicated. The technique remains expensive to implement, and the optical access required may result in a significant redesign of the combustion chamber. These factors make laser imaging diagnostics inappropriate for real industrial applications. Thus, a simple approach that can simultaneously track multiple radicals/ particles species is urgently required.

In this thesis, with the help of a novel image post-processing technique, the time-dependent simultaneous multiple flame light emission imaging from the visible to infrared spectrum is implemented by using a single high-speed complementary metal-oxide-semiconductor (CMOS) camera for the first time. It is found that the flame light emission is correlated to the flame colour that is captured by a digital colour camera. During the combustion process, the molecule/particle species emit at specific wavelengths. The CCD/CMOS sensor of the camera receives the light which is then converted to an electric signal via an image processor, and finally presented in various colours on the digital colour image. For the hydrocarbon flame, the orange portion of the flame is a consequence of soot blackbody radiation. The blue flame is attributed to

the flame chemiluminescence, which is mainly composed by excited-state CH (CH^*) and excited-state C_2 (C_2^*) (Gaydon, 1974). The excited-state OH (OH^*) locates in the ultraviolet (UV) spectrum which is beyond the human vision. The image post-processing technique that is introduced in this thesis can differentiate the CH^* , C_2^* and soot particle emission along with selective infrared flame emission according to their specific hue ranges in the 'Hue, Saturation, Value' (HSV) colour space. The captured infrared could be either the direct infrared light emission or the selective infrared scattering from the soot precursor. The technique has the potential for the monitoring of flame light emission evolution in real combustion devices at high pressure and temperature by applying a borescope.

In the thesis, flame case studies are carried out using the image processing technology combined with other optical diagnostic methodologies. An optical temperature measurement; a modified two-colour method on glowing thin silicon carbide (SiC) fibres in the flow field, is used to evaluate the flame temperature. Schlieren imaging is utilised to observe the hot gas propagation. Modified stereo imaging allows measurement of the flame propagation velocity in three dimensions.

1.2 Aims and Objectives

1.2.1 Aims

To develop various advanced imaging-based diagnostics techniques for lab-scale flame, industrial applications and wildfire studies.

1.2.2 Objectives

Flame diagnostic techniques:

- To develop an image post-processing method which can track multiple flame light emission (CH^* , C_2^* , soot and selective infrared flame emission) by using a single camera; Photron SA4. The OH^* detection is excluded since the camera is insensitive to the UV spectrum.
- To perform several confirmatory experiments to prove that the captured pinkish portion of the hydrocarbon flame image is from the infrared flame emission.

- To investigate the source of the captured infrared flame emission.
- To measure the local/global flame velocity in three dimensions with the help of stereo imaging.
- To develop an optical flow algorithm to determine the point correspondence between two sequential frames in the stereo imaging system.

Technical challenges:

- It is difficult to identify the captured infrared flame emission species since it may be the superposition of the various radicals/particles/molecules species which emit in the infrared region.
- The flame 3D reconstruction has the same line of sight problem, which is inextricable until now.

Case studies:

- Study of the co-flowing hydrocarbon normal diffusion flame (NDF) and inverse diffusion flame (IDF) with the help of the image post-processing method.
- Investigation into the effects of the ignition location, CO₂ concentration and plate surface temperature on the initial flame propagation properties, flame temperature and soot formation in the methane impinging flame ignition process via direct colour imaging, schlieren imaging, a modified two-colour method and the image post-processing techniques.
- Investigation into the co-flow effect on the ignition process of laminar methane diffusion flames by using high-speed schlieren and colour imaging techniques.
- Reconstruction of the pool fire in three dimensions and measurement of the soot propagation velocity.

1.3 Thesis Outline

This thesis is composed of nine chapters which introduce some advanced imaging diagnostic methods and their application on the flame ignition and propagation studies.

Chapter 2 gives a detailed review of the combustion theory, flame light emission, flame ignition and propagation characteristics, impinging flame and flame optical diagnostic methods.

Chapter 3 develops an image post-processing method which implements simultaneous visualisation and investigation of flame emission from the visible to infrared spectrum by a single image.

Chapter 4 shows some confirmatory experiments that prove that the captured pinkish portion of the hydrocarbon flame is infrared flame emission. The source of the detected infrared flame emission is inferred. The multiple light emission evolution in the ignition process is studied in co-flowing NDF and IDF, impinging flame models.

Chapter 5 introduces the effects of the ignition location, CO₂ concentration and plate surface temperature on the initial flame propagation properties and soot formation in the impinging flame ignition process by using simultaneous direct colour imaging and schlieren imaging techniques.

Chapter 6 introduces the effects of ignition location on flame propagation properties and soot formation of an impinging flame via the tracking of multiple light emission species and temperature.

Chapter 7 presents a co-flow flame study. The co-flow effect on the ignition process of laminar methane diffusion flames is investigated by high-speed schlieren and colour imaging techniques.

Chapter 8 presents the experimental research on measuring the soot velocity of pool fire via the high-speed stereo imaging method.

Chapter 9 lists the main finding of the thesis, as well as the suggestions for future work.

Chapter 2

Literature Review

2.1 Introduction

In this chapter, flames are classified as diffusion or premixed flames, and laminar or turbulent flames and are reviewed in detail. Section 2.3 reviews the features of multiple flame light emission in the ultraviolet, visible and infrared spectra, which include the OH, CH*, C₂*, CO₂, H₂O, soot and PAHs. Following that, a review of flame ignition and propagation processes will be given. Section 2.5 intensively reviews the impinging flame characteristics. Section 2.6 reviews various flame optical diagnostics methods, such as schlieren, thermal, laser and stereo imaging and image post-processing techniques.

2.2 Flame classification

Flames can be classified by the combustion properties (diffusion/ premixed/ partially premixed flames) and the flow properties (laminar/ turbulent flames).

2.2.1 Diffusion and premixed flames

2.2.1.1 Comparison of the diffusion and premixed flame

A flame can be classified as a premixed flame and a non-premixed flame depending on whether the fuel and the oxidiser are mixed before entering the reaction zone. If the fuel and oxidiser are mixed prior to the passage of the reaction zone, the flame is called the 'premixed flame'. The burning rate of the premixed flame is primarily affected by the chemical kinetics, which depends on the fuel concentration, initial temperature and the diameter of the nozzle exit (Law and Sung, 2000). The non-premixed flame represents the case when the fuel and oxidiser are separated at the initial stage before entering the reaction zone, which is also named the 'diffusion flame'. The reaction takes place at the interface between the fuel and oxidiser. The diffusion flame speed is influenced by both the chemical kinetics and the mixing rate of the reactants. Compared with the premixed flame, the burning rate and the temperature of the

diffusion flame are relatively low (Matalon, 2009). The combustion reaction zone of the diffusion flame is larger than that of the premixed flame. The good stability of the diffusion flame reduces the risk of flashback. Nevertheless, soot emissions of the diffusion flame are higher than for the premixed flame.

2.2.1.2 Equivalence ratio

The premixed flame can be divided into two categories: partially premixed (fuel rich) and completely premixed (fuel lean) flames according to the equivalence ratio, ϕ . Equivalence ratio is the ratio of the actual fuel-to-air ratio over the stoichiometric fuel-to-air ratio (Hardalupas *et al.*, 2004), which is expressed by

$$\phi = \frac{F:A}{(F:A)_{st}} = \frac{(A:F)_{st}}{A:F} = \frac{m_f/m_a}{(m_f/m_a)_{st}} = \frac{n_f/n_a}{(n_f/n_a)_{st}} \quad (2.1)$$

where $F:A$ is the fuel-to-air ratio; $A:F$ is the air-to-fuel ratio. m represents the mass, n represents the number of moles. $\phi > 1$ represents a fuel-rich mixture. $\phi < 1$ represents a fuel-lean mixture, which is the partially premixed flame. $\phi = 1$ represents stoichiometric combustion.

The stoichiometric fuel-to-air ratio can be calculated by

$$(F:A)_{st} = \frac{M_f}{(\alpha + \beta/4 - \gamma/2)M_a} \quad (2.2)$$

where α , β and γ are deduced from

$$C_\alpha H_\beta O_\gamma + (\alpha + \frac{\beta}{4} - \frac{\gamma}{2})(O_2 + 3.76N_2) = \alpha CO_2 + \frac{\beta}{4} H_2O + 3.76(\alpha + \frac{\beta}{4} - \frac{\gamma}{2})N_2 \quad (2.3)$$

and M_f and M_a are the molecular mass of the fuel and the air.

The equivalence ratio has a strong influence on the flame profile, flame speed and flame temperature (Cho and Lieuwen, 2005). Fig. 2. 1 shows the flame profiles with different air concentrations.

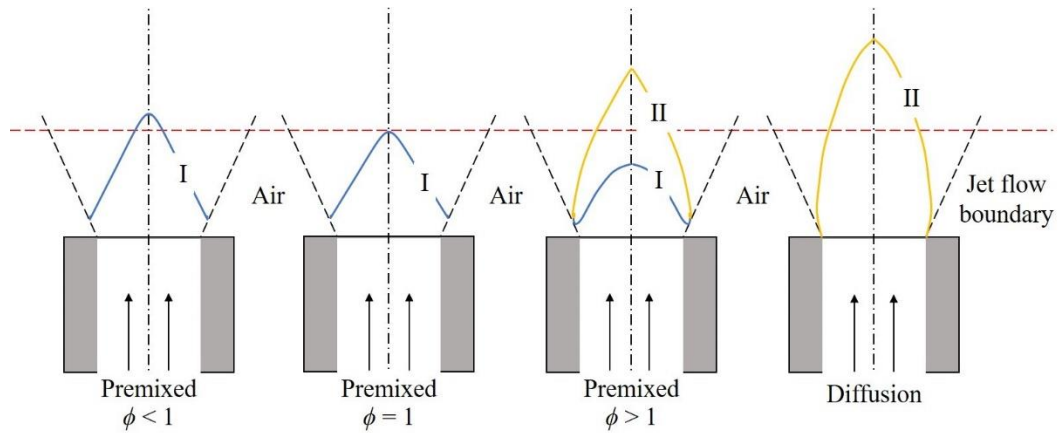


Fig. 2. 1 The flame profiles with various air concentration.

In the fuel lean condition, $\phi \leq 1$, the fuel and air are well premixed before ignition. Only one flame front can be observed, which is attributed to the chemical kinetics. All the fuel is consumed at the flame front. With an increase in air concentration, the height of the flame front gradually increases. In the fuel rich condition, two flame fronts form due to the insufficient air concentration in the premixed gas. The inner flame front I is induced by the chemical kinetics, while the outer flame front II is due to diffusion. Only a portion of the fuel is consumed by the oxygen at the flame front I. The rest of the unburnt fuel is then mixed with the high-temperature combustion products and jets outside the flame front I. Subsequently, the gas mixture is then mixed with the air and continues burning, meanwhile forming the flame front II. With a decrease in air concentration, the flame propagation speed becomes lower and the boundary of the flame front I rises. More unburnt fuel propagates outward of the flame front I, which requires a large amount of air, thereby stretching the flame front II. For the diffusion flame, the combustion develops along with the mixing of the fuel and air and the flame front I no longer exists. The fuel and air are entirely separated by the flame front II. Fig. 2. shows colour images of a methane flame with an increase in air concentration.

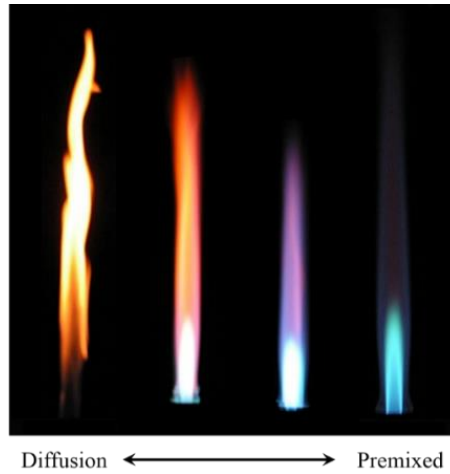


Fig. 2. 2 Colour images of a methane flame with an increase in air concentration (Fijałkowski, 2011).

2.2.1.3 Premixed flames

Premixed flame propagation speed, S_l , is affected by the fuel species, temperature, fuel concentration and pressure. The premixed flame has the highest propagation speed if the equivalence ratio is slightly higher than 1. The flame propagation speed is nearly zero under the super fuel-lean or fuel-rich conditions (Cho and Lieuwen, 2005). The hydrocarbon flame propagation speed is also related to its molecular structure. For the non-saturated hydrocarbons, the flame propagation speed is higher with a decrease in the number of the carbon atoms (Moldoveanu, 2010). On the contrary, S_l is nearly uncorrelated to the number of the carbon atoms in saturated hydrocarbon combustion. S_l will increase with an increase in the initial temperature of the premixed gas mixture, T_0 , as can be seen from Fig. 2. (Turns, 2000). The flame temperature, T_f increases with T_0 , which accelerates the chemical reaction rate and consequently increases the flame propagation speed.

$$T_f = T_0 + \frac{q C_f}{c_f} \quad (2.4)$$

where C_f is the fuel concentration factor. q represents the heat release for each mole of combustion, and c_f is the specific heat capacity of the gas mixture.

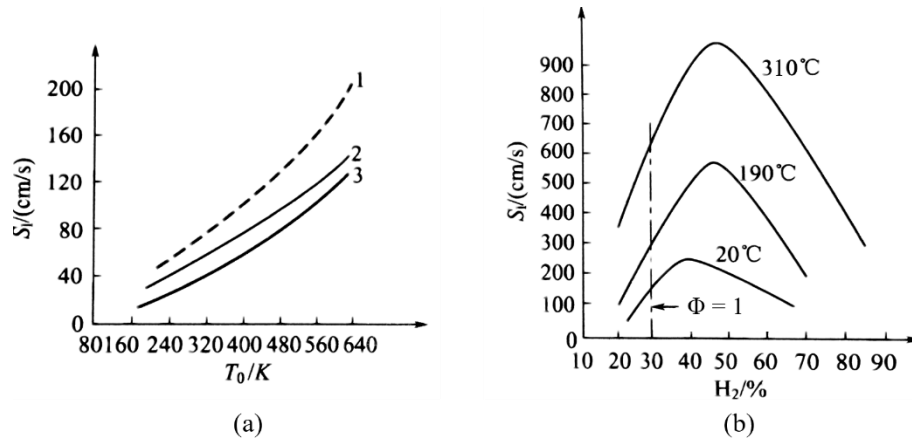


Fig. 2. 3 (a) The initial temperature effect on S_f ; 1: ethene/ air flame, 2: propane/ air flame, 3: methane/ air flame, (b) Hydrogen/ air premixed flame propagation speed under different T_0 (Turns, 2000).

There are quite a few differences between the laminar premixed flame and the turbulent premixed flame. The velocity of the turbulent premixed flame, S_t , is much higher than the laminar flame velocity, S_l . Fig. 2. 4 (a) shows the laminar and turbulent premixed flame profiles for a Bunsen burner. The laminar flame has a smooth conical surface and a thin luminous reaction zone. The turbulent premixed flame has a wrinkled surface, a vague outline and a thick luminous reaction zone (Lee, North and Santavicca, 1993). Generally, the laminar premixed flame is taller than the turbulent flame. With an increase in the jet flow rate of the fuel/ air mixture, the flame gradually changes from laminar to turbulent and the height of the flame dramatically shrinks, as shown in Fig. 2. (b).

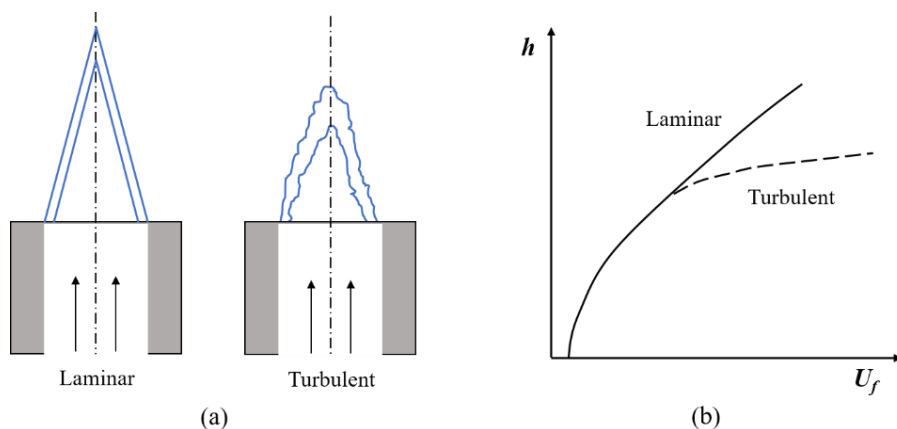


Fig. 2. 4 (a) The laminar and turbulent premixed flames profiles for a Bunsen burner, (b) The relation between the flow rate of the gas mixture, U_f , and height of the flame, h . (Lee, North and Santavicca, 1993)

2.2.2 Laminar and turbulent diffusion flames

2.2.2.1 Candle flame

The candle flame is a typical laminar diffusion flame model. The structure of the candle flame can be divided into four zones, as shown in Fig. 2. 5. The flame is composed of the yellowish flame and the bluish flame. The yellowish flame is induced by the blackbody radiation of the soot (Schefer *et al.*, 2009). The dark zone consists of a dark orange flame in the temperature range from 800 °C to 1000 °C (Roth, 2003). In the dark zone, the oxygen is deficient, which leads the pyrolysis of hydrocarbons, thereby resulting in soot formation. As the flame approaches the ambient air, the temperature of the flame increases which enhances the fuel pyrolysis. As a result, the luminous zone shows a bright yellow flame with a temperature of approximately 1200 °C (McAllister, Chen and Fernandez-Pello, 2011). The blue emission zone is a result of flame chemiluminescence. The excited radicals CH^* and C_2^* emit in the visible spectrum which presents in blue (Gaydon and Wolfhard, 1971). The primary reaction takes place in the non-luminous zone that is mainly composed of H_2O and CO_2 with an approximate temperature of 1400 °C. The H_2O and CO_2 emit in the infrared spectrum and the OH emits in the ultraviolet spectrum which is beyond the human vision and hence this region is called the non-luminous zone (Gaydon, 1941). The flame light emission will be introduced in detail in Section 2.3.

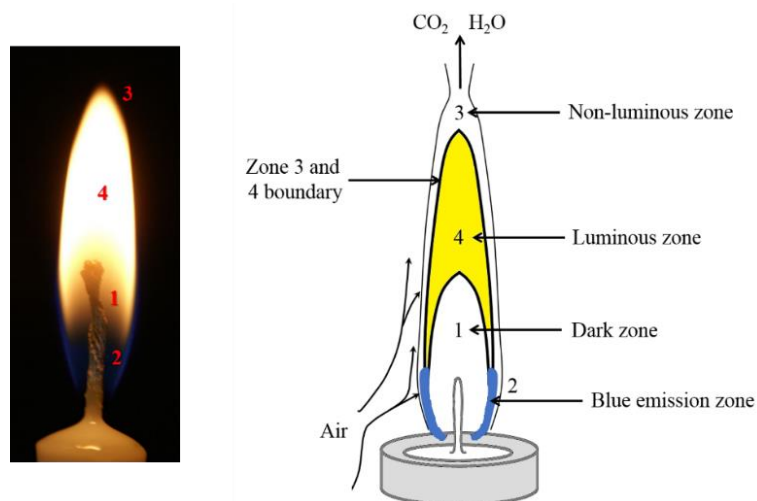


Fig. 2. 5 Structure of the candle flame (Roth, 2003).

2.2.2.2 Laminar jet diffusion flame

Fig. 2. 6 shows a radial cross-section of the gas concentration and the temperature distribution of an ideal laminar jet diffusion flame. The violent chemical reaction at the flame fronts contributes to a local high temperature and high concentration of combustion products. The temperature and the combustion products concentration tend to decrease when approaching the air and fuel zones due to the thermal diffusion effect (Drysdale, 2011). The air and fuel zones are completely separated by the flame front; hence the oxygen concentration gradually decreases from the air zone towards the flame front, and is consumed at the flame front. Similarly, the fuel concentration gradually decreases from the jet centreline towards the flame front and is consumed at the flame front (Irvin Glassman and Yetter, 2008).

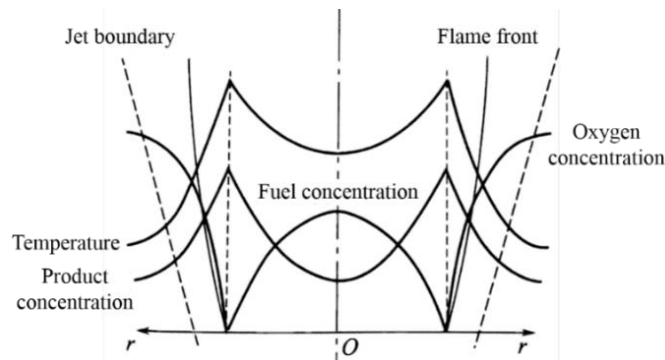


Fig. 2. 6 The radial cross-section of gas concentration and the temperature distribution of an ideal laminar jet diffusion flame (Irvin Glassman and Yetter, 2008).

However, the flame front has a finite thickness in real combustion. Shown in Fig. 2. 7, the fuel and air are consumed at the inner and outer boundary of the flame front respectively. The high temperature and low oxygen concentration of the pre-heating zone lead to the pyrolysis of the fuel near the flame inner surface (Guéret, Daroux and Billaud, 1997). The pyrolysis of the hydrocarbon fuel induces soot particle formation. The soot accumulated at the high-temperature flame zone emits bright yellow/orange light due to blackbody radiation. Some soot particles with lower temperature are blown up by the buoyancy and present as dark smoke over the luminous zone.

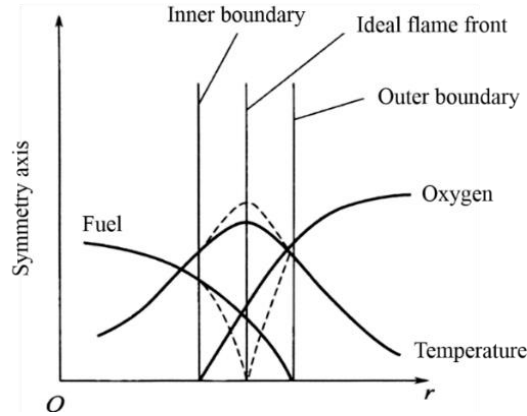


Fig. 2. 7 The real flame front structure of a laminar diffusion flame (Irvin Glassman and Yetter, 2008).

The level of hydrocarbon pyrolysis is ruled by the fuel properties and temperature (Savage, 2000). In general, a larger molecular weight will reduce the stability and increase the hydrocarbon pyrolysis possibility. The higher the temperature, the stronger the pyrolysis. For instance, methane starts to pyrolyse at 682 °C. 26 % methane pyrolyses at 950 °C; 99% methane pyrolyses at 1150°C. The pyrolysis temperatures of ethane, propane and butane are 485 °C, 400 °C and 430 °C respectively (Holmen, Rokstad and Solbakken, 1976). Hydrogen and carbon monoxide have good thermostability, which enables stability even at 2000 °C to 3000 °C (Wiley, Hepburn and Levenspiel, 1964). The highest temperature that an ideal laminar jet diffusion flame can achieve is

$$T_f = \left[(T_0 - T_\infty) + \frac{q_f}{c_p} \right] \frac{C_{0,\infty}}{\beta + C_{0,\infty}} + T_\infty \quad (2.5)$$

where T_0 is the initial temperature of the fuel. T_∞ is the surrounding environment temperature, q_f represents the fuel heat release and c_p is the specific heat capacity of the combustion products.

2.2.2.3 Turbulent jet diffusion flame

An increase in fuel gas initial velocity U_0 will change the gas flow from laminar to turbulent when the Reynolds number (Re) exceeds a critical value. This results in the combustion turning into the turbulent diffusion flame (Irvin. Glassman and Yetter, 2008), as illustrated in Fig. 2. 8.

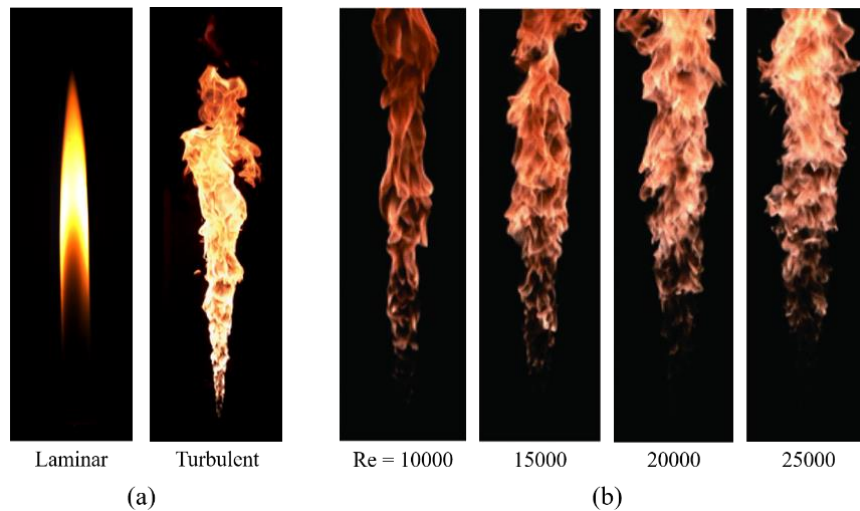


Fig. 2. 8 (a) Images of a laminar and turbulent propane diffusion flame and (b) Turbulent ethylene jet diffusion flames with various Re (Muñiz and Mungal, 2001).

Previous research has indicated that the laminar jet diffusion flame has a flat, smooth and precise flame surface. The height of the flame h_f will increase with an increase in Re . For the transition flow, the flame has a wrinkled surface and local turbulence at the tip of the flame. An increase in Re will enlarge the turbulent region, which enlarges and shrinks the height of the flame. The ‘breakpoint’ where the flame structure changes from laminar to turbulent gradually approaches the nozzle exit, as shown in Fig. 2. 9. The fully developed turbulent flame has an intensely wrinkled surface with a relatively low luminance (Lee and Lee, 2003). The h_f of the fully turbulent flame is irrelevant to the Re . The distance from the breakpoint to the nozzle exit shortens with the increase of Re (Hottel and Hawthorne, 1948).

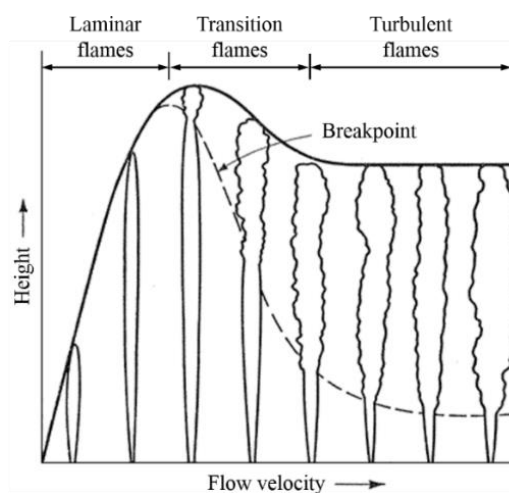


Fig. 2. 9 The relation between the flame height and Re (Molkov and Saffers, 2013).

2.3 Flame Light Emission

2.3.1 Flame chemiluminescence

Flame colour is an important property, which is correlated to the fuel species, flame temperature and fuel and oxidiser mixing level. Hydrocarbon gas is the common domestic-used fuel species. For the hydrocarbon flame, the dominant colours are induced by the flame chemiluminescence and the blackbody radiation of soot in the visible spectrum. The emission of OH, water and carbon dioxide are located in the UV and IR spectra.

For the premixed hydrocarbon flame, the blue light is attributed to flame chemiluminescence. Chemiluminescence is the emission of light due to a chemical reaction. It happens when excited molecules return to a lower energy state (Guyot *et al.*, 2010). When the electron decays to the lower energy state, it will emit photons at a specific wavelength. The blue light of the premixed hydrocarbon flame is induced by excited molecular radicals C_2^* and CH^* (Nori and Seitzman, 2007). The emission of the C_2^* has a Swan system; dominant emissive band heads at 473.71 nm and 516.52 nm (Gaydon, 1974). The emission of the CH^* has a primary head at 430 nm; as shown in Fig. 2. 10.

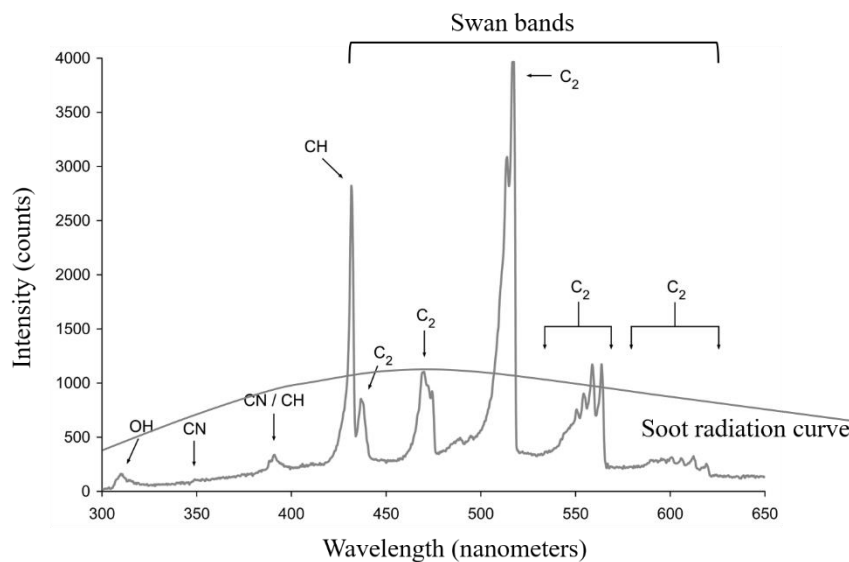


Fig. 2. 10 The CH^* and C_2^* emission of a hydrocarbon flame (Chemiluminescence, 2005).

The CH* and C₂* emissions are perceived in indigo and cyan/ green respectively. The direct imaging of a propane-air premixed flame is shown in Fig. 2. 10 (a). Fig. 2. 10 (b) and (c) show the CH* and C₂* emissions of a premixed propane flame. Narrowband filters of 430 ± 4 nm and 576 ± 4 nm are applied to the lens respectively.

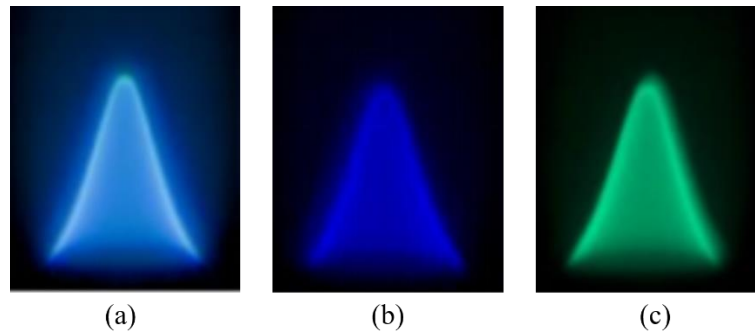
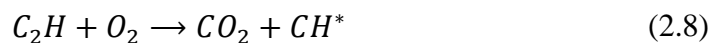


Fig. 2. 11 (a) Propane-air premixed flame image, (b) Flame CH* emission with narrow band filter of 430 ± 4 nm and (c) Flame C₂* emission with a narrow band filter of 576 ± 4 nm.

The formation process of the excited CH* and C₂* is controversial. Through the comparison of CH* emission in various flames, it is found that the CH* may not be directly formed by the cracking of acetylene, but by a side reaction (Gaydon and Wolfhard, 1953). Since more CH* forms in the reaction zone than C₂, the CH* is considered to be formed from C₂ (Martins *et al.*, 2005). The reaction process can be expressed by



Most of the research favours that the C₂* emission is formed by the following reaction:



The CH* and the C₂* are good indicators of chemical reactions in hydrocarbon flames. It is reported that the CH*/C₂* has a non-linear relationship to the equivalence ratio

(Raghunandan, Oommen and Sullerey, 2004). The ratio of the CH^*/C_2^* can be used to reflect the local fuel/ air mixing level (Yang *et al.*, 2015).

2.3.2 Blackbody radiation of soot

The yellow/orange light from the fuel-rich hydrocarbon flame is induced by the black/ grey body radiation of soot (Chatterjee *et al.*, 2011). On the one hand, the increase of soot radiation enhances the heat transfer, which is important in boilers and furnaces. On the other hand, soot is a typical carbonaceous particulate matter (PM) emission and major hazardous pollution in the air with considerable health detriment (Onursal and Gautam, 1997). Soot formation has an adverse impact on the combustion efficiency of IC engines. It also increases the wear and reduces the lifetimes of the components. A significant amount of soot is deposited in engines, turbines and furnaces (Penttinen *et al.*, 2001).

2.3.2.1 Soot formation mechanism

Soot formation occurs via precursor species which mainly consist of PAHs (Turns, 2000). Small particles form afterwards through chemical coagulation. Soot formation ceases as the soot particles travel through an oxidising region (Mansurov, 2005). The soot formation process is divided into four steps, as described below and is schematically shown in Fig. 2. 12.

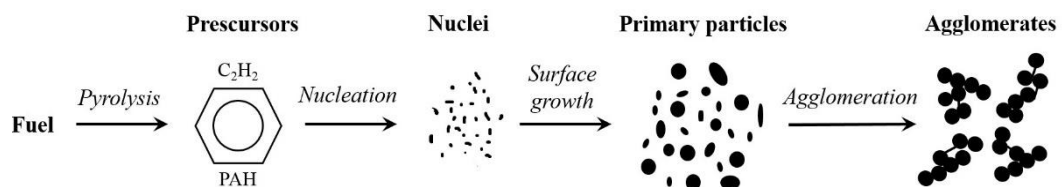


Fig. 2. 12 Schematic of the soot formation mechanism.

(i) Formation of soot precursors and soot particle inception.

The soot inception is the formation of the soot precursors which are induced by thermal decomposition of the polymers (Lahaye, 1990). The carbon particles are formed by dehydrogenation of the hydrocarbon molecules. Soot precursors are suspected to be polyacetylene, PAH and carbon vapour (Someya, 1993). Research widely recognises that PAH is the soot precursor of the carbon nuclei (Thomas Mckinnon and Howard, 1992). Garo *et al.* (Garo, Prado and Lahaye, 1990) applied the

laser scattering and fluorescence technique to track the profile of the PAH and carbon nuclei. They found that the PAH decreased at the inception of soot, as shown in Fig. 2. 13.

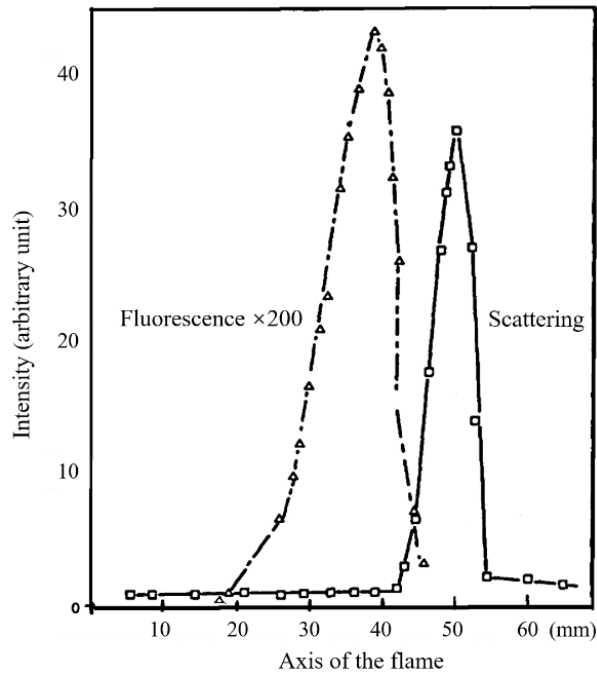


Fig. 2. 13 Axial profiles of intensities of scattering and fluorescence at 90° for a laminar methane diffusion flame (Garo, Prado and Lahaye, 1990).

Other research has drawn the same conclusion as Garo (Böhm, Jander and Tanke, 1998; Mao, van Duin and Luo, 2017). PAH is induced by the reactions between aromatics and acetylenic species (Richter and Howard, 2000) as shown in Fig. 2. 14. The reaction of the benzyl-type radical and C₂H₂ contributes to the cyclisation. The catalytic process takes place with an increase in the size of the cycle, the speed of methyl group substitution and the number of possible reactive zones.

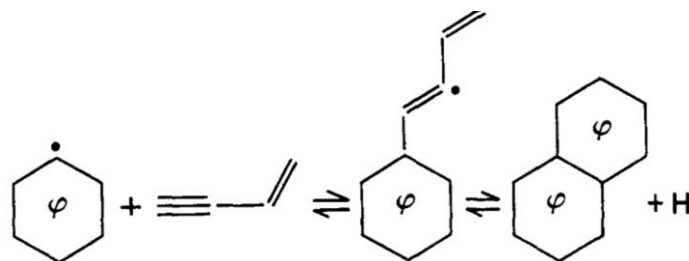


Fig. 2. 14 The formation of PAH (Richter and Howard, 2000).

- (ii) Aggregation of particles.

Large spherical particles are generated by the collision of large numbers of smaller particles, finally leading to the soot formation by agglomeration (Bhatt and Lindstedt, 2009), which is illustrated in Fig. 2. 12. Fig. 2. 15 shows the soot aggregates under micrograph observation.

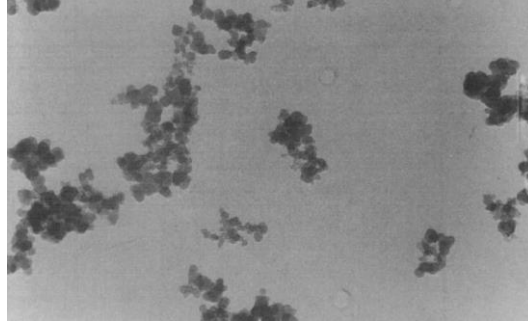


Fig. 2. 15 Micrograph of soot aggregates (Tian *et al.*, 2007).

(iii) Surface growth.

Only 10% of the soot mass is from the inception of soot particles whereas 90% is due to surface growth (Thomas Mckinnon and Howard, 1992). Research indicates that acetylene is the main factor contributing to the soot growth (Miller, 1991). The concept of soot volume fraction is introduced to describe the soot growth via the expression:

$$\frac{d}{d_t}(f_v) = k_E(f_v^* - f_v) \quad (2.12)$$

where k_E is a constant and f_v^* is a depletion reservoir for the soot growth. The surface growth is expressed by

$$\frac{d}{d_t}(f_v) = k_s \cdot S \quad (2.13)$$

where S represents the total soot surface area concentration and k_s represents the surface specific rate, which is first order in the partial pressure of acetylene:

$$k_s = K_{C_2H_2} P_{C_2H_2} \quad (2.14)$$

Through observation from electron microscopy, the surface growth can be initially found on the individual particles. The aggregation was found afterwards due to particle collision (Li and Wang, 2003). Aggregation-induced surface growth strongly affects the stability of soot aggregates. Long-distance strong carbon bonds increase the aggregates' stability (Mitchell and Frenklach, 2003).

(iv) Post-oxidation of soot:

Soot particles can be post-oxidised by multiple species such as atomic/molecular oxygen or the hydroxyl radical, $\cdot\text{OH}$. Research has demonstrated that soot oxidation is mainly affected by $\cdot\text{OH}$ radical (Edwards *et al.*, 2014).

2.3.2.2 Blackbody radiation

The soot emission is induced by the black/grey body radiation and glows in the reddish or yellowish colour depending on its temperature. Blackbody radiation is a thermal electromagnetic radiation within a body in thermodynamic equilibrium with its environment. Any opaque substance will emit thermal radiation. A perfect blackbody absorbs all incoming light and does not reflect any light (Csele, 2004). Most solid substances are considered to be grey bodies which include the soot particles. Blackbody radiation has a continuous spectrum which only relates to its temperature, which is described by Planck's law:

$$B_{\nu}(T) = \frac{2h\nu^3}{c^2} \frac{1}{e^{\frac{h\nu}{kT}} - 1} \quad (2.15)$$

where $B_{\nu}(T)$ represents the radiance; the density of frequency ν of radiation per unit frequency at thermal equilibrium at temperature T . h represents Planck's constant, c is the speed of light in a vacuum, k is the Boltzmann constant, ν is the frequency of the electromagnetic radiation and T is the absolute temperature of the body.

Wien's displacement law describes that the continuous blackbody spectrum has a peak which is shifted to shorter wavelengths for increasing temperatures (Lerner, 1996). The wavelength of maximum intensity per unit wavelength of radiation is given by

$$\lambda_{max} = \frac{b}{T} \quad (2.16)$$

where b is the Wien's displacement constant which is equal to 2.898×10^{-3} K·m. The intensity maximum at λ_{max} is expressed by

$$\nu_{max} = T \times 58.8 \text{ GHz/K} \quad (2.17)$$

The Planck emission of the soot particles is shown in Fig. 2. 16. The blackbody radiation of soot is mainly located in the infrared spectrum with peak emission at the

near-infrared spectrum. With the increase of soot temperature, the soot emission gradually shifts to the visible spectrum, which explains the colour difference (reddish/yellowish) of the soot particles. In the flame ignition process, the flame colour changes from dark red to bright yellow which reflects the rising temperature of the flame, as shown in Fig. 2. 16. The two-colour technique of the flame temperature measurement is based on the blackbody radiation theory.

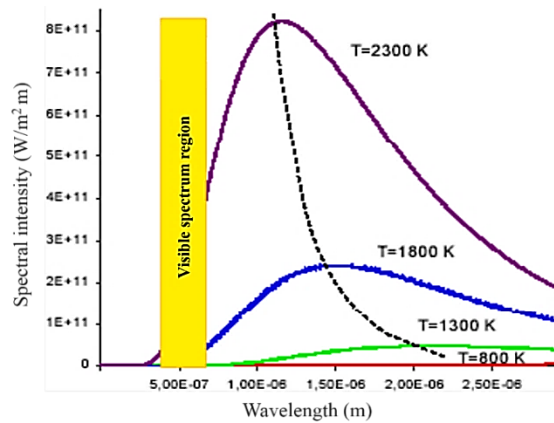


Fig. 2. 16 The Planck emission of the soot particles (*Black body radiation and Planck's radiation law*, 2017).

According to Planck's law and Wien's law, if the temperature is lower than a specific value, the peak of the blackbody radiation of the opaque substance will be located in the infrared spectrum, and so the glowing of the solid will be invisible. This specific temperature is called the 'Draper point' and established by John William in 1847, which is equal to 525 °C (977 °F, 798 K) (Mahan, 2002).

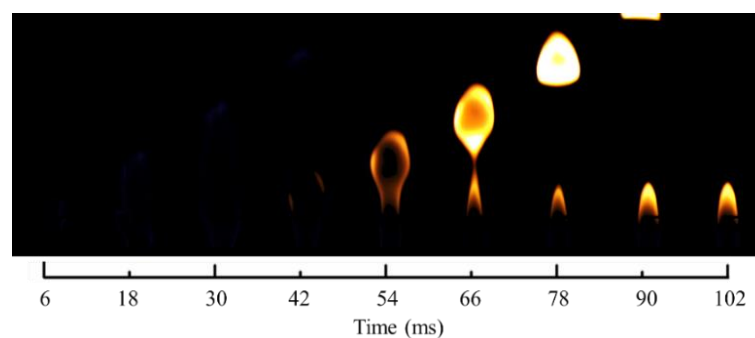


Fig. 2. 17 Image sequence of the ignition process of a methane diffusion flame with co-flow air.

2.3.3 IR emission of water and carbon dioxide

The infrared flame emission is mainly induced by the combustion products; water and carbon dioxide, which have strong bands with two primary peaks at 2.8 μm and 4.4 μm (Gaydon, 1974). The strongest band at 4.4 μm is due to CO_2 ; another strong band at 2.8 μm is the emission from both CO_2 and H_2O . The blackbody of heated soot particle also has continuum radiation with peak emission in the near-infrared spectrum, which has been mentioned in Section 2.3.2.

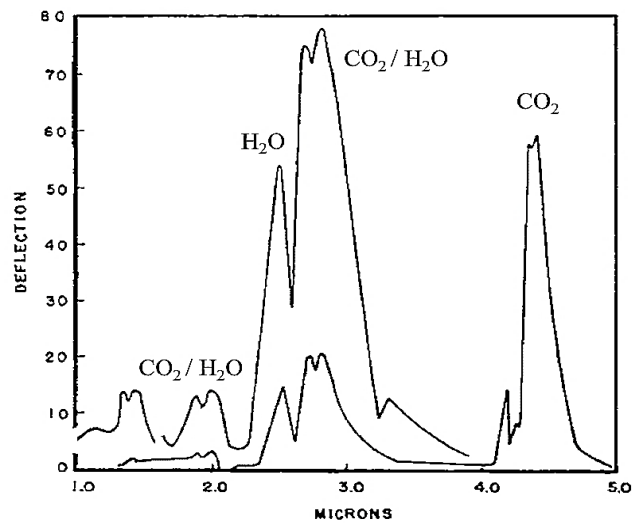


Fig. 2. 18 Flame infrared emission measured with a NaCl prism. The upper curve was measured with wider slits than the lower (Plyler and Plyler, 1948).

E.K. Plyler (Plyler and Plyler, 1948) investigated the infrared flame emission from a natural gas Bunsen flame with the help of prisms of lithium fluoride (LiF), sodium chloride (NaCl) and potassium bromide (KBr). The results are shown in Fig. 2. 18 to Fig. 2. 20. It is found that the small bands from 1.8 μm to 2 μm are produced by H_2O and CO_2 . The bands located at 2.49 μm and 2.7 μm are attributed to the H_2O and CO_2 respectively. The fine structure in the region from 2.8 μm to 3.1 μm may be induced by H_2O . A large number of pure rotational lines from 12 μm to 24 μm is produced by H_2O . Another two strong bands located at 14 μm and 15 μm are due to the CO_2 emission.

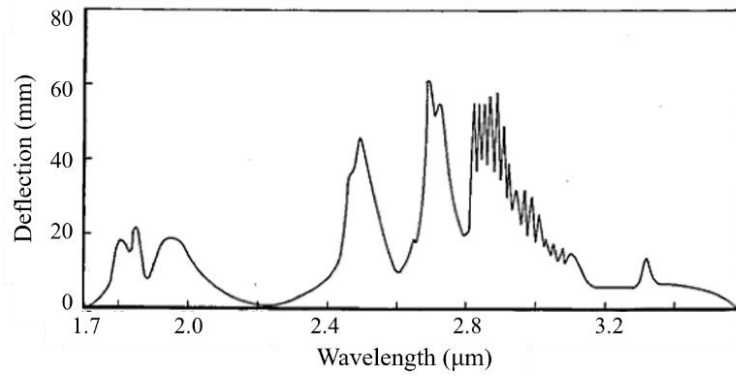


Fig. 2. 19 Infrared emission of a Bunsen flame measured with a LiF prism (Plyler and Plyler, 1948).

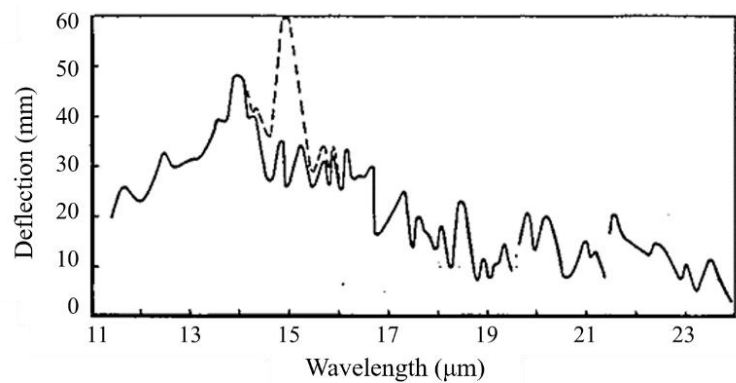


Fig. 2. 20 Infrared emission of a Bunsen flame in the region of 12 μm to 24 μm measured with a KBr prism (Plyler and Plyler, 1948).

Once the H_2O and CO_2 emission spectra are determined, the distribution of H_2O and CO_2 concentration can be investigated according to their emission characteristics. The infrared emission spectrum of methane-air premixed flat flames is measured at five height locations which are the visible flame zone and 1 mm and 3 mm above and below the visible flame zone (Plyler and Plyler, 1948). Fig. 2. 21 shows the comparison between the different flame positions of the flame spectra with $\phi = 0.8$ (fuel lean) and $\phi = 1.6$ (fuel rich). It is found that the H_2O and CO_2 lines get stronger with the increase of the measurement location which may be due to the buoyancy effect. The intensity of the emission spectrum of the fuel rich flame is higher than the lean flame due to its higher temperature. It may also be because the fuel rich reaction zone is larger or located closer to the burner surface than the lean flame.

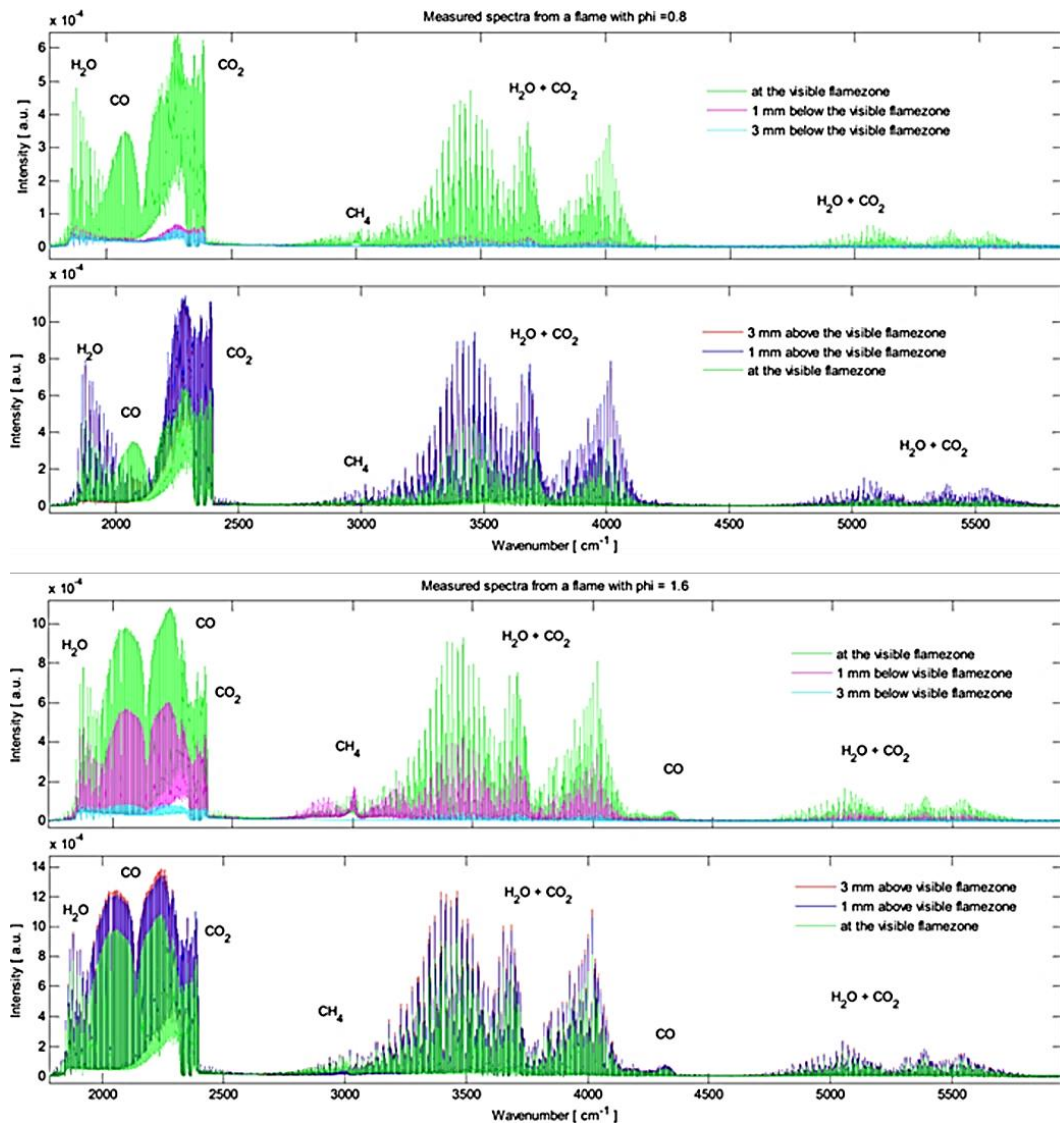


Fig. 2. 21 The comparison of flame spectra at different measurement positions (Lindecrantz, 2010).

2.3.4 IR emission of PAH

PAHs are the primary precursor of soot formation. Most of the PAHs studies in the flame area rely on the PLIF technique. The PAHs emission spectrum in flames is rarely reported but is highly investigated in astronomy (Léger *et al.*, 1989; Salama, 2008; Draine, 2011). It has been reported that the mysterious red radiation in interstellar space comes from PAHs (Allamandola, Tielens and Barker, 1987), shown in Fig. 2. 22. Molecular PAH absorbs stellar UV photons leading to the vibration of the carbon skeleton. PAHs relax to ground state by emitting several IR photons that come from their C-C and C-H vibrations (Sandford, Bernstein and Materese, 2013).

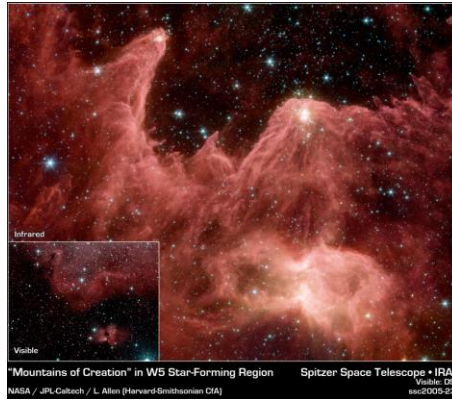


Fig. 2. 22 Telescope image of the W5 star forming in the VIS and IR regions. The infrared emission is shown in red, which originates in PAHs (Administrator, 2016).

PAHs emit in the Unidentified Infrared Bands (UIBs), which correspond to the discrete intense IR emission bands in the 3 – 20 μm spectral range, with major components near 3.3 μm , 6.2 μm , 7.7 μm , 8.6 μm , 11.3 μm and 12.7 μm due to C-H stretching, C-C stretching and C-H in-plane and out-of-plane bending (Ota, 2015), as shown in Fig. 2. 23 and Fig. 2. 24.

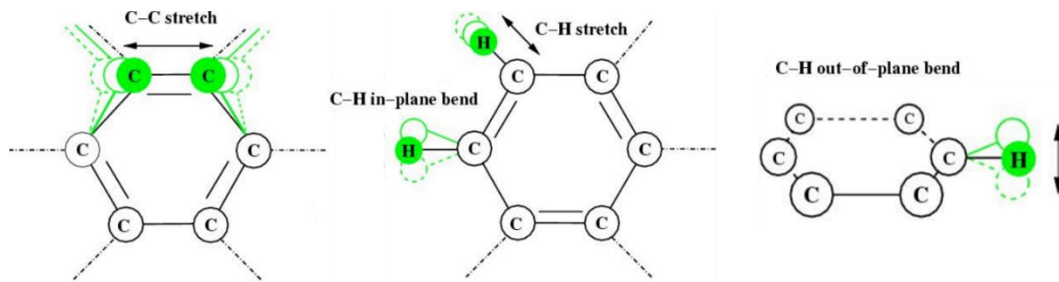


Fig. 2. 23 C-C and C-H vibrational modes (Ota, 2015).

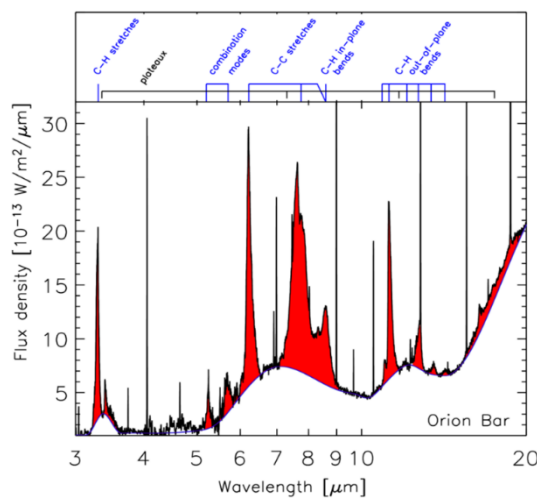


Fig. 2. 24 The PAH emission spectrum of the Orion Bar from 3 μm to 20 μm (Els Peeters, 2002).

Similar to the flame model, when PAHs molecularly adsorb energy from a chemical reaction, they emit photons located in the infrared spectrum. In 1996, Thomas et al. presented the infrared spectrum of dichloromethane (DCM) -soluble PAH samples which were extracted from sooty flames (Mckinnon, Meyer and Howard, 1996). A water-cooled quartz probe was used to extract the PAH samples. The samples were withdrawn from the flame through a liquid nitrogen trap and into a vacuum pump. The PAH sample was then dissolved in DCM. The infrared absorption spectrum of the DCM-soluble sample is shown in Fig. 2. 25, which is similar to the simulated PAH spectrum in galaxies. The corresponding infrared absorption peaks of the functional groups are presented in Table 2. 1.

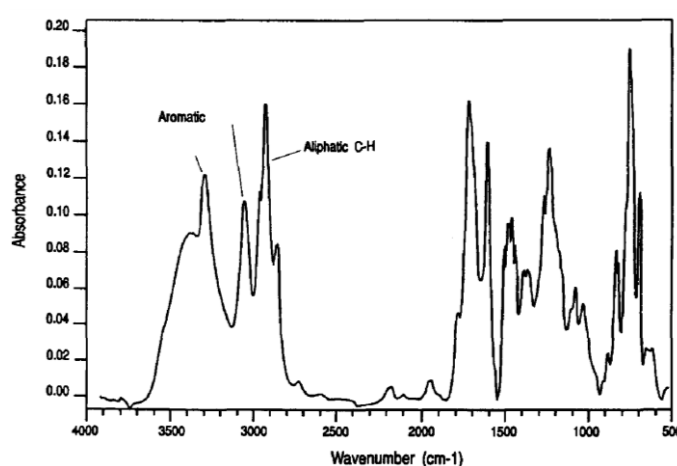


Fig. 2. 25 The infrared spectrum of the DCM-soluble material sample (Mckinnon, Meyer and Howard, 1996).

Table 2. 1 Assignments of infrared absorption peaks to functional groups.

Absorption peak (cm ⁻¹)	Absorption peak (μm)	Assignment	Peak type
1595	6.26	Aromatic C=C	Sharp
1700	5.89	Carbonyl C=O	Sharp
2875-2975	3.36-3.48	Aliphatic C-H stretch	Three sharp peaks
3050	3.28	Aromatic C-H stretch	Sharp
3300	3.03	Acetylenic C-H stretch	Sharp
3500	2.86	Acid or phenolic O-H stretch	Diffuse

2.3.5 Ultraviolet emission of OH*

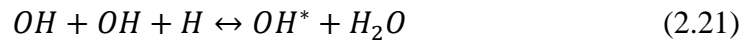
The excited radical, OH*, can be formed in the primary reaction zone. Gaydon and Wolfhard (Gaydon and Wolfhard, 1953) proposed that the OH* is formed by the following reaction, which is supported by the experimental study by Krishnamachari and Broida (Krishnamachari and Broida, 1961).



Smith et al. (Smith, Park and Luque, 2005) determined the rate constants for two additional formation paths of OH* based on the experiments of hydrogen-air and methane-nitrous oxide flames.



An OH radical can jump from the ground state into the excited state through the following reaction.



The OH* has a peak emission at 306 nm wavelength which is located in the ultraviolet spectrum as shown in Fig. 2. 26.

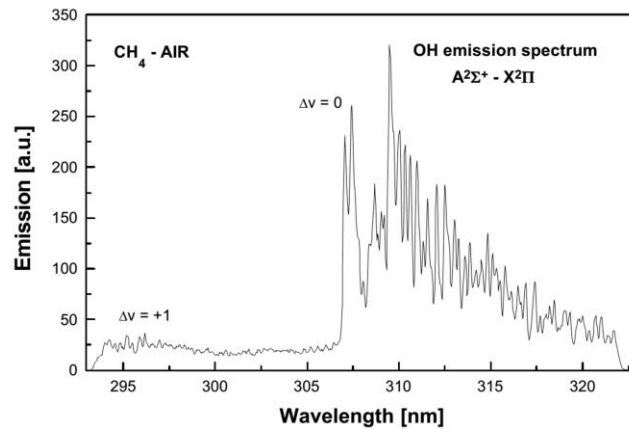


Fig. 2. 26 The OH spectrum in a lean premixed methane-air flame (Griebel, Siewert and Jansohn, 2007).

However, the OH emission has not been studied in the following sections, since the camera is insensitive to the UV spectrum.

2.4. Flame Ignition and Propagation

2.4.1 Ignition definition

Ignition is the process whereby the unburnt fuel starts to combust with the addition of a heat source. The ignition of a flammable gas mixture is always accompanied by complicated chemical reactions and multiple parameter variations, such as temperature, pressure and flame propagation velocity (Mastorakos, 2009; Xu *et al.*, 2010). The investigation of the ignition process is highly desirable in many combustion devices, especially in IC engines, and in particular the spark-ignition engine. Combustion in the SI engine is critically dependent on the ignition process, particularly the ignition energy and location because the inhomogeneous mixture of the fuel and air has to be ignited by a spark plug at a chosen location in each cycle.

2.4.2. Ignition systems

For most combustion systems, the flame is initiated by ignition rather than spontaneous combustion. The external heat provided by an ignition device leads to the local combustion of the flame. The rest of the fuel region is then heated by the local flame which contributes to the flame propagation. The standard ignition is performed by a spark or a heated object.

2.4.2.1 Heated object ignition theory

Electric current heat resistance wire is a typical hot object that can be used for the flame ignition. This kind of device has a simple structure but easy oxidation and ablation. Assume a hot object with a surface temperature T_w is placed into an environment that is filled with inert gas with temperature T_0 . If $T_w > T_0$, the heat transfer takes place between the hot object and the inert gas. The temperature distribution of the hot object in the surrounding inert gas is shown by Curve 1 in Fig. 2. 27. The normal temperature gradient of the hot object's surface is negative; $\frac{dT}{dx}|_{x=0} < 0$ (Yang, 1962).

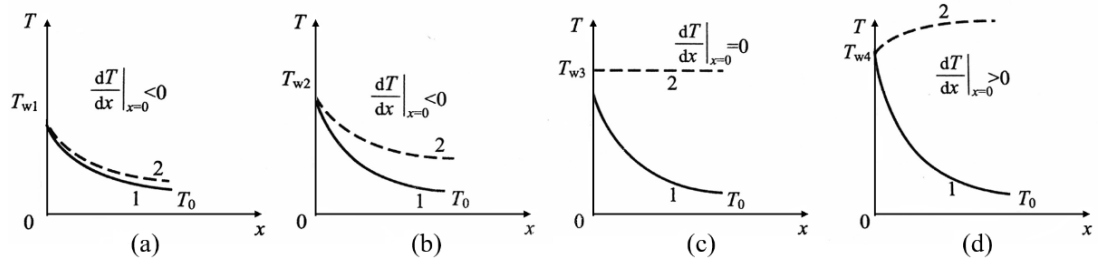


Fig. 2. 27 Zero-temperature-gradient of hot object ignition ($T_{w1} < T_{w2} < T_{w3} < T_{w4}$) (Yang, 1962).

If the hot object is placed into a premixed flammable gas field, as shown by Curve 2 in Fig. 2. 27, the temperature of the premixed flammable gas increases due to the exothermic reaction. Therefore, the temperature distribution of Curve 2 is higher than Curve 1, as shown in Fig. 2. 27 (a). However, the normal temperature gradient of the hot object's surface is still negative, $\frac{dT}{dx}|_{x=0} < 0$, due to the low T_{w1} compared to higher object temperatures, and less heat release from the chemical reaction. If the temperature of the hot object increases from T_{w1} to T_{w2} , the heat transfer between the hot object and the premixed gas is more intensive, thus Curve 2 raises up and deviates from Curve 1 as shown in Fig. 2. 27 (b). The increase of the normal temperature gradient demonstrates that the heat transfer from the hot object to the premixed gas becomes less, however, the value of $\frac{dT}{dx}|_{x=0}$ is still negative. When the surface temperature of the hot object increases to the ignition temperature of the premixed gas, T_C , the premixed gas surrounding the hot object is under the critical ignition state and the temperature remains constant at T_C . The heat transfer between the hot object and gas is suspended. The normal temperature gradient $\frac{dT}{dx}|_{x=0}$ is equal to zero, as shown in Fig. 2. 27 (c). The ignition critical condition is the zero-temperature-gradient boundary. Combustion will take place if the surface temperature of the hot object T_{w4} is higher than the gas critical ignition temperature. As the flame temperature is much higher than the hot object temperature, the heat will transfer from the flame to the hot object, thus the normal temperature gradient of the hot object is positive $\frac{dT}{dx}|_{x=0} > 0$, as shown in Fig. 2. 27 (d).

2.4.2.2 Spark ignition theory

Spark ignition is the most popular ignition method in engines. The spark is generated between the electrodes with the temperature range from 6000 K to 20000 K (Kimura and Kumagai, 1956; Adelman, 1981). The electric spark first ignites the local premixed gas and forms the initial flame. The flame finally establishes when the initial flame propagates towards the unburnt premixed gas. The process of the spark-induced ignition starts when the mixture of the fuel and oxidiser reaches a high enough temperature and forms a flame kernel. The flame kernel exists in a short time span from the ignition moment to either a self-growing flame or extinction when the kernel gradually grows or vanishes respectively. In general, the pattern of the flame kernel evolves from a cylindrical shape to a spherical shape. The success of spark ignition depends on the formation of the initial flame and its propagation conditions, which are related to the premixed gas properties; composition, pressure and initial temperature, flow conditions and the electric spark energy (Aggarwal, 1998). Research demonstrates that the initial flame can form and stably propagate unless the spark energy $E > E_{min}$, where E_{min} is the minimum spark energy that is required for the ignition.

Fig. 2. 28 (a) shows the relationship between E_{min} and the electrode interval d . If the electrode interval is too small, the intensive heat transfer from the initial flame to the electrodes leads to insufficient heat for the propagation of the surrounding gas; thereby the flame fails to propagate (Ballal and Lefebvre, 1979). If d is smaller than quenching distance d_q , the premixed gas will not be ignited no matter how large the spark energy. When $d > d_q$, the ignition energy gradually decreases with an increase in electrode interval, until E_{min} is achieved, and then increases afterwards. Fig. 2. 28 (b) shows the relationship between the minimum ignition energy and the equivalence ratio. The value of E_{min} is smallest when the equivalence ratio is around 1. The gas mixture cannot be ignited under over-rich or over-lean conditions. The smaller the ignition energy, the narrower the range of the ignition boundary and the equivalence ratio of the gas mixture. Besides, research has demonstrated that spark ignition systems are also affected by the material, size and shape of the electrodes (Taylor, 1985; Terao, 2007).

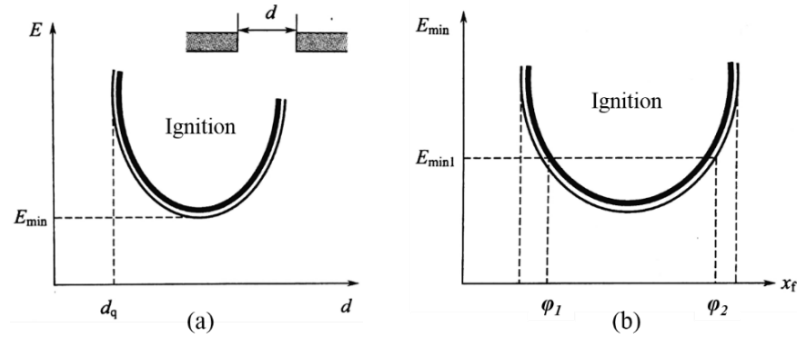


Fig. 2. 28 (a) The relationship between the minimum ignition energy E_{min} and the electrode interval d , and (b) The relationship between the minimum ignition energy E_{min} and the equivalence ratio ϕ (Ballal and Lefebvre, 1979).

2.4.3 Ignition location

During the ignition process, the initiation point needs to be carefully determined. A proper ignition location will largely increase the combustion effectivity. For example, combustion in the SI engine is critically dependent on ignition location because the inhomogeneous mixture of the fuel and air has to be ignited by a spark plug at a chosen location in each cycle. The combustion efficiency and the evolution of the distribution of the air/fuel/products are strongly affected by the ignition location in a non-uniform and unsteady turbulent flow field. A computational investigation of the SI engine demonstrated that when the rotational speed is over 100 rad/s, the power output and efficiency were increased by 10 % and 2 % respectively when the spark plug was centrally located (Medina *et al.*, 2014). At the very low rotational speed, the situation is reversed.

The ignition location also has a remarkable influence on closed and partially opened vessels. Kondracki *et al.* (Kondracki *et al.*, 2007a) studied explosion development in methane/air mixtures in a closed vessel. They reported that the ignition location strongly influenced the maximum combustion pressure and rising rate of pressure. The maximum pressure was higher with the central ignition than the other locations, due to the time span of the heat exchange between the high-temperature combustion products and the cold vessel walls. When the vertical tube was filled with a lean mixture, combustion with obstacles and central ignition was more than 2.5 times faster than when ignited at the top or the bottom of the tube.

Xiao et al. (Xiao *et al.*, 2014) investigated premixed hydrogen/air flame propagation in a closed combustion tube with different ignition locations. It was found that tulip and distorted tulip flames could be formed if the flame was initiated at a short distance away from the tube ends. When the flame was initiated at the centre and the ends of a closed tube, the flame propagation was largely restrained due to the inability of the mixture to expand freely toward the end wall of the duct. Guo et al. (Guo *et al.*, 2015) tested back, central and front ignition positions in a vented vessel. They reported that the central ignition contributed to the maximum internal overpressure for all equivalence ratios and the back ignition exhibited the maximum external overpressure for fuel rich conditions. For turbulent hydrogen jet flames (Ahmed and Mastorakos, 2006b), the flame propagated both upstream and downstream when ignited at 800 mm away from the nozzle exit. If the flame propagation speed was over 100 m/s at the centreline of the fuel jet, the flame propagated upstream only. If the flame was initiated at 900 mm away from the nozzle, the flame spread downstream only. Therefore, the ignition location needs to be carefully determined.

2.4.4 Burning velocity and flame speed

For the laminar flame, a stationary flame will form if the fuel propagation velocity is equal to the laminar flame speed, S_l . If the fuel velocity is lower than S_l , the flame will propagate towards the unburned fuel and air mixture, while if the fuel velocity is higher than S_l , the flame will propagate away from the unburned mixture. The burning velocity, S_u indicates the conversion speed between the reactants and products. The turbulent burning velocity S_t is for flames where there exists turbulence in the unburned gases, causing an increase in the flame surface area due to wrinkling and flame front distortions, and increasing the overall mass consumption rate (Lawes *et al.*, 2012).

2.5 Impinging Flames

2.5.1 Introduction

Flame impingement happens when the flame comes into direct contact with the surface of a wall, which often takes place in daily life and industry. Flame impingement is

appreciated in aerospace due to the vertical take-off and landing of aircraft and rockets. It also occurs during heat-treatment of metal parts for surface hardening, joining, and shrink fitting (Baukal, 2013). On the other hand, the interaction between the flame and wall surface is undesirable in some combustion devices, for example, the combustion chamber of IC engines. The flame impingement to a wall/piston may lead to hot spots or wall quenching. Temperature gradients on wall surfaces may also lead to uneven heating. If the temperature exceeds the design limit, the combustor wall may become damaged. Therefore, the study of impinging flames is highly desirable in the foundational study of combustion.

2.5.2 Impinging flame structure

2.5.2.1 Impinging non-reacting jet

Research has demonstrated that flame impingement characteristics are highly dependent on the non-reacting flow field before ignition (Viskanta, 1993). The non-reacting impinging jet has three distinct regions: (I) free jet region; (II) stagnation region; (III) radial wall-jet region (Fu *et al.*, 2013), as shown in Fig. 2. 29. The fuel jets from the nozzle with a near-uniform velocity in the free jet region. Subsequently, the fuel mixes with the ambient air which entrains mass, momentum and energy in the shear layer. In the stagnation region, the gas jet approaches the plate. The velocity becomes zero at the stagnation point since the gas flow direction changes. In the radial wall-jet region, gas propagates towards the edges of the plate from the stagnation point.

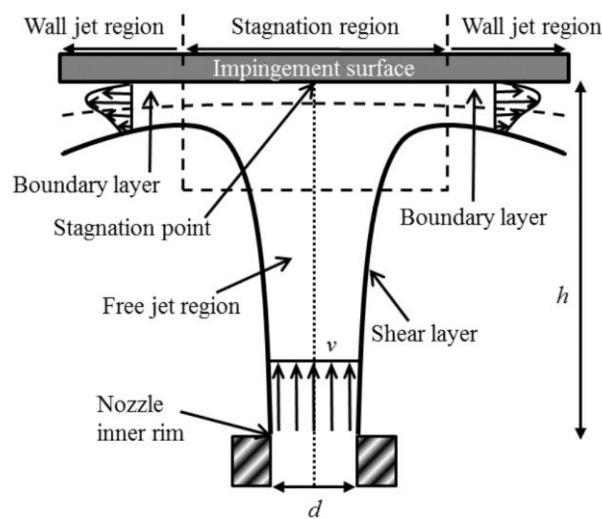


Fig. 2. 29 Structure of an impinging non-reacting jet (Chloe and Mcdaid, 2013).

2.5.2.2 Impinging reacting jet

The impinging reacting jet differs from the non-reacting jet due to its reaction zone and temperature gradients, as shown in Fig. 2. 30. There is an intense reaction zone that is located slightly away from the stagnation point. In some conditions, such as shorter nozzle-to-plate distance, high fuel flow rate will lead to the unburnt gases forming a cool central core inside the flame, thereby causing the temperature of the stagnation point to be lower than the region away from the stagnation point (Chander and Ray, 2008).

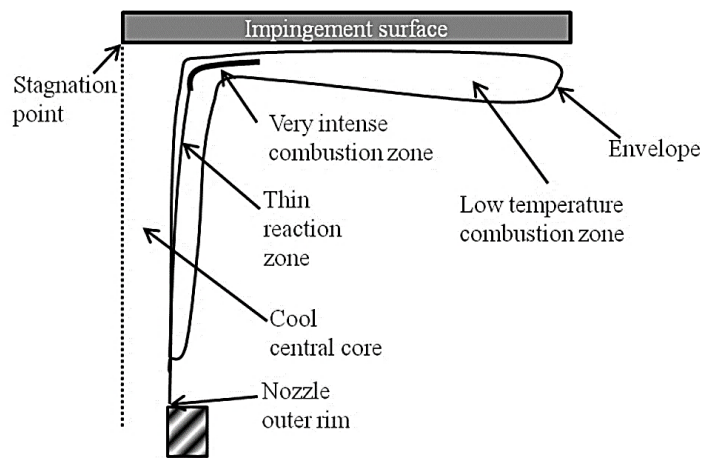


Fig. 2. 30 Structure of an impinging reacting jet (Chloe and Mcdaid, 2013).

2.5.3 Impinging flame patterns

Shown in Fig. 2. 31, eight flame modes can usually be observed in an impinging configuration, which are identified as conic, cool central core, envelope, blown ring, disc, ring, detached conic and complex flame (Foat, Yap and Zhang, 2001). These flame modes can be classified into three categories; nozzle-attached, plate stabilised and detached flames.

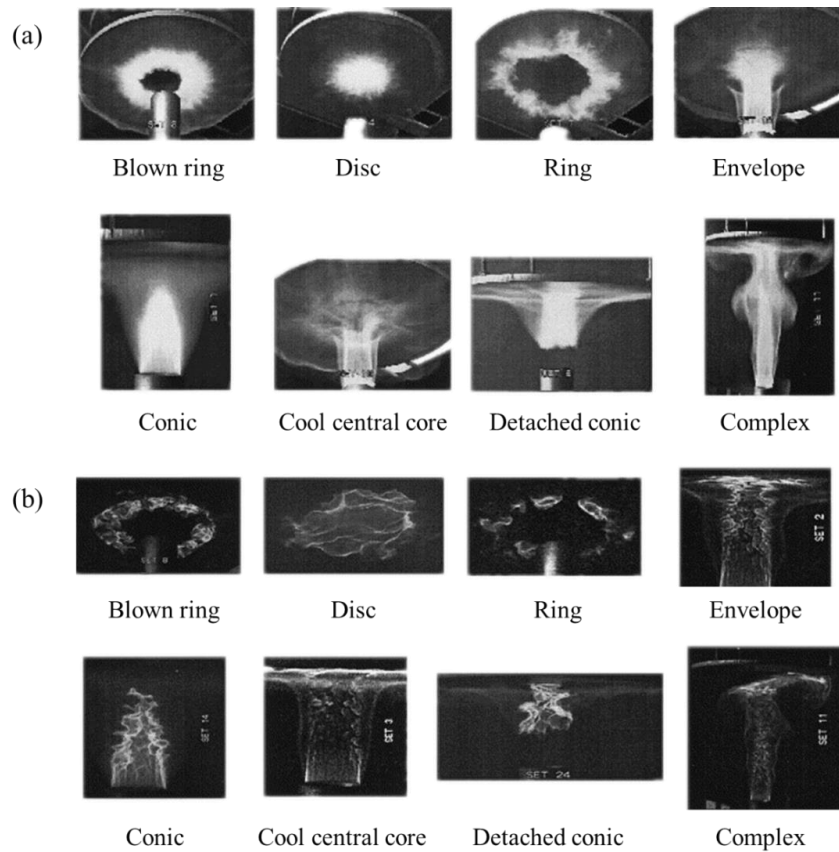


Fig. 2.31 Eight typical flame patterns. The flames are captured under (a) 1/50 s shutter speed and (b) 1/4000 s shutter speed (Foat, Yap and Zhang, 2001).

The blown ring flame is a plate-stabilised flame with a green appearance surrounded by a blue light emission layer. There is a central region without combustion taking place. It is reported that the blown ring flame only took place when the ratio of nozzle-to-plate distance to the nozzle diameter H/d was relatively low, and the jet velocity was high. It often occurred in the fuel-rich mixture conditions. The blown ring flame pattern was hard to form without a turbulence generator if the impinging plate was not cooled. If the flow rate was decreased to a critical value, the blown ring became a disc flame.

The disc flame takes place in a wide range of conditions with a blue appearance. It can be formed with or without a turbulence generator. It is found that the stable disc flame is easier to form if the plate is heated. A stable disc flame always forms at the lowest equivalence ratios. If the fuel flow rate is gradually increased, the flame becomes more wrinkled. As the fuel flow keeps increasing, the flame converts to a detached flame and then attaches to the nozzle. Research demonstrated that the flame was more stable

at a relatively low H/d . If $H/d < 1$, the flame structure formed with a flat central section with a surrounding wider ring section. When $H/d = 3$, the flat central section disappeared, and the disc flame became unstable.

A ring flame is one of the least stable flame modes and occurs over a narrow range of equivalence ratio with the help of turbulence generator. When captured at a lower shutter speed or visualised directly by the eyes, the flame showed a complete ring structure. However, one or more breaks were shown on the ring when captured at high shutter speeds. It was found that when the flame initiated at one point, the flame propagated circumferentially in both directions. The flame front may meet another flame front which was initiated at a different point. Also, the flame no longer propagated outwards in the radial direction (Foat, Yap and Zhang, 2001).

A conical flame is a Bunsen-type flame which stabilises on the burner nozzle rim since the plate is relatively far away from the nozzle. If the mixture was ignited near the plate, the flame propagated towards the nozzle and stabilised around the nozzle rim.

Both the envelope and cool central core flames exist in fuel rich conditions. The main difference between them is that the cool central core flame has an unreacted zone around the stagnation region since insufficient air is entrained into the jet before impinging. When the fuel flow was increased, a conic flame could change to an envelope flame, and then to a cool central core flame. Once the distance between the nozzle and plate was increased, the transition between the envelope and the cool central core flames took place at relatively higher equivalence ratios. At low H/d , the cool central core flame was easier to establish at lower equivalence ratios than an envelope flame. The transition between two flame modes was less affected by changing the flow velocity, while greatly influenced by the turbulence generator (Zhang and Bray, 1999).

The detached conic flame is an unsteady dancing flame between the nozzle and the plate, which was only formed at fuel-rich conditions. It could be converted from a disc flame by increasing the fuel flow velocity. If the fuel flow kept increasing, the flame could reattach to the nozzle rim due to the self-generated large-scale turbulence with the help of a turbulence generator. The flame could attach to the nozzle by re-igniting at the nozzle exit.

A complex flame is composed of different flame modes. It took place at larger H/d values and fuel-rich conditions, with surrounding blue light emission from lean secondary burning. The complex flame intermittently impinges on the plate (Foat, Yap and Zhang, 2001).

2.5.4 Impact factors of impinging flames

From Section 2.5.3, it is found that the impinging flame is strongly influenced by flow velocity, H/d , equivalence ratio, plate temperature and a turbulence generator. Besides, some other variables also affect impinging flames, such as ignition location, impingement angle, plate surface conditions and plate inclination angle (Sang-Joon, Jung-Ho and Dae-Hee, 1994; Yan and Saniei, 1997; San and Shiao, 2006; Katti and Prabhu, 2008; Phalnikar, Kumar and Alvi, 2008; Koched, Pavageau and Aloui, 2011; Tummers, Jacobse and Voorbrood, 2011; El Hassan *et al.*, 2012, 2013; Zhang *et al.*, 2013).

Research has demonstrated that ignition location significantly affected the flame propagation speed and flame structure in the impinging flame settings (Konracki *et al.*, 2007a; Ming-wei, 2012; Park and Lee, 2012). The investigation of ignition effect on the propagation of diffusion or premixed flames in an impinging configuration was conducted by McDaid and Zhang (McDaid, Zhou and Zhang, 2013). Three ignition locations were attempted, which are the nozzle exit, halfway between the nozzle and plate and at the plate centre. They found that the total ignition duration from the flame being ignited until a steady state was greatly influenced by the ignition location variation. Non-linear velocity/acceleration was found for flame edges when ignited downstream. Delays of downwards propagation were observed when the flame was ignited at the plate; the flame spread across the plate first then propagated downward, since the opposite fuel flow from the jet blocked the downwards propagation. Zhang and Bray (Zhang and Bray, 1999) reported that by changing the ignition location only, it would directly affect the final steady flame structure, including the envelope, ring, conic, disc and cool central core flames. Foat and Zhang (Foat, Yap and Zhang, 2001) reported that up to four different flame modes had been established under identical nozzle flow conditions. Huang *et al.* (Huang and Zhang, 2011) reported that the flame colour variation is also related to the ignition location. Methane diffusion flames were

established with various initiated points. It was found that the chemiluminescence bluish-green flame distribution gradually enlarged with the increase of ignition distance from the nozzle exit. When the flame was initiated near the plate, it was entirely blue.

H/d represents the ratio of nozzle-to-plate distance to the nozzle diameter. The effect of the H/d on impinging flames has been extensively studied (Dong, Cheung and Leung, 2002; Dong, Leung and Cheung, 2003; Chander and Ray, 2008). It has been found that the heat transfer and the interaction between the flame and wall depend on the distribution of the unburned fuel region in the impinging flame, which is closely related to H/d . A dip in heat flux at the stagnation region was more pronounced when the H/d value was small. The mean heat flux grew with the increase of H/d and decreased afterwards because of impingement of a partial flame. In addition, the plate temperature is another critical factor. Many studies have applied the water-cooled plate for the impinging flame study (Baukal and Gebhart, 1997, 1998, Chander and Ray, 2007a, 2007b, 2008). The water-cooled plate is regarded as isothermal. The temperature gradients of the plate are significantly reduced by water cooling. If the plate is not cooled, it will lead to a high radiation loss during impingement. It was found that plate temperature affected the flame properties near the plate, such as the flame pattern, quantity of soot formation and the flame propagation speed along the plate (Foat, Yap and Zhang, 2001; Malikov *et al.*, 2001; Li *et al.*, 2010).

2.6 Experimental Flame Imaging Diagnostic Techniques

2.6.1 Introduction

Flame diagnostics are highly required in most industrial combustion systems. Combustion performances in the combustion chamber and boiler furnace, which include flame stability, flame velocity and chemical reaction rate need to be monitored to avoid wall quenching and explosion. Common flame detectors launch a flame protection device when vanishing of the flame is detected, which often gives false alarms. Fortunately, the flame imaging diagnostic approaches implement an optical and non-intrusive measurement which can monitor the spatial combustion performance without interfering with the combustion systems.

The ignition of a flammable gas mixture is always accompanied by complicated chemical reactions and multiple parameter variations, such as temperature, pressure and flame propagation velocity. However, the standard digital camera is not able to capture this rapid process. Therefore, a high-speed camera is always used in the experimental combustion studies. High-speed cameras can capture images under a high frame rate from 50 to more than 650,000 frames per second. The recording process can be viewed in slow motion; a high temporal resolution, which allows the detail to be seen. Modern experiment methods combined with the digital high-speed imaging technique are widely applied to study combustion mechanisms, such as a laser, thermal and schlieren imaging.

2.6.2 Schlieren imaging

The propagation of light through inhomogeneous media leads to refraction. Schlieren occurs due to the bending of the initial path of the rays. The schlieren imaging method is based on the deflection of light due to a refractive index gradient, which is correlated with the flow density gradient. A knife edge is placed vertically to the flow density gradient, which obstructs partial undisturbed light rays and leads to a degree difference on the screen illumination (Llowarch, 1964; Mazumdar, 2011). Hooke (Rienitz, 1975) established the first schlieren setup which consists of two candles and a convex lens in 1665. For the following hundred years, the developed schlieren systems have usually been used to investigate invisible phenomena.

Schlieren imaging is utilised in fluid dynamics investigations. Fig. 2. 32 shows a typical Z-type schlieren system, which contains a digital camera, a point light source and a pair of spherical concave mirrors, which are placed in parallel. A knife-edge is placed at the focal point in front of the camera to visualise the degree difference on the screen. The light slit is fixed at a distance of one focal length from Mirror A. Mirror A refracts the light, which travels through the target region and propagates towards Mirror B. Mirror B bends the rays to be received by the camera afterwards (Settles and Covert, 2002).

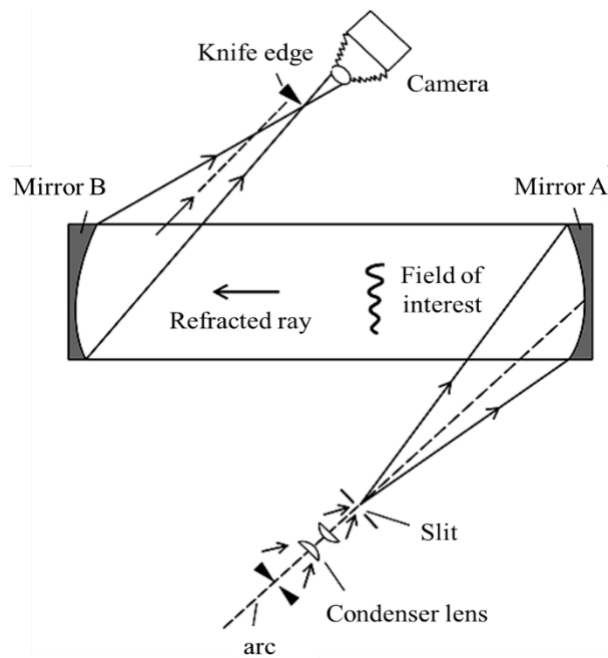


Fig. 2. 32 A standard Z-configuration parallel-light schlieren system (Gnani *et al.*, 2015).

Colour schlieren systems rely on the same theory as general black-and-white systems. The only difference is that the changes with deflection angle and direction are distinguished by different colours (Stevenson and Skews, 2015). In some cases, the black-and-white schlieren systems cannot provide sufficient information and details. For instance, the colour schlieren is exerted to observe the complex flow structure, since the grayscale image is not clear enough. The colouring technique can be summarised by three methods:

- Using the colour optical filter to add colour to the knife-edge.
- Making a source mask; i.e. placing several strips of the coloured filter in front of the light source.
- Replacing the usual knife-edge with a corresponding change in a slit shape, e.g. in the chromatic dispersion prism method, which utilised electro-optical technology to provide different optical densities with specific colours (Settles, 1985).

Advanced schlieren techniques are modernised nowadays, in consequence of expensive optical elements and limitations of traditional schlieren systems. The background-oriented schlieren (BOS) technique is based on the same theory of

traditional schlieren systems combined with computer processing (Raffel, 2015). Compared with the traditional schlieren, BOS systems have three advantages:

- i. A simple BOS configuration consists of a CCD and a suitable background image which saves the high expense of precise optical elements.
- ii. The low-cost equipment of BOS is utilised in many experiments, such as wind tunnels, helicopters and combustion flow fields. Richard and Raffel (Richard and Raffel, 2001) adopted the BOS method to measure the density distribution of the flow field caused by a helicopter's rotor wings, using the nearby buildings as the background. The traditional schlieren cannot achieve this.
- iii. BOS can measure the density field quantitatively.

However, if the flow density changes rapidly, high background image resolution will be required.

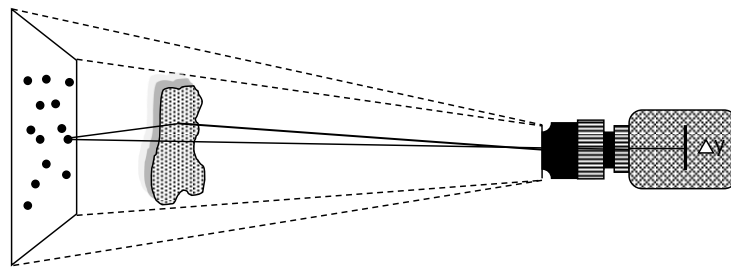


Fig. 2. 33 A typical BOS system using a digital CCD camera to focus a background image with random oriented points.

A digital CCD camera is applied to typical BOS systems to focus a background image with random oriented points (Hargather and Settles, 2010). The region of interest is located between the camera and background image, as shown in the Fig. 2. 33. The background image is captured as a reference image before setting up the flow field. Once the flow field is established, the rays from the background image are bent due to interaction with the flow field, thereby leading to the displacement of the corresponding points between the reference and the experimental images. The value of displacement is proportional to the integration of the density gradient.

The main advantage of schlieren imaging in the flame studies is the time-dependent visualisation of the hot gas movement. In the previous study, the detection of the velocity distribution of a flow field of schlieren images can be implemented via the

image analysis technique. The fluid movement between the two consecutive images is gained via functional analysis that gives the local function deformation at each image position (Fu and Wu, 2001).

On the other hand, schlieren imaging is ineffective if the flame pattern has a large out-of-plane region, for instance, the impinging flame propagation in a radial direction along the plate. Some flame properties cannot be obtained by schlieren imaging, such as flame temperature, colour and three-dimensional movement.

2.6.3 Laser imaging

Laser imaging diagnostics can visualise the spatial and temporal flame evolution and are often applied to investigate the flame characteristics in laboratories. PIV and PLIF techniques provide flame velocity measurements of flow fields and species concentrations of OH and CH in the reaction zone, along with quantity of the pollutants, such as NO, CO and SO₂ (Nye *et al.*, 1996; Fu and Wu, 2001; Petersson *et al.*, 2007; Fan, Suzuki and Kasagi, 2011; Fu *et al.*, 2013; Weinkauff *et al.*, 2013). PIV is a method of non-intrusive, instantaneous velocity field measurement, which has great research and practical value in the field of fluid dynamics and aerodynamics. The schematic of a typical PIV imaging system is shown in Fig. 2. 34.

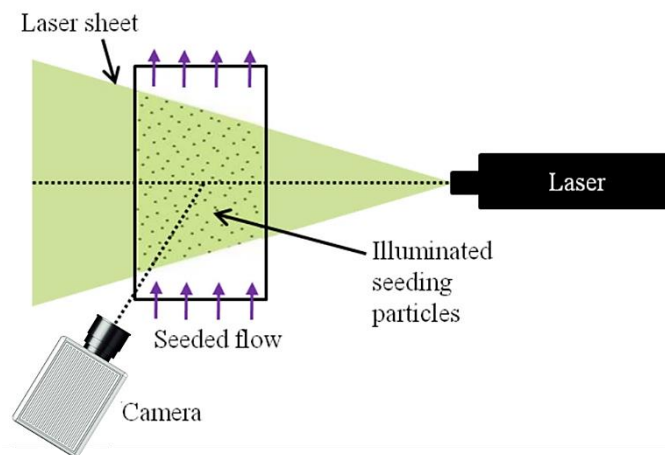


Fig. 2. 34 Schematic of a typical PIV imaging system.

PIV records the position of particles in a flow field by multiple shots and analyses the captured image to determine the flow velocity. Tracer particles are seeded in the flow field; their velocity represents the velocity of the fluid at the corresponding location in

the flow field. A laser produces high-power light beams with short pulse durations to the plane, which allows imaging of the positions of the particles for each frame. The displacement of each particle is obtained by the image processing technique. The flow velocity field can be gained according to the displacement and the exposure time (Elsinga and Scarano, 2014). Due to the difference of recording equipment, PIV is classified to film recording (FPIV) and digital particle image velocimetry (DPIV); recorded by a CCD camera (Ryerson and Schwenk, 2012).

Tracer particles have to be non-toxic, non-corrosive, non-abrasive, chemically stable and clean (Adrian and Westerweel, 2011). In addition, the tracer particle must follow the flow, and its refractive index must be different from the fluid. The diameter of the seeding particles has to be small to follow the flow field. Therefore, the density of the particle should be equal to the density of the fluid. The particle diameter should be just large enough to suitably scatter the light. Seeding particles usually include polystyrene, aluminium, magnesium, zinc oxide and glass balls (Raffel, 2007). The particle concentration also has to be considered. The particle may superimpose each other on the image with a high particle concentration since the laser is interference light, which will form laser speckles on the photographic film. The displacement of the extracted speckle field can be relatively difficult to extract due to the poor stability of the speckle field. Conversely, the number of the particle may be too small with low concentrations, which will largely reduce the accuracy of the flow velocity field. A typical PIV imaging system is composed of a dual-pulse laser light source, lens and camera (Elsinga and Scarano, 2014). A light sheet is formed by a pulsed laser shone through a lens to illuminate the particle field. The camera is perpendicular to the light sheet. The exposure time should be short, and the light sheet should be as thin as possible. A thick light sheet will compress the 3D flow field to a 2D flow field, which cannot correctly represent the 2D flow field. Double pulsed lasers are usually applied to provide sufficient light energy for exposure.

Another laser imaging technique, PLIF is used for flow visualisation and quantitative measurements. It has been applied to measure velocity, temperature, pressure and particle concentration (Richard and Raffel, 2001; Hult *et al.*, 2007; Raffel, 2007; Rosell *et al.*, 2017). PLIF systems contain a laser light source, lenses, fluorescent

medium (specific molecules), collection optics and a detector, as shown in the Fig. 2. 35. The specific molecules jump to an excited state when illuminated by the laser. The excited molecules will then return to the ground state and emit photons, thereby fluorescing, which are captured by the detector. The fluorescence distribution can be used to determine the particle species. The fluorescence intensity reflects the concentration and temperature of the particles.

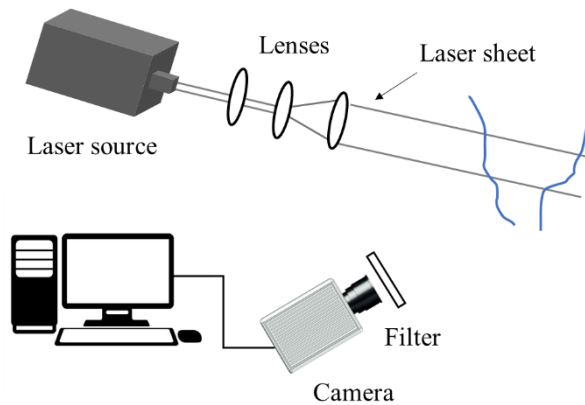


Fig. 2. 35 Schematic of a typical PLIF system.

Overall, laser imaging is a precise diagnostic method, which is often used in flame laboratory studies. The complicated setup is the main weakness of laser imaging, which results in difficulties for industrial applications. In addition, the gained information is limited to a single plane.

2.6.4 Digital flame colour discrimination methodology

2.6.4.1 Colour space of images

It is known that flame light emission is closely related to the flame colour. Huang and Zhang (Shimura *et al.*, 2011; Huang and Zhang, 2012, 2013; Huang *et al.*, 2013) introduced Digital Flame Colour Discrimination (DFCD) method which establishes a relationship between the flame multiple emission species and their corresponding colour signal presences. Since the specific molecules will emit photons at certain wavelengths, their emissions present as specific colours in the captured images. For example, for hydrocarbon flames, the orange/ yellow colour presence of the flame is due to the soot radiation only. There is no other matter emitting in orange/yellow. The blue flame is the flame chemiluminescence which is primarily due to CH^* and C_2^*

emission. Therefore, multiple flame light emission species can be differentiated via their presented colour in the images. Huang and Zhang (Huang *et al.*, 2008) used the HSV colour model instead of the RGB model to differentiate the flame chemiluminescence and sooty flame regions. It is known that digital cameras output images in the RGB model. The RGB model characterisation has a very similar function as the human visual system. RGB is an additive colour model which is created by mixing three primaries: Red, Green and Blue with different proportions to produce various colours. It is used for the sensing, representation and display of images in electronic systems, such as computers and televisions. The output images from a digital camera are composed of three layers, which correspond to Red, Green and Blue channels, as shown in Fig. 2. 36. Each pixel is specified by the coordinate of $[I_R, I_G, I_B]$. When describing the blue colour, it does not necessarily refer to pure blue, it may include tints of the blue or bluish colour. When determining a broad range of the blue colour, processing the image in the RGB model may not be valid, since three parameters need to be determined to identify a single colour, which is hard to perform. Therefore, the HSV colour model space is used instead.

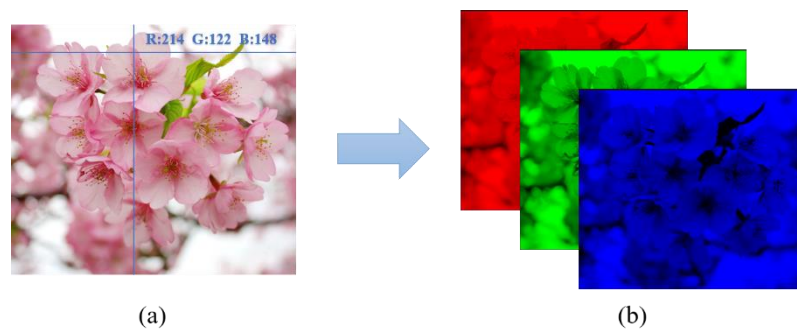


Fig. 2. 36 (a) The sakura photo displayed in the RGB colour model space; (b) The photo is separated into Red, Green and Blue channels, respectively (*Cherry Blossoms in Japan: All About Sakura and Hanami - LIVE JAPAN*, 2018).

The HSV space is presented as a Hexcone Model, as shown in Fig. 2. 37. It stands for Hue, Saturation and Value. The hue represents which pure colour it resembles (Solomon and Breckon, 2013). Saturation describes the intensity of colour, which represents the amount of grey from 0 to 100 % for each colour. For example, the pure blue colour is fully saturated with a saturation of 1. The saturation of tints of blue is less than 1. The saturation of white is 0. The value represents the brightness of the

colour, which describes how dark the colour is. A value of 0 is black, with increasing lightness moving away from black. Here, hue is used to differentiate the colours. For instance, the blue colour with various tints, tones and shades have the same hue. The hue is expressed as a number from 0 to 360 degrees, where the hues of reddish start from 0 degree, yellowish from 60 degrees and greenish start from 120 degrees. The target colour can be separately extracted from the hue domain with specific degree ranges, which is easier than performing in the RGB model.

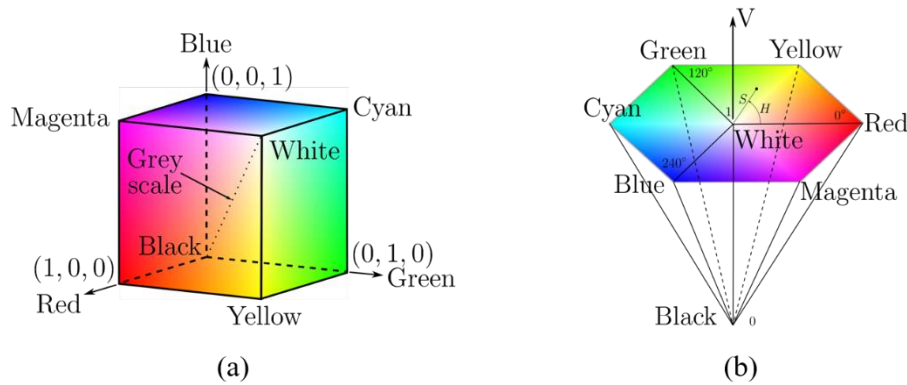


Fig. 2. 37 (a) The RGB colour model space (Nishad and Manicka Chezian, 2013) and (b) the HSV colour model space (Cardani, 2001).

2.6.4.2 Flame colour analysis

It was reported that the chemiluminescence-induced blue flame was located in a range of 180 to 300 degrees in the hue domain and the orange/ yellow sooty flame was located from 0 to 80 degrees when applying an Olympus E-100RS digital CCD camera (Huang and Zhang, 2008a), as shown in Fig. 2. 38. CH^* , C_2^* and soot particles can be extracted and analysed separately through the Digital Flame Colour Discrimination. Moreover, it is known that the blue flame is obscured under a high shutter speed since the flame chemiluminescence signal is relatively weak. With the help of the DFCD approach, the blue flame can be selectively enhanced.

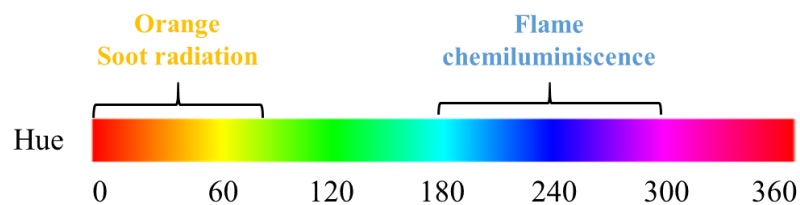


Fig. 2. 38 The hue value distribution of orange soot and flame chemiluminescence (CH^* and C_2^*) are from 0 to 80 degrees and 180 to 300 degrees respectively.

The DFCD method can allow the time-dependent simultaneous visualisation of CH*, C₂* and soot light emission when combined with a high-speed camera. Only a single high-speed camera is required, which is more suitable for industrial fire diagnostics. The weakness of this method is that the captured signal is the overlap of the light emission in the same line of sight. The orange sooty flame always obscures the blue flame. Therefore, the quantitative analysis is limited to flame feature comparison between different cases. Compared with the spectral analysis of flame emission, e.g. spectrometer, the DFCD method provides the spatial information of the flame, which clearly presents the flame profile in 2D.

2.6.5 Thermal imaging and thermal couples

Thermal imaging allows the non-intrusive measurement of flame temperature in 2D. Thermal radiation is detected by thermal imaging cameras and then converted to a thermogram, which shows the temperature distribution of an object according to the wavelength of the detected radiation (Kreith, Bohn and Kirkpatrick, 1997; Incropera *et al.*, 2007).

Thermal imaging cameras have limitations for applications in combustion due to several drawbacks (Malalasekera, Versteeg and Gilchrist, 1996; Blunck *et al.*, 2009):

- The inaccuracy of the flame temperature measurement due to the high spectral range of the flame.
- Inaccurate emissivity input values which relate to the temperature and viewing angle.
- Different surfaces types can also lead to the low accuracy of the cameras.

Thermocouples are a common temperature measurement instrument, which directly measures the temperature, converted into electric signals (Shaddix, 1999). The working mechanism is as follows: when two different conductors or semiconductors with different temperatures are placed together, an electric loop can be formed. The current created between these two materials is the thermo electromotive force (emf). This is also called the Seebeck effect and can be expressed by

$$dE_s = \alpha_{A,B} dT \quad (2.22)$$

where E_s is the Seebeck voltage, T is the temperature and $\alpha_{A,B}$ is the Seebeck coefficient. The ‘hot’ point temperature can be obtained via the equation. Thermocouples can affect the surface temperature, leading to inaccuracy in the emfs, therefore insulated wires are usually applied during the research. Thermocouples should have good contact with the materials’ surfaces to reduce unnecessary effects to the surface temperature. In order to get an accurate temperature measurement, the materials’ surfaces are also modified to match the thermocouples. Time limits and the insulation problem are the main drawbacks for using the thermocouples.

2.6.6 Stereo imaging

The main drawback of the 2D imaging techniques is the deficiency of the 3D information. The 2D imaging techniques can only provide limited information when the flame has complex 3D flame-flow interactions and large out-of-plane propagation, such as the impinging flames and swirl flames (Ebi and Clemens, 2016). Stereo imaging is a considerable 3D reconstruction method which consists of a two-camera system.

2.6.6.1 Stereo imaging principle

Sometimes, 2D images will deceive our eyes. Shown in Fig. 2. 39, the photographer uses optical illusions to present interesting photos.



Fig. 2. 39 Optical illusions examples (*Fun Optical Illusions*, 2015).

The optical illusion phenomena can be explained via a single camera system. In Fig. 2. 40 (a), π and O represent the image plane and the optical centre receptively. The points P and Q project onto the same image point, which is expressed as $p \equiv q$. If the

object located at point Q is opaque, then point P is completely obscured by Q , as well as other points along the same line of sight. For general 2D imaging flame diagnostics, the overlap of the flame sheets may lead to results becoming deviated from reality. Thus, 3D imaging is desirable for flame studies, which can be achieved by applying two or more cameras. In the two-camera system, the points P and Q can be differentiated in the other plane π_T (Mattoccia, 2013).

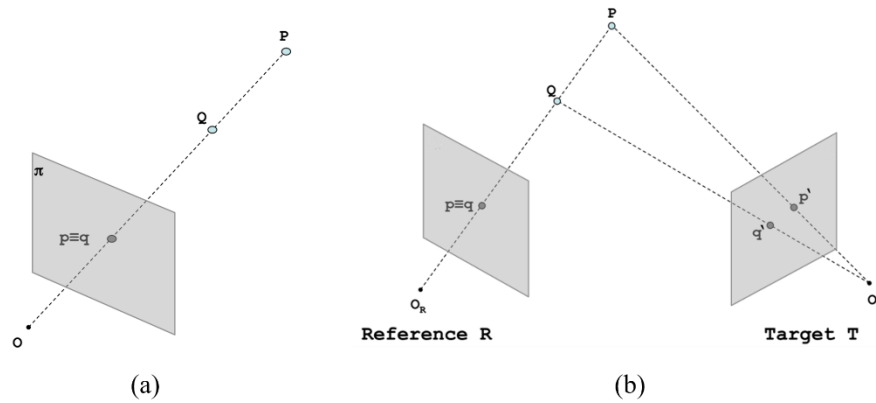


Fig. 2. 40 (a) Single camera system. (b) Two-camera system. (Tombari *et al.*, 2008)

Stereo imaging is based on the two-camera system. The depth of the target point can be inferred from triangulation. The corresponding points in the two images have to be determined at first. The epipolar constraint is used to solve the correspondence problem. The epipolar constraint states that the correspondence for points on the green line \overline{pq} lies on the red line $\overline{p'q'}$ on the image plane π_T , as shown in Fig. 2. 41 (a). The stereo-camera system then transforms this into a standard form in which the corresponding points are constrained on the same image scan line, as shown in Fig. 2. 41 (b).

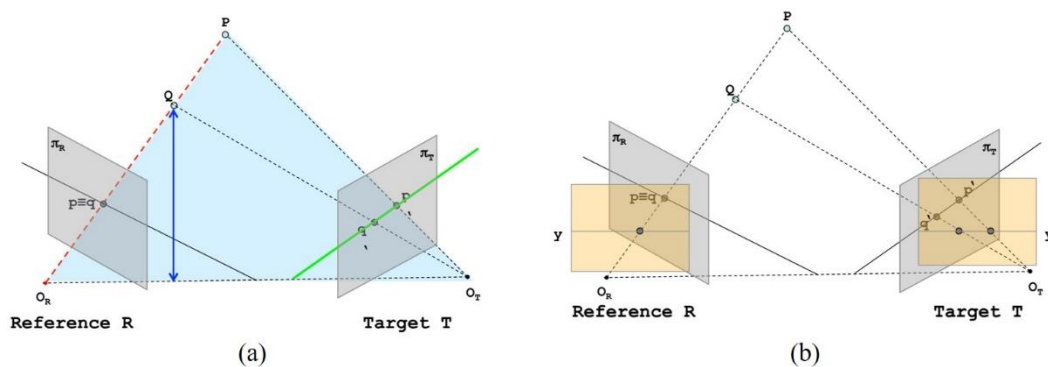


Fig. 2. 41 (a) Schematic of the epipolar constraint and (b) The stereo-camera system in a standard form. (Mattoccia, 2014)

Finally, the depth of the point P can be measured according to the similar triangles $\angle PO_R O_T$ and $\angle Ppp'$ in Fig. 2. 42 (a). The disparity is expressed as $X_R - X_T$, which represents the difference between the x coordinates of the two corresponding points. The relationship between the disparity $X_R - X_T$ and the depth of the target point Z is expressed by

$$\frac{b}{Z} = \frac{(b + x_T) - x_R}{Z - f} \quad (2.23)$$

$$Z = \frac{b \cdot f}{x_R - x_T} = \frac{b \cdot f}{d} \quad (2.24)$$

where b represents the baseline in the stereo system and f represents the focal length. The stereo system is constrained by the disparity range from d_{min} to d_{max} . Shown in Fig. 2. 42 (b), the depth measurement is discretised into parallel planes. If the disparity is beyond d_{max} , the horopter will shrink.

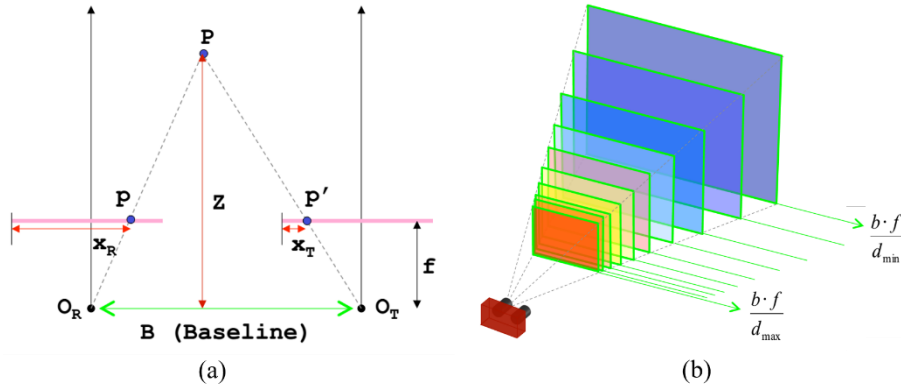


Fig. 2. 42 (a) Schematic of the depth measurement and (b) Horopter in the stereo imaging system. (Mattoccia, 2013)

Point correspondence can also be worked out via optical flow method. The concept of optical flow was first proposed by Gibson in 1950 (Horn and Schunck, 1981). When the human eye observes a moving object, the scene of the object forms a series of continuously changing images on the retina of the human eye. The optical flow expresses the evolution of the image, which can be used to determine the motion of the target. The optical flow estimation assumes that the object does not have a

significant displacement between two sequential frames. The images depict a natural scene containing textured objects exhibiting shades of grey which change smoothly. Hence the optical flow is formed by the change of the brightness of the image sequence. Therefore, the optical flow field is similar to the motion field. The basic rule of optical flow is expressed as

$$\frac{\partial I}{\partial x} V_x + \frac{\partial I}{\partial y} V_y + \frac{\partial I}{\partial t} = 0 \quad (2.25)$$

where V_x and V_y are the vector of optical flow. $\frac{\partial I}{\partial x}$, $\frac{\partial I}{\partial y}$ and $\frac{\partial I}{\partial t}$ are the finite difference of (x, y, t) . The exact values of V_x and V_y cannot be obtained since the constraint equation has two variables, which is called the aperture problem. The calculation of the optical flow field was first resolved by Horn and Schunck (Bruhn, Weickert and Schnörr, 2005) in 1981. Lucas and Kanade proposed an improved optical flow algorithm. The detail of the algorithm is introduced in Section 8.3.2. There are dozens of algorithms can work out optical flow until now.

Fig. 2. 43 shows a flame stereo image pair which has a little angle difference to each other. The stereo flame images that obtained from the two-camera system can be treated as two sequential frames that captured by a single camera since the stereo image pair has a small displacement and continuously changing the brightness.



Fig. 2. 43 A pair of flame stereo images.

2.6.6.2 Stereo imaging for flame studies

Wang (Wang, 2009) simplified the stereo imaging setup by using a single camera and a stereo adapter, which is easy to operate and more economical. The stereo adapter works as two virtual cameras, as shown in Fig. 2. 44. The incident light from the focus area enters the outer mirrors, is reflected and enters the inner mirrors. Consequently,

the ray is reflected again by the inner mirrors and enters the lens of the camera. Finally, a synchronous image pair with slight displacement is generated which provides two virtual views.

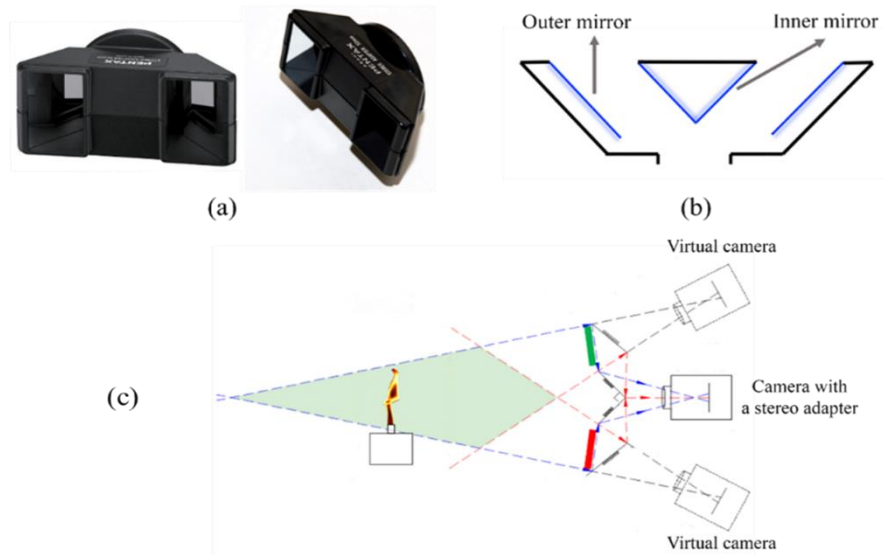


Fig. 2. 44 (a) Stereo adapter, (b) Structure of the stereo adapter and (c) Schematic of the stereo adapter function (Wang, 2009).

A previous study successfully reconstructed the impinging flames (Wang *et al.*, 2013), as shown in Fig. 2. 45. With the help of the image processing technique, the 3D flame chemiluminescence blue region and the soot emission region can be reconstructed separately.

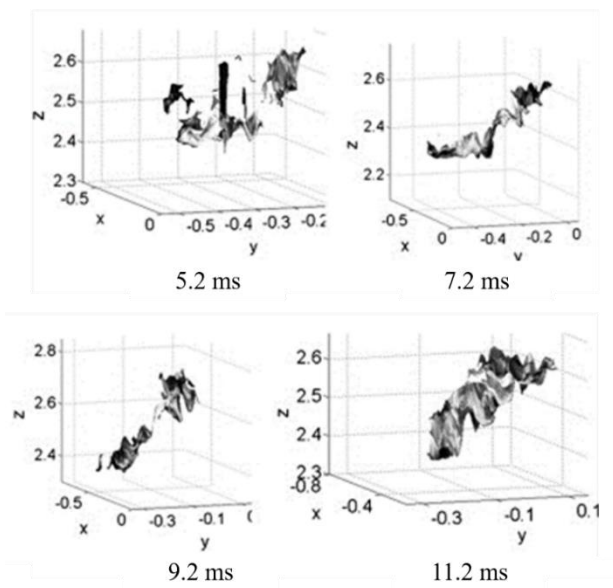


Fig. 2. 45 Time-resolved 3D structure reconstruction of an enhanced blue flame in the impinging configuration (Wang *et al.*, 2013).

The main drawback of this technique is that the 3D flame structure shows only the outer layer. The technique is based on the 2D imaging and the flame core and back-view details are lost during the 3D reconstruction.

2.7 Summary

The literature review section has reviewed the combustion theory, flame light emission, flame ignition and propagation, impinging flame characteristics and experimental flame imaging diagnostic techniques, which introduces the research works conducted by the other researcher and produces clear targets for the following research projects. Some research gaps were found through the literature review, such as the simultaneous flame emission visualisation in multiple spectra, experimental 3D flame propagation velocity measurement and PAH emission study.

Chapter 3

Simultaneous Multiple Light Emission Tracking by a Single Camera: Method and Algorithm

3.1 Introduction

Laser imaging diagnostics allows visualisation of the spatial and temporal flame evolution and are often applied to investigate flame characteristics in laboratories. PIV and PLIF techniques can provide flame velocity measurements of flow fields, species concentrations of OH and CH in the reaction zone and quantity of the pollutants, such as NO, CO and SO₂. Common laser imaging can allow tracking of only a single radical species by using a set of the laser system and a camera. Recent research has imaged four radicals simultaneously. Sjöholm et al. (Sjöholm *et al.*, 2013) achieved simultaneous visualisation of OH, CH, CH₂O and toluene PLIF in a methane jet flame. Although the setup was already simplified, four ICCD cameras were needed. The experimental setup and operation procedure are complicated. Moreover, these techniques remain expensive to implement, and the optical access required may result in a significant redesign of the combustion chamber. These factors make laser imaging diagnostics inappropriate for real industrial applications. Thus, a simple approach that can simultaneously track multiple radicals/particle species is urgently required.

It is evident that the flame light emission is closely related to the flame colour captured by a digital colour camera. In the combustion zone, many molecule/particle species emit at specific wavelengths. The light emission is received by the CCD/CMOS sensor of the camera and then converted to an electric signal via an image processor, and finally displayed as various colours on the digital colour image. This chapter introduces a flame colour imaging diagnostic technique which is capable of time-dependent simultaneous multiple flame light emission species imaging from the visible to infrared spectrum by using a single high-speed CMOS camera. With the help of a novel image post-processing technique, CH*, C₂*, soot particles and infrared emission can be differentiated according to their specific hue ranges in the HSV colour space. The obscured CH*, C₂* and infrared emissions under a high shutter speed are

selectively enhanced. The infrared-emission-only region is found in between the chemiluminescence-induced blue flame and yellow sooty flame.

3.2 Light Emission of Hydrocarbon Flames

The light emission of a typical hydrocarbon flame consists of the broadband orange coloured soot particle radiation and spectral band emission of excited species in the ultraviolet, visible and infrared spectra. The perceptible orange colour is the result of the grey-body radiation of incandescent soot in the visible spectrum. The OH* has the strongest band with the primary peak at 309 nm within the UV spectrum. The 'bluish' light of the flame is mainly composed of excited molecular radicals C₂* (Swan system, dominant emissive band heads at 473.71 nm and 516.52 nm) and CH* (430 nm) (Gaydon, 1974), which is known as chemiluminescence. The CH* and C₂* are good indicators of the chemical reactions within the hydrocarbon flame. The chemiluminescence can be explained as the radiation which forms during the process when the excited molecules return to a lower energy state, which always occurs in a combustion reaction. In the infrared spectrum, the combustion products CO₂ and H₂O have strong bands with two primary peaks at 2.8 μm and 4.4 μm (Gaydon, 1974). The strongest band at 4.4μm is due to CO₂; the other strong band at 2.8 μm is the emission from both CO₂ and H₂O. The heated soot particles also have continuum radiation with peak emission in the mid-infrared region of the spectrum.

3.3 Digital Flame Colour Discrimination Methodology

As mentioned in Section 3.2, the flame light emission is related to the apparent flame colour. An image post-processing method, named Digital Flame Colour Discrimination, establishes a relationship between the flame multiple emission species and their corresponding colour signal presences (Huang and Zhang, 2008a). Since specific molecules will emit photons at certain wavelengths, their emissions present as specific colours in the captured images. The captured images are converted from the RGB to HSV colour model to differentiate the flame chemiluminescence (blue) and sooty flame (orange) regions. It is reported that the chemiluminescence-induced blue flame is located in a range of 180 to 300 degrees in the hue domain and the

orange/yellow sooty flame is located from 0 to 80 degrees by applying an Olympus E-100RS digital CCD camera (Huang and Zhang, 2008b). The CH*, C₂* and soot particles can be extracted and analysed separately via the DFCD method.

3.4 Flame Visualisation from the Infrared to Visible Spectrum via an Optimised Digital Imaging Processing Method

A high-speed camera; Photron SA4, is used in this research to study the flame propagation characteristics, especially the flame ignition process. Since the light sensitivities of the high-speed CMOS camera and Olympus E-100RS digital CCD camera have a big difference, the hue ranges mentioned in Section 3.3 can no longer be used. Based on the principle of the DFCD method, a programme is developed and applied to the post-processed flame image captured by the high-speed Photron SA4 camera. It is found that there is another hue range from 252 to 350 degrees, which is proven to be the infrared flame emission discussed in Chapter 4. The source of this infrared emission is discussed in Section 4.2.

Fig. 3. 1 (f) shows an example of the hue histogram of a propane non-premixed flame image taken under 1/2000 s shutter speed, 0.102 s after ignition. The x-axis of the histograms indicates the hue domain. The y-axis is the ratio of the intensity of each specific hue range to the total pixel intensity of the image. The pixel intensity represents the brightness of the pixel. The intensity threshold of pixel intensity is from 0 to 2¹⁶.

Compared with the determined hue range from the digital CCD camera, the hue ranges of the blue flame and orange sooty flame shift under the high-speed imaging. New hue ranges of various flame emission for the Photron SA4 are determined based on a large number of tests which include varying flame composition, equivalence ratio and temperature. The emission of the blue part and orange sooty part of the hydrocarbon flame are located in ranges of 180 to 252 degrees and 10 to 70 degrees respectively, which do not overlap with each other; the gap between these two ranges is wide enough to distinguish them. It is observed that the hue value is also concentrated from H14 to H18, corresponding to 252 to 350 degrees and shown in pinkish when processing the hydrocarbon flame images. It is demonstrated in Section 4.2 that the

emission of these pinkish signals is in the infrared spectrum.

It is seen that both chemiluminescence (CH^* and C_2^*) and infrared emission signals are weak in comparison with the orange-coloured soot emission. After image post-processing, the colourations of the blue flame and pinkish infrared emission are enhanced 20 and 15 times respectively according to their hue ranges with the help of a MATLAB programme. Fig. 3. 1 (a) and (e) compare the original and the combination of selectively enhanced flame images, demonstrating the usefulness of selective image enhancement in revealing the real physical process. Here the arbitrary values of 15 and 20 are only chosen for enhanced visualisation. It is observed that the flame infrared emission zone is between the blue and orange flames.

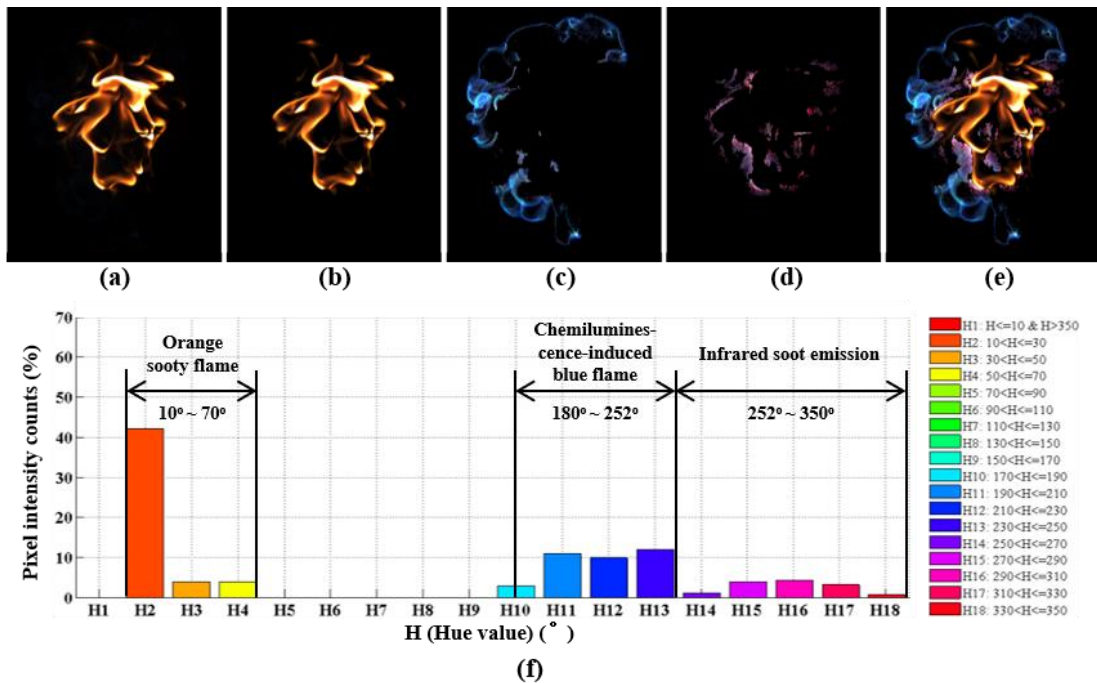


Fig. 3. 1 Images of a propane non-premixed flame at 0.102 s after ignition: (a) The original image at a shutter speed of 1/2000 s; (b) the orange sooty flame region; (c) the chemiluminescence-induced blue flame which is enhanced 20 times; (d) the infrared soot emission which is enhanced 15 times; (e) the entire image after selective image enhancement and (f) the colour distribution histogram in hue space.

3.5 Algorithm of the Image Post-processing Technique

3.5.1 Conversion from RGB to HSV colour model.

The HSV colour model is introduced to separate the flame emissions according to their colour. The captured RGB images are converted to the HSV colour model by the following equations:

$$h = \begin{cases} 0^\circ & \text{if } max = min \\ 60^\circ \times \frac{g-b}{max-min} + 0^\circ, & \text{if } max = r \text{ and } g \geq b \\ 60^\circ \times \frac{g-b}{max-min} + 360^\circ, & \text{if } max = r \text{ and } g < b \\ 60^\circ \times \frac{b-r}{max-min} + 120^\circ, & \text{if } max = g \\ 60^\circ \times \frac{r-g}{max-min} + 240^\circ, & \text{if } max = b \end{cases} \quad (3.1)$$

$$s = \begin{cases} 0, & \text{if } max = 0 \\ \frac{max-min}{max} = 1 - \frac{min}{max}, & \text{otherwise} \end{cases} \quad (3.2)$$

$$v = max \quad (3.3)$$

where *min* and *max* are the smallest and largest of the R, G, and B values respectively.

3.5.2 Denoising the mask of the flame image

The masks of the orange flame, blue flame and pinkish infrared emission can be extracted according to their specific hue ranges. An example of the blue signal's mask is shown in Fig. 3. 2 (a), which has many noisy points in the background. The noise is removed via the following four steps.

- i) An appropriate threshold is applied to pixels' intensity on the mask which can eliminate the noise.
- ii) A 3×3 nonlinear digital filtering technique is used to reduce the noise further. The result is shown in Fig. 3. 2 (c). In the 3×3 matrix, each pixel has eight nearby pixels, as shown in Fig. 3. 3, where the target pixel has coordinates (n, nn). The program is commanded that if three or more nearby pixels are valid (with the value of 1), the target pixel will be retained. Otherwise, the target pixel will be removed, with a value of 0.

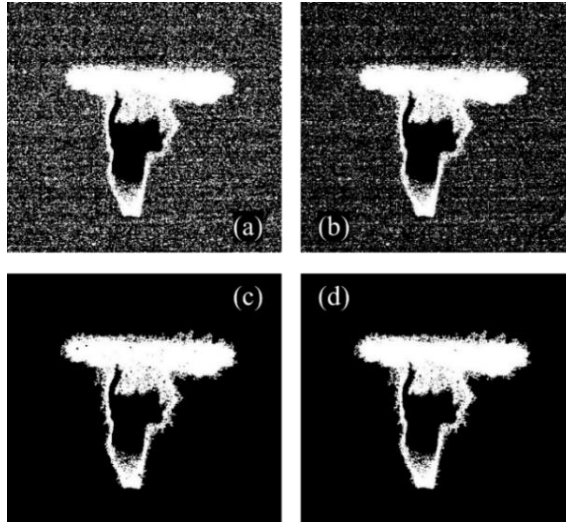


Fig. 3. 2 (a) The flame mask is composed of the blue pixels with hue values from 180 to 252 degrees, (b) The specific blue pixels whose intensity is larger than 500, (c) The mask after the nonlinear digital filtering technique and (d) Small objects are removed from the binary image.

(n-1, nn-1)	(n, nn-1)	(n+1, nn-1)
(n-1, nn)	(n, nn)	(n+1, nn)
(n-1, nn+1)	(n, nn+1)	(n+1, nn+1)

Fig. 3. 3 The 3×3 nonlinear digital filtering technique model.

- iii) The mask is transferred to a binary image. With the help of thresholding, small objects can be removed
- iv) Some small holes will be generated in the integrated flame mask, which will be filled.

The entire image denoising procedure is carried out in the blue flame, orange flame and infrared flame emission zone, respectively.

3.5.3 Conversion of images from the HSV to RGB model with selective enhancement of weak emission

Finally, the images are converted to the RGB colour model by the following equations:

$$\begin{aligned}
 h_i &\equiv \left\lfloor \frac{h}{60} \right\rfloor \pmod{6} \\
 f &= \frac{h}{60} - h_i \\
 p &= v \times (1 - s) \\
 q &= v \times (1 - f \times s) \\
 t &= v \times (1 - (1 - f) \times s)
 \end{aligned}
 \quad (r, g, b) = \begin{cases} (v, t, p), & \text{if } h_i = 0 \\ (q, v, p), & \text{if } h_i = 1 \\ (p, v, t), & \text{if } h_i = 2 \\ (p, q, v), & \text{if } h_i = 3 \\ (t, p, v), & \text{if } h_i = 4 \\ (v, p, q), & \text{if } h_i = 5 \end{cases} \quad (3.4)$$

It can be converted simply through MATLAB with the commands:

$$\begin{aligned}
 R &= (R_{\text{soot}} \cdot \text{BW}2_s) + R_{\text{blue}} \cdot \text{BW}2_b \cdot X_b + R_{\text{infrared}} \cdot \text{BW}2_b \cdot X_i; \\
 G &= (G_{\text{soot}} \cdot \text{BW}2_s) + G_{\text{blue}} \cdot \text{BW}2_b \cdot X_b + G_{\text{infrared}} \cdot \text{BW}2_b \cdot X_i; \\
 B &= (B_{\text{soot}} \cdot \text{BW}2_s) + B_{\text{blue}} \cdot \text{BW}2_b \cdot X_b + B_{\text{infrared}} \cdot \text{BW}2_b \cdot X_i; \\
 \text{rgb} &= \text{cat}(3, R, G, B);
 \end{aligned}$$

where X represents the amplification coefficient. The three clean masks; $BW2$, of the blue, orange and pinkish flames are multiplied by the original hue masks, which will provide the valid pixel. The intensities of the blue and pinkish colourations are amplified by an appropriate coefficient in each RGB layer. The new R/G/B channel is constituted by the red/green/blue component of selective blue, orange and pinkish flame regions. The chemiluminescence-induced blue flame, sooty flame and infrared emission can be analysed separately from the algorithm above. The number of pixels of each flame's colour components (blue flame, sooty flame and infrared flame emission) can be measured by calculating the total intensity of the denoising binary mask for each component.

3.6 Flame Chemiluminescence Measurement

As mentioned before, the blue luminous flame is due to the flame chemiluminescence of excited CH^* and C_2^* emission. The relative concentration of the CH^* and C_2^* can be estimated according to the sensitivity of the camera in the RGB channels. Huang and Zhang tested the spectral response of an Olympus E-100RS digital CCD camera (Huang and Zhang, 2008a, 2013). The calibration system was composed of a tungsten

lamp, a monochromator and a computer which controlled the monochromator for tuning specific wavelengths. They found that only the Green and Blue channels were sensitive to the blue flame chemiluminescence emission. To estimate the CH* and C₂* emissions, two narrow band optical filters 430 nm (± 5 nm) and 516 nm (± 2.5 nm) were applied to the left and right lens of a stereo adaptor, respectively. They found that the global C₂* and CH* emission concentrations were modelled well by the averaged intensities of the Green and the Blue channels, respectively. This meant that the relative CH* and C₂* concentrations could be obtained by calculating the intensities of Blue and Green channels, which can be expressed by

$$I_b = f_b(CH^*, C_2^*) \approx f_b'(CH^*) \quad (3.5)$$

$$I_g = f_g(CH^*, C_2^*) \approx f_g'(C_2^*) \quad (3.6)$$

where I_b and I_g represent the intensities of Blue and Green channels. However, another group claimed that Huang and Zhang's result could not be repeated (Migliorini *et al.*, 2014). Yang et al. (Yang, Ma and Zhang, 2015) have demonstrated that different cameras have different the spectral sensitivities of the R, G, and B channels. Therefore, Huang's method can not be directly applied to other works using other cameras. Yang et al. (Yang, Ma and Zhang, 2015) measured the spectral sensitivity of the high-speed Photron SA4 camera. Fig. 3. 4 shows the response of the sensor spectral sensitivity from 400 nm to 700 nm.

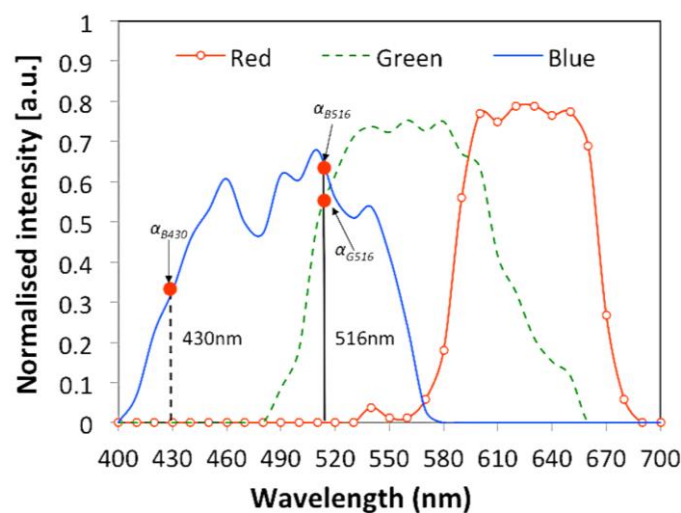


Fig. 3. 4 The spectral sensitivity of the high-speed Photron SA4 camera (Yang, Ma and Zhang, 2015).

It should be noted that the camera is also sensitive to the near-infrared spectrum. The infrared spectrum response is not shown here, because the light source that was used for the measurement emitted in the visible spectrum only.

It is observed that the G channel is not sensitive to the wavelength at 430 nm, which demonstrates that the CH* only relates to the B channel. The average spectral sensitivity ratio of B/G at 516 nm is 1.1. Consequently, the relative concentration of CH* and C₂* can be calculated.

$$CH^* \approx I_b - 1.1 I_g \quad (3.7)$$

$$C_2^* \approx I_g \quad (3.8)$$

Yang et al. (Yang, Ma and Zhang, 2015) have indicated that the ratio of CH*/C₂* concentration from colour-based measurements matches well with the exact CH*/C₂* with a 99% coefficient of determination, which demonstrated the validity of the method. They have reported that the concentration of CH*/C₂* is related to the fuel/air mixing conditions and has a linear response to the equivalence ratio, ϕ . A premixed propane flame with equivalence ratio ranging from 0.93 to 1.53 was established. The relationship between the equivalence ratio and the colour-calculated CH*/C₂* is shown as the following:

$$\phi = 0.1083 \mu_e^6 - 0.963 \mu_e^5 + 3.4235 \mu_e^4 - 6.2347 \mu_e^3 + 6.1488 \mu_e^2 - 3.2872 \mu_e + 2.01 \quad (3.9)$$

$$\mu_e = (I_b - 1.1 I_g) / 1.1 I_g \quad (3.10)$$

where μ_e is the value of the colour-calculated CH*/C₂* concentration.

3.7 Summary

Simultaneous visualisation and investigation of flame emissions from the visible to infrared spectrum in a single image have been achieved with the help of a unique image post-processing method. The images are converted from the RGB to the HSV colour model space. The emission of the blue and the orange sooty parts of the hydrocarbon flame are located in the ranges of 180 to 252 degrees and 10 to 70 degrees respectively. The infrared flame emission is concentrated from 252 to 350 degrees and

is shown in the pinkish colour when processing the flame images. The weaker chemiluminescence-induced blue flame and infrared signals can be resolved through selective digital image enhancement techniques.

It is demonstrated that direct high-speed imaging and visualisation can be misleading due to the large disparity in signal strength of the various flame light emissions. Much more physical insight can be gained into the combustion process if a modern high-speed colour camera is combined with the innovative image processing technique.

Chapter 4

Simultaneous Multiple Light Emission Tracking by a Single Camera: Infrared Flame Emission Study

4.1 Introduction

In Chapter 3, flame images were converted from the RGB to the HSV colour model to separate the different flame emissions. Compared with the results from the old DFCD methodology, there is another hue range located between 252 and 350 degrees in the hue histogram, emitting in the pinkish. The source of this detected pinkish-coloured emission is studied in this chapter.

4.2 Identification of Infrared Flame Emission

It is shown in this section that infrared signals always present as the pinkish colour on the photos. Once the pinkish-coloured emission has been detected, it is assumed to be the infrared emission. It is known that infrared blocking filters are installed to most of the CCD/ CMOS colour cameras, but some cameras are still sensitive to the near-infrared spectrum due to the inefficient and uneven infrared blocking of the RGB channels.

In this section, the high-speed camera SA4 is proven to be sensitive to the near-infrared spectrum. A large area of infrared emission was captured when the narrowband infrared filters (700 ± 8 nm, 780 ± 8 nm, 1064 ± 8 nm) were respectively installed to the front of the lens to image the sooty flame. Several experiments were carried out to prove that the captured pinkish-coloured emission is due to the infrared light, which is discussed in the following sections.

4.2.1 Identification of infrared emission via a stereo adapter and optical filters

A Pentax stereo adapter is installed to the front of the lens, which separates the image into two parallel images with slight displacement. The stereo adapter consists of two

inner mirrors and two outer mirrors, all at 45 degrees to the lens and placed orthogonally to the each other, as shown in Fig. 2. 44 (b).

The stereo adapter simulates two virtual cameras, as shown in Fig. 2. 44 (c). The incident light from the focus area enters the outer mirrors and the ray is reflected and enters the inner mirrors. Consequently, the ray is reflected again by the inner mirrors and enters the lens of the camera. Finally, a synchronous image pair with slight displacement is generated.

Fig. 4. 1 (a) shows an example of a synchronous image pair. The stereo image pair is post-processed in a black and white format. The synchronous images on the left and right have 25811 and 25669 pixels respectively. The displacement of the images on the left and right view is shown in Fig. 4. 1 (c). The deviation between the images is approximately 0.55 %. Through collecting the statistics of thousands of image pairs, the threshold of deviation of an image pair is [0.0015, 0.016], which indicates that the size of the captured synchronous images are almost the same.

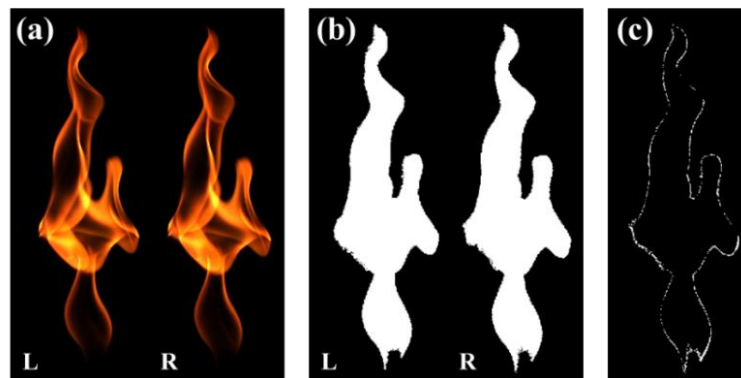


Fig. 4. 1 (a) An example of a captured synchronous flame image pair, (b) The processed synchronous image pair in black and white format and (c) The displacement of the left and right images.

Different optical filters were applied to the left and right views of the adapter. The left view without any filter directly captured the flame images. A broadband filter (385 – 725 nm wavelength, transmittance > 96 %) was applied to the right view which allowed only the visible light to pass through. An example of a flame synchronous image pair and their corresponding colour distribution histograms in hue space are shown in Fig. 4. 2 (a) and (b) respectively. It is found that the flame image without the filter has an additional region which surrounds the orange sooty flame, and its colour

distribution locates from H2 to H18. The image with the visible broadband filter dominates the hue domain from H2 to H13. It has been tested that the Photron SA4 camera cannot detect ultra-violet signals with the applied camera settings. Therefore the colour distribution from H14 to H18 has to be infrared signals from the flame. It should be noted that the presented flame images are post-processed through a selective enhancement technique. The original images are analysed in order to plot the histograms.

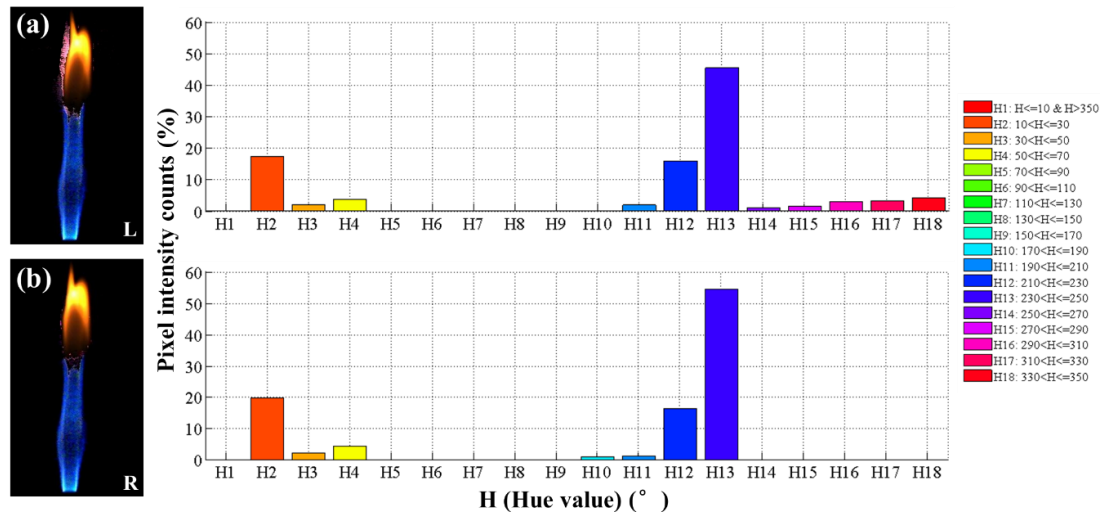


Fig. 4. 2 The synchronous images of a propane partially premixed flame (a) without a filter and (b) with a visible wideband filter (385 – 725 nm wavelength) and their corresponding colour distribution histograms in hue space.

In the second attempt, an infrared filter (760 nm wavelength, transmittance > 96 %) was applied to the left lens; only infrared emission longer than 760 nm can pass through. The visible light filter (385 – 725 nm) was applied to the right lens. The colour distribution of the captured flame image with the infrared filter is located between H14 and H18, while no signal is detected between H14 and H18 with the visible light filter as shown in Fig. 4. 3. Therefore, the deviation region of the synchronous images pair is proven to be the region of the infrared emission only without overlapping the visible flame. The deviation of the example synchronous images is 24.7 % as shown in Fig. 4. 4. The average deviation between the synchronous images is 24.5 % according to the statistics of a large number of synchronous image pairs, which is much higher than the maximum deviation of 1.6 % produced by the images without any filters applied

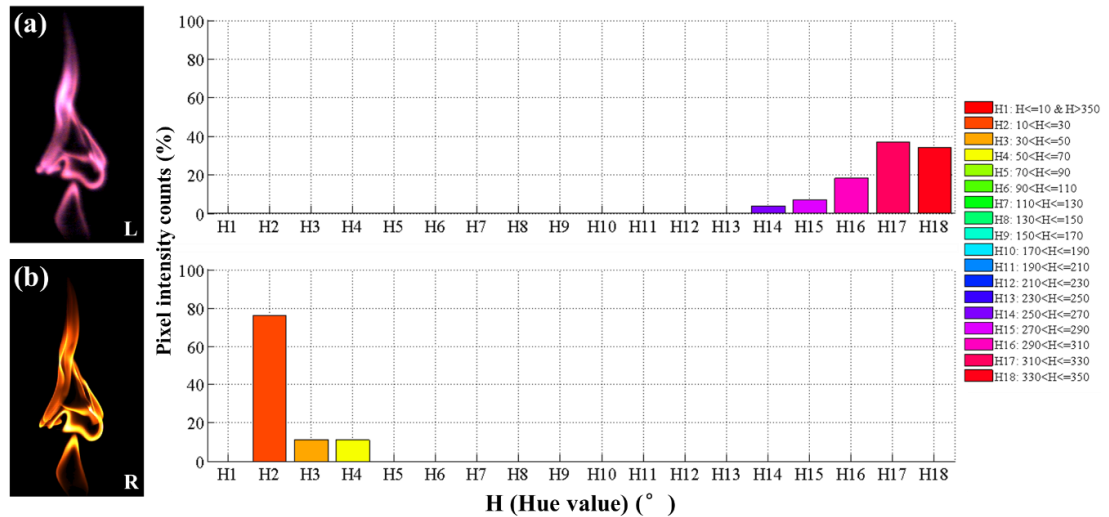


Fig. 4. 3 The synchronous images of a propane diffusion flame with (a) an infrared filter (760 nm cut-on wavelength) and (b) a visible light filter (385 – 725 nm) and their corresponding colour distribution histograms in hue space.

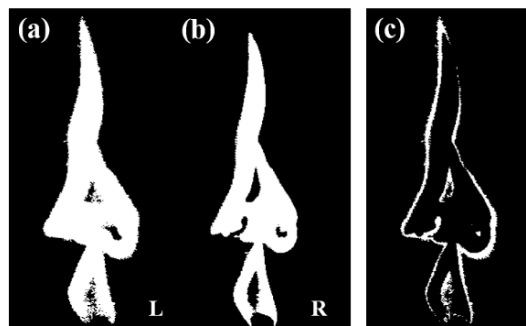


Fig. 4. 4 The processed synchronous image pair with (a) an infrared filter and (b) a visible light filter (385 – 725 nm) in black and white format. The number of pixels of the left and right images are 20814 and 15673 respectively. (c) The deviation between the synchronous images is 24.7 %.

4.2.2 Identification of infrared emission via a blackbody infrared calibrator and heated wire

The confirmatory experiment is based on a colour comparison between the flame pinkish-coloured emission and blackbody calibrator induced infrared emission in the hue domain. A blackbody infrared calibrator (Omega BB-4A) was regulated to different temperatures below the Draper point of 524.85 °C (Mahan, 2002). It is known that blackbody radiation of all solid materials glow in the visible spectrum when the temperature achieves the Draper point. In other words, if the temperature is below 524.85 °C, the blackbody radiation of the solid matter will emit only in the infrared

spectrum. Fig. 4. 5 (a) to (c) show images of the emission of the calibrator captured by the high-speed camera and the corresponding colour distribution at temperatures of 480 °C, 490 °C and 510 °C respectively. It is found that the infrared signals dominate the hue domain from 230 to 350 degrees, shown as H13 to H18. Its colour distribution is similar to the flame pinkish-coloured emission in Fig. 4. 2 (a). The non-intersecting region of the calibration and the infrared flame emission in the hue domain is only at H13, which is due to their species and temperature difference. Therefore, the flame colour distribution from H14 to H18 is thought to be denoted by the flame infrared emission. Also, it is an interesting analogue to Wien's displacement law (Serway and Jewett, 2006); with the increase of the temperature of the blackbody calibrator, the peak of the infrared bars gradually shift to higher hue values.

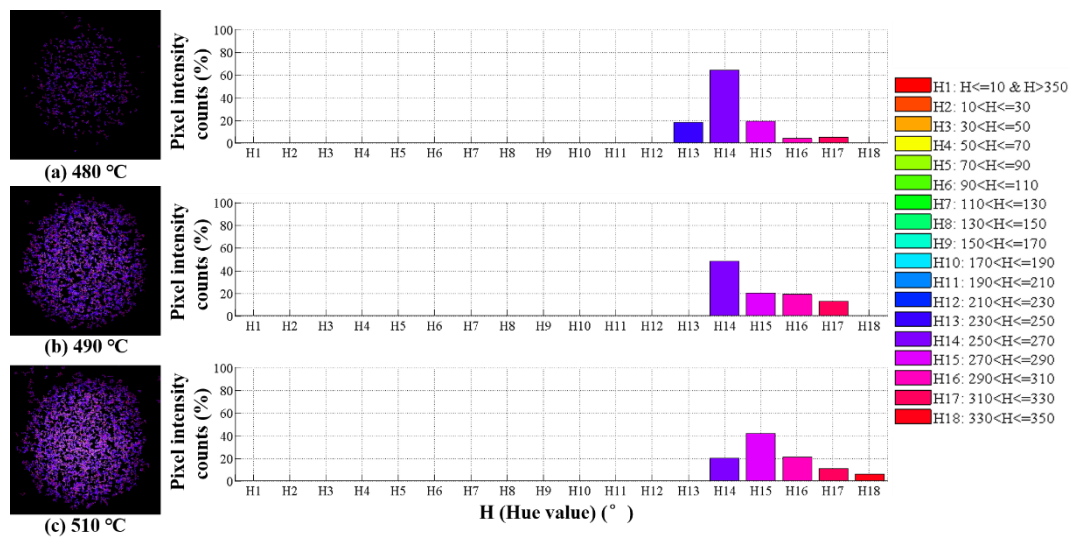


Fig. 4. 5 (a)-(c) The emission of the calibrator captured by the high-speed camera and the corresponding colour distribution histograms in hue space at temperatures of 480 °C, 490 °C and 510 °C, respectively.

A similar experiment was also conducted using the heater wire. An experiment of blackbody radiation of the hot wire (Fe-Cr-Al), with an emissivity of 0.43 (Yoo, Hong and Yang, 2007), was performed by applying a thermal imaging camera and the high-speed Photron SA4 camera. The temperature increased with the increase of the current in the hot wire, and the high-speed camera gradually detected the invisible infrared emitted from the hot wire until it turned 'red hot' (visual inspection by human eyes). In this range, the corresponding mean temperature of the hot wire increased from 472 °C to the Draper point of 524.85 °C, which was measured by the thermal imaging

camera. Fig. 4. 6 (a) to (c) show the hot wire images captured by the high-speed camera and their corresponding colour distribution histograms in the hue domain at temperatures of 472 °C, 506 °C and 522 °C respectively. It is found that the infrared signals dominate the hue domain from 230° to 350°, which is similar to the result of both the calibrator in Fig. 4. 5 and the flame pinkish-coloured emission in Fig. 4. 2 (a). Overall, it is determined that the captured pinkish region of the flame is due to the infrared flame emission, which is located at the hue range from 252 to 350 degrees.

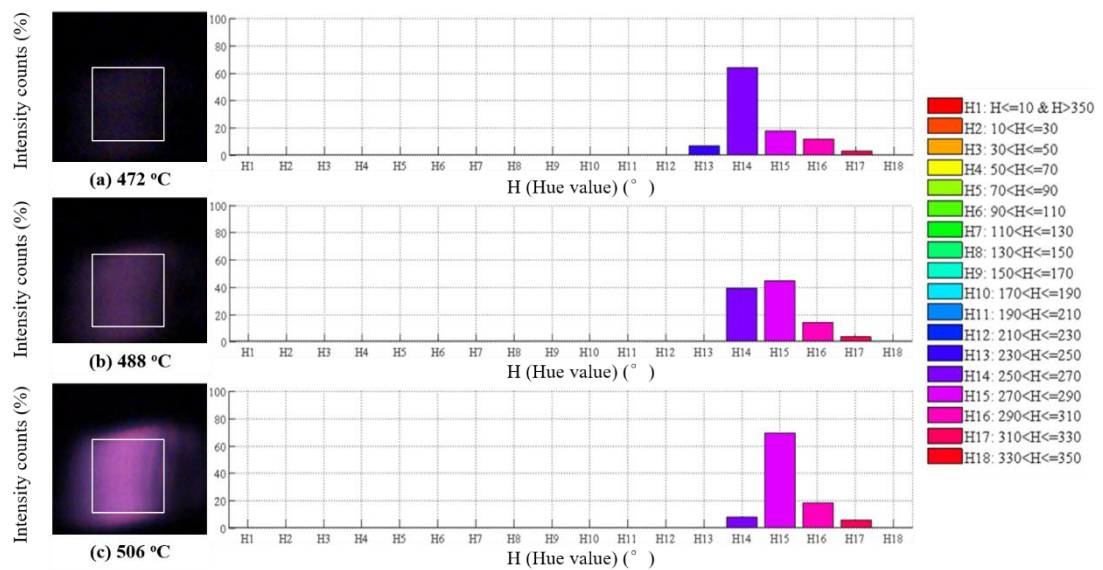


Fig. 4. 6 (a)-(c) The hot wire images captured by the high-speed camera and corresponding colour distribution histograms in the hue space at temperatures of 472 °C, 506 °C and 522 °C respectively.

4.3 Source of Captured Infrared Flame Emission

Once the pinkish emission is proven to be the infrared flame emission, its source needs to be identified. In this section, various conjectures of the source of infrared flame emission are discussed. Many supporting evidences indicate that the captured infrared emission is associated with the soot precursor region.

4.3.1 Combination of colouration of the blue and orange flames

It is doubted that the captured infrared flame emission is a combination of the blue and orange flame colourations due to the pinkish colouration being composed of blue and

orange in the colour system. Both the chemiluminescence-induced blue flame and orange sooty flame emit in the visible spectrum. The captured pinkish flame emission forms in between the orange and the blue flame and emits in the infrared spectrum. If it is the colour combination, the pinkish flame emission must emit in the visible spectrum as well. Besides, Fig. 4. 7 shows the image of a pure sooty flame without any blue flame emission; a large area of infrared emission is still observable. Therefore, the statement regarding the colour combination can be denied.

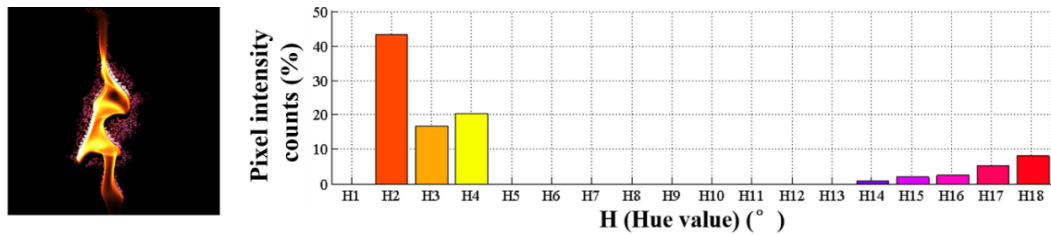


Fig. 4. 7 Left: The captured image of a propane diffusion where the infrared emission is enhanced 15 times. Right: The colour distribution histogram in hue domain regarding the original captured image without enhancement.

4.3.2 Over-exposure of the sooty flame

It may be considered that the captured pinkish-coloured emission is due to the over-exposure of the orange sooty flame. However, this viewpoint cannot explain the captured pinkish region emitting in the infrared spectrum as well, as shown in Section 4.2. In Fig. 4. 8, there is no over-exposure/over-saturation in the region of orange sooty flame, which further denies this viewpoint.

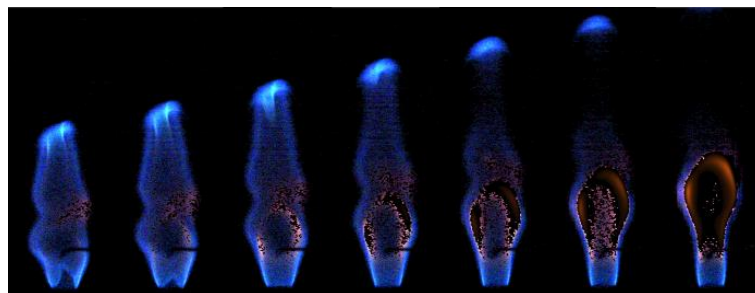


Fig. 4. 8 Image sequence of the early stage of the ignition process of co-flowing methane flame.

4.3.3 Water and carbon dioxide

It has been proven that the high-speed Photron SA4 camera is sensitive to both the visible and the near-infrared spectra due to the inefficient and uneven infrared blocking

of the RGB channels. The spectral response of common CMOS imagers is situated from the near-ultraviolet (around 320 – 370 nm) to 1100 nm (the limit of near-infrared) and insensitive to mid-infrared light (Edwards and Vandenabeele, 2012), which rules out the possibility of water vapour and carbon dioxide as the source of the detected infrared emission. However, since the spectral response of the Photron SA4 CMOS camera has not been tested, confirmatory experiments were conducted as discussed below.

Premixed propane/air and methane/air flames were established under the fuel lean condition at an equivalence ratio of 0.98. The captured images and corresponding colour distribution histograms in hue space are shown in Fig. 4. 9 (a) and (b). The hue range from 252 to 350 degrees is enhanced 20 times in the presented images. It is found that the pixel intensity counts are concentrated in the chemiluminescence-induced blue flame region. The emission from H14 to H18 is smaller than 0.5 %, which is negligible and considered to be background noise. If the captured infrared emission belongs to water and carbon dioxide, it will exist in a large area and be located surrounding the flame. Therefore, it is demonstrated that the captured infrared emission is neither from the CO₂ nor the H₂O infrared bands.

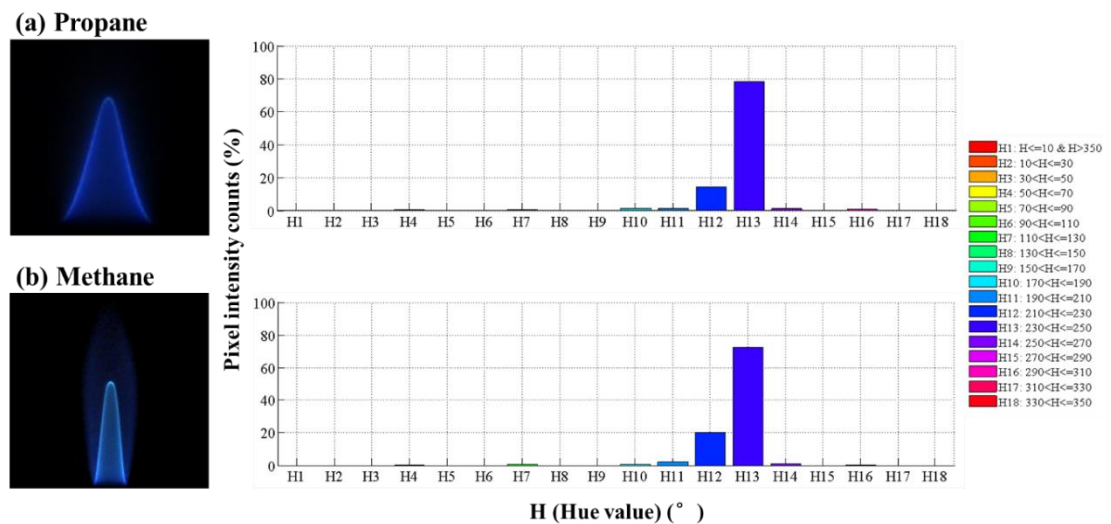


Fig. 4. 9 The captured images of lean premixed flames of (a) propane/air and (b) methane/air at an equivalence ratio of 0.98 and their corresponding colour distribution histograms in hue space.

4.3.4 Blackbody radiation of low-temperature-soot

Through the selective enhancement of the yellow sooty flame portion in the initial

ignition frames in Fig. 4. 8, the captured infrared and visible yellow sooty flame are simultaneously visualised after the blue flame occurrence. Therefore, it is inferred the captured infrared emission is associated with the soot formation. The source of the infrared flame emission is conjectured to be the soot particle radiation or the soot precursor emission. The soot precursor conjecture is discussed in detail in the Section 4.3.5. The low-temperature soot hypothesis is discussed in this section.

It is known that the common camera is more sensitive to visible light than infrared light. If the substance emits both in the visible and the infrared spectra, the infrared emission would be overshadowed by the visible emission when entering CCD/CMOS. Therefore, the detected infrared flame emission is in a region that only emits relatively strongly in the infrared. The blackbody radiation of soot has a continuum band from visible to the infrared spectrum, as shown in Fig. 4. 10. If the infrared flame emission is induced by soot radiation, the temperature of the soot has to be below the Draper point 524.85 °C. However, the tests have shown that the Photron SA4 camera can only detect emission from a blackbody oven around 523 °C with very long exposure time. At a shutter speed of 1/2000 s chosen in this study only background noise was detected.

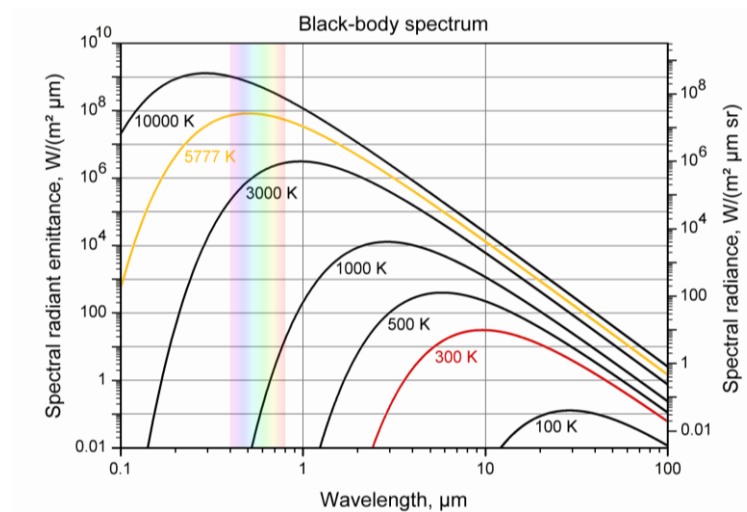


Fig. 4. 10 The black body radiation spectrum for temperatures between 300 K and 10,000 K in a log-log diagram (Tinetti, Encrenaz and Coustenis, 2013).

The low-temperature soot conjecture is not able to explain some combustion phenomena. Shown in Fig. 4. 11, the infrared emission always forms between the orange sooty flame and the blue flame. The possibility of a pocket of low-temperature-soot sandwiched in between two high-temperature zones in so many locations are very

low. Consequently, the source of the captured infrared emission is unlikely from the soot blackbody/greybody radiation.

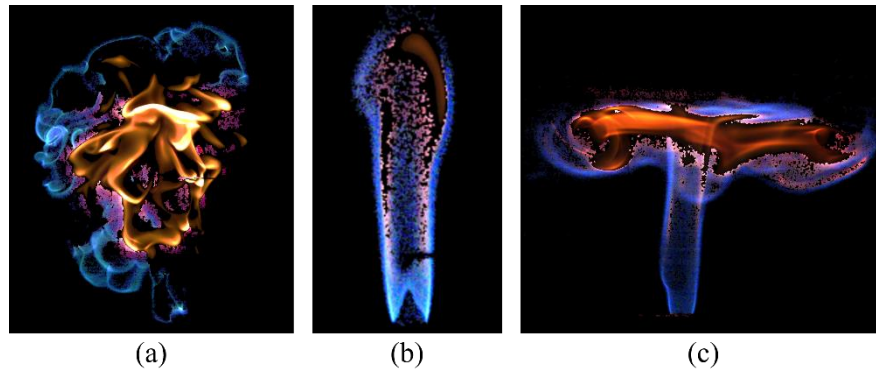


Fig. 4. 11 (a) Ignition instance of (a) diffusion propane flame, (b) methane co-flow flame and (c) methane impinging flame.

4.3.5 Soot Precursor

Soot formation occurs via precursor species which mainly consists of PAHs. PAHs are a group of hundreds of persistent organic compounds, which largely form in the fuel-rich combustion of incineration, engine systems and wildfire, and may be carcinogenic to humans. Since the emission of PAHs is also located in the infrared region, PAHs could potentially be the source of the captured infrared flame emission.

The emission spectrum of PAHs is rarely studied in combustion research but highly investigated in astronomy. It has been reported that the mysterious red radiation in interstellar space comes from PAHs (Allamandola, Tielens and Barker, 1987). PAH molecules absorb stellar ultraviolet photons and then relax to the ground state by emitting several infrared photons due to the vibration of the carbon skeleton. All the PAHs emit in the Unidentified Infrared Bands which correspond to the discrete intense infrared emission bands in 3 – 20 μm , spectral range with major components near 3.3 μm , 6.2 μm , 7.7 μm , 8.6 μm , 11.3 μm and 12.7 μm due to C-H stretching, C-C stretching and C-H in-plane and out-of-plane bending (Salama, 2008). In the combustion area, a large number of PAHs molecules emit infrared photons by absorbing energy from fuel-rich combustion. The infrared analysis of flame-generated PAH samples shows the same prominent peaks to the Unidentified Infrared Bands in galaxies (Mckinnon, Meyer and Howard, 1996). The emission spectrum of PAHs is referred to Section 2.3.5.

Most of the fundamental experimental studies used the PAH PLIF and planar laser-induced incandescence (PLII) diagnostic techniques to trace the PAHs and soot. Some research has applied the simultaneous PAH and OH PLIF and PLII imaging to implement multiple species tracking. The relative position of the PAHs, OH and soot can be obtained by superimposing the images. PAH studies always apply the laminar hydrocarbon co-flowing NDF or IDF model, since this can provide a relatively stable flame with rich PAH concentration.

In carrying out extensive literature survey, it is found that the relative distribution of the captured infrared region in both co-flowing NDF and IDF in current experiments coincide with the region of PAH resolved in the laser experiments (Mikofski *et al.*, 2007; Xiong, Cha and Chung, 2015). Xiong *et al.* (Xiong, Cha and Chung, 2015) used light scattering, PLIF and PLII imaging to identify OH, PAHs and soot relative positions in a laminar propane co-flowing NDF. Fig. 4. 12 (a), (b) and (c) show the direct image, soot PLII image and the instantaneous superimposed image of the OH and PAH PLIF measurement. It is seen that the soot is concentrated in the top zone with a cone shape. The blue flame zone is located near the nozzle exit, and the PAH region exists beyond a certain distance from the nozzle exit. It should be noted that the absence of the flame at the bottom of Fig. 4. 12 (a) is due to the weak chemiluminescence-induced blue flame emission under the high shutter speed. Similar flame configuration is carried out in the current research. Fig. 4. 12 (d) and (e) show post-processed images of methane and propane co-flowing NDFs at the steady state, where the blue flame and infrared emission are both enhanced 20 times. It is apparent that the distribution of the soot and the blue flame are identical to the laser imaged results. The relative position of the pinkish region in between the blue and sooty flames that are emitting in the infrared match well with the PAH PLIF measurement.

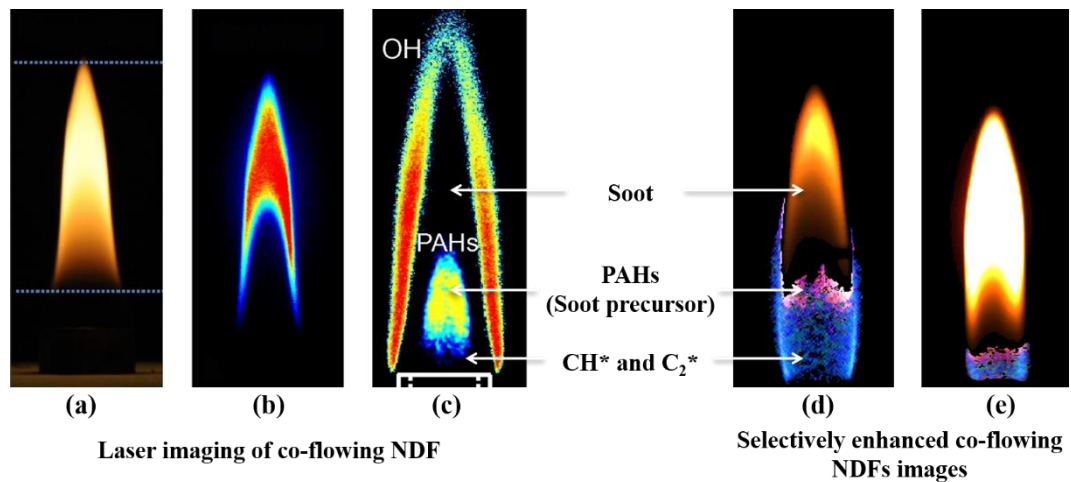


Fig. 4. 12 (a) Direct imaging photo; (b) soot volume fraction from PLII; (c) superimposed PLIF images of OH and PAHs of a laminar propane co-flowing NDF (Xiong, Cha and Chung, 2015). Post-processed flame images of (d) methane and (e) propane co-flowing NDF at the steady state.

Fig. 4. 13 (a) and (b) show the visible colour image and colour-map of a laminar sooty ethylene-air co-flowing IDF with contours of peak time-averaged PLIF and PLII signals overlaid (Mikofski *et al.*, 2007). The blue reaction zone is located at the nozzle exit. The OH layer forms at the top of the burner. The relative position of the soot and PAHs is contrary to the co-flowing NDF. A long sooty region mainly occupies the top zone with a thin PAH outer layer. A similar co-flowing sooty IDF model is established for comparison. Shown in Fig. 4. 13 (c), the relative position between the infrared emission and the sooty flame is identical to the presence of the PAHs and soot in the laser imaging method. A slight difference of the flame profiles is due to the different nozzle dimensions. The detailed dimensions are referred to in (Wang *et al.*, 2012). The absence of the blue flame at the bottom centre is due to the high air flow rate. With an increase in the co-flow air flow rate, the soot region shrinks significantly, and blue flame gradually envelops the soot region with a thin infrared layer in between, as shown in Fig. 4. 13 (d).

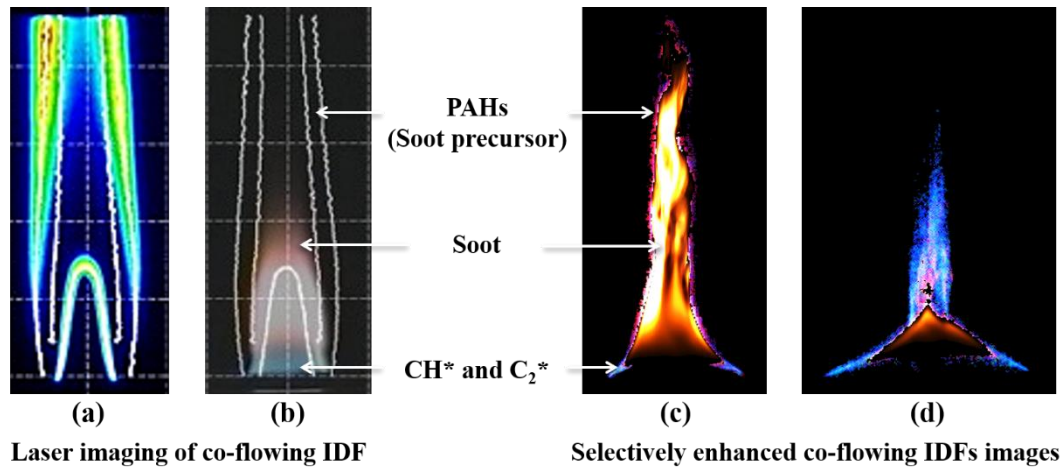


Fig. 4. 13 (a) Colour-map and (b) the visible colour image of ethylene-air IDFs with contours of peak time-averaged PLIF and PLII signals overlaid (Mikofski *et al.*, 2007). Post-processed image of propane-air IDFs flowing with (c) low and (d) high air velocities.

The evidence shown above indicates that the captured infrared flame emission is likely to be the emission from the PAHs or closely related to the PAHs. However, standard CMOS cameras are insensitive to the mid-infrared spectrum. The shortest peak emission of PAHs is around 3.3 μm , which is far away from the near-infrared spectrum. In addition, a confirmatory experiment was conducted which demonstrated that the captured infrared flame emission is unlikely to be PAHs emission. According to the Planck–Einstein relation (Ross, 1967),

$$E = \frac{hc}{\lambda} \quad (4.1)$$

where E represents the energy of a photon, h is the Planck constant, c is the speed of light and λ is the wavelength. The energy of the photon will decrease with an increase in wavelength. This means that the peak emission of PAHs located at 3.38 μm and 6.8 μm wavelength are most likely to be detected if the emission in the longer wavelength is not strong enough. Therefore, a bandpass infrared filter with the central wavelength of 3317 ± 40 nm was applied in front of the lens to image the flames in different conditions. The details of the filter are shown in Fig. 4. 14. The camera cannot detect signals in every condition, which rules out the possibility of the PAHs as the source of the detected infrared flame emission.

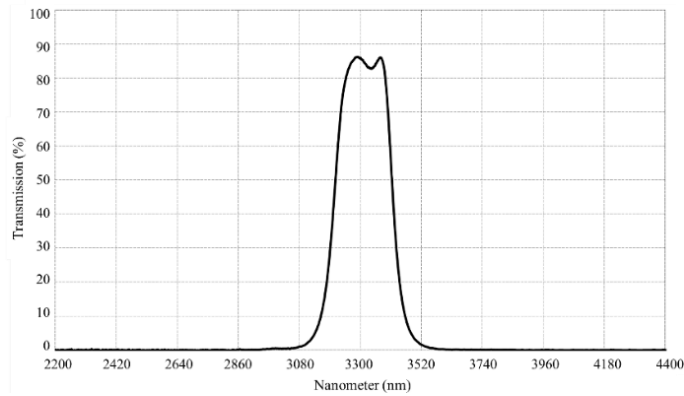


Fig. 4. 14 The transmission of the bandpass infrared filter (Winder, 2002).

The soot formation process consists of nucleation, coagulation, surface growth, aggregation, agglomeration and oxidation (Mansurov, 2005b), experiences a complicated gas-to-particle transition. Soot precursor forms at the initial stage of the process, which contains various species, such as PAHs and acetylene molecules (D’Anna, 2009; Totton *et al.*, 2010; Wang, 2011a). The specific soot precursor species are still unclear until now. The physical/chemical properties in this region may be of great interest for further research because it encompasses from gas, nanostructure to solid soot particles. The captured infrared emission could have been the direct infrared light emission of the soot precursor. Besides the PAHs, some other unidentified soot precursor species may also emit infrared. The infrared light scattering from the soot precursor is another conjecture, as illustrated in Fig. 4. 15.

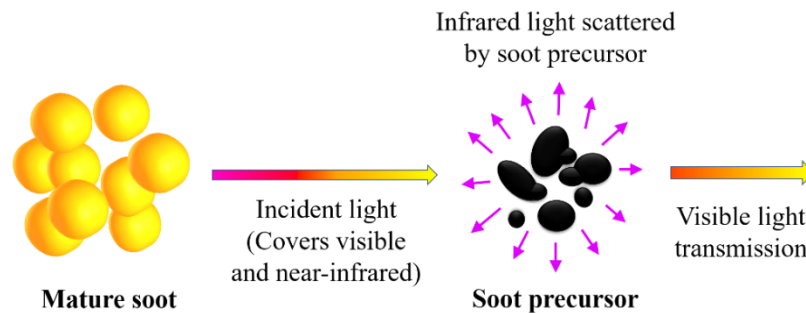


Fig. 4. 15 Schematic of selective infrared scattering from soot precursor.

The blackbody radiation of the nearby soot particles emits light from the visible to the infrared spectrum. Partial infrared light from the soot radiation may have been selectively scattered by the soot precursor; visible light is absorbed or transmit through the soot precursor, thereby resulting in an infrared-emission-only region that detected

by the camera. This theory is widely recognised for the ‘blue-tint’ sky (Tilley, 2010) and ‘red-tint’ gold nanoparticles (Shah *et al.*, 2014) in the human eyes. Overall, the soot precursor is inferred to be the source of the captured infrared emission through the comparison of various conjectures. However, the exact mechanism needs further study to confirm.

4.4 Multiple Light Emission Evolution in the Ignition Process of Fundamental Flame Models

4.4.1 Ignition process of a free jet propane non-premixed flame

The ignition process of a free jet propane non-premixed flame is captured by the high-speed digital camera, Photron SA4, under frame rate of 1000 fps and shutter speed of 1/2000 s. The ignition is initiated by a Kawasaki ignition-coil (TEC-KP02), with an output voltage of 30 kV. The spark is generated by a pair of steel electrodes with a 10 mm gap, located 100 mm above the nozzle. Fig. 4. 16 (a) and (b) show the original and selectively enhanced image sequences. The blue flame colourations of the captured images are filtered within the hue value band from 180 to 252 degrees in the HSV colour model space and then enhanced 20 times; the region of infrared emission only is filtered from 252 to 330 degrees and then enhanced 15 times. The noise from the camera and background is removed. Fig. 4. 17 gives the time-dependent number of pixels of the soot-induced orange flame, infrared emission and the chemiluminescence-induced blue flame in the given hue band. The number of pixels is used to define the area of the different flame colour regions.

It is observed that the combustion process starts with the development of a spherical blue flame. The captured infrared emission and visible yellow sooty flame simultaneously occur afterwards at 9ms after the ignition. At the early stage of the ignition, the flame rapidly forms a high-temperature blue reaction zone. The hot gas of combustion matter obstructs the access of the air to the encircled fuel pocket. In the elevated-temperature blue reaction zone, the continuous injection of the fuel leads to the absence of oxygen, which promotes the pyrolysis of unreacted propane. The pyrolysis leads to the formation of the soot precursor and soot particles in the flame centre zone. Mature soot forms inside the infrared soot precursor region. The soot with

incandescence emits blackbody/greybody radiation and glows in yellow/orange. The soot precursor directly emits or selectively scatters the infrared and presents as pinkish tints on the captured images. Shown in Fig. 4. 17, the mature soot and infrared soot precursor regions increase rapidly from 0.117 s when the bottom of the flame attaches to the fuel nozzle exit. The fuel jets through the inner flame zone which leads to the accumulation of soot in the flame centre, thereby enlarging the soot and soot precursor regions. Subsequently, the sooty flame and infrared soot precursor regions expand and encompass the outer premixed flame. At 0.196 s after ignition, the blue flame region completely vanishes.

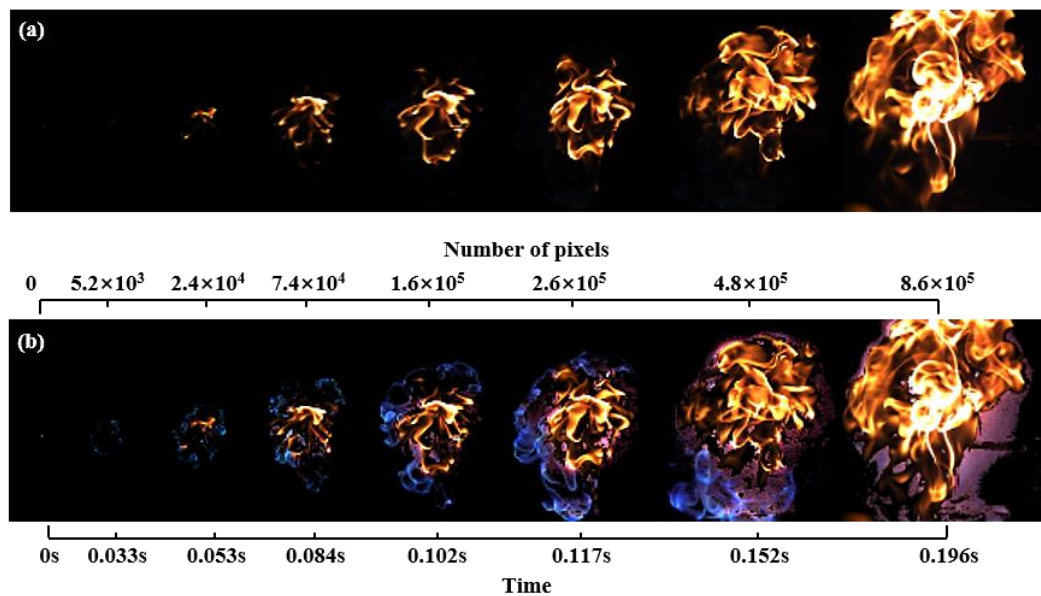


Fig. 4. 16 (a) The original and (b) selectively enhanced image sequences of the ignition process in a propane non-premixed flame with the corresponding number of pixels.

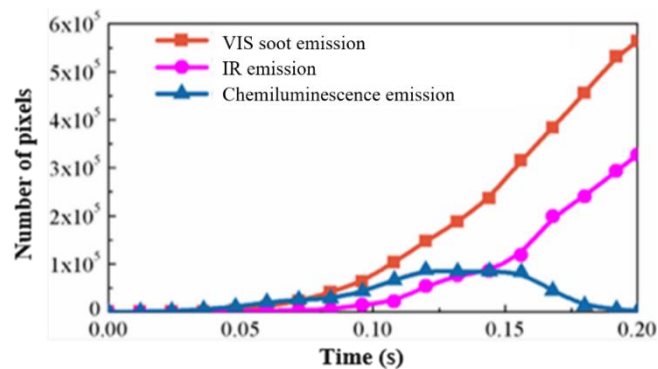


Fig. 4. 17 The time-dependent number of pixels of the soot-induced orange flame, infrared soot precursor and the chemiluminescence-induced blue flame. Lines are provided to guide the eyes.

4.4.2 Ignition process of co-flowing normal diffusion and inverse diffusion flames

The ignition process of co-flowing NDF and IDF were simultaneously visualised using the Photron SA4 high-speed camera with a frame rate of 500 fps and exposure time of 1/500 s. The igniter was located 10 mm above the nozzle. Fig. 4. 18 (a) shows the original and post-processed image sequences of the methane-air co-flowing NDF ignition process. The combustion also starts with the development of a blue flame, followed by the infrared emission and visible yellow sooty flame. Subsequently, the infrared soot precursor region gradually becomes a thin layer between the blue flame and yellow soot emission. The soot formation largely increases with the extinction of the blue flame. The soot precursor dramatically reduces and no longer wraps the soot region. At 56 ms after ignition, flame necking takes place due to the buoyancy. Soot concentrated in the upper zone emerges from the primary structure and propagates upwards. Finally, a cone-shaped flame stabilises on the nozzle exit with a blue flame bottom, a sooty flame tip and a pinkish infrared soot precursor region in between.

Fig. 4. 18 (b) shows the ignition process of the propane-air coflowing IDF. The infrared soot precursor and soot emissions are also simultaneously observed after the blue flame. The flame develops in a radial direction at the beginning of ignition, since the high-density propane largely accumulates near the nozzle. Contrary to the co-flowing NDF, the infrared soot precursor layer keeps enveloping the soot region during the entire ignition process. The IDF flame finally stabilises with a blue bottom and a long orange sooty flame region with a thin soot precursor region at the outer layer.

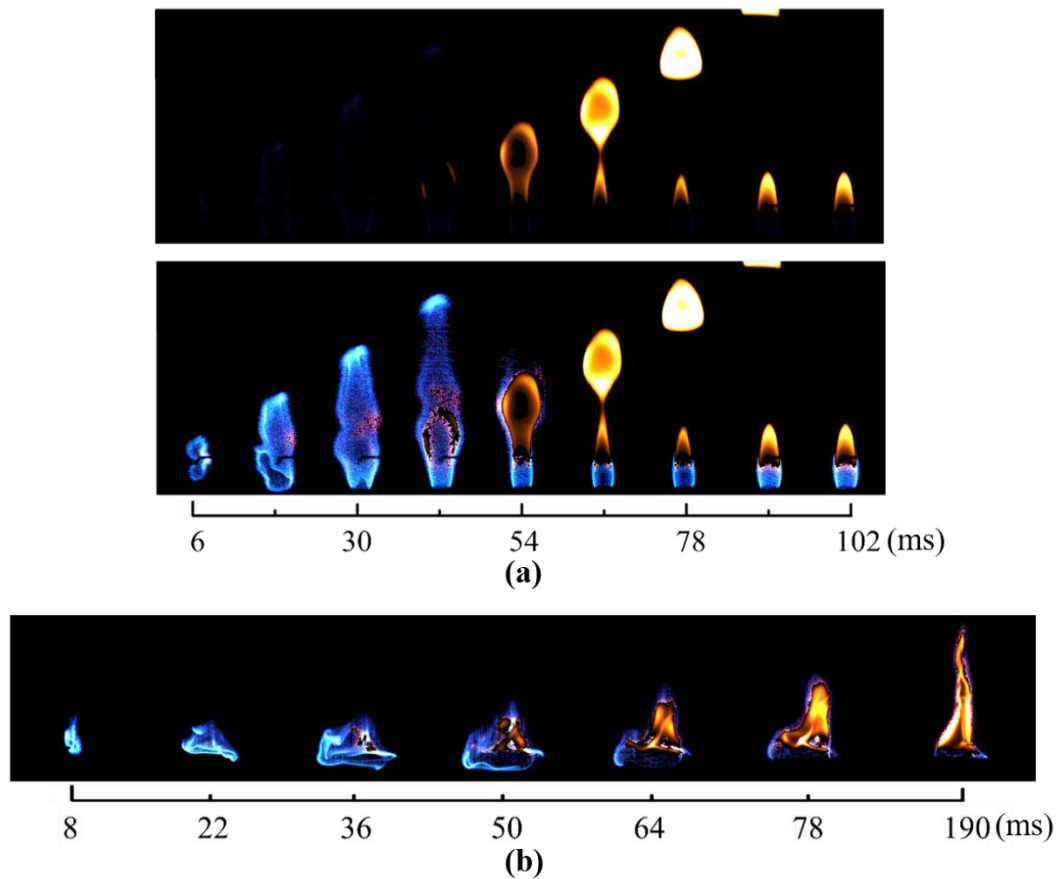
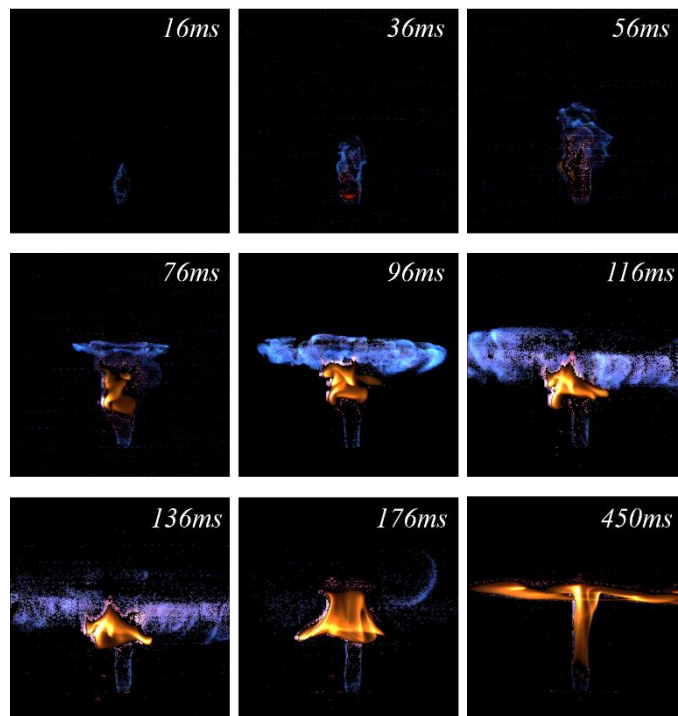


Fig. 4. 18 (a) Original and post-processed image sequence of a methane-air co-flowing NDF ignition process and (b) Post-processed image sequence of a propane-air sooty co-flowing IDF ignition process.

4.4.3 Ignition process of a methane impinging flame

A heavily oxidised stainless steel plate, 300 mm in diameter and 10 mm in thickness, was held 100 mm from the nozzle exit by a steel holding frame. Methane was injected through a nozzle of 8 mm inner diameter at 6 l/min flow rate, corresponding to a jet velocity of 2 m/s and Reynolds number of 932. The ignition process was recorded with the high-speed camera with a frame rate of 500 fps and shutter speed of 1/1000 s and positioned at an inclined angle to the plate. The image sequence of the impinging flame ignition process is shown in Fig. 4. 19 (a). The time-dependent number of pixels of the captured infrared emission, yellow soot and blue flame emission is shown in Fig. 4. 19 (b), which reflects the quantity of the soot precursor, the soot and the blue flame presence respectively.

It is shown that the initial blue flame propagates in the axial direction. The soot precursor and mature soot formation start 20 ms after ignition. The soot forms inside the soot precursor zone. The blue flame pocket gradually breaks with the enlargement of the mature soot and soot precursor regions. The upper boundary of the flame strikes the cold plate at 68 ms. The upper blue flame front develops with beach marks and propagates fast towards the edge of the plate with many small vortex structures. The heat transfer between the flame and the cold plate triggers a sudden flame temperature drop. The fuel pyrolysis is hindered due to the lack of temperature, which leads to a stagnation of the soot formation. Hence, the ‘Soot precursor’ and the ‘Soot’ curves remain stable from 90 ms to 126 ms. Wall quenching takes place 114 ms after ignition. The flame-temperature-drop suspends the chemical reaction in the plate region and leads to the extinction of blue flame. The ‘CH* & C₂*’ curve dramatically decreases. Subsequently, the interaction between the plate and flame rebounds the soot region. As the fuel continuous jetting from the nozzle, the soot region re-raises, shrinks and propagates along the plate. The soot precursor region keeps tightly enveloping the soot region. Finally, the flame reaches a relatively steady state at 450 ms with a blue flame bottom and concentric ring-shaped sooty flame emanating from the stagnation region with a thin soot precursor layer at the outside.



(a)

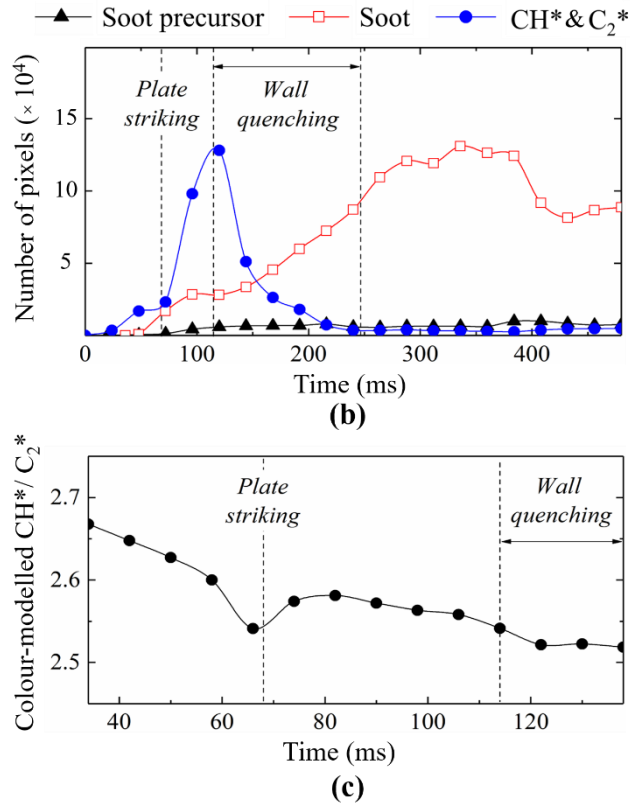


Fig. 4. 19 (a) Post-processed image sequences. The infrared emission and blue flame are enhanced 30 times, (b) Time-dependent number of pixels of soot precursor, soot and chemiluminescence-induced blue flame emission and (c) Time-dependent colour-modelled CH*/C₂* of the blue flame region in an impinging methane flame.

Fig. 4. 19 (c) represents the time-dependent colour-modelled CH*/C₂* of the bluish flame region. Previous research (Yang, Ma and Zhang, 2015) has indicated that the CH* and C₂* can be inferred from the Blue and Green intensity in the RGB colour model. CH*/C₂* is a function of the equivalence ratio, which is expressed by Eq. 3.7, Eq. 3.8 and Eq. 3.10.

The higher the CH*/C₂* value, the leaner the combustion condition. The value of the colour-modelled CH*/C₂* has a maximum of 1 % deviation from the 99 % confidence interval range. Only the flame with a large area of the blue flame region is analysed for accuracy, which is between 34 ms and 138 ms. The first valley near 68 ms after the ignition owes to the flame impingement. The colour-modelled CH*/C₂* curve declines in the beginning since the flame front approaches the fuel-rich stagnation point. The curve increases afterwards as the flame propagates in the radial direction along the fuel-leaner plate region. The drop at 114 ms corresponds to flame wall quenching due

to the extinction of the well-mixed blue flame. After that, the curve stays constant with a slight fluctuation when the flame reaches a relatively steady state.

Repeated cases were conducted, which shows good repeatability. Based on the curve fitting from the least squares regression analysis, the minimum values of the coefficient of determination R^2 ($0 < R^2 < 1$) are calculated as 0.97 and 0.96, in terms of the number of pixels and the colour-modelled CH^*/C_2^* respectively. All of the case studies indicate that the source of the detected infrared-emission-only region is closely related to the initial soot formation process.

4.5 Summary

The results from the confirmatory experiments prove that the pinkish region presenting on the flame images is due to the infrared flame emission. The comparative investigation indicates that the captured infrared-emission-only region is associated with the soot precursor region because the presence of the captured infrared flame emission in co-flowing NDF and IDF in our experiments coincide with the region of PAH resolved in published laser experiment. The captured infrared could be either the direct infrared light emission or selective infrared scattering from the soot precursor.

With the help of the selective digital image enhancement technique, the time-dependent spatial evolution of multiple light emission species, which includes the CH^* and C_2^* radicals, the infrared soot precursor and the mature soot emissions are visualised simultaneously by using a single high-speed camera. It is found that the ignition process starts with the development of a blue flame. Subsequently, the infrared soot precursor and visible yellow sooty flame simultaneously occur in the co-flowing NDF, IDF and impinging flame models. The infrared soot precursor region and the yellow sooty flame region in the co-flowing NDF and IDF have an inverse spatial distribution at the steady state. In the impinging flame ignition process, when the flame strikes the cold plate, the sudden temperature drop of the flame hinders the soot formation, and also suppresses the chemical reaction, leading to wall quenching in the following few milliseconds. The potential of visualising and tracking multiple species and soot are still to be fully explored, especially for applications at high pressure and temperature.

Chapter 5

Ignition Location Effect on Soot and Species Formation Using Simultaneous Multiple Light Emission Tracking and Schlieren Imaging

5.1 Introduction

The ignition of a flammable gas mixture is always accompanied by complicated chemical reactions and multiple parameter variations, such as temperature, pressure and flame propagation velocity. The investigation of ignition processes is highly desirable in many combustion devices, especially in IC engines. Combustion in an SI engine is critically dependent on ignition energy and location due to the inhomogeneous mixture of fuel and air being ignited by a spark plug at a chosen location in each cycle. Combustion efficiency and the evolution of the distribution of the air/fuel/products are strongly affected by the ignition location in a non-uniform and unsteady turbulent flow field. Therefore, the study of ignition location is of great importance. A computational investigation of the SI engine demonstrated that when the rotational speed was over 100 rad/s, the power output and efficiency were each increased by 10 % and 2 % when the spark plug was centrally located (Medina *et al.*, 2014). At a very low rotational speed, the situation was reversed. Likewise, the ignition location also has a remarkable influence on closed and partially opened vessels (Solberg, Pappas and Skramstad, 1981; Kindracki *et al.*, 2007b). Xiao *et al.* (Xiao *et al.*, 2014) reported that the flame propagation and acceleration speeds were higher and the tulip and distorted tulip flame patterns were more obvious if the flame was initiated at a short distance away from the tube ends than when initiated at the centre and the ends of a closed tube. Guo *et al.* (Guo *et al.*, 2015) tested the back, central and front ignition positions in a vented vessel. They reported that the central ignition contributed to the maximum internal overpressure for all equivalence ratios and the back ignition exhibited the maximum external overpressure for fuel rich conditions. Unfortunately, the above research did not track the essential chemical species. In this chapter, a single camera imaging technique, which can simultaneously

track the evolution of soot, infrared flame emission and two species with the help of a novel imaging processing technique, is applied to investigate the development of an impinging flame initiated at the various locations. In the combustion zone, the hot gas boundary is always ahead of the boundary of the visible flame emission region. Hence, the schlieren imaging system is also applied to visualise the hot gas propagation, which can help determine the time of the plate striking moment.

An impinging configuration is often applied to investigate the interaction between the flame and wall/piston in a combustion chamber due to easy visualisation and experimentation. Research has demonstrated that the ignition location can significantly affect flame propagation speed and flame structure in impinging flame settings. McDaid and Zhang (McDaid, Zhou and Zhang, 2013) attempted three ignition locations, which are the nozzle exit, halfway between the nozzle and plate and the plate centre. They found that the total ignition duration, from the flame being ignited until reaching a steady state, was greatly influenced by the ignition location variation. Bray and Zhang (Zhang and Bray, 1999) reported that multiple flame modes could be established at a steady state by changing the ignition location only, which include enveloped flame, ring flame, conic flames, disc flame and cool central core flame. Huang *et al.* (Huang *et al.*, 2013) found that the ignition location could also influence the flame colour variation. However, their study only focused on the Reynolds number effects on the presence of the orange and blue flame. It is well known that the orange coloured flame is induced by the incandescent soot emission, which is a typical carbonaceous PM emission and major hazardous pollution in the air with a considerable health detriment (Penttinen *et al.*, 2001). Soot formation has an adverse impact on the combustion efficiency in an IC engine. Although the quantity of soot is much less in SI engines than diesel compression-ignition (CI) engines, the perniciousness of soot emission should not be overlooked. As a result, the ignition location should be carefully determined to minimise the soot formation.

Soot formation occurs via precursor species which mainly consist of PAHs. Small particles form afterwards through chemical coagulation. Soot formation ceases as the soot particles travel through an oxidising region. Research demonstrates that soot formation is also strongly affected by carbon dioxide (D'Anna, 2009; Totton *et al.*,

2010; Wang, 2011b). Mancarella et al. (Mze Ahmed *et al.*, 2016) reported that CO₂ could chemically reduce the PAHs and soot emissions and improve the OH oxidative attack of the PAHs, soot particles, and their gaseous precursors. Some new technologies have recycled burned gases (CO₂ and H₂O) to reduce NO_x and soot emissions, such as Exhaust Gas Recirculation (EGR), Flue Gas Recirculation (FGR) and Flameless Combustion. For EGR, the high specific heat capacity of the exhaust gas will reduce the temperature in the combustion chamber and dilute the oxygen concentration. Research indicates that the EGR will increase the soot formation in CI engines (Thangaraja and Kannan, 2016a), but minimise the soot emission in gasoline SI engines (Gu *et al.*, 2012; Luján *et al.*, 2015a). Therefore, the impact of CO₂ concentration on the flame propagation properties and soot formation is also studied.

5.2 Experimental Procedure

5.2.1 Experimental setup

The schematic of the experimental setup is shown in Fig. 5. 1. A standard Z-type schlieren arrangement was constructed from a pair of $\lambda/10$, 0.3048 m diameter and 3.048 m focal length parabolic mirrors and a 75 W Halogen lamp source. A heavily oxidised stainless-steel plate, 300 mm in diameter and 10 mm thick was held 100 mm from the nozzle exit using a steel holding frame. Methane and carbon dioxide were premixed in a mixing cylinder and then injected through a nozzle of 8 mm inner diameter. The gas flow rates were controlled by rotameters. The methane flow rate remained at 6 l/min in all cases, which corresponds to a jet velocity of 2 m/s and Re of 932. The CO₂ flow rate varied from 0 l/min to 9 l/min. The corresponding jet velocities and Reynolds numbers of CO₂ are shown in Table 5. 1. The gas mixture compositions are referred to as '6CH₄', '6CH₄+3CO₂', '6CH₄+4CO₂', etc., where the numbers in front of the gases represent the fuel flow rate in l/min. The ignition was initiated by a Kawasaki ignition-coil (TEC-KP02), with an output voltage of 30 kV. The spark was generated by a pair of steel electrodes with a 10 mm gap. The plate temperature remained at room temperature, 23 °C, before each attempt. The schlieren images of the ignition process were captured by high-speed camera A; Photron FASTCAM SA5, with a full frame resolution of 1024 by 1024 pixels, the frame rate of 500 fps and

1/30000 s shutter speed, from a direction perpendicular to the plate. High-speed camera B; Photron FASTCAM SA4, was synchronised with camera A to capture the direct colour images with a full frame resolution of 1024×1024 pixels positioned at an inclined angle to the plate. A Sigma 24 – 70 mm lens was applied to the camera B with a constant aperture of f/2.8. With an increase in CO₂ concentration, the flame appearance gradually tended to weak blue. Thus different camera settings were applied in each case, as shown in Table 5. 1.

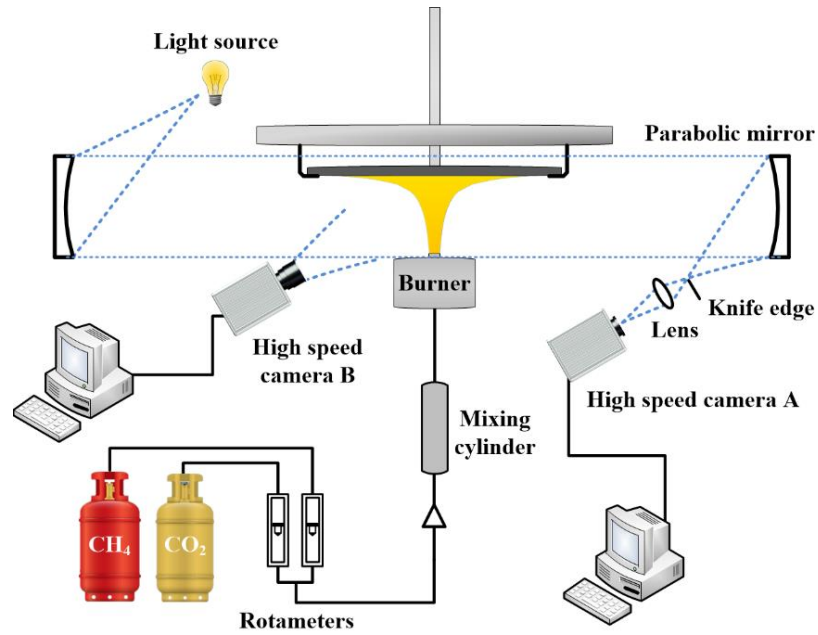


Fig. 5. 1 Schematic of the experimental setup.

Table 5. 1 CO₂ flow conditions and corresponding camera (Photron SA4) settings in each case.

CO ₂ flow conditions				Camera settings	
Volume flow rate (l/min)	Velocity (m/s)	Re	Flame mode	Shutter speed (1/s)	Frame rate (fps)
0	–	–	Envelope	1/500	500
3	1	951	Envelope	1/250	250
4	1.3	1268	Envelope	1/250	250
5	1.7	1585	Envelope/ detached	1/125	125
6	2	1902	Detached	1/125	125
7	2.3	2219	Detached	1/125	125
8	2.7	2536	Disc	1/125	125
9	3	2849	Disc	1/125	125

5.2.2 Selective digital image enhancement technique

In Chapter 4, it was reported that the high-speed camera (Photron SA4) is also sensitive in the infrared. The captured infrared-emission-only region is associated with the soot precursor region. The captured infrared could be either the direct infrared light emission or the selective infrared scattering from the soot precursor. The CH^* , C_2^* and infrared signals are weak, only the orange sooty flame is visible in original flame images, e.g., Fig. 5. 2 (a). Fig. 5. 2 (a) and (d) show a comparison between the original and the enhanced flame images. Here, both the blue flame and infrared emission are enhanced 15 times, which is chosen arbitrarily for the best visualisation.

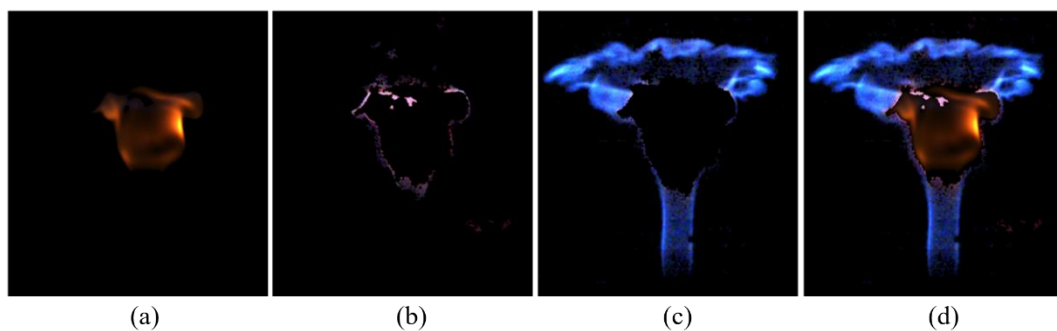


Fig. 5. 2 (a) Original image; 15 times enhancement of (b) Infrared flame emission and (c) Chemiluminescence-induced blue flame and (d) Image after selective image enhancement of the ‘ $6\text{CH}_4+3\text{CO}_2$ ’ case 96 ms after ignition.

5.3 Results and Discussion

Shown in Fig. 5. 3, the flame is initiated at five ignition locations under each flow condition, which are 10 mm above the nozzle, the halfway between the nozzle and the plate, the centre of the plate, and along the plate, 25 mm and 50 mm away from the plate centre in the radial direction, named ‘Nozzle’, ‘Middle’, ‘Plate’, ‘Plate 25’ and ‘Plate 50’ respectively. Based on repeated data curve fitting from least squares regression analysis, the minimum value of the coefficient of determination R^2 ($0 < R^2 < 1$) are calculated as 0.97, 0.95 and 0.99, in terms of the number of pixels, the blue/green ratio and the mean intensity of the orange soot emission respectively, which indicates a very good repeatability.

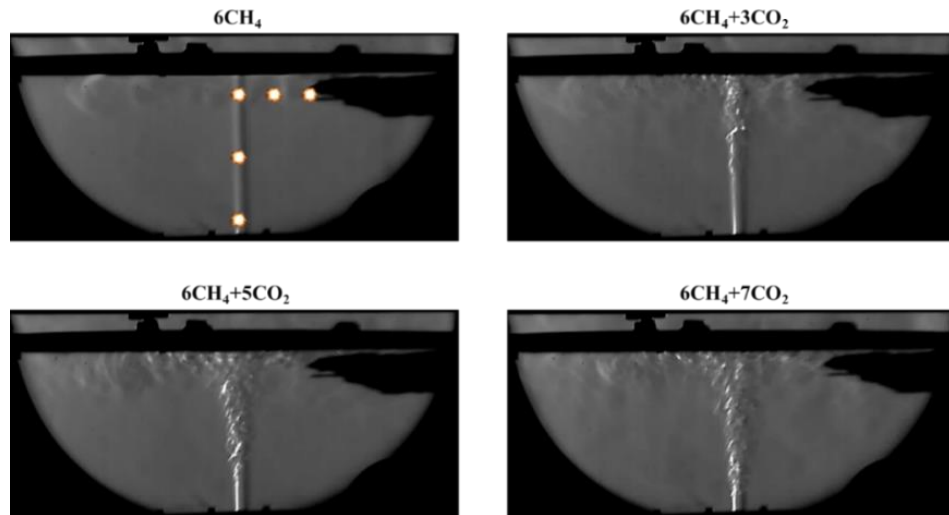


Fig. 5. 3 The five selected ignition locations (top left) and the unburned fuel streams under different flow conditions.

5.3.1 Sooty flame dominated ignition process

Fig. 5. 3 shows the unburned fuel stream under different flow conditions. The ‘Nozzle’, ‘Middle’ and ‘Plate’ cases are ignited along the center of the stream. With an increase in the CO_2 flow rate, the fuel jet angle becomes wider and more vortices form along the plate and near the ‘Plate 25’ and ‘Plate 50’ ignition locations. Figs. 5.4 to 5.8 show image sequences of the ‘ 6CH_4 ’ ignition processes. It is observed that when the flame is ignited at different locations, the flame structure and flame colour distribution are very different during the propagation stage but the final flame pattern is the same at the steady state. In each case, the combustion process starts with the development of a blue flame, followed by the infrared soot precursor emission and visible sooty flame. The infrared flame emission is found in between the blue flame and visible sooty flame. At the early stage of ignition, the flame rapidly forms a high-temperature blue flame region. The hot products obstruct the access of air to the encircled fuel pocket. In the blue flame region, the continuous injection of the fuel further promotes the pyrolysis of unreacted methane, which causes the formation of the infrared flame emission and carbon soot in the flame centre zone. It should be noted that the orange soot also emits in the infrared but is shadowed by the more energetic visible photon emissions.

When the flame is ignited at the ‘Nozzle’ and ‘Middle’ locations, an orange sooty flame quickly forms along the centreline of the fuel jet before impinging on the plate.

In the ‘Plate’, the ‘Plate 25’ and the ‘Plate 50’ cases, when the flame front reaches the central plate zone, the initial orange sooty flame forms and develops from the stagnation point, where the velocity is zero (Chander and Ray, 2008). This leads to a large amount of unburnt fuel accumulating at the plate centre and then cracking. In other words, the initial orange sooty flame always forms along the fuel jet; even when the ignition location is far away from the fuel jet. The formation of the orange flame forms earlier when the ignition location approaches the plate centre.

At the impingement stage, wall quenching is observed in each case due to the cool plate effect, which is signalled by the disappearance of a large amount of CH^* and C_2^* emission, e.g. 152 ms in the ‘Middle’ case (Fig. 5. 5). The flame reforms at the plate region afterwards due to the continuous flowing of the fuel. Finally, the flame becomes stable with a concentric ring-shaped sooty flame emanating from the stagnation region.

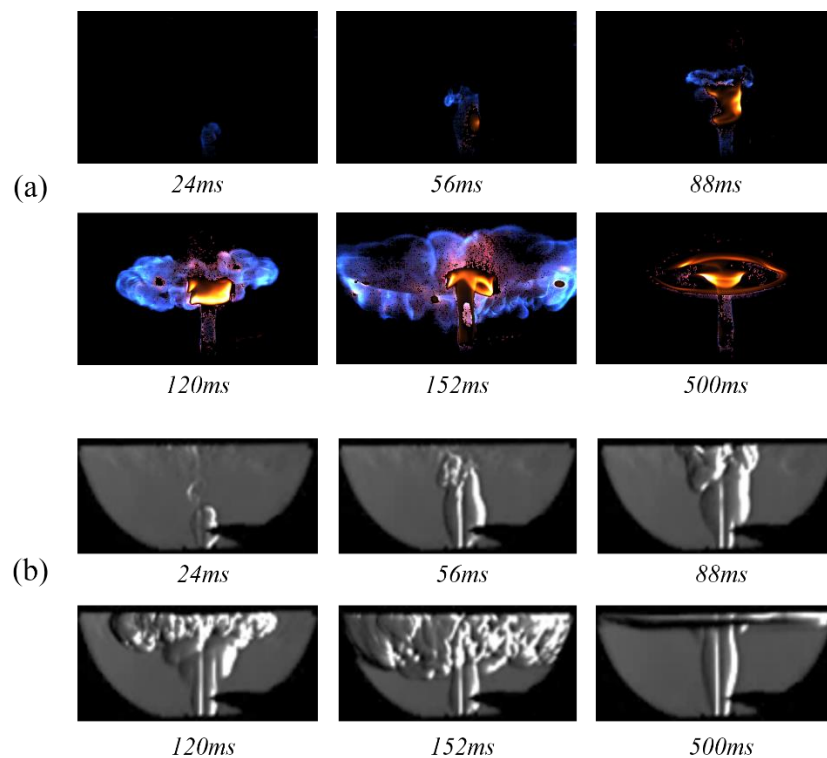


Fig. 5. 4 Simultaneous (a) Enhanced colour and (b) Schlieren image sequences of the ‘6CH₄’ ignition process initiated at the ‘Nozzle’ location.

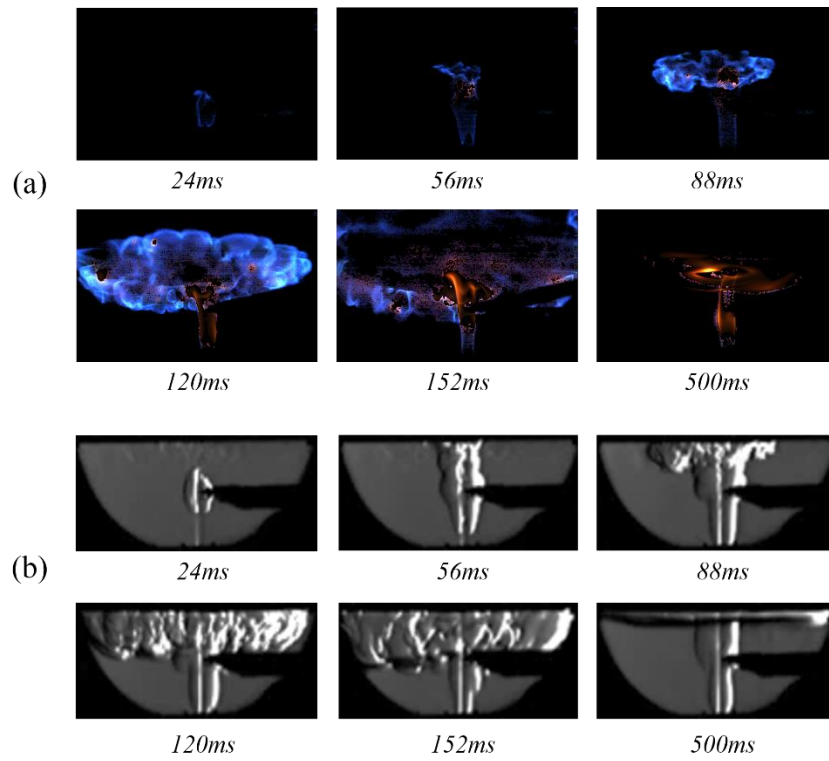


Fig. 5. 5 Simultaneous (a) Enhanced colour and (b) Schlieren image sequences of the ‘6CH₄’ ignition process initiated at the ‘Middle’ location.

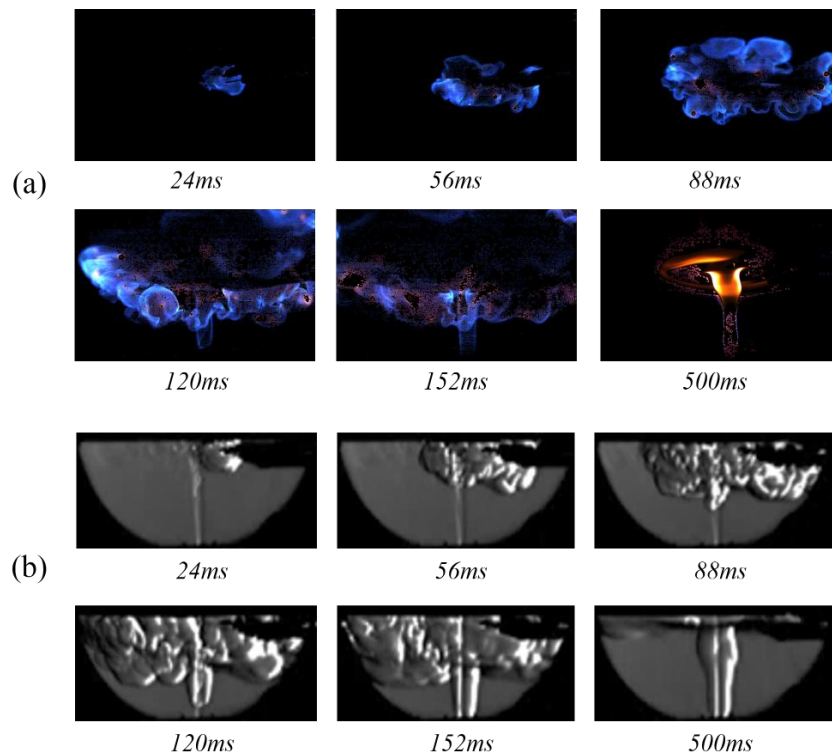


Fig. 5. 6 Simultaneous (a) Enhanced colour and (b) Schlieren image sequences of the ‘6CH₄’ ignition process initiated at the ‘Plate’ location.

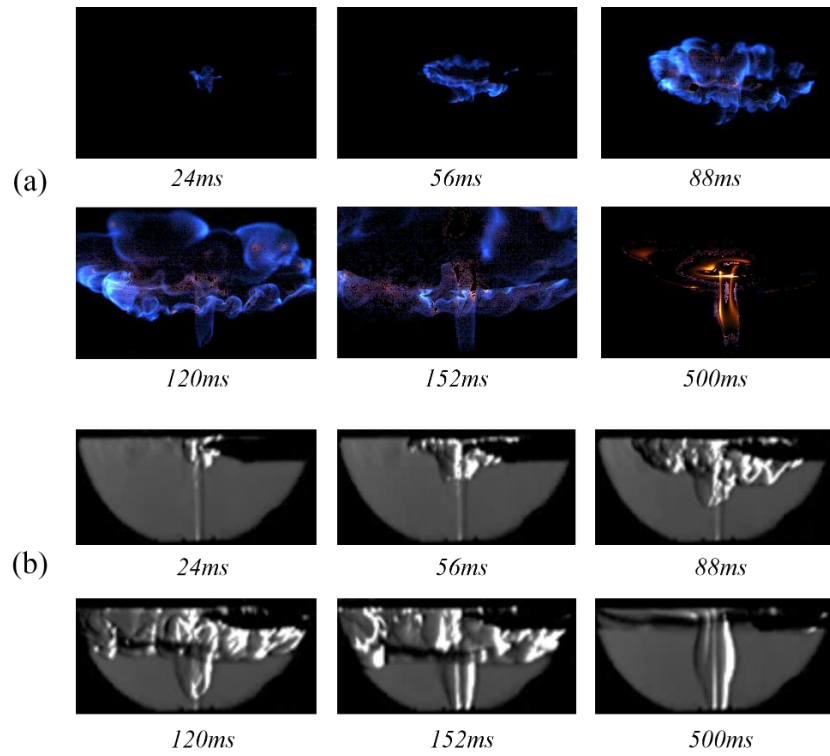


Fig. 5. 7 Simultaneous (a) Enhanced colour and (b) Schlieren images sequences of the '6CH₄' ignition process initiated at the 'Plate 25' location.

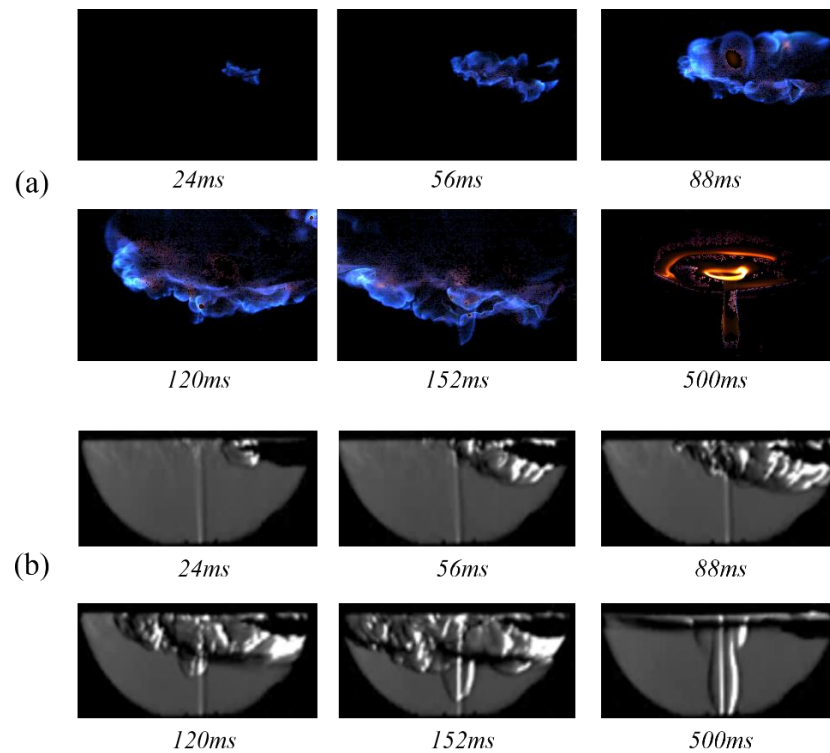


Fig. 5. 8 Simultaneous (a) Enhanced colour and (b) Schlieren image sequences of the '6CH₄' ignition process initiated at the 'Plate 50' location.

The time-dependent number of pixels of the infrared soot precursor emission and the soot-induced orange flame of the '6CH₄' cases are shown in Fig. 5. 9 (a) and (b), which reflect the evolution of infrared flame emission and visible soot emission presence respectively. It is found that the quantity of infrared flame emission increases in the wall quenching process when the flame starts to contact the wall. The impingement on the cool plate leads to a sudden temperature drop and a suspension of chemical reaction in the plate region, which results in excess of the unburnt fuel near the plate, which subsequently interacts with the residual hot gas to produce more infrared flame emission. After that, the orange soot emission greatly increases, as shown in Fig. 5. 9 (b). It is observed that the formation of the orange soot is delayed when the flame is ignited at the plate; the largest amount of soot forms in the 'Nozzle' case, followed by the 'Middle', 'Plate', 'Plate 25' and 'Plate 50' cases respectively. This is because that in the 'Plate', 'Plate 25' and 'Plate 50' cases, the flame propagates in the axial direction with a blue film at the outer layer and a hollow core in the centre; the sooty flame forms after the flame attaches to the nozzle, as shown in Figs. 5. 6, 5. 7 and 5. 8. The quantity of soot formation is therefore significantly reduced in these initial stages of the ignition process.

Fig. 5. 9 (c) shows the time-dependent mean intensities of the soot-induced orange flame. The mean intensity is defined as the ratio of total pixel intensity over the total number of pixels in a given region. The intensity threshold of pixel intensity is 0 to 2¹⁶. The intensity of the orange sooty flame is proportional to the sooty flame temperature which can be used to infer the approximate temperature evolution of a global flame. It is observed that the global flame temperature in the 'Nozzle' is higher than the other cases at the early stage of ignition. A notable drop of the 'Nozzle' curve at 144 ms is due to the wall quenching effect, which demonstrates that the flame impingement behaviour has a great influence on the flame temperature, especially in the 'Nozzle' case. It is interesting to find that there is a hump on the 'Plate 50' curve, located between 88 ms and 120 ms. This is due to the sporadic soot regions near the plate as shown in Fig. 5. 8, which is very common in soot dominated flames. The sporadic soot regions always form at the high-temperature intense reaction zone which is slightly away from the stagnation point.

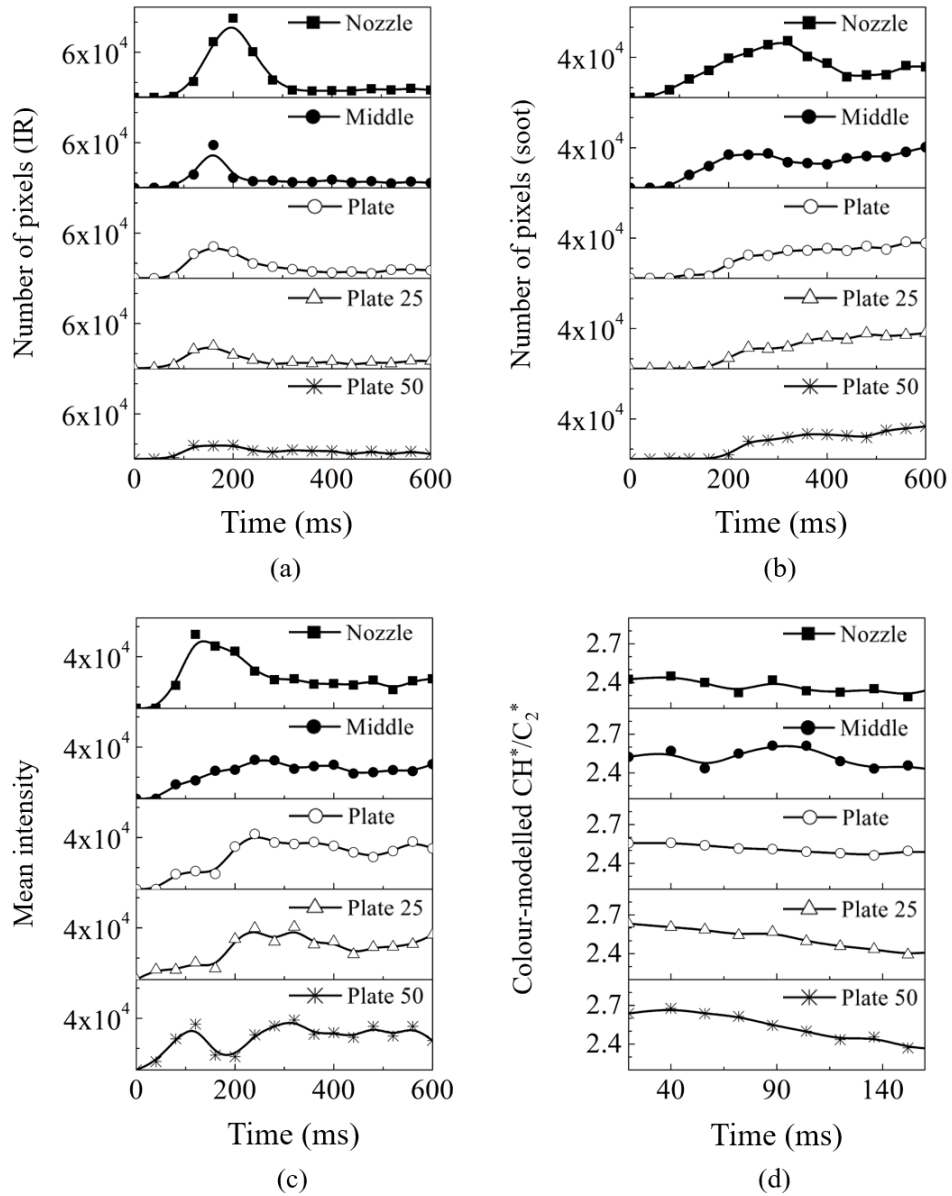


Fig. 5.9 Time-dependent (a) Number of pixels of infrared flame emission, (b) Number of pixels of the visible orange sooty flame, (c) Mean intensity of the visible sooty flame and (d) Colour-modelled CH^*/C_2^* of the chemiluminescence-induced blue flame, of the '6CH₄' cases.

Fig. 5.9 (d) represents the time-dependent colour-modelled CH^*/C_2^* of the bluish flame region in the '6CH₄' cases. From Section 3.6, the relative concentration of the CH^* and C_2^* could be deduced from the intensities of the Blue and Green channels in the RGB colour model. As the CH^*/C_2^* has a non-linear relation to the equivalence ratio, the fuel and air mixing level can be expressed in Eq. 3.7, Eq. 3.8 and Eq. 3.10.

Only the flame with a large area of the bluish flame region is analysed for accuracy, which is from 20 ms to 160 ms. The initial CH^*/C_2^* values are higher in the ‘Plate 25’ and the ‘Plate 50’ cases, due to the flames initiating at fuel lean conditions. The ‘Nozzle’ and ‘Middle’ curves have valleys at 72 ms and 56 ms respectively due to the flame impingement. In the beginning, these two curves decline, since the flame front approaches the fuel-rich stagnation point. They then increase as the flame propagates along the plate in the axial direction. When the flame initiates at the ‘Plate 25’ and ‘Plate 50’ locations, the curves gradually decrease since the flame propagates from a relatively fuel-lean region toward the fuel rich regions: the centre of the plate and the nozzle exit.

Fig. 5. 10 shows a time-dependent colour map of the colour-modelled CH^*/C_2^* ratio distribution of the ‘6CH₄ Nozzle’ case. When compared with the images of the sooty flame emission, it is found that the soot pocket is always located in a fuel rich zone. The red circles mark a representative sporadic soot region, which also demonstrates that the soot is surrounded by the fuel-rich blue flame. The colour maps of the other cases are shown in Fig. 5. 11.

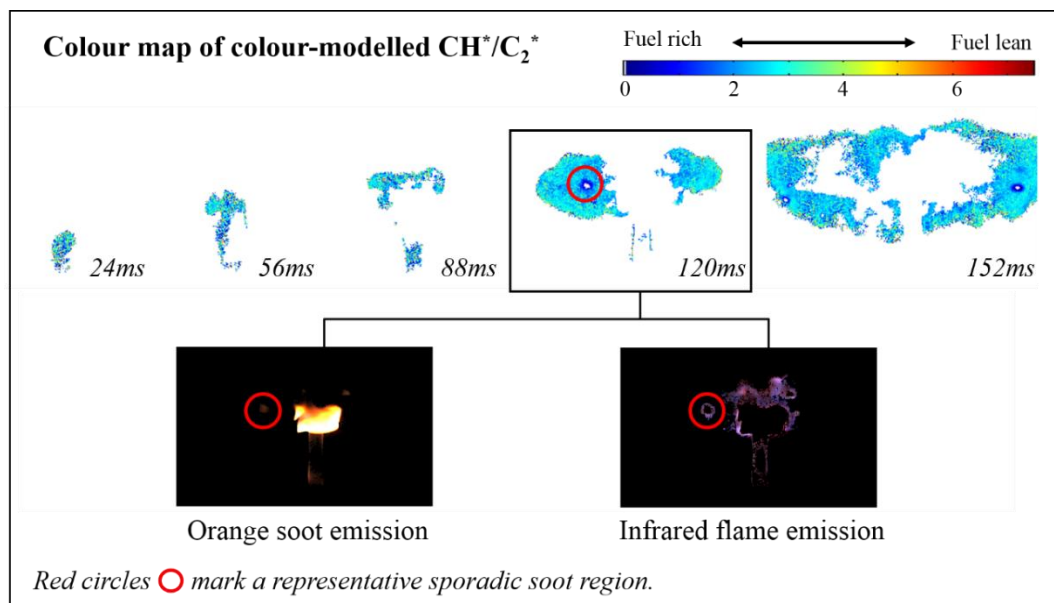


Fig. 5. 10 Colour map of the colour-modelled CH^*/C_2^* ratio distribution for the ‘6CH₄ Nozzle’ case and the images of the sooty flame emission in the visible and infrared spectra respectively of the ‘6CH₄ Nozzle’ case, 120 ms after ignition.

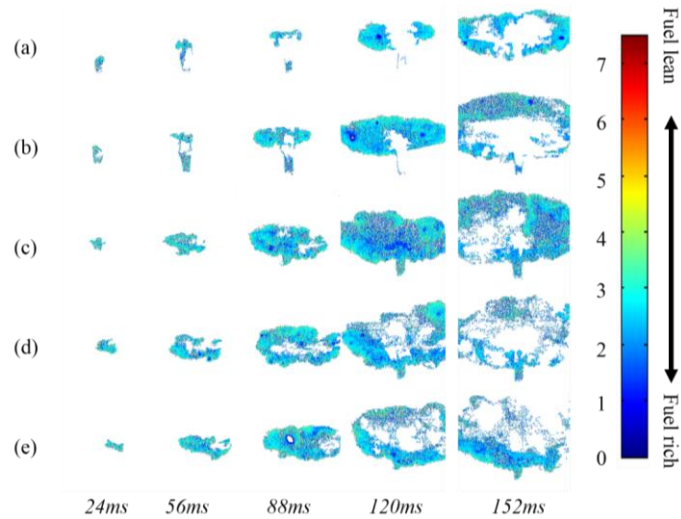


Fig. 5. 11 Colour maps of the colour-modelled CH^*/C_2^* ratio distribution of the (a) ‘Nozzle’, (b) ‘Middle’, (c) ‘Plate’, (d) ‘Plate 25’ and (e) ‘Plate 50’ ‘6CH₄’ cases.

When 3 l/min of CO₂ is introduced into the CH₄, the soot formation is delayed in each case. The quantity of soot is reduced significantly because the increase in CO₂ concentration chemically reduces the infrared flame and the soot emissions. The lower flame temperature also suppresses the soot formation. The reaction zone consists of the blue flame, the infrared flame and the orange soot and its structure looks more laminar at steady state. When the CO₂ flow rate increases to 4 l/min, the flame forms a smooth sheet along the plate, dispersing radially outwards at steady state. In contrast to the lower fuel flow rate cases, the downward flame propagation is delayed when the flame initiates at the ‘Middle’ location due to the high jet velocity. Shown in Fig. 5. 12, the blue flame develops with a hollow core and attaches the nozzle exit 280 ms after ignition. The soot has a short time to accumulate and be heated before reaching a steady state, which causes the reduction in the overall quantity of soot.

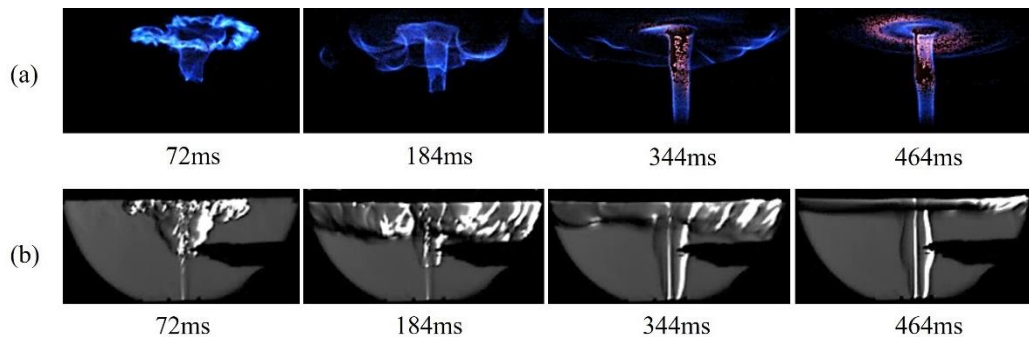


Fig. 5. 12 (a) Enhanced colour and (b) Schlieren image sequences of the ‘6CH₄+4CO₂ Middle’ ignition process captured simultaneously. The blue and infrared region are enhanced 15 times.

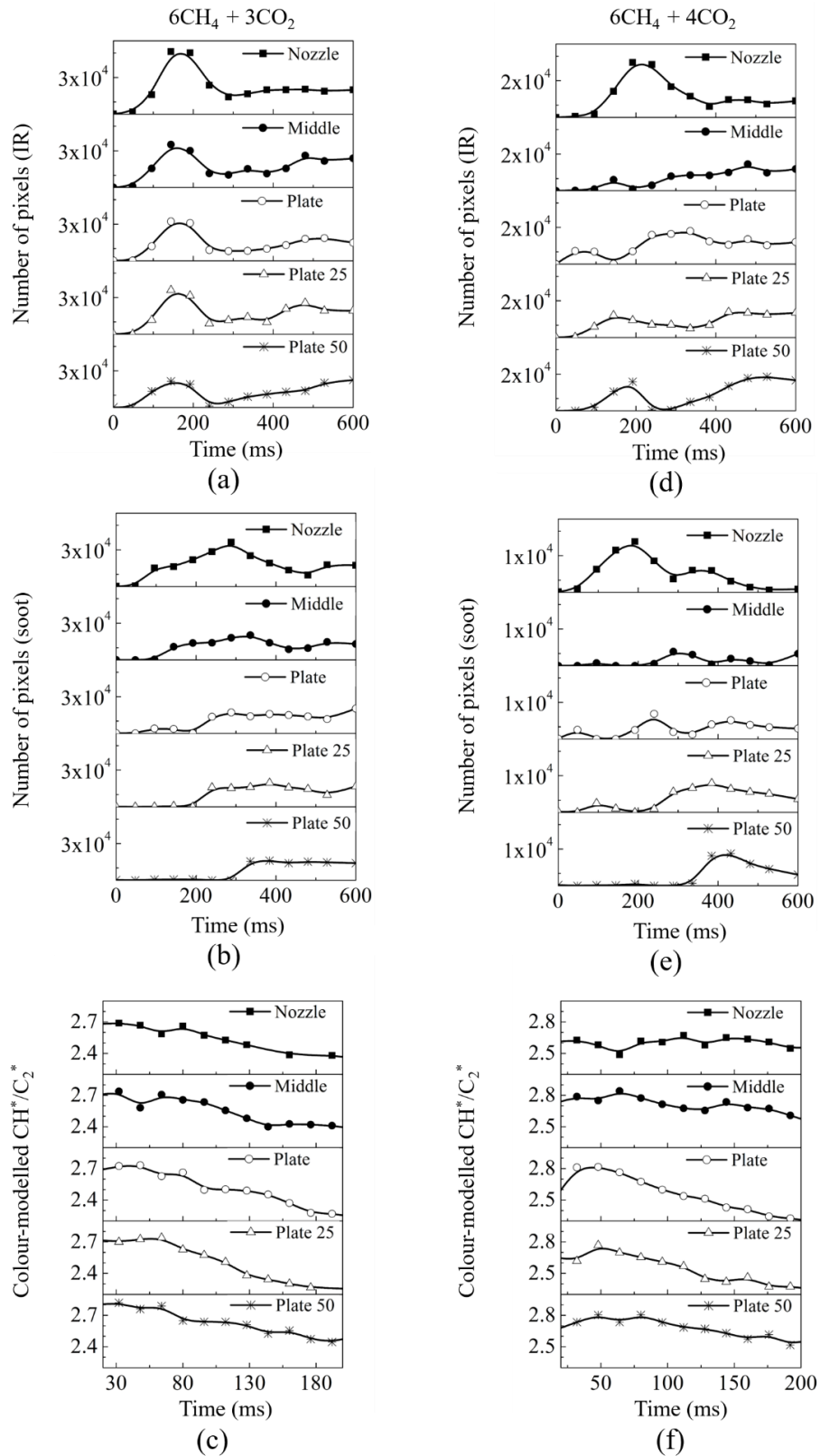
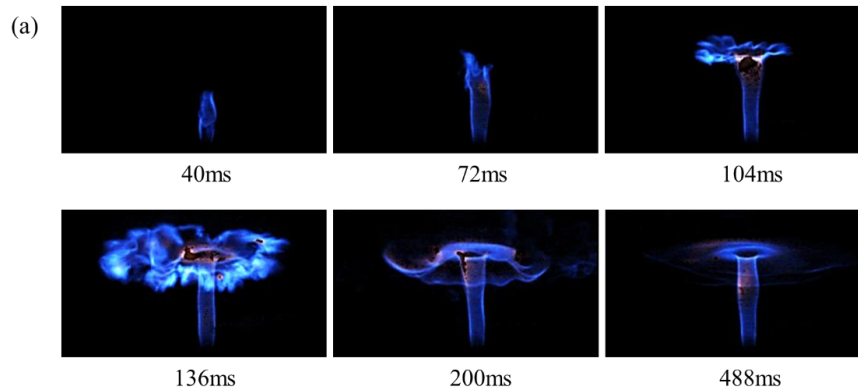


Fig. 5. 13 Time-dependent number of pixels of the infrared flame emission, the soot-induced orange flame and the blue/green intensity ratios of the chemiluminescence-induced blue flame of (a)-(c) the ' $6\text{CH}_4+3\text{CO}_2$ ' and (d)-(f) the ' $6\text{CH}_4+4\text{CO}_2$ ', respectively.

5.3.2 Blue flame dominated ignition process

When the CO₂ flow rate increases to 5 l/min and above, the flame is composed of a large area of blue flame with tiny infrared and sooty flame. Two flame profiles can be formed by changing the ignition location only in the cases of '6CH₄+5CO₂'. Shown in Fig. 5. 14 (a), a cool central core flame forms when the flame is initiated at the nozzle exit. A large amount of unburnt fuel concentrates around the plate centre and forms an unreacted zone at the stagnation region due to the high jet velocity. At 488 ms, the flame becomes stable with a little-infrared emission and forms a smooth ring structure in the plate zone. If the flame is ignited at other locations (Fig. 5. 14 (b – e)), the bottom boundary of the flame will detach from the nozzle exit, which demonstrates that the ignition location will directly affect the flame structure. It is found that the downward flame propagation is obstructed by the resistance of the jet flow. The bottom boundary of the flame is unstable due to the unbalanced system, hence forms an unsteady 'dancing' flame between the plate and the nozzle. In a relatively steady state, the blue flame with a cool central core forms a rippled sheet along the plate. An arched boundary is observed at the bottom of the flame due to the varying flow speed distribution. The results demonstrate the ignition location can directly affect the flame structure.



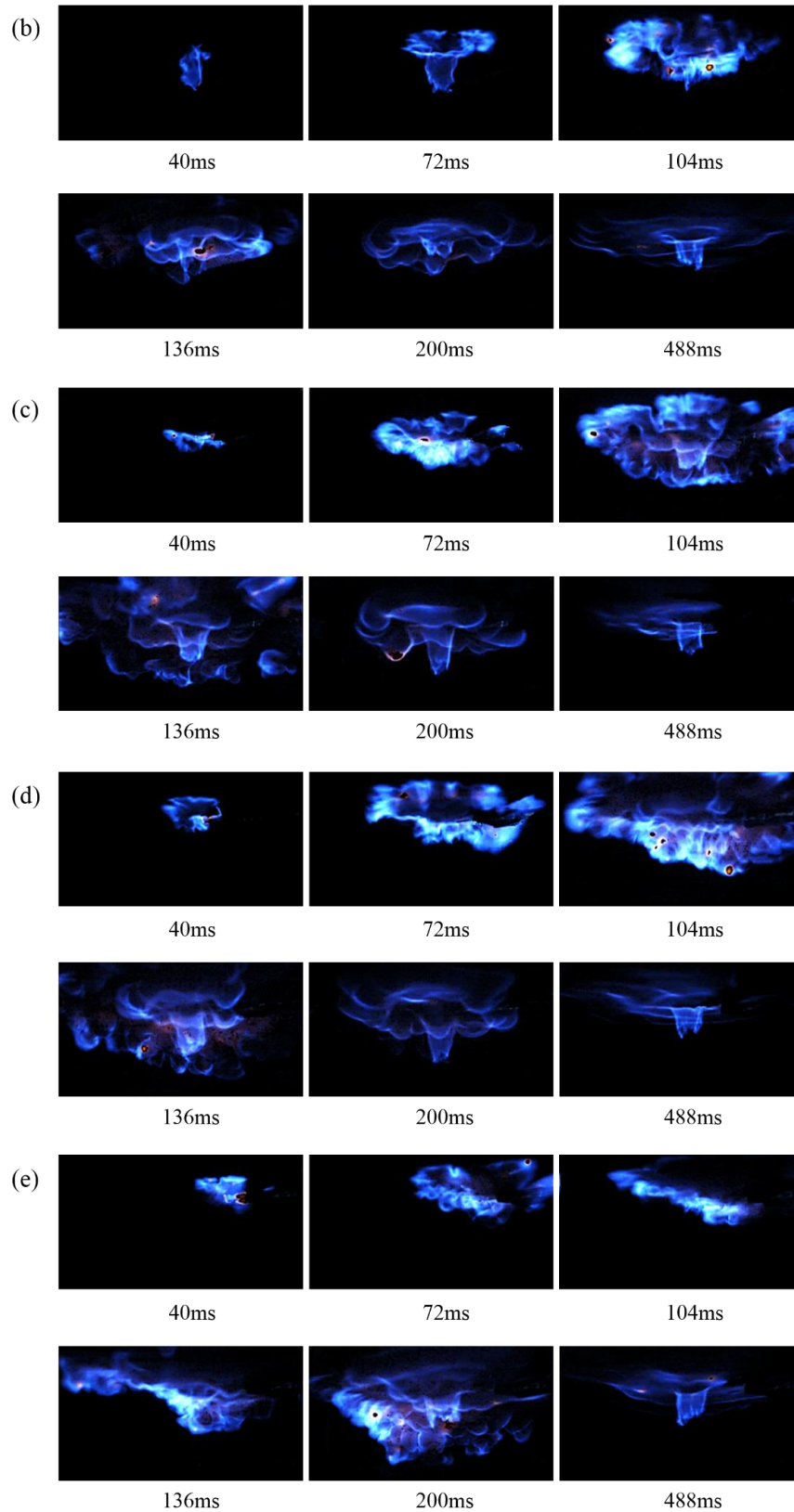


Fig. 5. 14 Image sequences of the ' $6\text{CH}_4+5\text{CO}_2$ ' ignition process initiated at the (a-e) 'Nozzle', 'Middle', 'Plate', 'Plate 25' and 'Plate 50' locations, respectively. The blue flame and infrared emission colourations are enhanced 10 times.

It is observed that the evolution of the infrared flame emission in the ‘Nozzle’ is different from the other cases due to the different flame structure in the ‘6CH₄+5CO₂’, as shown in Fig. 5. 15 (a). The infrared emission continuously accumulates from 80 ms to 240 ms in the ‘Nozzle’ case, while the infrared flame forms in the wall quenching process and disappears at the end of the quenching in all of the other cases (Fig. 5. 15 (a)). The open bottom of the detached flame enhances the air going through the hollow core, which provides a fuel-lean environment and takes away much heat, thereby impeding the soot formation (Fig. 5. 15 (b)). The fuel is enveloped in the ‘Nozzle’ case which enhances the accumulation of the infrared emission and sooty flame. In Fig. 5. 15 (c), the curve of the colour-modelled CH*/C₂* ratio of the ‘Nozzle’ case has a rapid decline, which resembles the trends in the lower jet velocity cases. The other curves slightly decrease and then increase, since the bottom boundary of flame front re-rises afterwards. The curves of the ‘Middle’, ‘Plate’, ‘Plate 25’ and ‘Plate 50’ locations are higher than the ‘Nozzle’ case, since the high jet velocity entrains surrounded air to the cool centre of the flame from the open bottom and improves the fuel/air mixing level in the detached flame.

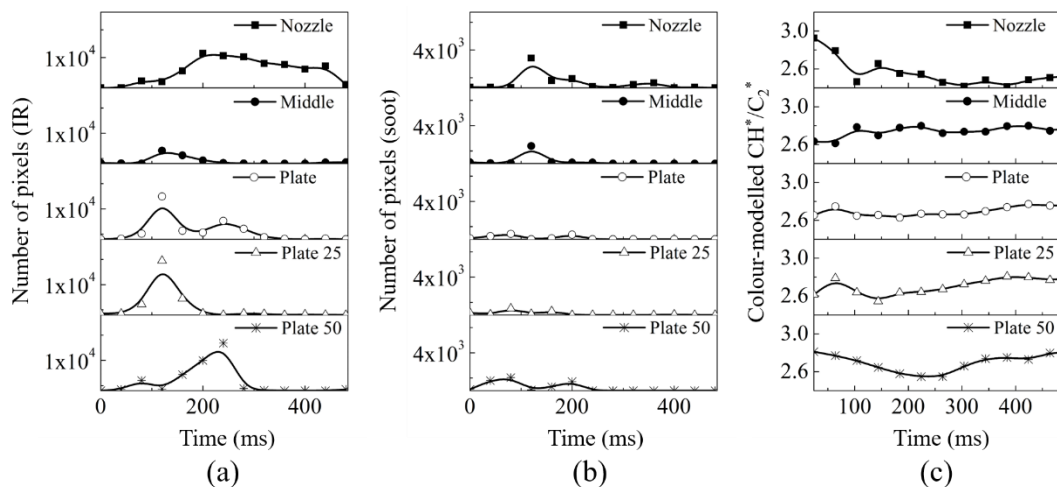


Fig. 5. 15 Time-dependent (a) Number of pixels of the infrared emission, (b) Number of pixels of the soot-induced orange flame and (c) Blue/green intensity ratios of the chemiluminescence-induced blue flame of the ‘6CH₄+5CO₂’ flame.

With an increase in CO₂ jet velocity, the effect of ignition location on flame colour variation gradually shrinks. The flame fails to ignite in the ‘Nozzle’ and ‘Plate’ cases, when the CO₂ flow rate exceeds 6 l/min, while the fuel can be ignited at the ‘Middle’

only in the ‘6CH₄+9CO₂’ cases. The flame forms a ring shape (Sjoholm *et al.*, 2013) without any soot emission in the ‘6CH₄+8CO₂’ and the ‘6CH₄+9CO₂’ cases. When the flame is initiated at the ‘Middle’, the flame propagates upwards with a hollow core, and the lower boundary of the flame rises afterwards. The flame propagates radially and develops with a ring structure. In the ‘Plate 25’ and ‘Plate 50’ cases, the flame propagates from two edges of the stagnation zone and encircles the unburnt plate centre, as shown in Fig. 5. 16.

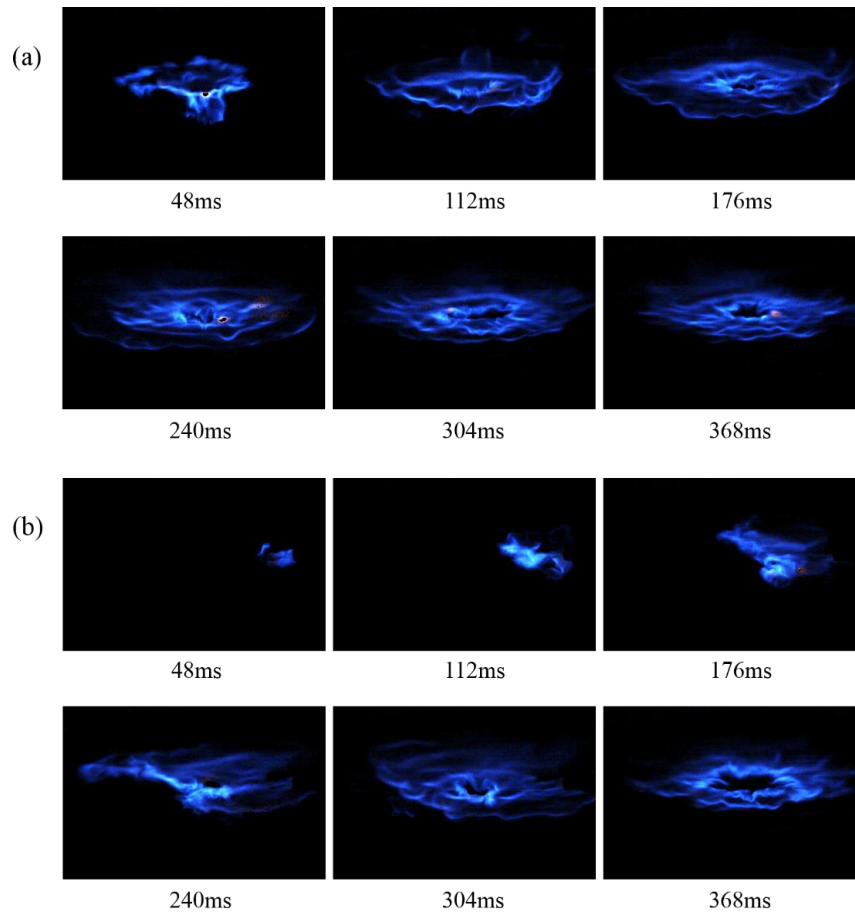


Fig. 5. 16 Image sequences of the ‘6CH₄+8CO₂’ ignition process initiated at the (a) ‘Middle’ and (b) ‘Plate 50’ locations, respectively. The blue flame and infrared emission colourations are enhanced ten times.

Fig. 5. 17 shows the influences of CO₂ concentration on the flame propagation properties and soot formation. The ‘Middle’ cases are shown as an example. In the legend of the graph, ‘Quantity (Peak)’ represents the maximum quantity of the infrared and soot emission in the ignition process, and ‘Quantity (Stable)’ represents the quantity of the infrared and soot at steady state. It can be observed that the soot

formation decreases rapidly with an increase in CO₂ concentration. The ‘Mean intensity’ curves reveal that the introduction of the CO₂ will largely reduce the flame temperature. Shown in Fig. 5. 17 (b), the time taken from ignition to steady state is shortened with an increase in CO₂ concentration. A rapid drop from 4 l/min to 5 l/min is due to the flame structure evolution from the envelope to detached flame.

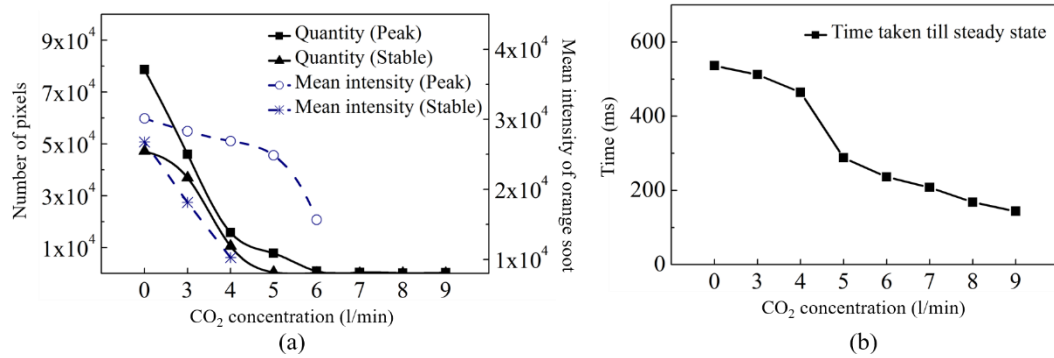


Fig. 5. 17 (a) Quantity and mean intensity of the soot emission with varying CO₂ concentration and (b) Time taken until reaching a steady state with different CO₂ concentrations.

5.3.3 Plate temperature effects on flame characteristics

The effects of plate temperature on flame characteristics, such as the flame temperature, light emission and propagation properties are studied in this section. The results presented in Section 5.3.1 and 5.3.2 were conducted with the plate temperature at 23 °C before ignition. Another set of experiments with 100 °C initial plate temperature were conducted for comparison. Fig. 5. 18 (a) and (b) show schlieren images of the unignited methane flow with plate temperatures of 23 °C and 100 °C respectively.

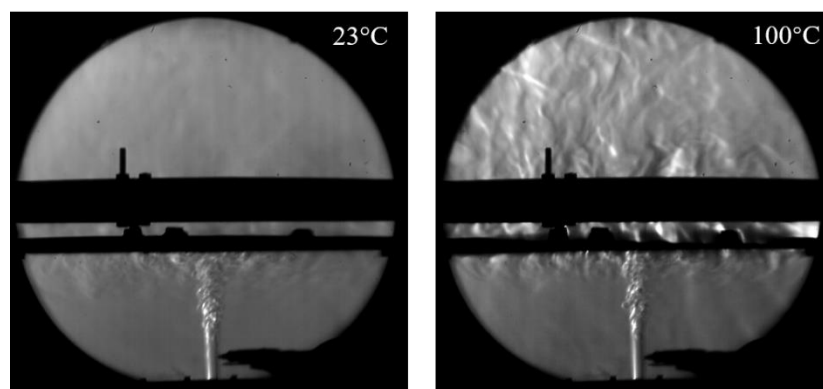


Fig. 5. 18 Schlieren images of the cold methane flow with the plate temperature 23 °C and 100 °C.

The total number of pixels of the infrared flame emission and orange soot emission of the ‘Nozzle’ cases with different plate initial temperatures are shown in Fig. 5. 19. In the cases with higher initial plate temperature, less soot forms in the ignition process and the flame takes less time to reach a steady state. This is because the fuel gas near the plate is heated by the hotter plate surface which enhances the combustion process, hence the soot formation reduces and the ignition time span therefore shortens. The higher CH^*/C_2^* ratios in the cases of the higher plate temperature also support this statement.

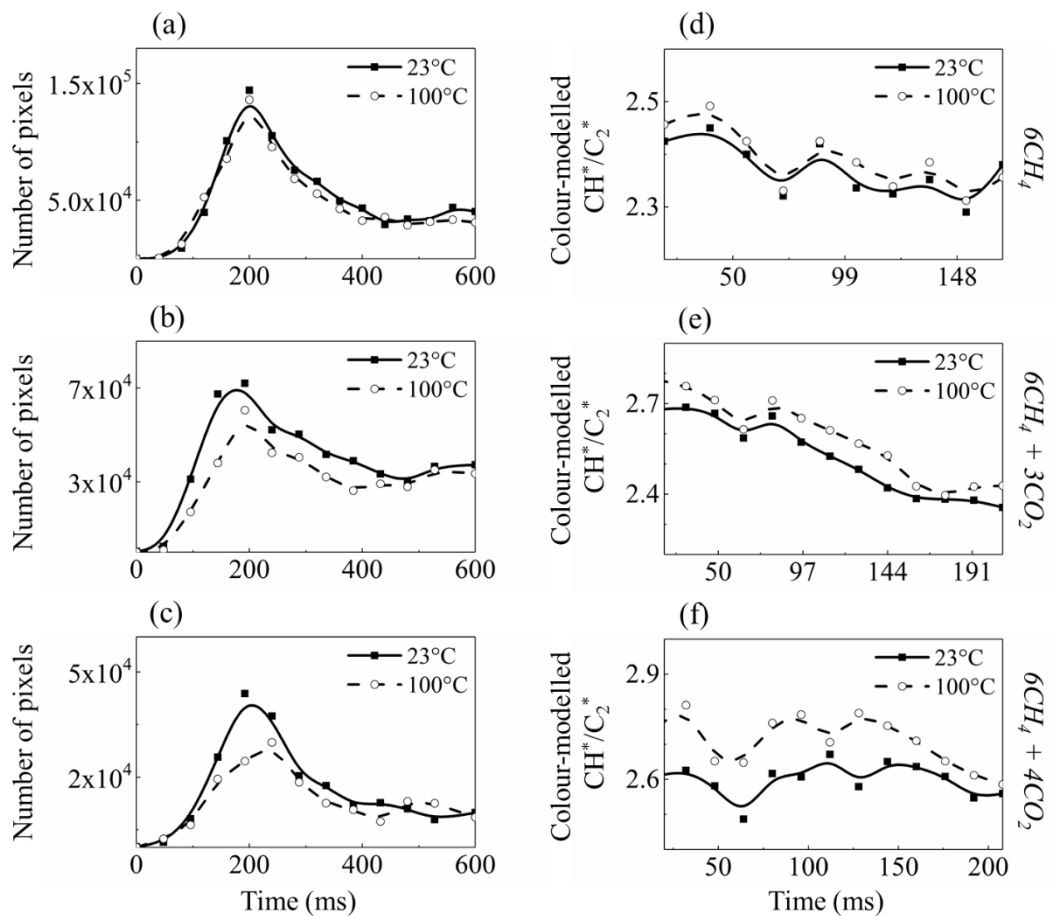


Fig. 5. 19 Time-dependent (a)-(c) Total number of pixels of infrared flame emission and orange soot emission and (d)-(f) CH^*/C_2^* ratio with different initial plate temperatures for the ‘ $6CH_4$ ’, the ‘ $6CH_4+3CO_2$ ’, and the ‘ $6CH_4+4CO_2$ ’ cases respectively. The flames are all initiated at the nozzle exit.

5.4 Summary

The effects of ignition location, CO₂ concentration and plate surface temperature on the initial flame propagation properties and soot formation in impinging flame ignition processes are investigated by using simultaneous direct colour imaging and schlieren imaging techniques. With the help of a unique image processing method, the time-dependent spatial evolution of multiple emission species, which includes the two chemiluminescence radicals CH* and C₂*, the soot emissions and infrared soot precursor are visualised and analysed. It is evident that the soot production is susceptible to the ignition location from the stage of ignition to a stable flame condition, and so are the active chemical species such as CH* and C₂*. The largest amount of soot accumulates during the ignition process when the flame is ignited at the nozzle exit. Soot formation significantly reduces when the flame is initiated at the 'Plate 50' and 'Middle' locations in the cases of lower and higher CO₂ concentration respectively. It is found that the initial orange sooty flame always forms along the fuel jet regardless of the flame initiated locations. The sporadic soot emission regions always take place in the high-temperature intense reaction zone, which is slightly away from the stagnation point. In the '6CH₄+5CO₂' cases, both the cool central core flame and detached flame structures can be developed by varying the ignition location only. A flame with a ring-shaped structure can be formed when the CO₂ flow rate increases to 8 l/min. With an increase in CO₂, the soot emission quantity and the flame temperature gradually reduce. Wall quenching is observed in each case due to the cool plate effect; when the flame impinges onto the cool plate surface, the flame temperature suddenly drops, and the chemical reaction pauses in the plate zone which boosts the soot formation. It is also found that a hotter plate surface will shorten the time span from flame ignition to a steady state and suppress the soot formation.

Chapter 6

Effects of Ignition Location on Soot and Species Formation in the Impinging Configuration through Tracking Flame Light Emission and Temperature

6.1 Introduction

Flame temperature, as an important parameter in IC engines, can be correlated with combustion characteristics such as thermal efficiency and level of soot concentration and may vary with different ignition locations. With the use of traditional temperature measurement techniques such as thermocouples, the limitations of low-thermal responses and degradation with time in a harsh environment are unavoidable. Hence, an optical temperature measurement, a modified two-colour method using glowing thin silicon carbide fibres in the flow field is used to evaluate the flame temperature. With the help of a selective digital image enhancement method, the time-dependent spatial evolutions of multiple flame emissions are simultaneously tracked and quantitatively analysed at variable ignition locations by using a single high-speed colour camera.

6.2 Two-colour Method

Temperature measurement can be classified as intrusive, semi-intrusive and non-intrusive methodologies. For the intrusive measurement, thermocouple and thermometers are widely applied in industry. However, the intrusiveness of the instruments causes flow disturbance when measuring the flame, which tends to lead to a big deviation between the measured flame temperature and its actual temperature. Semi-intrusive measurements are performed by coating the objects with thermochromic liquid crystals, heat sensitive paints and thermographic phosphors, which can be applied to flame temperature measurement. The two-colour method is a non-intrusive measurement technique, which is based on the objective radiation energy measurement. The traditional two-colour method uses narrow-bandpass and

beam splitting filtering techniques (Teini, Karwat and Atreya, 2012; Liu *et al.*, 2015; Gu, Chu and Liu, 2016; Mze Ahmed *et al.*, 2016). The temperature of the object can be inferred from the gained ratio between two grey levels at selected wavelengths λ_1 and λ_2 , which is expressed by Eq. 6.1 and Eq. 6.2. Furthermore, Hossain *et al.* (Hossain *et al.*, 2013) implemented the 3D reconstruction of flame temperature using a tomographic and two-colour method.

$$\frac{G(\lambda_1, T)}{G(\lambda_2, T)} = \frac{S_{\lambda_1} \varepsilon_{\lambda_1}}{S_{\lambda_2} \varepsilon_{\lambda_2}} \left(\frac{\lambda_2}{\lambda_1}\right)^5 \exp\left[\frac{C_2}{T} \left(\frac{1}{\lambda_2} - \frac{1}{\lambda_1}\right)\right] \quad (6.1)$$

$$T = \frac{C_2 \left(\frac{1}{\lambda_2} - \frac{1}{\lambda_1}\right)}{\ln \frac{G(\lambda_1, T)}{G(\lambda_2, T)} + \ln \frac{S_{\lambda_2}}{S_{\lambda_1}} + \ln \left(\frac{\lambda_1}{\lambda_2}\right)^5 + \ln \frac{\varepsilon_{\lambda_2}}{\varepsilon_{\lambda_1}}} \quad (6.2)$$

where C_2 is the second Planck's radiation constant, $S_{\lambda_1}/S_{\lambda_2}$ is the spectral sensitivity, ε_{λ_1} and ε_{λ_2} are two spectral emissivity and T is the measurement temperature.

Since the traditional two-colour technique is still complicated, Ma *et al.* (Ma *et al.*, 2016) developed a modified two-colour method to measure flame temperature based on the built-in colour-banded filter in the high-speed camera; Photron SA4. The ratio of the intensities in the Red and Green channels are used to estimate the soot-rich flame temperature. The result shows good consistency between the measured and actual flame temperature. This technique has a limitation in that it cannot be applied to flames with soot deficiency because the emission of the blue flame is due to the flame chemiluminescence. Therefore, the SiC fibre (Fig. 6. 1) is introduced to measure flame temperature, especially the premixed blue flame temperature.



Fig. 6. 1 The SiC bundle containing 500 ultra-thin filaments.

The fibre performs as a radiation emitter, similar to the soot particles. The SiC fibre has high strength at high temperature with a high melting point and fast thermal response, which makes it suitable for flame temperature measurement. Since the diameter of the fibre is just 15 μm , which is thinner than a human hair, the fibre is unlikely to make flow disturbances in the flame. The SiC fibre thermal properties are shown in Table 6. 1.

Table 6. 1 SiC fibre thermal properties.

Material	Nicalon SiC CF tow
Density	2550 kg/m ³
Thermal Conductivity	12 Wm ⁻¹ K ⁻¹
Specific Heat	1120 J K ⁻¹ kg ⁻¹
Emissivity	0.88

6.3 Experimental Procedure

6.3.1 Experimental setup

The schematic of the experimental setup is shown in Fig. 6. 2. Methane and air were premixed in a mixing cylinder and then injected through a nozzle with 8.0 mm inner diameter. The gas flow rates were controlled by rotameters. The test conditions are shown in Table 6. 2.

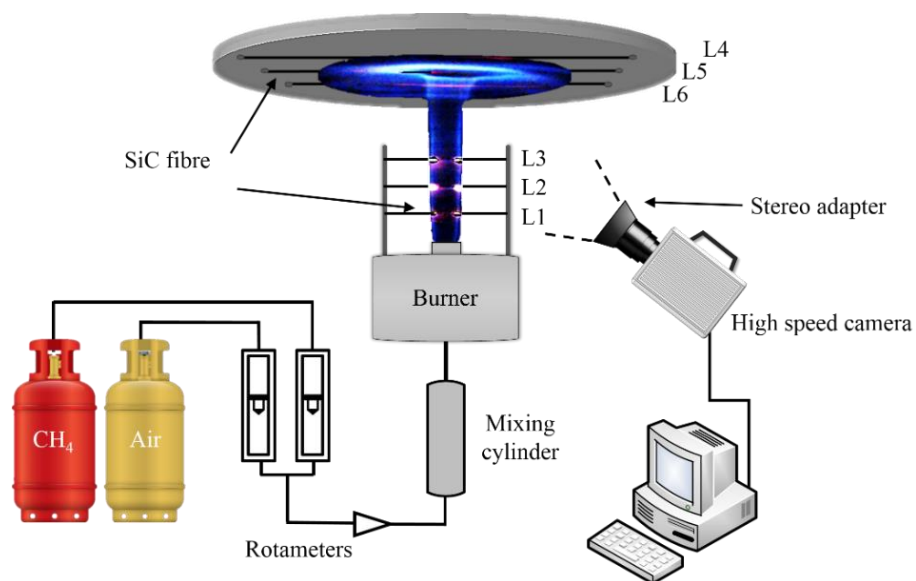


Fig. 6. 2 Experimental setup.

Table 6. 2 Test conditions

Gas type	Volume flow rate (l/min)	Velocity (m/s)	Re	ϕ
CH ₄	5	1.66	778	-
Air	4	1.37	695	2.5
Air	8	2.65	1343	1.25
Air	10	3.32	1683	1
Air	12	3.98	2018	0.83

The methane flow rate remained at 5 l/min in all cases. The air flow rate was varied from 4 l/min to 12 l/min, referred to as ‘Air 4’, ‘Air 8’, ‘Air 10’ and ‘Air 12’ for simplicity. The flame was ignited by a Kawasaki ignition-coil (TEC-KP02) with an output voltage of 30 kV. The spark was generated by a pair of steel electrodes with a 10 mm gap. A heavily oxidised stainless-steel plate, 0.3 m in diameter and 10 mm thick was positioned 100 mm from the nozzle exit. The ignition processes were captured by a high-speed camera (Photron FASTCAM SA4) with a full frame resolution of 1024 × 1024 pixels, the frame rate of 125 fps and 1/125 s shutter speed, positioned at an inclined angle to the plate.

Thin filaments of SiC were applied to measure the flame temperature. Three SiC fibres L1, L2, L3 (Fig. 6. 2) were tightened on a frame at distances of 20, 35 and 50 mm from the nozzle exit respectively. Another three fibres L4, L5 and L6 were suspended tautly onto the plate with a 2 mm gap, with intervals of 50 mm between fibres. The hot gas temperature was measured according to the emission of the fibres in the captured images. Since the glowing fibre was much brighter than the flame, it was impossible to image the fibre and flame simultaneously without image saturation. To overcome this issue, a Pentax stereo adapter was applied to the front of the lens to simultaneously generate two parallel images with a slight displacement. A 10-stop neutral density (ND) filter was applied to the left view to reduce the amount of light and prevented over-exposure. The right view directly captured the flame images without any filter. A pair of example images is shown in Fig. 6. 3 (b). With the aid of the adapter, the flame light emission could be analysed by the right view and the flame temperature measurement could be measured by the left view.

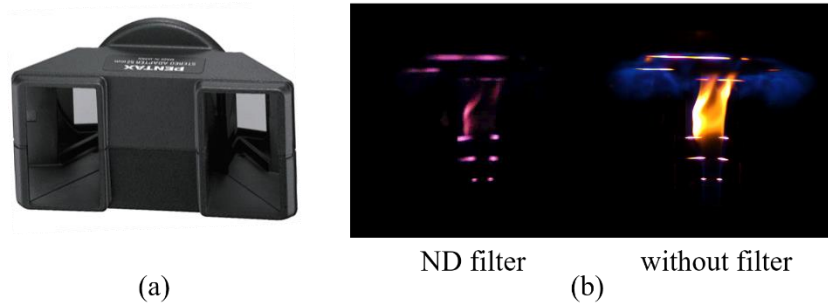


Fig. 6. 3 (a) Stereo adaptor, (b) Stereo images pair. A 10-stop ND filter is applied on the left side and the right side directly images the flame without any filter.

6.3.2 Flame temperature measurement

Optical measurements are desirable for flame temperature monitoring due to their non-intrusiveness, fast response, and potentially relatively low-cost. A modified two-colour method is thus applied to this investigation. Before the flame temperature measurement, the two-colour system was calibrated with a standard temperature source (blackbody cavity) ranging from 973 K to 1773 K; the system was validated via measuring the temperature of this standard source. As shown in Fig. 6. 4, the maximum root mean squared (RMS) error of 5 % occurred at 973 K, with an average error in the measured temperature of 2 %. A thin SiC fibre will glow brightly in the reaction zone and emit radiation at nearly constant emissivity, which is a requirement for the two-colour temperature measurement. Since the fibre temperature is proportional to the flame temperature, it is reasonable to determine flame temperature variation by tracking the fibre temperature. The flow disturbance caused by the fibre is negligible due to its small diameter of 15 μm .

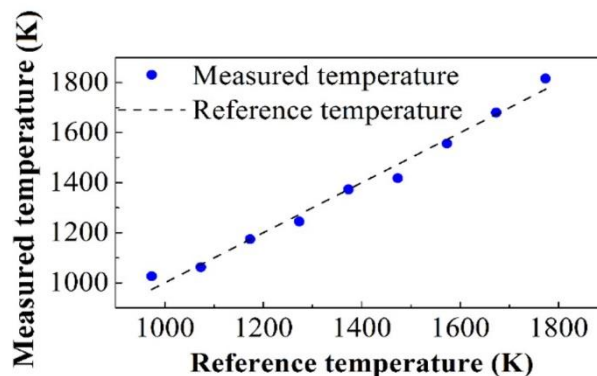


Fig. 6. 4 Comparison between measured and reference temperature of calibration source.

6.3.3 Selective digital image enhancement technique

The flame images are post-processed by selective digital image enhancement method. Both the blue flame and infrared emission are enhanced ten times in the presented images, as shown in Fig. 6. 5.

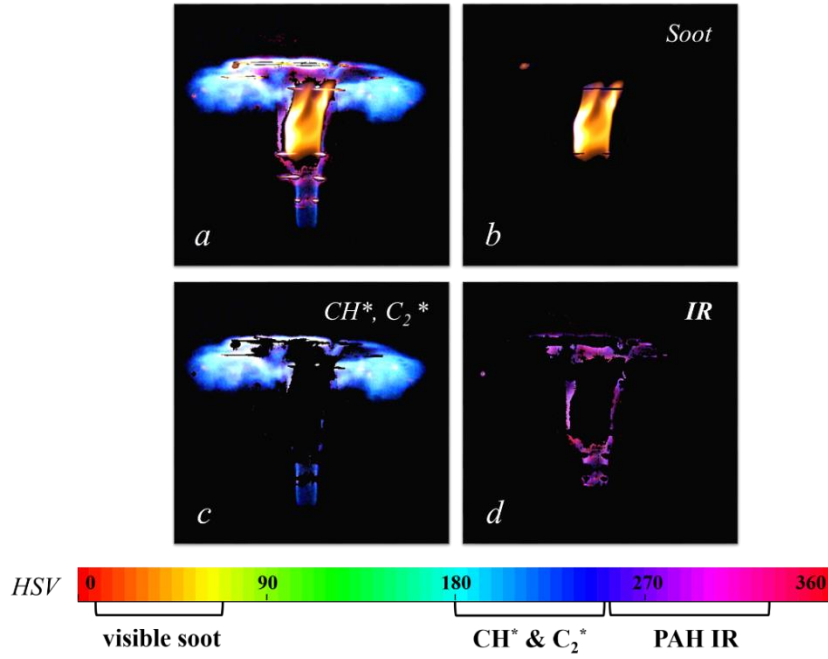
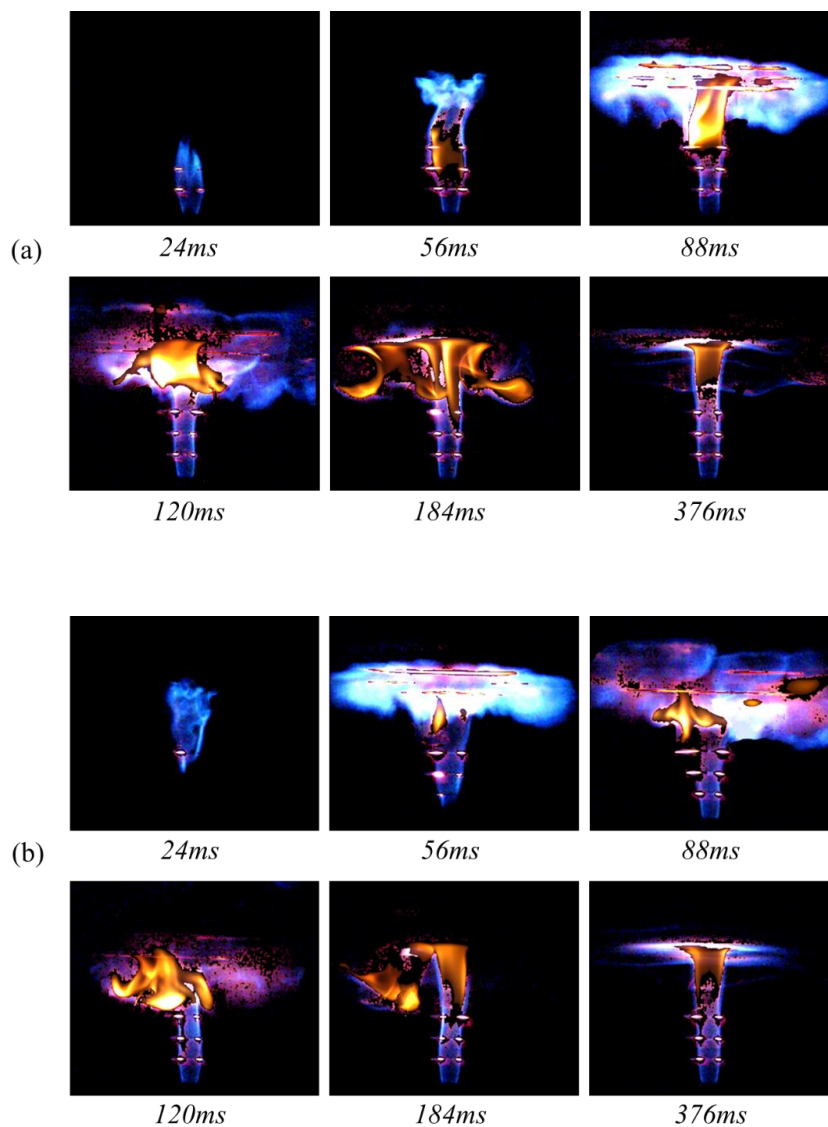


Fig. 6. 5 (a) Image after selective image enhancement, (b) Visible soot emission, (c) Blue flame enhanced 10 times and (d) Infrared soot precursor emission enhanced 10 times.

6.4 Results and Discussion

Under each test condition, the flame was ignited at three locations: 10 mm above the nozzle, halfway between the nozzle and plate, and the centre of the plate, named ‘Nozzle’, ‘Middle’, and ‘Plate’ respectively. Fig. 6. 6 shows the image sequences of ‘Air 4’ cases from the flames being ignited until reaching a relatively stable state. The flame characteristics are similar in the final steady state even given different ignition locations, but discrepancies are found in the flame structure and colour distribution during the propagation stage. The common trend in all cases shows that the combustion process starts with the development of a blue flame, followed by the infrared emission and sooty flame. The infrared emission is found in between the blue flame and the visible sooty flame. At the early stage of ignition, the flame rapidly forms a high-temperature blue flame region. The pyrolysis of plenty of unreacted

methane in the fuel pocket forms carbon soot in the flame centre zone. The soot emits blackbody radiation in the visible spectrum and glows orange. Wall quenching is observed at the impinging stage due to the cool plate effect, reflected by the disappearance of a large amount of CH^* and C_2^* emission. As the fuel flow continues, the flame re-forms gradually near the plate region. Finally, the flame becomes stable with orange soot emission near the plate centre, surrounded by a thin-film of blue flame along the plate. The duration of ignition for the ‘Nozzle’, ‘Middle’ and ‘Plate’ cases was 376 ms, 352 ms and 328 ms respectively, with a maximum deviation of 8 ms.



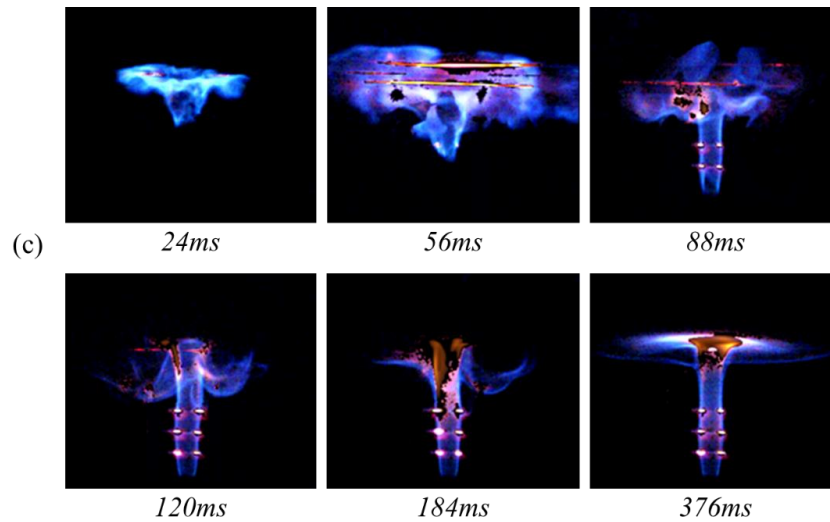


Fig. 6. 6 Image sequences of the ‘Air 4’ ignition process initiated at the (a) ‘Nozzle’, (b) ‘Middle’ and (c) ‘Plate’ cases respectively.

Through tracking the light emission of the SiC fibres, it was found that the centre of fibres L1, L2, L3 and L5 show weak visible emission due to the presence of fuel pockets. Shown in Fig. 6. 7, each point is the average value of the temperature along a selected length of fibre L6 during the wall quenching process.

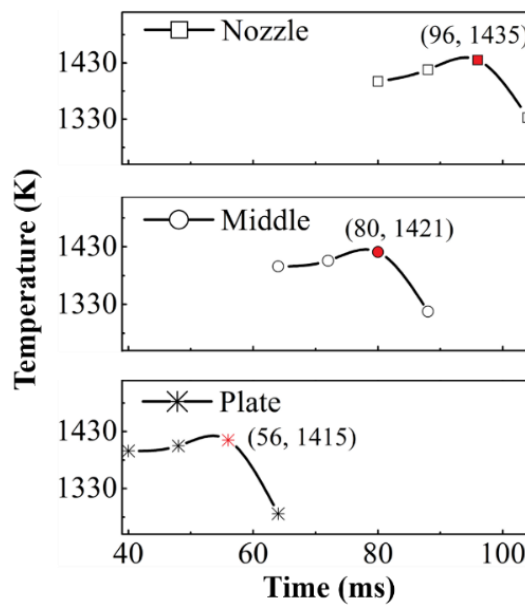


Fig. 6. 7 Fibre L6 temperature evolution in the wall quenching process of the ‘Air 4’ cases ignited at the ‘Nozzle’, ‘Middle’ and ‘Plate’ locations.

It is observed that the temperature is higher in the ‘Nozzle’ case with a peak temperature (marked in red) of 1435 K at 96 ms after ignition. The ‘Middle’ and ‘Plate’

cases show maximum temperatures of 1421 K and 1415 K respectively. Each case experiences a temperature drop due to wall quenching; the most notable one is a drop of 129 K, found in ‘Plate’ case due to stronger convection induced by the higher flame propagation velocity, and drops of 101 K and 102 K within 8 ms in the ‘Nozzle’ and ‘Middle’ cases respectively.

Fig. 6. 8 (a) and (b) show the time-dependent number of pixels of the visible sooty flame and the infrared flame emission in the ‘Air 4’ case. The number of pixels reflects the area occupied by the different colour regions. It is found that the quantity of soot formation rapidly increases after wall quenching occurs. In the quenching process, the chemical reaction suddenly suspends near the plate leading to the pyrolysis of a large amount of unburnt fuel initially accumulated in the region. It can be observed that more soot forms in the ‘Nozzle’ case, while the infrared flame largely forms in the ‘Middle’ case, as shown in Fig. 6. 8 (a) and (b). This may be because the ‘Nozzle’ ignition allows sufficient time for the transformation from the soot precursor to the mature soot. In the ‘Plate’ case, the upward flame propagation is blocked; the effect of flame impingement is hence minimised. Therefore, the quantity of soot formation and infrared emission are reduced significantly.

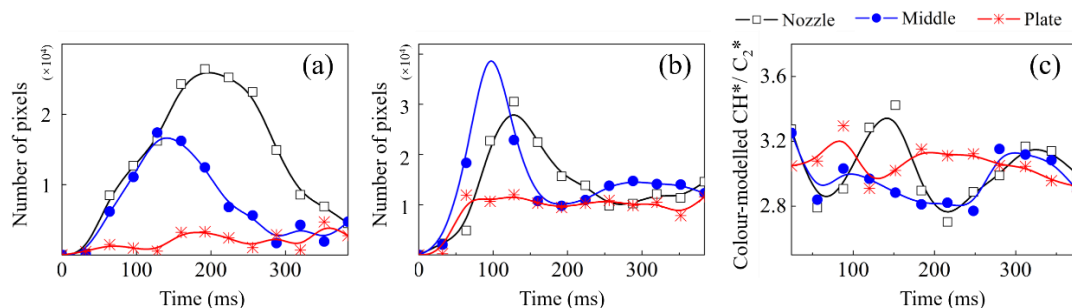
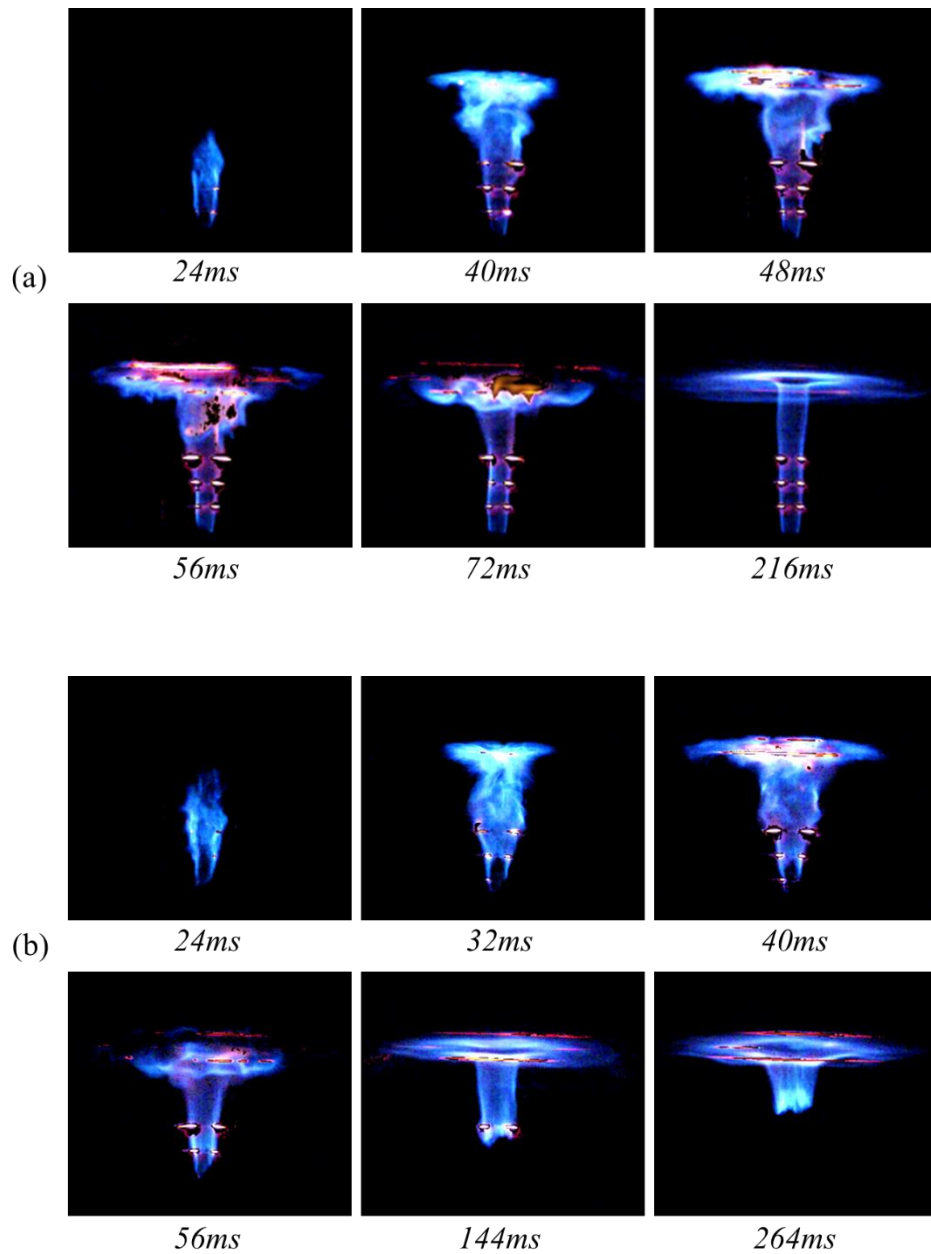


Fig. 6. 8 Time-dependent number of pixels of (a) Soot-induced orange flame and (b) Infrared soot precursor and (c) colour-modelled CH^*/C_2^* ratios of the chemiluminescence-induced blue flame, of the ‘Air 4’ cases.

The time-dependent blue/green intensity ratio of the blue flame region is shown in Fig. 6. 8 (c). Only the flame with a large area of the blue flame region is analysed for accuracy, which is from 24 ms to 376 ms. The ‘Nozzle’ and ‘Middle’ curves decline at the beginning of ignition since the flame front approaches the fuel-rich plate centre. The plate centre is the stagnation point at zero velocity, accumulating a large amount

of unburnt fuel. These curves increase afterwards as the flame propagates along the plate and then drop again at 152 ms and 88 ms respectively due to the wall quenching. Finally, the measured CH^*/C_2^* ratios increase as the flames stabilise near the plate. The relative tolerances of repeated experiments are found to be less than 5 %, based on the quantification of soot formation and the CH^*/C_2^* ratio determination, which indicates excellent repeatability.



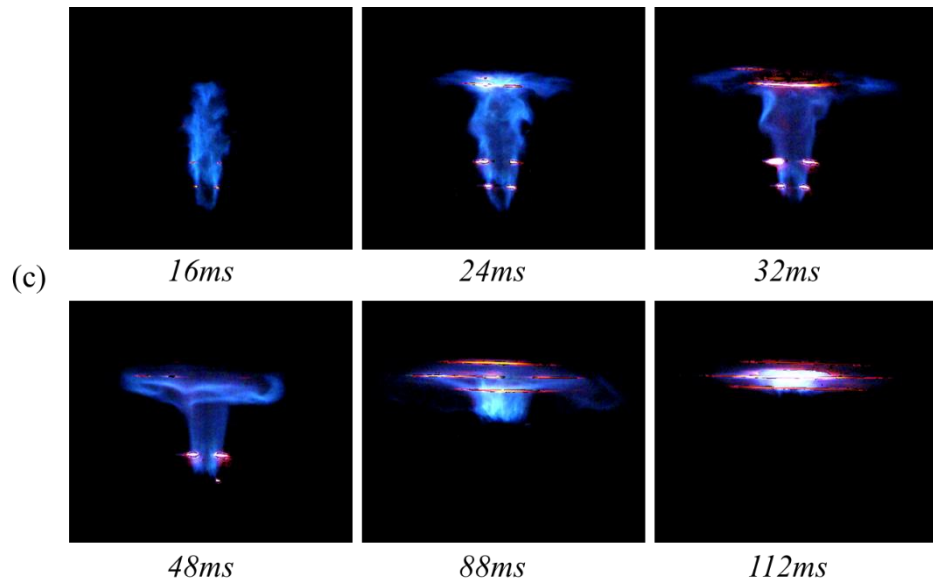


Fig. 6. 9 Image sequences of the ignition process of (a) the ‘Air 8’, (b) ‘Air 10’ and (c) ‘Air 12’ cases. The flames are initiated at the nozzle exit.

Fig. 6. 9 shows the image sequences of the ‘Air 8’, ‘Air 10’ and ‘Air 12’ cases. The flames are initiated at the nozzle exit. The time-dependent temperature measurements of L1, L2 and L3 for the ‘Air 8’ and ‘Air 10’ cases are shown in Fig. 6. 10, where the temperatures are the averages of the lines. With an increase in air concentration, the quantity of soot is reduced. In the ‘Air 8’ case, the flame right side propagation is faster than the left, due to the randomness which leads to a lower flame temperature on the right side due to the faster propagation induced by the higher convection, as shown in Fig. 6. 10. The temperatures of L1, L2 and L3 simultaneously drop at 56 ms after ignition due to wall quenching. The flame turns to completely blue with a hollow core at steady state. A detached flame is observed in the ‘Air 10’ case. The bottom boundary of the flame gradually moves away from the fibres with a continuous temperature drop. As the air flow rate increases to 12 l/min, a disc flame is formed which attaches to the plate. The flame temperature near the fibre L6 is approximately 1324 K, 1342 K and 1327 K at steady state of these three cases, which have equivalence ratios of 1.25, 1 and 0.83 respectively. This indicates that the flame temperature increases when the equivalence ratio approaches unity.

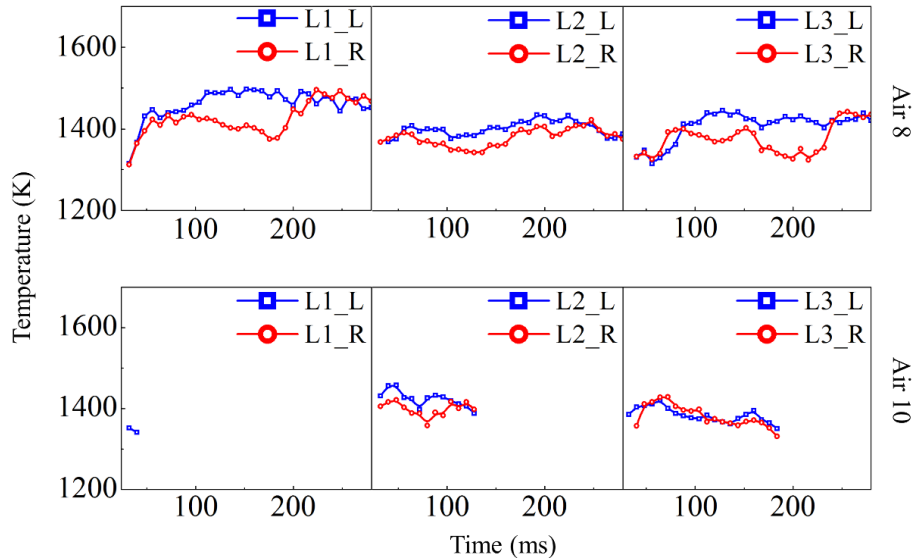


Fig. 6. 10 Time-dependent temperature variation of the L1, L2 and L3 fibres, ignited at nozzle in the ‘Air 8’ and ‘Air 10’ cases. ‘L’ and ‘R’ represent flame left and right sides of the respectively.

6.5 Summary

The ignition location effects on flame propagation properties and soot formation in an impinging flame have been investigated via tracking multiple light emission species and temperature using a single high-speed camera. The flame temperature was evaluated using a modified two-colour method to measure the glowing thin SiC fibres positioned in the flow field. The time-dependent spatial evolutions of chemiluminescence radicals CH^* and C_2^* , soot and the infrared soot precursor were investigated via image processing techniques. It was found that the evolution of temperature, soot formation, and chemical species are quite sensitive to ignition locations. More soot forms in the ‘Nozzle’ case, while more infrared flame forms in the ‘Middle’ case. The soot formation reduces greatly in the ‘Plate’ case. Wall quenching is observed in all cases at the impinging stage due to the cool plate effect. In the wall quenching process, the chemical reaction suddenly suspends near the plate leading to the pyrolysis of plenty of unburnt fuel initially accumulated in the region. There is a larger quenching-induced temperature drop in the ‘Plate’ case because of the strong convection resulting from the higher flame propagation velocity. Detached and disc flames are observed when increasing the air concentration respectively. The results show that the flame temperature increases when the equivalence ratio approaches unity.

Chapter 7

Co-Flow Effect on the Ignition Process

7.1 Introduction

Laminar gas jet diffusion flames have been intensively studied in combustion (Gu *et al.*, 2012; Luján *et al.*, 2015b; Thangaraja and Kannan, 2016b). Co-flow is often added to improve the stability of diffusion flames. Research has investigated lift-off for highly diluted propane flames with co-flow (Won *et al.*, 2000). The effect on soot formation and NO in co-flow ethylene air diffusion flames was studied by applying computational and experimental methods (Connelly *et al.*, 2009). However, the co-flow effect on the ignition process of diffusion flames is rarely investigated. A good understanding of the ignition process of methane diffusion flames with co-flowing air can be implemented via simultaneous multispectral time-dependent visualisation of the ignition process.

Flame ignition process studies rely on high-speed cameras. It is known that soot emission tends to obscure the CH* and C₂* signals under high shutter speeds. Research for the Rolls-Royce gas-turbine combustor has indicated that the flame seemed to be discontinuous under direct high-speed imaging. However, Huang and Zhang (Huang and Zhang, 2013) found that the discontinuous flame phenomenon was due to the existence of a weak blue-coloured flame via post-processing of the images through the DFCD method. It has been reported that the high-speed Photron SA4 is also sensitive in the infrared (Wang *et al.*, 2016). Combined with this novel method, some infrared flame emission can be visualised and extracted separately.

In this chapter, the temporal ignition development of methane diffusion flames with co-flowing air and the evolving light emission from the visible to infrared spectrum is investigated in detail.

7.2 Experimental Setup

Methane was injected through a central nozzle of 18.28mm diameter. Co-flow air surrounded the fuel in a coaxial condition. A fine-meshed honeycomb was placed

inside the co-flow nozzle to straighten the air. The co-flow air nozzle diameter was 37.8mm. The details of the burner are shown in Fig. 7. 1.

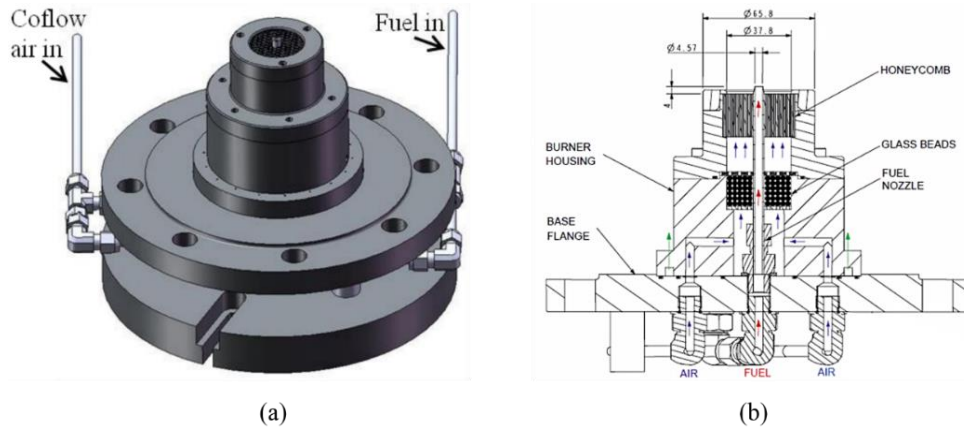


Fig. 7. 1 (a) The schematic of the burner and (b) cross-sectional drawings of the burner (Chloe and Mcdaid, 2013).

The gas flow rate was regulated by a mass flow controller. The fuel flow rate was kept constant at 0.182 l/min, which corresponds to a fuel jet velocity of 0.216 m/s and Reynolds number of 55.4, with co-flow air flows at 0 l/min, 14 l/min and 75 l/min, respectively. The flow conditions are presented in Table 7. 1.

Table 7. 1 Flow conditions

Air volume flow rate (l/min)	Velocity (m/s)	Re
14	0.216	479
75	1.155	2565

The schematic of the experimental setup is shown in Fig. 7. 2. A Z-type schlieren imaging system was used to investigate the flow dynamics and structures. The schlieren system consisted of an LED lamp for the light source and two parabolic mirrors, 0.3048 m (12 in.) in diameter and 3.048 m (10 feet) in focal length. The ignition was initiated with a Kawasaki ignition-coil (TEC-KP02), with an approximate output voltage of 30 kV. The spark was created between a pair of steel electrodes separated by a 9 mm gap. The electrodes were fixed at a distance of 14 mm above the nozzle. The ignition process was captured by a high-speed camera (Photron FASTCAM SA4) at a frame rate of 500 fps and 1/500 s exposure time with a full

frame resolution of 1024×1024 pixels. A Sigma 24 – 70 mm lens was applied to the camera. The aperture was set at f/2.8 in all the cases. The schlieren images were recorded by a high-speed camera (Photron FASTCAM SA5) at a frame rate of 1000 fps and 1/2000 s shutter speed with a resolution of 1024×1024 pixels. Although the two cameras were not synchronised, the spark could be used as a reference moment to achieve the synchronisation of the two cameras.

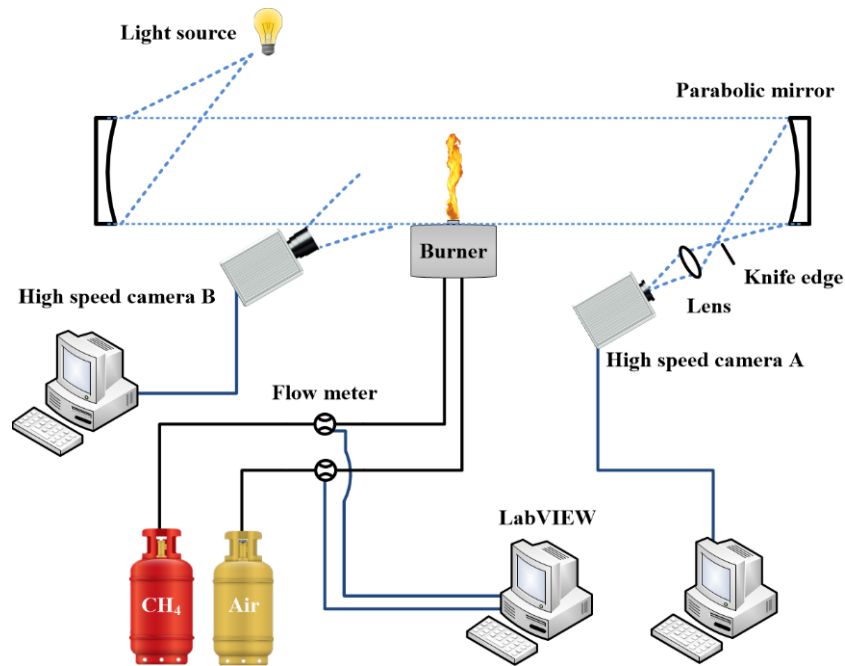


Fig. 7. 2 Schematic of the experimental setup.

7.3 Results and Discussion

7.3.1 Image processing method

Fig. 7. 3 shows the comparison between the original flame image and the colour-enhanced image. With the help of the selective digital image enhancement technique, the intensity of the weak bluish flame was selectively enhanced 25 times, and the infrared soot precursor was enhanced 30 times. The intensity of the bluish flame and infrared soot precursor was dozens of times weaker than the yellowish flame and completely masked, due to the limitations of the high-speed digital camera. The results demonstrate that the interpretation of high speed or high shutter speed flame colour images can be quite misleading without careful digital enhancement.

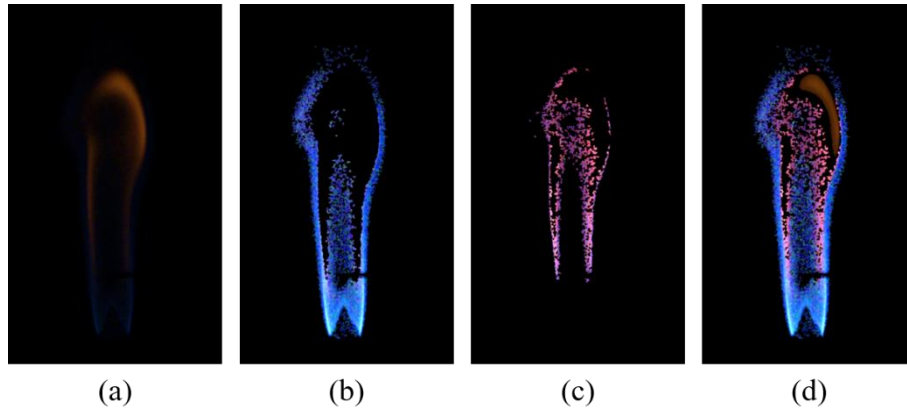
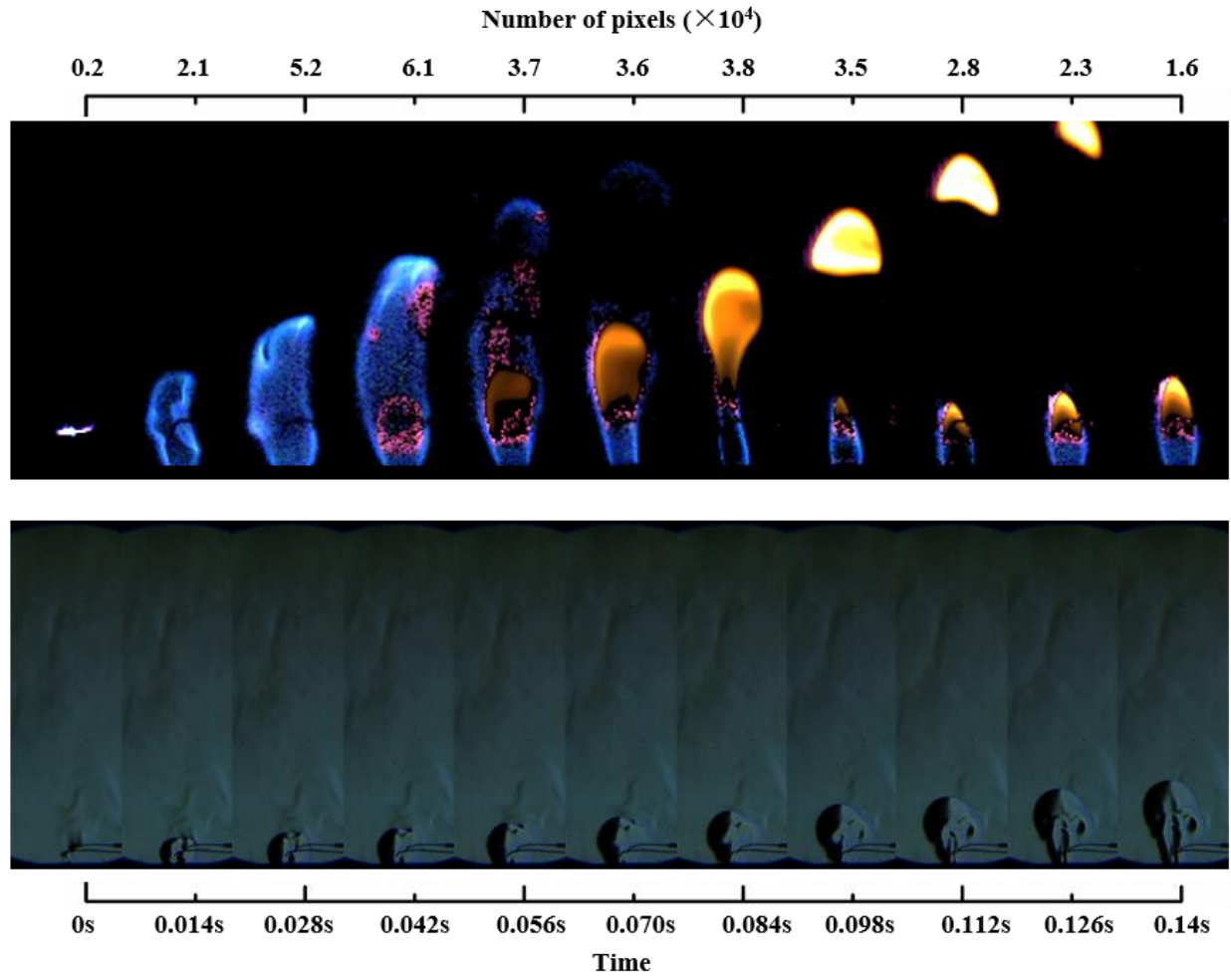


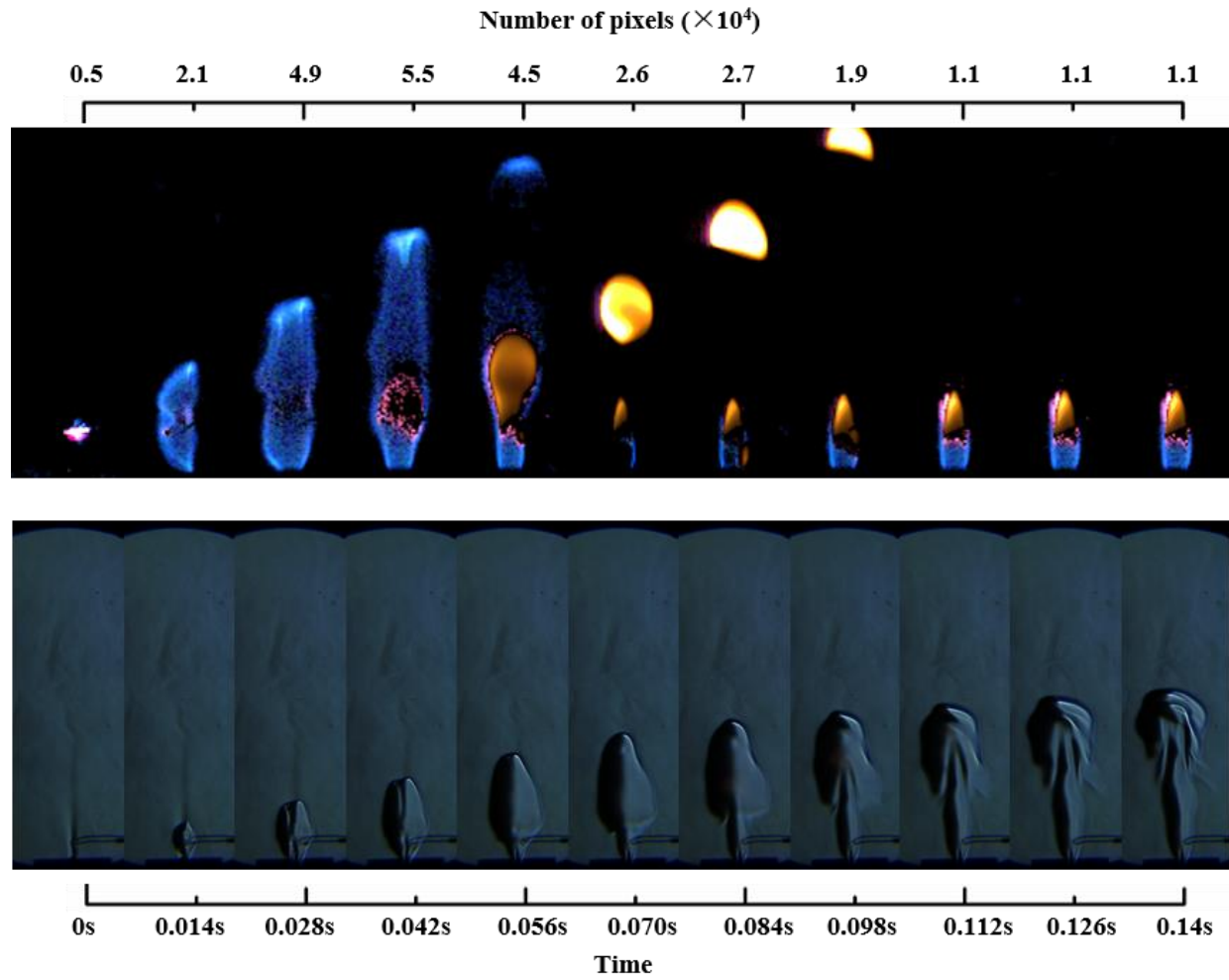
Fig. 7. 3 (a) The original image with 1/500 s shutter speed, (b) The chemiluminescence-induced bluish flame regime enhanced 25 times, (c) The infrared soot precursor enhanced 30 times and (d) The entire image after selective imaging enhancement.

The ignition processes of the methane non-premixed jet flame with 0 l/min, 14 l/min and 75 l/min co-flowing air are named 'Pure methane', 'Air 14' and 'Air 75' respectively. The flame colour image and schlieren image sequences of the three conditions are shown in Fig. 7. 4. These will be discussed in the following sections. Fig. 7. 5 shows the histograms of the flame colour distribution evolution in the hue domain during the ignition process.

(a) Air 0 *l/min*



(b) Air 14 *l/min*



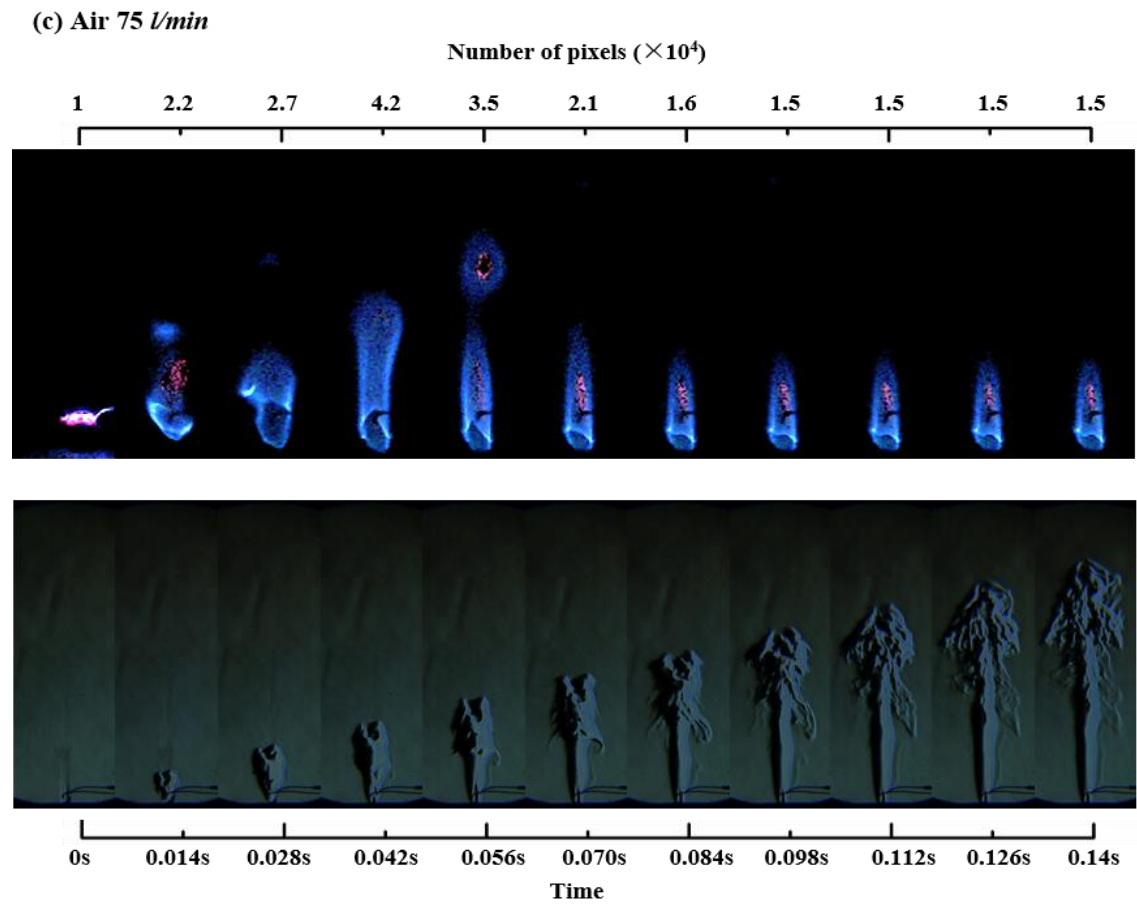


Fig. 7. 4 The schlieren and the enhanced image sequences of the ignition processes in the (a) ‘Pure methane’, (b) ‘Air 14’ and (c) ‘Air 75’ with the corresponding number of pixels.

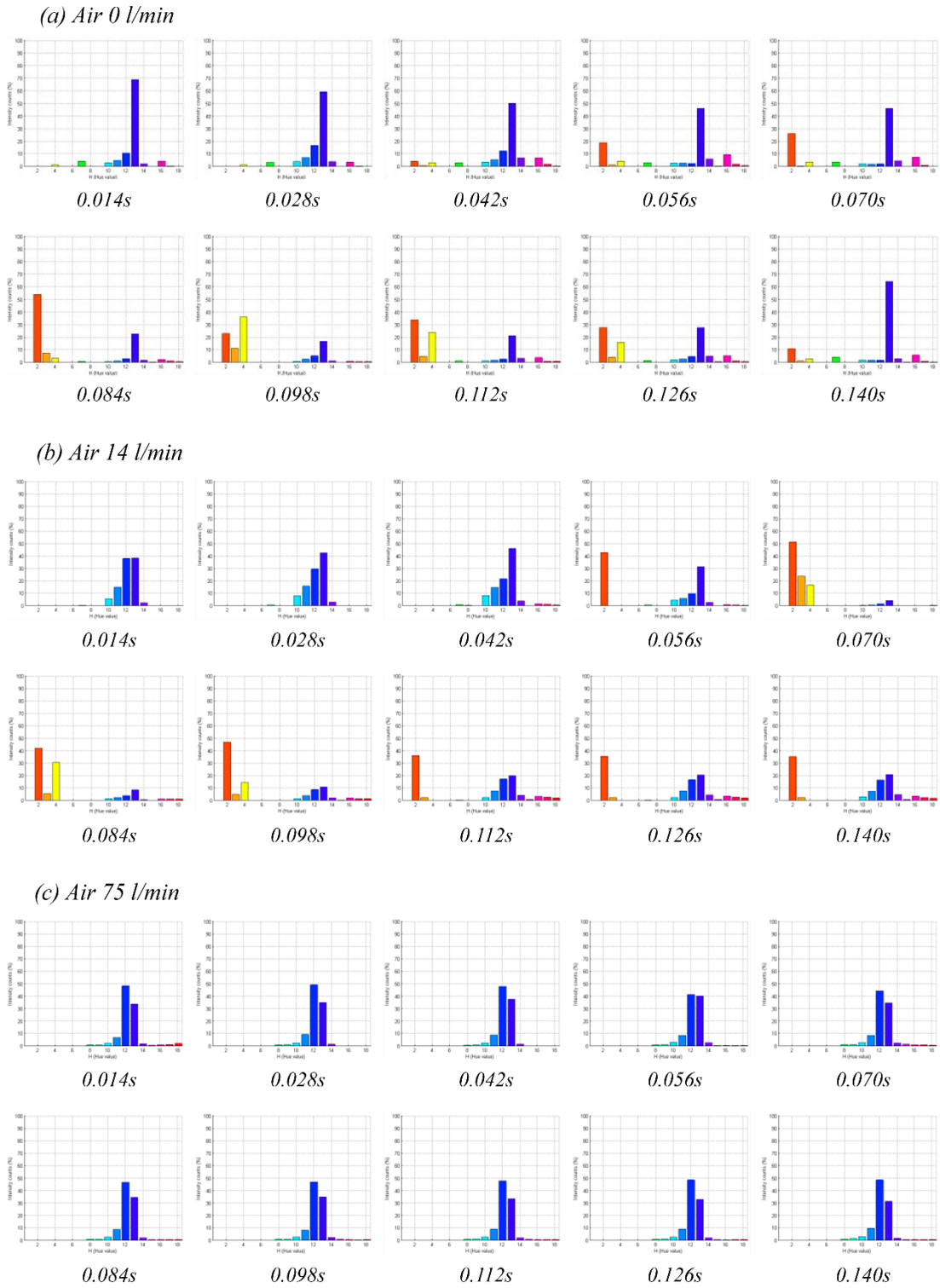


Fig. 7. 5 Histograms of the flame colour distribution evolution in the hue domain during the ignition processes of the (a) ‘Pure methane’, (b) ‘Air 14’ and (c) ‘Air 75’ cases.

7.3.2 Colour images analysis

As shown in Fig. 7. 4 (a) for the ‘Pure methane’ case, a blue flame with a bright tip stretched and propagated in the jet axial direction at the early stage of ignition. At 0.032s, infrared soot precursor can be observed inside the blue flame primarily located around the electrodes and near the tip of the flame. In the meantime, a soot-radiation-induced orange flame forms inside the infrared flame pocket. The orange flame region rapidly grows and dominates most of the area inside the blue premixed flame. It changes colour from weak orange to bright yellow indicating that the temperature is increasing. Meanwhile, the infrared emission region becomes a thin layer between the blue and orange emission regions. The bright blue flame tip then gradually separates from the primary structure of the flame. At 0.078s, a sooty orange flame with an outer layer of infrared emission emerges from the broken blue flame pocket. Subsequently, flame necking occurs due to buoyancy. The soot which is concentrated in the upper section of the flame emerges from the primary structure and propagates upwards, then gradually burns out. Finally, a cone-shaped flame stabilised on the nozzle exit can be observed 0.114s after ignition. This short stable flame is formed with a blue bottom and yellow top with soot, with infrared emission only being observed in between.

When 14 l/min of co-flow air is introduced, a tulip flame was formed at the beginning of the ignition process as shown in Fig. 7. 4 (b). The phenomenon is similar to the ‘Pure methane’ case. However, the initial blue flame region is narrower and the infrared emission only forms near the tips of the electrodes. For a co-flow air of 75 l/min, the orange sooty flame region is not observable, as shown in Fig. 7. 4 (c); only the blue flame with a little-infrared emission is observed. A blue flame forms first, and then the infrared emission occurs 0.006 s after ignition. At 0.018 s, the infrared emission disappears and then reappears at 0.048 s when the flame necking occurs. At 0.084s, the flame becomes stable with a blue appearance and a little-infrared emission inside. It is found that with an increase in co-flow rate, the tip of the final stable flame becomes sharper.

Shown in Fig. 7. 6 (a – c) are the time-dependent number of pixels of the soot-induced orange flame, infrared soot precursor and the chemiluminescence-induced blue flame for the pure methane and co-flow flames of increasing flow respectively. The trends

for ‘Pure methane’ and ‘Air 14’ are similar. At the early stages, as co-flow is introduced, the number of chemiluminescent pixels decreases, since the flame length decreases and soot formation occurs sooner. The flame also takes less time to reach a steady state when increasing the co-flow air velocity. Moreover, the peak values of orange flame and infrared emission become smaller as the co-flow air increases, which indicates that the co-flow air enhances the air/fuel mixing and reduces the quantity of soot formation.

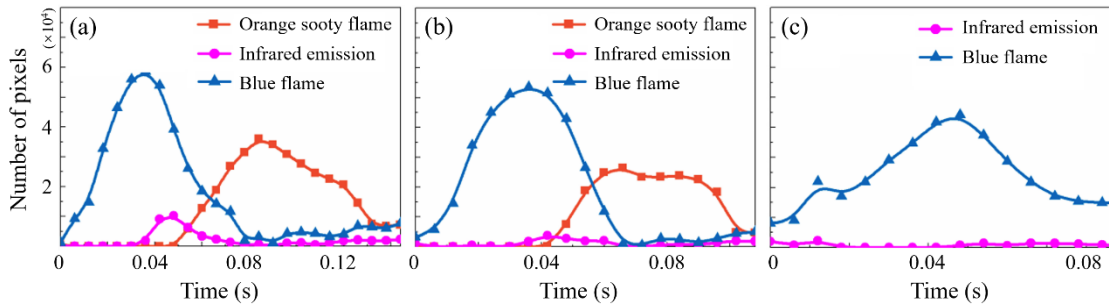


Fig. 7. 6 The time-dependent number of pixels of the soot-induced orange flame, infrared soot precursor and the chemiluminescence-induced blue flame of the (a)-(c) ‘Pure methane’, ‘Air 14’ and ‘Air 75’ flames respectively.

Shown in Fig. 7. 7 (a) and (b) are the time-dependent mean intensities of the soot-induced orange flame and the infrared soot precursor regions. The mean intensity is the ratio of total pixel intensity over the total number of pixels for each region. For a single image, some pixels may have the same hue value but different intensity. Combined with the flame colour division in the hue domain, the mean intensity is used to describe an average pixel brightness of the specified flame region (e.g. soot-induced orange flame region). The intensity of soot-radiation reflects the flame temperature. In Fig. 7. 7 (a) the intensity of the ‘Pure methane’ flame can be seen to initially increase which indicates a significant rise in temperature. After that, the intensity drops when the high-temperature soot which is concentrated in the upper section of the flame, emerges from the base of the flame and then burns out. The curve of the ‘Air 14’ flame shows a similar trend but the intensity is weaker. The mean intensities of infrared emission reduce with an increase in air flow rate when the flame reaches a steady state, as shown in Fig. 7. 7 (b).

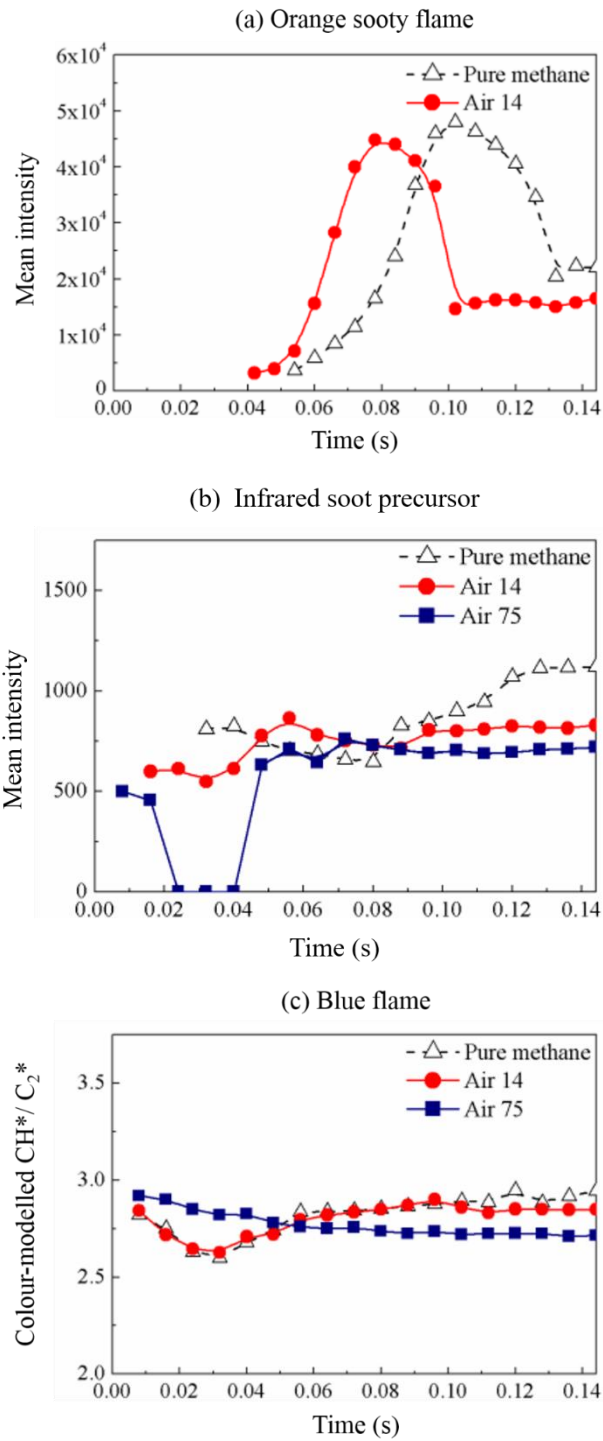
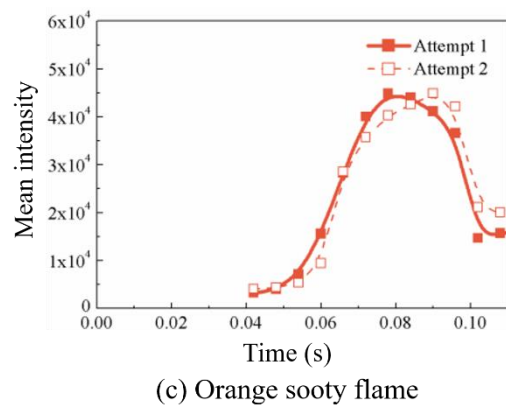
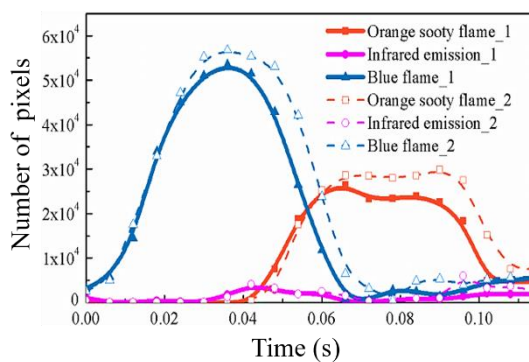
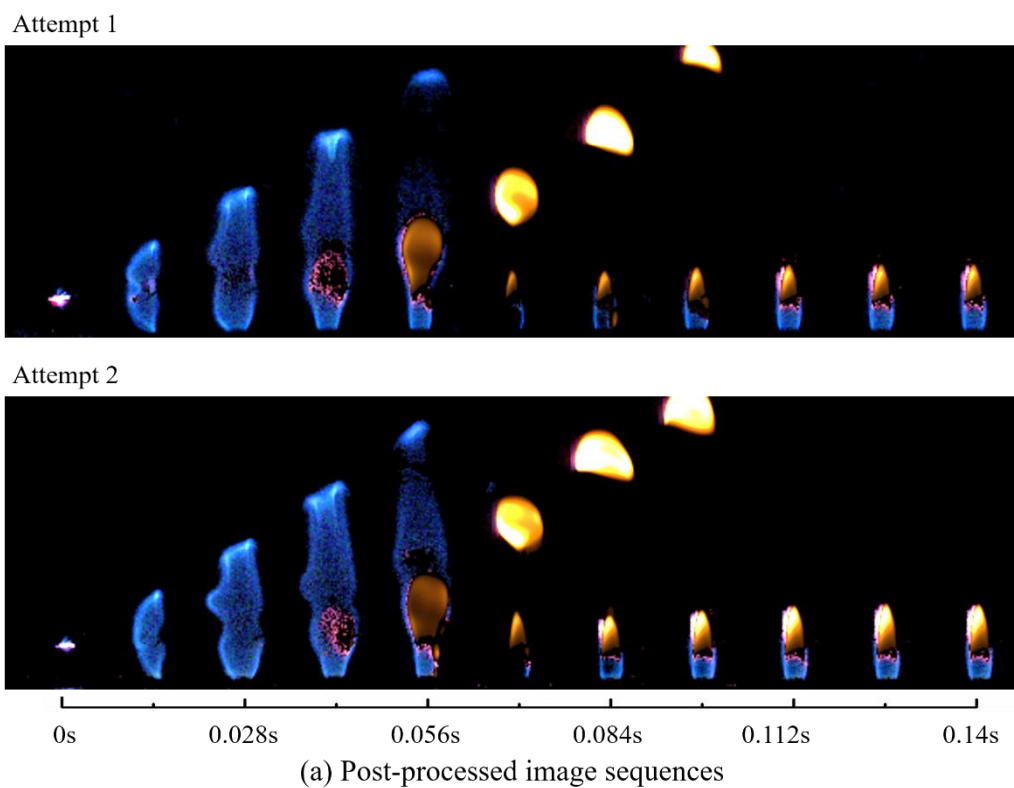


Fig. 7. 7 The time-dependent mean intensities of the (a) Soot-induced orange flame and (b) Infrared emission regions and (c) Colour-modelled CH^*/C_2^* ratios of the chemiluminescence-induced blue flame.

Fig. 7. 7 (c) shows the time-dependent colour-modelled CH^*/C_2^* ratio, which can be used to indicate the global air/fuel mixture condition and the equivalence ratio of the blue flame region. In the Fig. 7. 7 (c), the curves of ‘Pure methane’ and ‘Air 14’

initially decrease, which indicates the ignition condition moves towards fuel rich condition. The curves then increase due to further mixing with the air. The curve of ‘Air 75’ is nearly flat, indicating that the fuel and air mixing state is fairly constant. In the beginning, the curve of ‘Air 75’ is higher than the others which indicating a leaner local burn. The initial lower infrared emission and no orange coloured sooty flame for ‘Air 75’ in Fig. 7. 7 (b) and (a) respectively also support this.

Fig. 7. 8 shows the comparisons of ‘Air 14’ repeat test results, which demonstrates reasonable repeatability of the tests. Similar reproducibility was observed for other attempts.



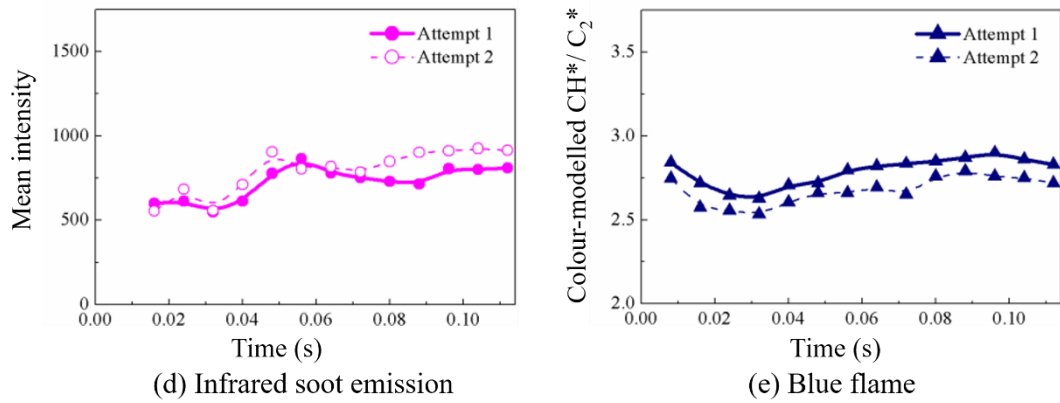


Fig. 7. 8 Comparisons of repeated attempts for the 'Air 14' flame: (a) Enhanced images, (b) Number of pixels, (c) and (d) Mean intensity of the soot and infrared emission respectively and (e) Measured CH^*/C_2^* .

7.3.3 Schlieren image analysis

The cold fuel flow pattern can be visualised through high-speed schlieren imaging before ignition at different air co-flow velocities, as shown in Fig. 7. 9. The cold flow patterns of the 'Pure methane' and 'Air 14' cases show the laminar fuel jet structure; while the 'Air 75' shows a vortex shedding structure. The differences in cold flow pattern may influence the ignition process.

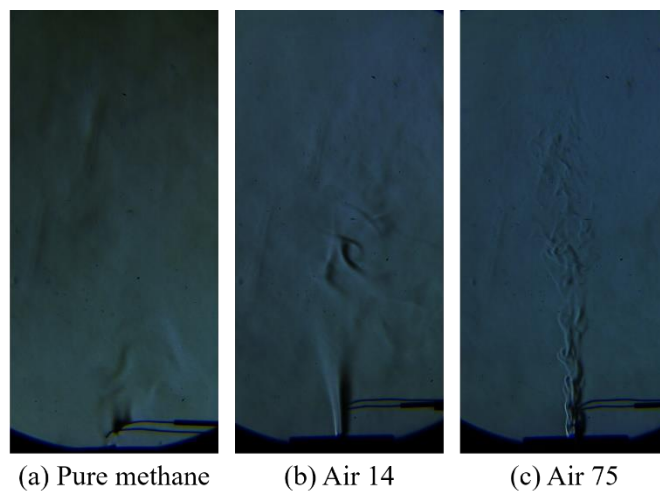


Fig. 7. 9 The cold fuel flow patterns at different co-flow air flow rates

The hot gas evolution in the ignition process is shown in Fig. 7. 4. It is worth pointing out that the hot gas volume generated by flame is much larger and higher than the visible flame. Two typical structures can be recognised at the early stages of ignition: a hot gas bulge at the upper part, due to excessive fuel accumulation, and a laminar

central jet, which develops from the nozzle exit. Even the corresponding cold jet is turbulent, as indicated in Fig. 7. 10. The tip (upper boundary) and bottom (middle boundary) positions of the bulge, shown in Fig. 7. 10 (a), were tracked for the different co-flow cases, as plotted in Fig. 7. 10 (b) and (c), respectively. It can be seen that with an increase in air flow rate, both the tip and bottom bulge velocity increase accordingly but not in a linear form. This is a result of both the buoyancy and co-flow effect.

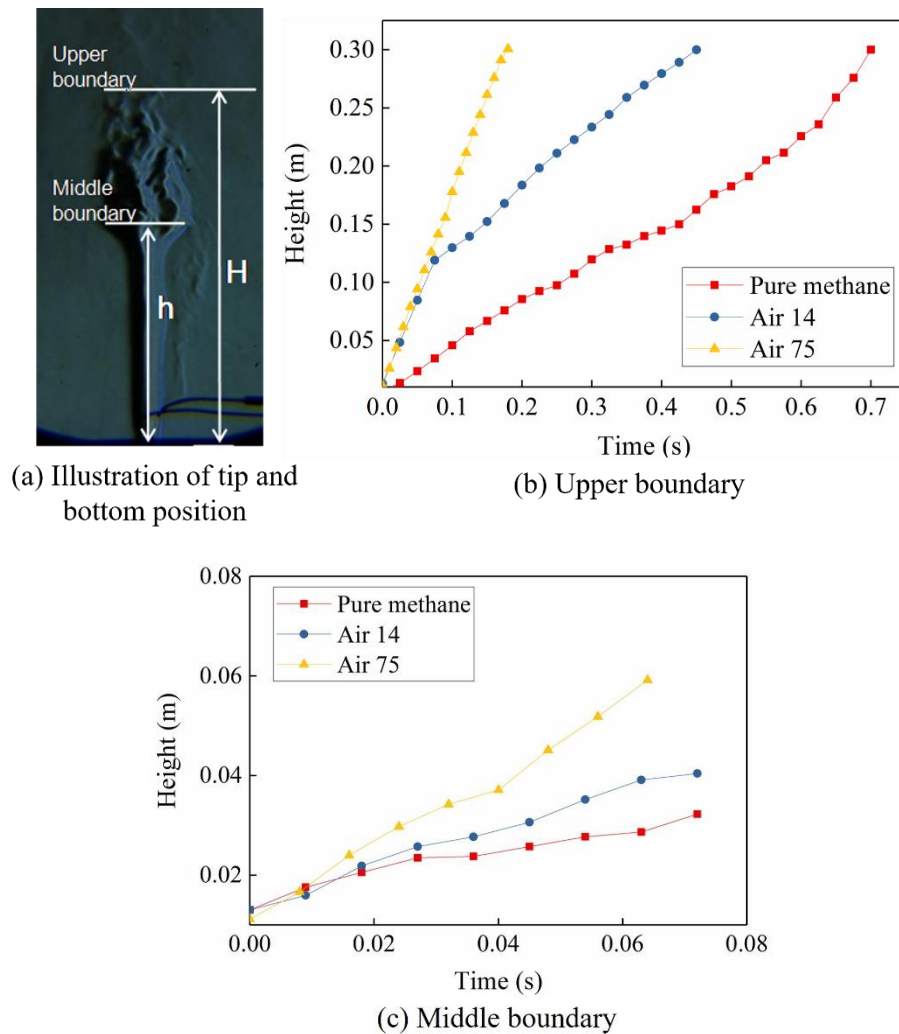


Fig. 7. 10 (a) Illustration of the tip and bottom positions, (b) the tip position tracing with time and (c) the bottom position tracing with time at different air flow rates.

The repeatability of the experiments was verified by measuring the hot gas movement on the schlieren images. The mean relative tolerance based on the flame propagation measurement is less than 5 %, which indicates that the experiments are reasonably repeatable.

7.4 Summary

The co-flow effect on the ignition process of laminar methane diffusion flames has been investigated using high-speed schlieren and colour imaging techniques. With the help of the selective digital image enhancement techniques, the simultaneous visualisation and investigation of flame emission from the visible to a limited portion of infrared spectrum in a single image has been performed. The results demonstrate that there exists infrared soot precursor between the flame front chemiluminescence and the orange soot emission. When the flow rate of the co-flow air was increased, the formation of infrared soot precursor and orange sooty flame occurred earlier in the ignition process. Furthermore, the increase of flow rate of co-flow air affected the variation of the fuel and air mixture state in the ignition process. The research has demonstrated that direct high-speed imaging and visualisation can be misleading due to the large disparity in signal strength from the flame light emission. Much more physical insights can be gained into the combustion process if a modern high-speed colour camera is combined with the innovative image processing technique.

The penetrating process of the hot gas generated by the flame has been visualised by high-speed schlieren imaging. A hot gas bulge is formed due to the fuel accumulation before ignition. It was found that both the hot gas bulge and laminar pattern move upwards faster with an increase in co-flow air velocity. The nonlinear increasing trend may be due to the complex interactions between the hot gas buoyancy, the burning velocity and the velocity gradient between the co-flow air and hot gas.

Chapter 8

3D Flame Reconstruction and Flame Velocity Measurement

8.1. Background of the Stereo Imaging Technique

The PIV method non-intrusively measures the experimental flame velocity. Besides this, much research has applied schlieren imaging to measure the flame speed by tracking the flame front propagation. However, the obtained velocity is based on two-dimensional calculations. These techniques have limitation for flames which with complex 3D flame-flow interactions and out-of-plane propagation, such as impinging and swirl flames (Ebi and Clemens, 2016). Therefore, the three-dimensional flame velocity measurement is highly desired.

Recently, some techniques have been able to obtain three-dimensional flame information in reacting flows, such as multiple light sheets (Pick and Lehmann, 2009), a scanning light sheet (Santi, 2011) and computed tomography (CT). Hossain *et al.* (Hossain *et al.*, 2013) implemented the 3D reconstruction of flame temperature and emissivity by using tomographic and two-colour methods. However, the techniques remain challenging to implement, and the experimental procedures are complicated. For tomography, several simultaneous views and eight CCD cameras were required to gain the instantaneous flame surface (Tokarev *et al.*, 2015). The high cost of the equipment also hinders its application. Stereo imaging is a considerable flame 3D reconstruction method. Only a camera and stereo adapter are required for the experiment, which is easier to operate and more economical. A previous study has successfully reconstructed impinging flames (Wang *et al.*, 2013). With the help of the image processing technique, the 3D flame chemiluminescence blue region and the soot emission region can be reconstructed separately.

8.2 Stereo Imaging Procedure

Only a single camera and a stereo adapter are required, rather than a two-camera system, for the flame stereo imaging. A stereo adaptor with two inner mirrors and two outer mirrors is applied to the standard high-speed camera to give a stereo camera system. The dimensions of the adapter are given in Section 4.2.1. With the help of the stereo adapter, a pair of views is formed on the imaging screen with slight angle difference. The high-speed camera connected to the stereo adapter can be considered as a two-virtual-camera system.

Fig. 8. 1 (a) shows the overview of a stereo imaging procedure which has four steps. First of all, the calibration process is conducted to obtain the intrinsic and the extrinsic parameters of the two cameras. The intrinsic parameters include the focal length, the image centre and lens distortion of the cameras. The extrinsic parameters are the reference and target optical centre that are used to align the two cameras. A known pattern, typically a checkerboard is applied for calibration. The checkerboard has to be located at five angles towards the camera; depression, elevation, right, left and in parallel to the camera, as shown in Fig. 8. 1 (b). The more images that captured in the calibration process the higher the measurement accuracy.

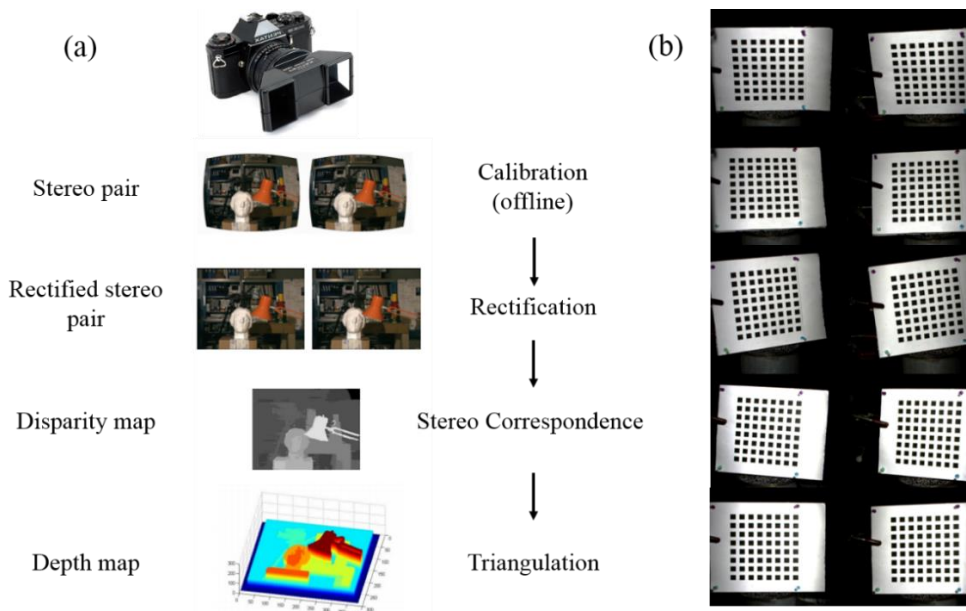


Fig. 8. 1 (a) Overview of a stereo imaging procedure (Mattoccia, 2014) and (b) Stereo images pairs imaged from the angles of depression 30° , elevation 30° , right 30° , left 30° and in parallel to the camera.

The obtained parameters from the calibration are applied to the rectification step to remove the lens distortions and convert the stereo pair to the standard form. Shown in Fig. 8. 2, the cameras are aligned with the same focal length. The rectification leads to pairs of conjugate epipolar lines becoming collinear and parallel to the horizontal axis (top to bottom pictures respectively). The epipolar constraint aims to find matching points in a stereo image pair. The search for corresponding points is reduced from the 2D domain to 1D and the disparity between the stereo image pair is restricted to the x-direction only, which simplifies the correspondence searching.

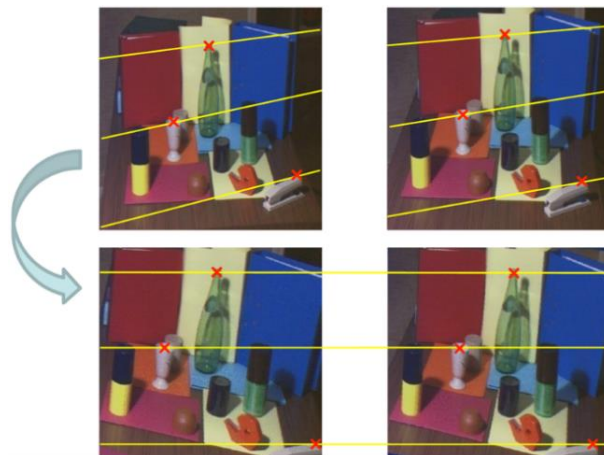


Fig. 8. 2 The schematic of the rectification process. The stereo imaging is rectified to the standard form (Mattoccia, 2013).

According to the disparity map, the baseline and the focal length, the depth of each point is computed via triangulation. The 3D coordinate of each point is obtained, as shown in the Fig. 8. 3.

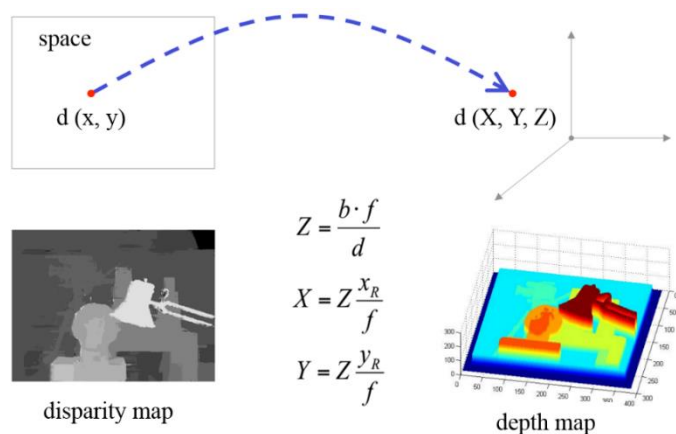


Fig. 8. 3 3D coordinate measurement via triangulation (Tombari *et al.*, 2008).

8.2 3D Reconstruction of Flame

The 3D reconstruction of a pool fire is presented. A pool fire is composed of 15 kW ethylene-air buoyant turbulent flames surrounded by 21 % oxygen concentration. The checkerboard is an arrangement of 64 black squares with 1 cm sides and 0.76 cm gaps. The calibration board is placed at five angles towards the camera, which are angles of depression 30° , elevation 30° , right 30° , left 30° and in parallel to the camera. Fig. 8. 4 (a) shows the five calibrating locations based on the left view.

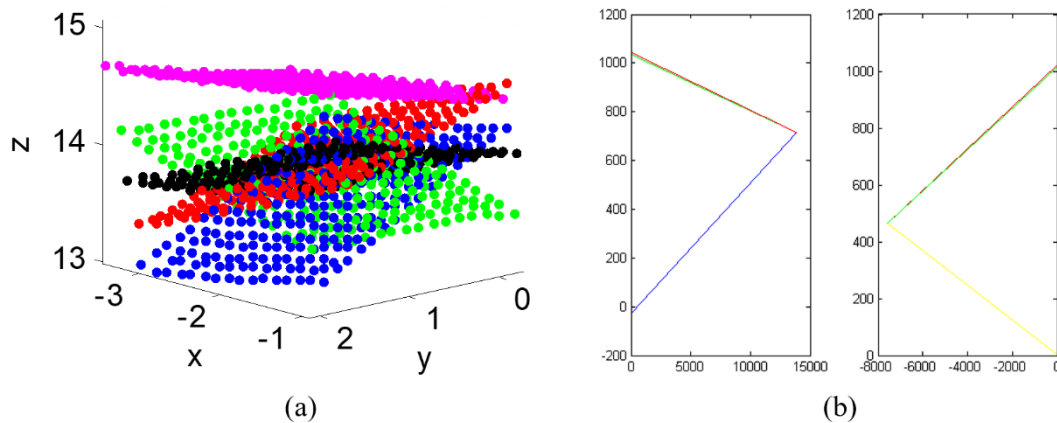


Fig. 8. 4 (a) The five calibrating locations based on the left view of the stereo imaging and (b) The epipolar between the left and right views.

The algorithms of the epipolar constraint and triangulation are encoded into the programme. Finally, the flames are reconstructed in 3D according to the 3D coordinate of each point, as shown in Fig. 8. 5. The time-dependent 3D flame evolution is shown in Fig. 8. 6 (c). The flame images were taken at a frame rate of 500 fps and 1/500 s shutter speed. Since the flame is relatively thin, its movement in the Z-axis is small. In Fig. 8. 6 (b), the blue circled regions (in Fig. 8. 5) are zoomed in to present the precise 3D structures.

The main drawback of this technique is that the 3D flame structure shows only the front layer. The technique is based on 2D imaging. The flame core and the back-view details are lost during the 3D reconstruction. In other words, the front view of the flame will cover the other flame sheet behind. In the future, two cameras with adaptors can be used for a front and back views imaging, which may optimise the results.

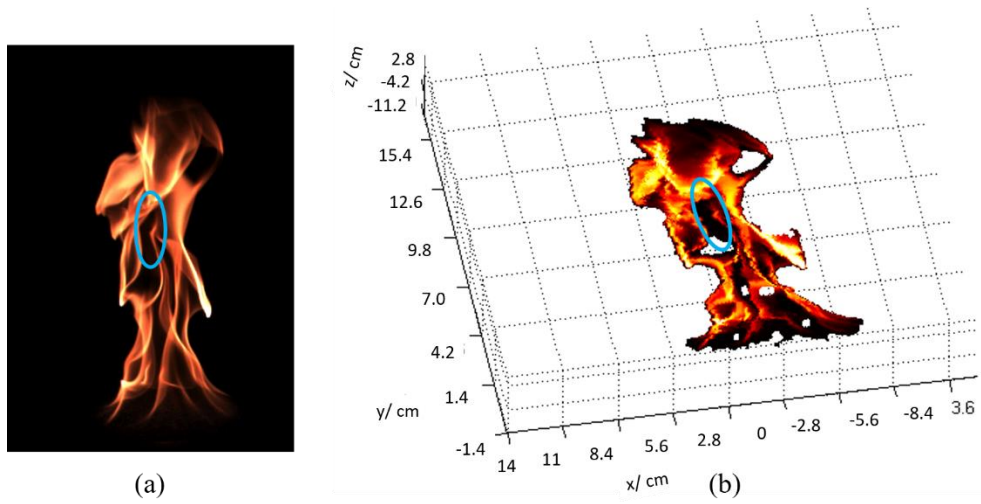
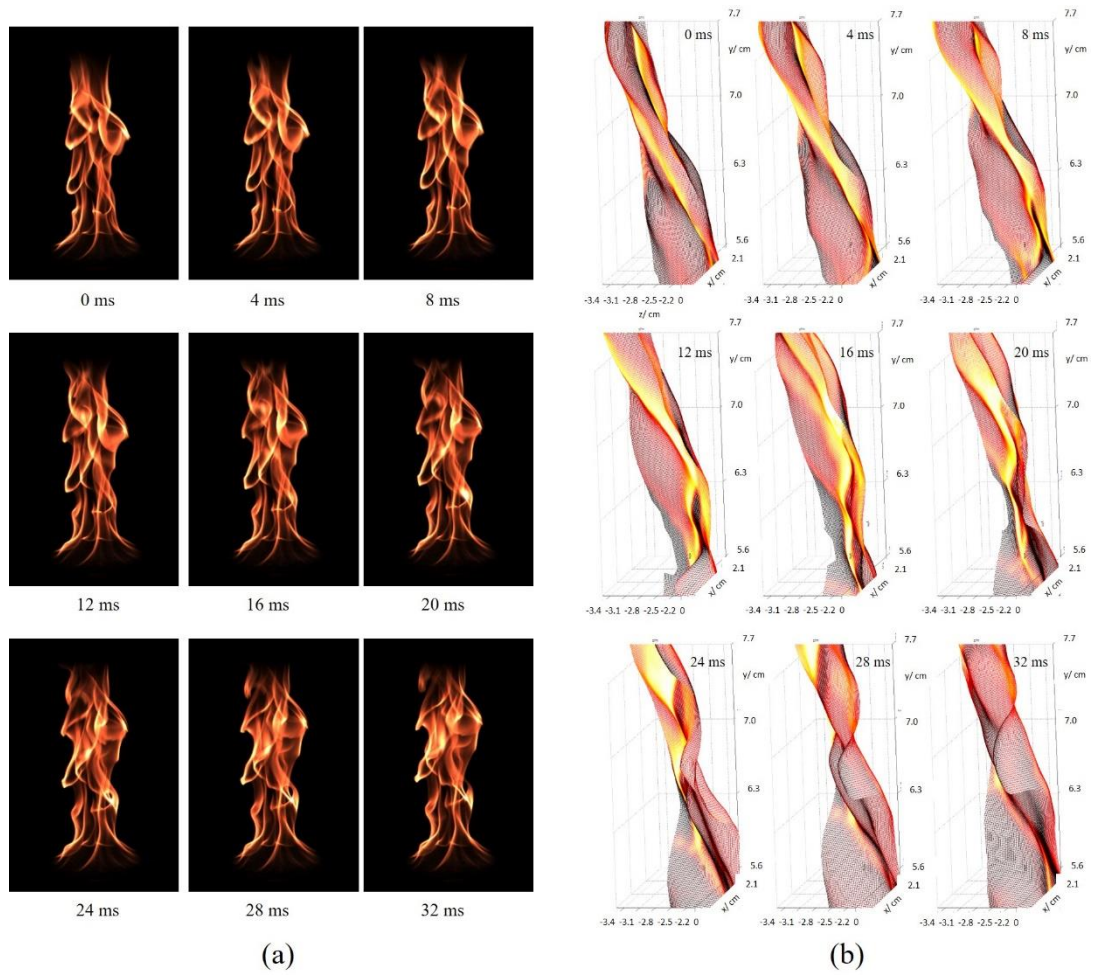


Fig. 8. 5 (a) The captured pool fire image and its corresponding (b) flame 3D reconstruction result. The blue circle marks the magnified region in Fig. 8.6.



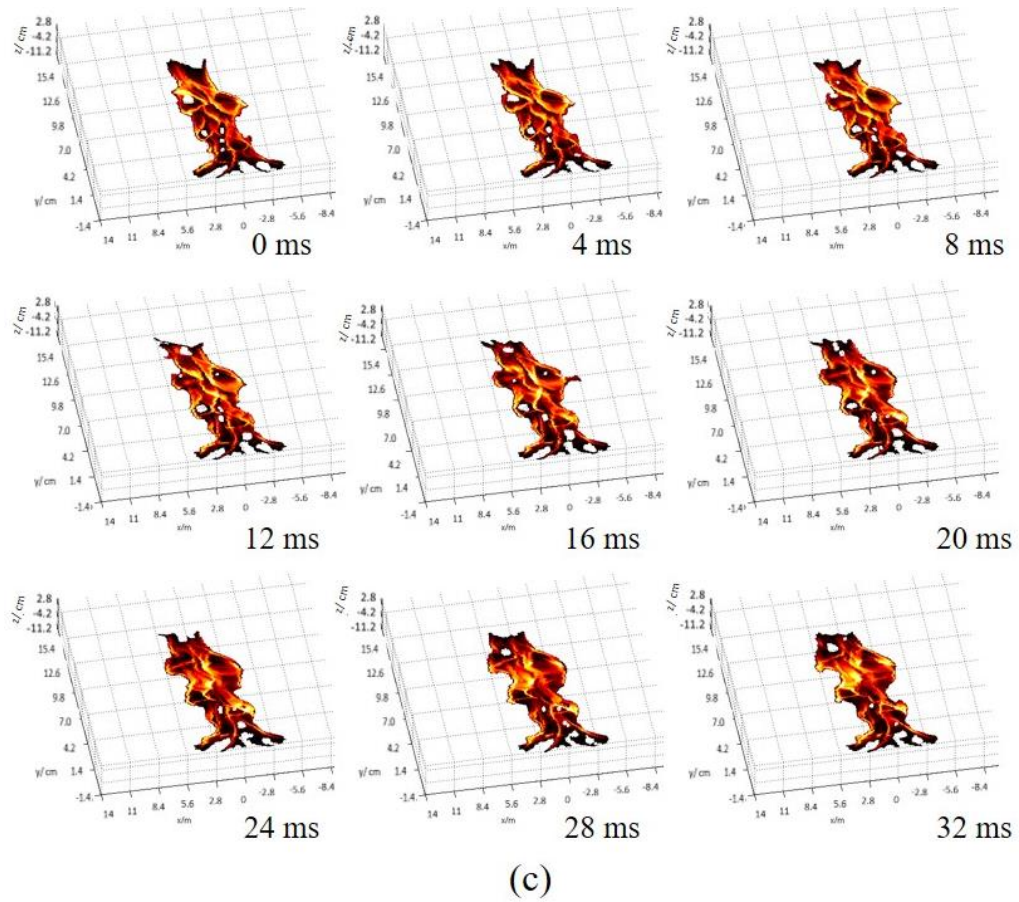


Fig. 8. 6 (a) The time-dependent flame image sequence, (b) The 3D structure magnification of the blue circled region in Fig. 8.5 and (c) The time-dependent 3D flame structures.

The 3D reconstruction has a good accuracy. The dimension of the burner (Fig. 8. 7) was measured as 15.15 cm in diameter from the reconstruction result. The real dimension of the burner is 15.24 cm.

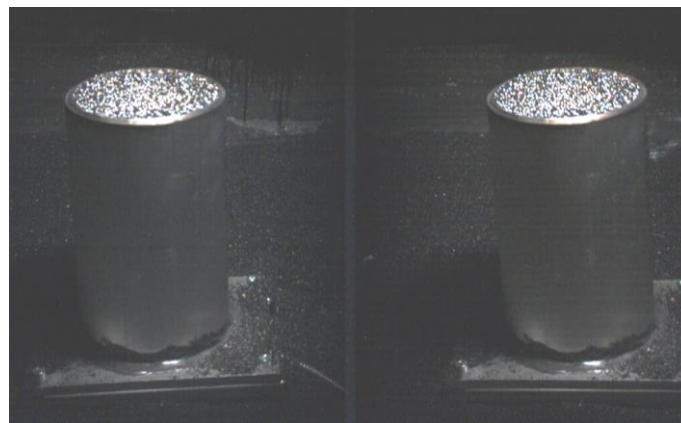


Fig. 8. 7 The stereo image pair of the burner, enhanced 20 times.

8.3 Flame Velocity Measurement

The 3D measurement of flame velocity is rarely studied. The experimental flame velocity is highly desirable for comparison with Large Eddy Simulation (LES) results. To solve this problem, the corresponding points between the adjacent frames need to be determined at first. Once the 2D matching points are determined, the 3D correspondence can therefore be gained via their 2D mapping. This is because the 3D flame reconstruction profile is a single layer on the x-y mesh grid with depth (z), which means that each (x, y) coordinate corresponds to only one z value. The velocity of the target point movement is the ratio of the distance between the corresponding points over the time interval (frame rate) between two frames. In this sooty flame study, the measured velocity can be defined as the soot absolute propagation velocity in the space. It is found that the 2D pixel correspondence is the most prominent challenge. Two different methods are applied to search for the matching points.

8.3.1 Pixel intensity threshold and geometry

The first method aims to track the movement of the brighter regions. A certain pixel intensity threshold is applied to the images, which filters out several brighter regions. A small window is defined as a local area, which further confirms the target region, as shown in Fig. 8. 8. Since the bright target region is an area that is composed of many pixels, the centre or edge pixel of the target region in each frame is used as a reference.

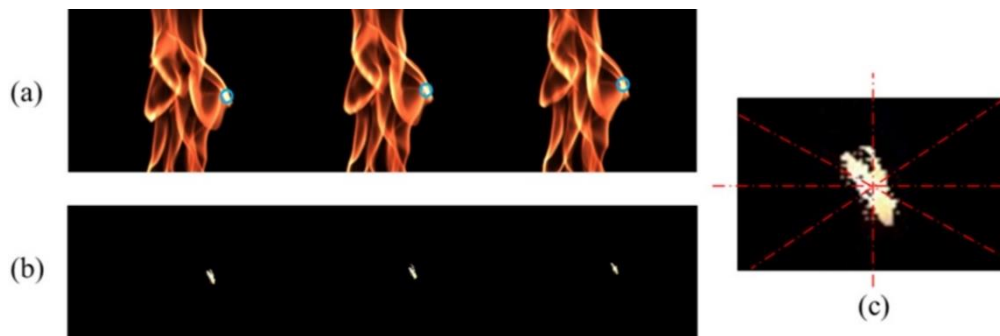
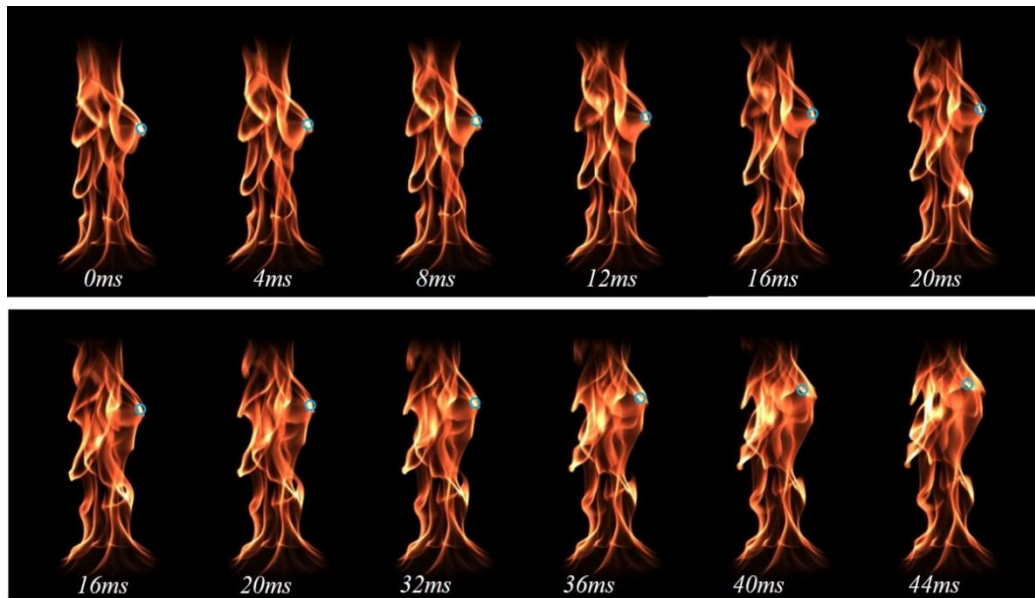


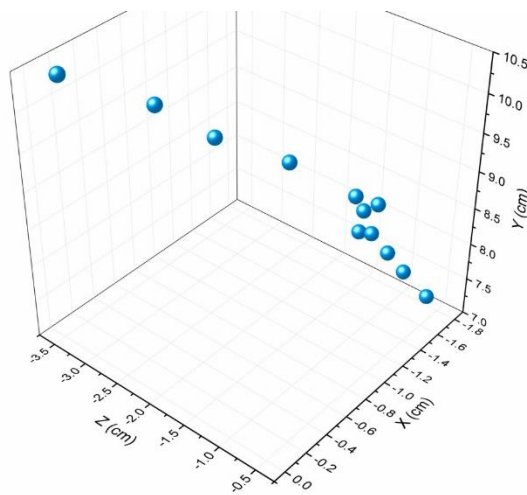
Fig. 8. 8 The target region (b) is filtered from the local area marked in (a). (c) The centre of the target region.

The velocity of four target points in a short time span is measured and shown in Fig. 8. 9 to Fig. 8. 12, respectively. It is difficult to measure the velocity evolution over a long-time span since the brighter region enlarges very quickly. Besides, the overlap of

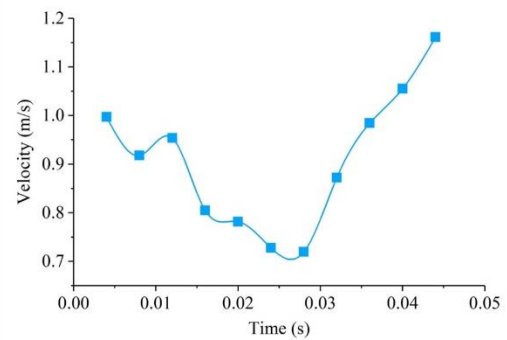
the flame sheets will mislead the target region tracking. In Fig. 8. 9 (b), the movement of the centre point of the blue circled region is plotted in 3D space. The instantaneous soot absolute propagation speed decreases first and then increases in the range of 0.7m/s to 1.2m/s.



(a)



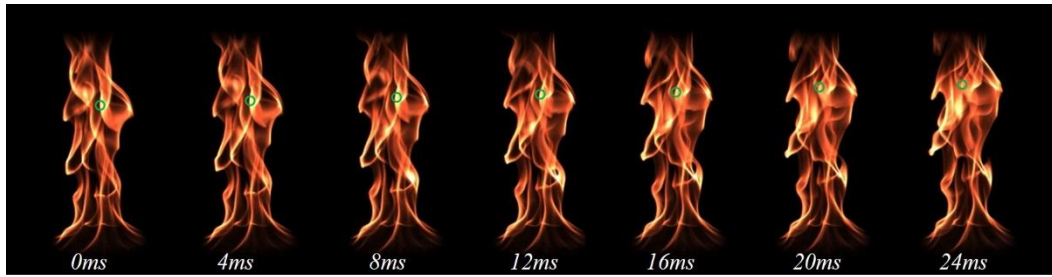
(b)



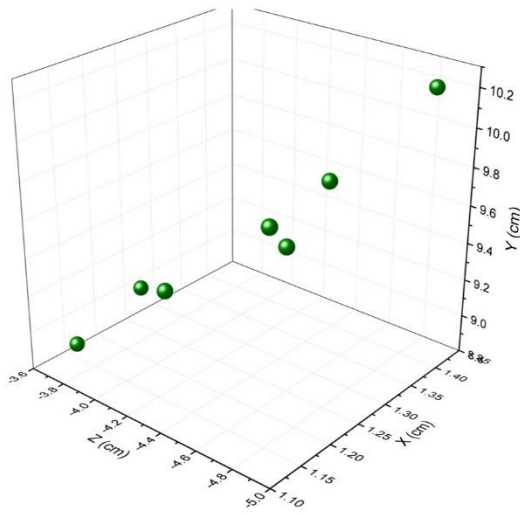
(c)

Fig. 8. 9 (a) The path of the target region (blue circle), (b) The 3D movement of the target region and (c) The time-dependent velocity development of the target region.

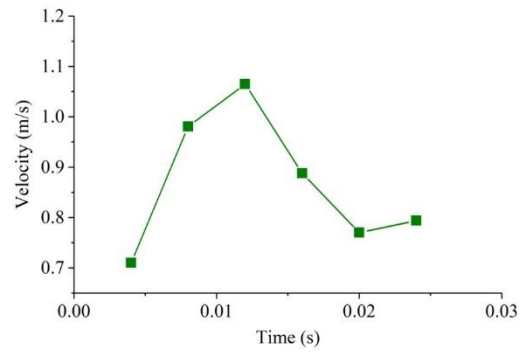
In Fig. 8. 10, the target region marked by the green circle is nearly at the same height as the region in Fig. 8. 9, but closer to the centreline of the fuel jet. The velocity varies in the range of 0.7 m/s to 1.2 m/s, which is similar to the target region in Fig. 8. 9.



(a)



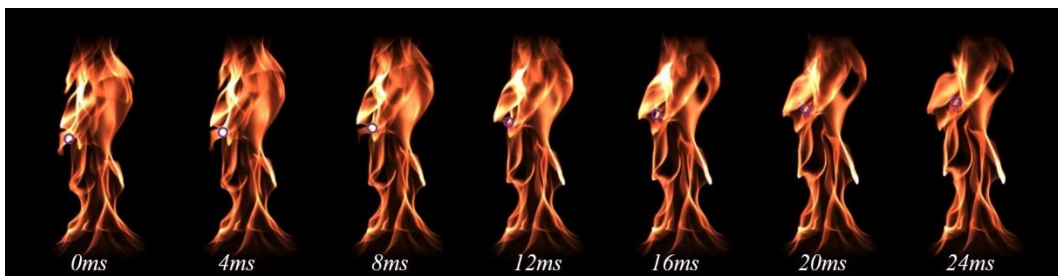
(b)



(c)

Fig. 8. 10 (a) The path of the target region (green circle), (b) The 3D movement of the target region and (c) The time-dependent velocity development of the target region.

The region marked by the purple circle in Fig. 8. 11 is located at a lower position in the flame. It propagates from the edge of the centreline with the decrease movement speed. Its propagation speed is higher than the last two regions; ranging from 1.6 m/s to 2.6 m/s. The region marked by a yellow circle in Fig. 8. 12 is located at the lowest position compared to the other regions previously mentioned; the tip of the flame sheet is tracked. Fig. 8. 12 (c) shows that the velocity is nearly constant around 1.2 m/s.



(a)

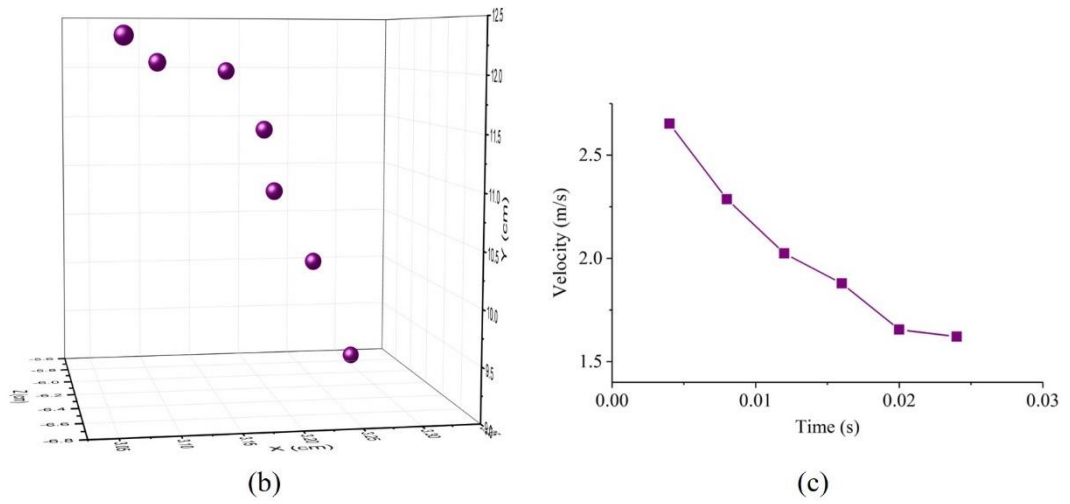


Fig. 8. 11 (a) The path of the target region (purple circle), (b) The 3D movement of the target region, and (c) The time-dependent velocity development of the target region.

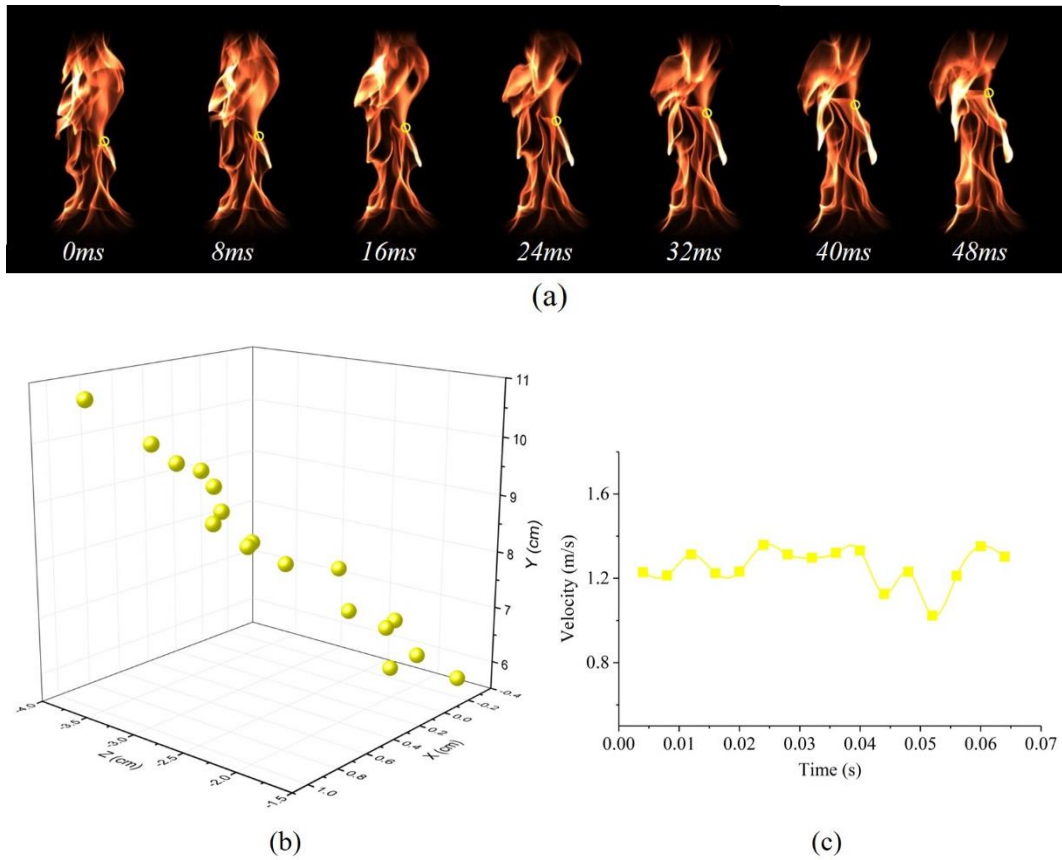


Fig. 8. 12 (a) The path of the target region (yellow circle), (b) The 3D movement of the target region and (c) The time-dependent velocity development of the target region.

However, only the 3D propagation velocity of regions with high pixel intensity can be tracked via this method. The velocities of other interesting regions are still unknown.

Therefore, an optimised algorithm is applied to identify the corresponding pixels between two sequential frames.

8.3.2 Optical flow estimation: Lucas-Kanade method

Optical flow is defined as the apparent motion of pixels in an image between two sequential frames caused by the movement of an object. It presents as a 2D vector field. Vectors represent the displacement of each pixel between two consecutive frames. The optical flow estimation assumes that the object does not have a significant displacement between two frames and that the images depict a natural scene containing textured objects exhibiting shades of grey (different intensity levels) which change smoothly. The high-speed flame image sequences just satisfy these two assumptions. An example optical flow sequence of the flame images is shown in Fig. 8. 13. The time-dependent vector field evolution is presented in Fig. 8. 14.

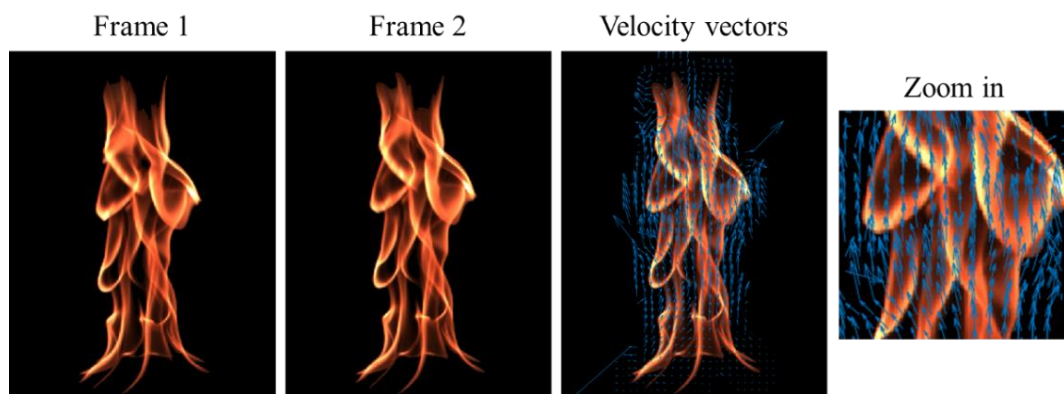


Fig. 8. 13 The optical flow of two sequential frames. The vector scales were enhanced 30 times.

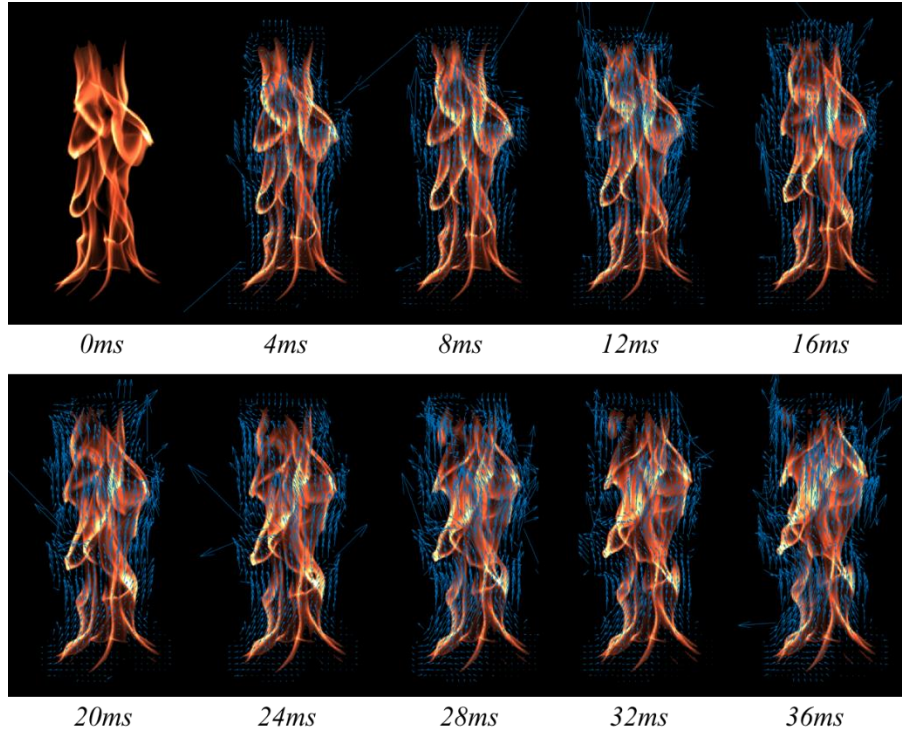


Fig. 8. 14 The time-dependent vector field evolution of the flame images. The vector scales were enhanced 30 times.

The images are processed via the Lucas-Kanade optical flow algorithm (Bruhn, Weickert and Schnörr, 2005). The Lucas-Kanade measures the movement of each pixel in a small time increment Δt , which is based on the Taylor series of the image signal. The image constraint equation can be expressed as

$$I(x, y, t) = I(x + \delta x, y + \delta y, t + \delta t) \quad (8.1)$$

where I is the intensity of the pixel. As the displacement is quite small in Δt , the equation can be transformed to

$$I(x + \delta x, y + \delta y, t + \delta t) = I(x, y, t) + \frac{\partial I}{\partial x} \delta x + \frac{\partial I}{\partial y} \delta y + \frac{\partial I}{\partial t} \delta t + H.O.T \quad (8.2)$$

The $H.O.T$ represents the higher order, which can be ignored in the small displacement. Thus the equation is modified to

$$\frac{\partial I}{\partial x} \delta x + \frac{\partial I}{\partial y} \delta y + \frac{\partial I}{\partial t} \delta t = 0 \quad (8.3)$$

Or

$$\frac{\partial I}{\partial x} \frac{\delta x}{\delta t} + \frac{\partial I}{\partial y} \frac{\delta y}{\delta t} + \frac{\partial I}{\partial t} \frac{\delta t}{\delta t} = 0 \quad (8.4)$$

Then

$$\frac{\partial I}{\partial x} V_x + \frac{\partial I}{\partial y} V_y + \frac{\partial I}{\partial t} = 0 \quad (8.5)$$

where V_x and V_y are the x and y velocity of the optical flow respectively and $\frac{\partial I}{\partial x}$, $\frac{\partial I}{\partial y}$ and $\frac{\partial I}{\partial t}$ are the finite differences of (x, y, t) when written as I_x, I_y and I_t respectively.

Therefore

$$I_x V_x + I_y V_y = -I_t \quad (8.6)$$

Eq. 8.6 can be written as:

$$\nabla I^T \cdot \vec{V} = -I_t \quad (8.7)$$

where I^T is the transpose of I . Lucas-Kanade is used to determine \vec{V} , which assumes that the motion field is smooth, in other words, the pixels in a small region have the same \vec{V} . This yields

$$\begin{aligned} I_x(q_1) V_x + I_y(q_1) V_y &= I_t(q_1) \\ I_x(q_2) V_x + I_y(q_2) V_y &= I_t(q_2) \\ &\dots \\ I_x(q_n) V_x + I_y(q_n) V_y &= I_t(q_n) \end{aligned} \quad (8.8)$$

where $q_1, q_2, q_3 \dots$ are pixels inside the window and $I_x(q_i), I_y(q_i), I_t(q_i)$ represent the partial derivatives. The equation can be transformed to

$$Av = b \quad (8.9)$$

where

$$A = \begin{bmatrix} I_x(q_1) & I_y(q_1) \\ I_x(q_2) & I_y(q_2) \\ I_x(q_3) & I_y(q_3) \\ \vdots & \vdots \\ I_x(q_n) & I_y(q_n) \end{bmatrix} \quad v = \begin{bmatrix} v_x \\ v_y \end{bmatrix} \quad b = \begin{bmatrix} -I_t(q_1) \\ -I_t(q_2) \\ -I_t(q_3) \\ \vdots \\ -I_t(q_n) \end{bmatrix}$$

The optical flow method aims to get the smallest $\|Av - b\|$. The least squares principle is used to solve the over-determined equations. Then

$$A^T Av = A^T b \quad \text{or} \quad (8.10)$$

$$v = (A^T A)^{-1} A^T b \quad (8.11)$$

where A^T is the transpose of A . Then

$$\begin{bmatrix} v_x \\ v_y \end{bmatrix} = \begin{bmatrix} \sum_i I_x(q_i)^2 & \sum_i I_x(q_i) I_y(q_i) \\ \sum_i I_y(q_i) I_x(q_i) & \sum_i I_y(q_i)^2 \end{bmatrix}^{-1} \begin{bmatrix} -\sum_i I_x(q_i) I_t(q_i) \\ -\sum_i I_y(q_i) I_t(q_i) \end{bmatrix} \quad (8.12)$$

It is more logical to give more weight to the pixels that are closer to the central pixel p . Thus the equation can be written as

$$\begin{bmatrix} v_x \\ v_y \end{bmatrix} = \begin{bmatrix} \sum_i w_i I_x(q_i)^2 & \sum_i w_i I_x(q_i) I_y(q_i) \\ \sum_i w_i I_y(q_i) I_x(q_i) & \sum_i w_i I_y(q_i)^2 \end{bmatrix}^{-1} \begin{bmatrix} -\sum_i w_i I_x(q_i) I_t(q_i) \\ -\sum_i w_i I_y(q_i) I_t(q_i) \end{bmatrix} \quad (8.13)$$

The weight w_i can be determined by the Gaussian function according to the distance between q_i and the central pixel p . Finally, the vector of the pixel movement is obtained, thereby solving the correspondence problem.

The 3D coordinates can be gained from their 2D mapping. The correspondence of 3D coordinates is determined via the pixels correspondence on the 2D image, similar to the Pixel Intensity Threshold and Geometry method. This process is represented in Fig. 8. 15.

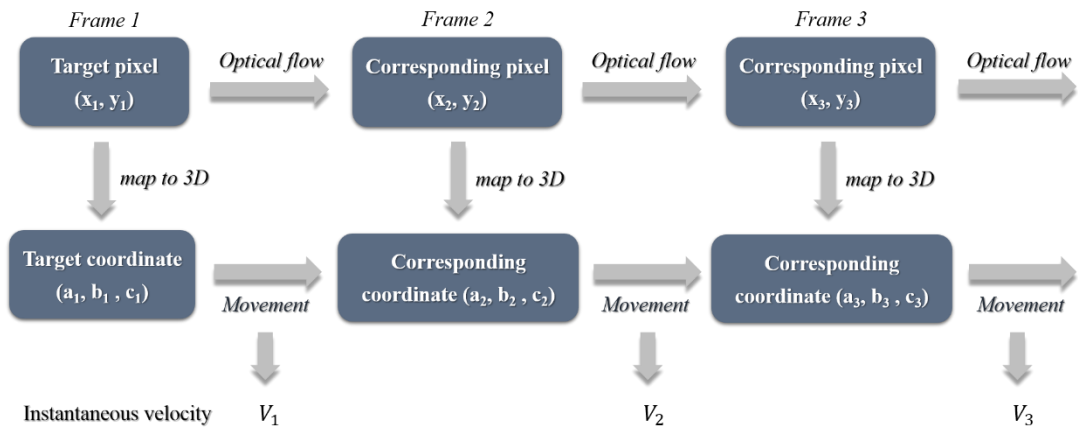


Fig. 8. 15 Schematic of the velocity measurement process.

The instantaneous velocity, V , is:

$$V = \frac{\sqrt{(a_{i+1} - a_i)^2 + (b_{i+1} - b_i)^2 + (c_{i+1} - c_i)^2}}{1/f} \quad (8.14)$$

where a_i , b_i , c_i are the coordinates in the x , y and z -axes directions and f represents the frame rate.

Fig. 8. 16 shows the time-dependent 3D velocity vector field variation. Each vector field is composed of approximately 40000 valid vectors.

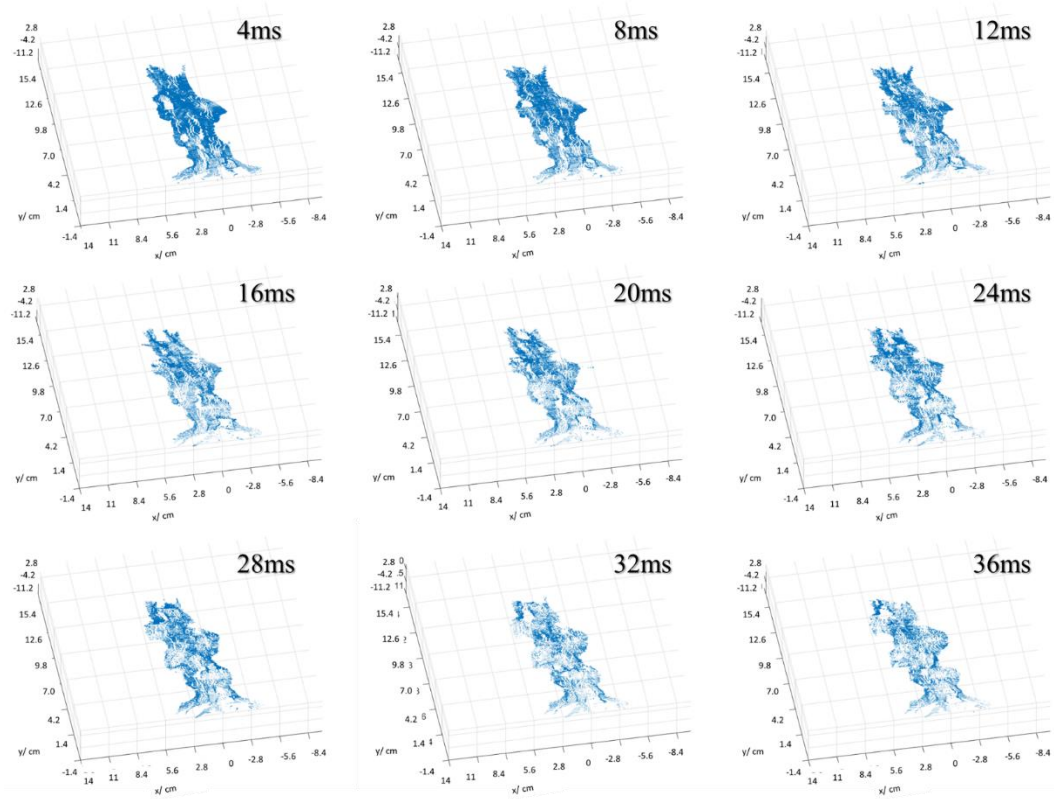


Fig. 8. 16 The time-dependent 3D velocity vector field variation.

Fig. 8. 17 shows the velocity variation in the local regions with a small window size of 45×45 . It is found in general that the soot propagates more slowly when approaching the burner or the centreline of the fuel jet.

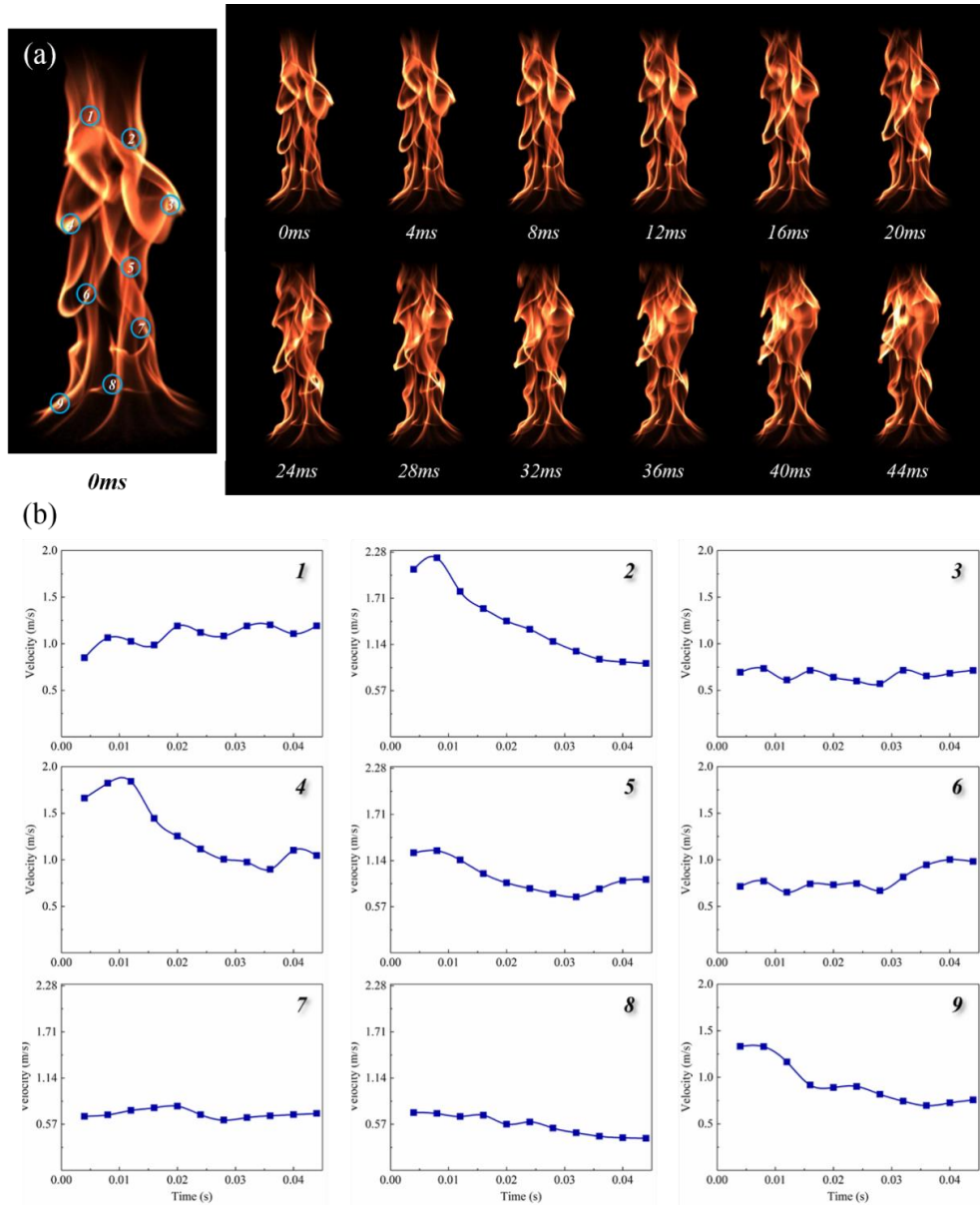


Fig. 8.17 (a) The target regions marked by the blue circles on the flame image and (b) The velocity variation in the selective regions.

The comparison of the 2D vector field between different window sizes is shown in Fig. 8.18. It is observed that the vector field is smoother with an increase in the size of the small window; the larger window size will strongly denoise the vector field. Fig. 8.19 shows the comparison of velocity measurement results with different window sizes. In Region 1, the measured velocity based on the 5×5 pixel window deviates from the others. In Region 2, the 100×100 pixel window result is different from the other curves. It is found that very large or small window sizes lead to the results largely deviating from the actual velocity. The optical flow estimation has strong robustness

with the large windows but also obscures local velocity characteristics. The small window will improve the accuracy of the measurement but leads to more much noise in the vector field. The oversized window may violate the movement consistency assumption. On the contrary, when the window is too small, the optical flow estimation is difficult to implement for the relative dramatic movement. Therefore, the size of the small window needs to be carefully determined by the image resolution, the flame propagation speed and the frame rate.

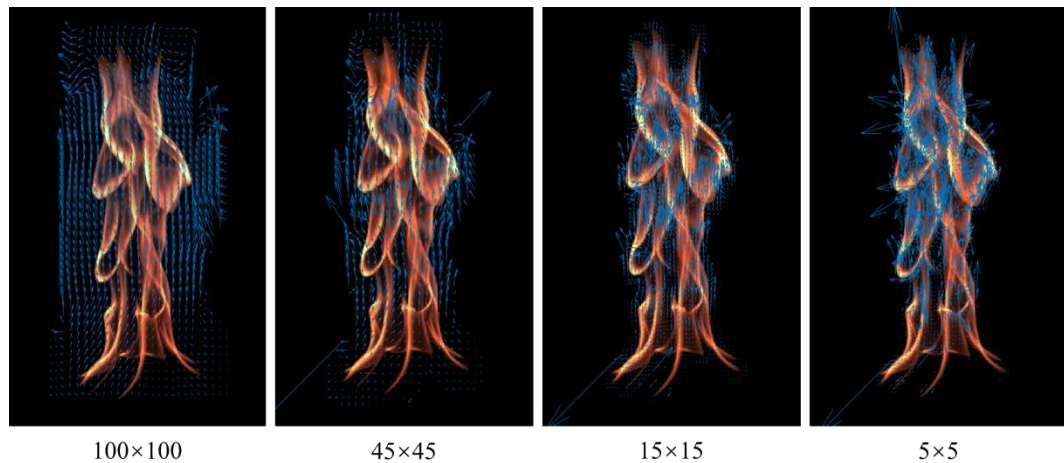


Fig. 8. 18 2D vector field based on different window sizes.

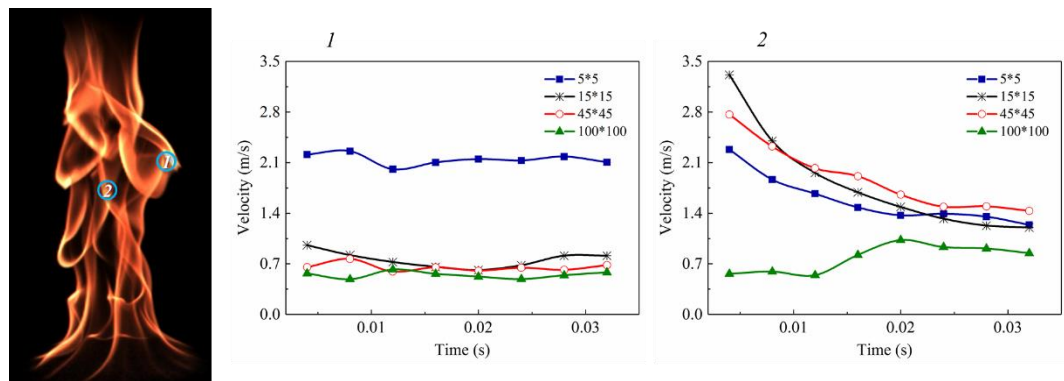


Fig. 8. 19 The velocity measurement results of local regions with different window sizes.

8.3.3 Comparison of two methods

It is found that the trend of the soot velocity variation between the two results are entirely consistent, while the range of the measured velocity in the same target region is similar. An example is shown in Fig. 8. 20. It is observed that the optical flow method provides a more reasonable result. The measured velocity is more stable than the results obtained from the pixel intensity threshold method. This is because the

algorithm of the optical flow method is more logical for solving the correspondence problem and is accurate to a sub-pixel level. Arbitrary point tracking is an advantage of the optical flow method, along with the lack in limitation of the pixel intensity.

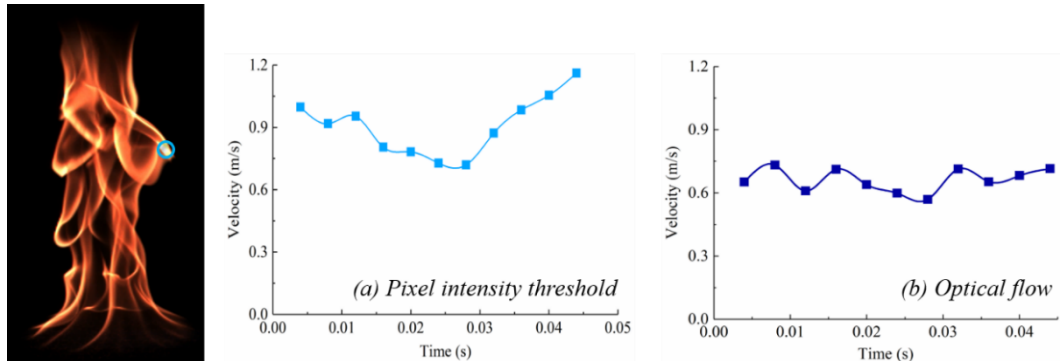


Fig. 8. 20 The soot velocity variation of the target region measured by the (a) Pixel intensity threshold and (b) Optical flow methods.

8.4 Optical Flow of a Schlieren Image Sequence

The optical flow method is also suitable for processing the high-speed schlieren image sequences, as shown in Fig. 8. 21. The vortices are well identified and tracked, therefore the calculation of flame front velocity becomes easier.

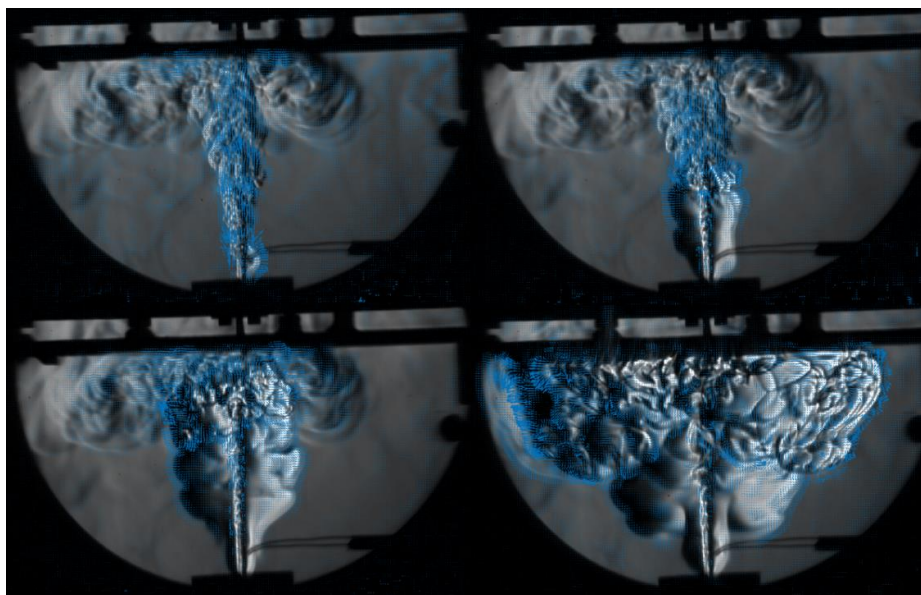


Fig. 8. 21 Schlieren images processed by the optical flow method.

8.5 Summary

In conclusion, stereo imaging is a promising method to measure the soot velocity via high-speed image sequencing. The optical flow Lucas-Kanade method is a relatively better algorithm to determine point correspondence between two sequential frames. The correspondence of the 3D coordinates can be gained from their corresponding 2D mapping, thereby determining the instantaneous soot propagation speed. The optical flow method is suitable for processing the schlieren image sequences as well. This method may also be appropriate to measure the blue flame propagation speed. Its accuracy can be determined in the future.

Chapter 9

Conclusion and Future Work

9.1 Conclusion

This research has demonstrated that direct high-speed imaging and visualisation can be misleading due to the large disparity in signal strength from the flame light emission. Much more physical insights can be gained into the combustion process if a modern high-speed colour camera is combined with innovative image processing techniques.

The main findings of this thesis regarding the development of optical flame diagnostic techniques and their applications to flame ignition and propagation studies are listed as follows:

- A pinkish coloured flame region is captured by a high-speed Photron SA4 camera. The pinkish flame region is always observed in between the chemiluminescence-induced blue flame and orange sooty flame during the ignition process of the hydrocarbon flame. Confirmatory experiments are carried out which prove that the pinkish flame region presenting on the flame image is due to infrared flame emission.
- The comparative investigation indicates that the captured infrared-emission-only region is associated with the soot precursor region because the presence of the captured infrared flame emission in co-flowing NDFs and IDFs in our experiments coincide with the region of PAH resolved in published laser experiment. The captured infrared could be either the direct infrared light emission or the selective infrared scattering from the soot precursor.
- Simultaneous visualisation and investigation of flame emission from the visible to infrared spectrum have been achieved using a single camera with the help of a unique image post-processing method. It is known that the flame light emission is closely related to the flame colour captured by a digital colour camera. In the combustion zone, the molecules/particle species emit at specific wavelengths. The lights are received by the CCD/CMOS sensor and then converted to electric

signals via an image processor, and finally shown as various colours on the digital colour image. The image post-processing method establishes relationships between the flame multiple emission species and their corresponding colour signal presences. The captured flame images are first converted from the RGB to HSV colour model space. It is determined that the orange sooty flame, blue flame and infrared flame emissions of the hydrocarbon flame are concentrated in ranges of 10 to 70 degrees, 180 to 252 degrees and 252 to 350 degrees respectively in the hue domain. Thus, the CH^* , C_2^* , soot particles and infrared soot precursor can be differentiated according to their specific hue ranges. In the meantime, the obscured CH^* , C_2^* and infrared emissions under high shutter speeds can be selectively enhanced.

- The image post-processing method mentioned above has been applied to study flame ignition and propagation. It is found that the ignition process starts with the development of a blue flame. Subsequently, the infrared soot precursor and visible yellow sooty flame simultaneously occur in co-flowing NDF, IDF and impinging flame configurations. The infrared soot precursor region and the yellow sooty flame regions in co-flowing NDFs and IDFs have an inverse spatial distribution at the steady state. In the impinging flame ignition process, when the flame strikes the cold plate, the sudden temperature drop of the flame hinders the soot formation, and also suppresses the chemical reaction, leading to wall quenching during the following few milliseconds.
- It is found that soot production is susceptible to ignition location from the stage of ignition to a stable flame condition, and so are the active chemical species, such as CH^* and C_2^* , in an impinging configuration. The largest amount of soot accumulates during the ignition process when the flame is ignited at the nozzle exit. Soot formation significantly reduces when the flame is initiated at the edge of the plate and the middle position between the nozzle and plate, with lower and higher CO_2 concentration respectively. The initial orange sooty flame always forms along the fuel jet regardless of the initiated locations. The sporadic soot emission regions always take place in the high-temperature intense reaction zone, which is slightly away from the stagnation point. When 6 l/min CH_4 is premixed

with 5 l/min CO₂ gas, both the cool central core flame and detached flame structures can be developed by varying the ignition location only. The flame with a ring-shaped structure can be formed when the CO₂ flow rate increases to 8 l/min. With an increase in CO₂, the soot emission quantity and the flame temperature gradually reduce. The wall quenching phenomenon is observed in each case due to the cool plate effect. It is also found that a hotter plate surface will shorten the time span from ignition to steady state and suppress the soot formation. The flame temperature can be evaluated using a modified two-colour method to measure glowing thin SiC fibres positioned in the flow field. For the CH₄/air premixed flame, the flame temperature increases when the equivalence ratio approaches unity.

- The co-flow effect on the ignition process of laminar methane diffusion flames has been investigated using high-speed schlieren and colour imaging techniques. When the flow rate of the co-flow air was increased, the formation of the infrared soot precursor and orange sooty flame occurred earlier in the ignition process. An increase in flow rate of co-flow air affects the variation of the fuel and air mixture state in the ignition process. The penetrating process of the hot gas generated by the flame has been visualised via high-speed schlieren images. A hot gas bulge is formed due to fuel accumulation before ignition. A laminar pattern can be observed from the nozzle exit due to the strong upward co-flow air momentum coupled with combustion. Both the hot gas bulge and laminar pattern move faster with an increase in co-flow air velocity. The nonlinear increasing trend may be due to the complex interactions among the hot gas buoyancy, the burning velocity and the velocity gradient between the co-flow air and hot gas.
- Stereo imaging can be utilised to reconstruct the flame in three dimensions. It is also a promising method to measure the 3D soot velocity. The optical flow Lucas-Kanade method is a relatively better algorithm to determine the point correspondence between two sequential frames. The correspondence of the 3D coordinates can be gained from their corresponding 2D mapping, thereby determining the instantaneous soot propagation speed.

9.2 Scope of Future Work

The scope for future work is summarised as follows:

- The optical emission spectrometer can be applied to measure hydrocarbon flame emission under fuel lean and rich conditions, in reference to the image post-processing results.
- Chapter 8 introduced a 3D velocity measurement of a pool fire via the stereo imaging technique. It could also be applied to other flame models. Since the impinging flame has a large area of out-of-plane propagation, 3D velocity measurement is therefore highly desirable.
- Multiple optical flame diagnostic techniques can be combined to investigate flame ignition and propagation. It is desirable to implement these in flame studies via simultaneous stereo imaging, schlieren imaging, two-colour temperature measurements and the image post-processing method.
- Thermal imaging of impinging flames can also be implemented and can be compared with the modified two-colour flame temperature measurement results.
- In Chapter 6, three SiC fibres were used to measure the flame temperature along the nozzle-to-plate region, and another three fibres along the plate. Since the intensity of the ND filter was not enough, only a little temperature data was valid due to over-exposure. Therefore, it would be better to image the luminous fibre with a higher-intensity ND filter in the future. A SiC fibre mesh box can also be developed which is able to measure the flame in 3D space.
- The optical flow Lucas-Kanade method has been used to resolve point correspondence between two sequential frames when measuring the flame velocity. Lucas-Kanade is a non-iterative algorithm, which acquires the small displacement, constant brightness and motion consistency in a local area. When the moving speed of an object is fast, the assumption is not valid, which results in a larger error in the optical flow value. Thus, the Lucas-Kanade algorithm can be optimised, for instance, using the pyramid hierarchy.

References

- Adelman, H. G. (1981) 'A time dependent theory of spark ignition', *Symposium (International) on Combustion*, 18(1), pp. 1333–1342. doi: 10.1016/S0082-0784(81)80137-3.
- Administrator, N. C. (2016) *Mountains of Creation*. Available at: https://www.nasa.gov/multimedia/imagegallery/image_feature_483.html (Accessed: 17 March 2018).
- Adrian, R. J. (Ronald J. . and Westerweel, J. (Jerry) (2011) *Particle Image Velocimetry*. Cambridge University Press.
- Aggarwal, S. K. (1998) 'A review of spray ignition phenomena: Present status and future research', *Progress in Energy and Combustion Science*, pp. 565–600. doi: 10.1016/S0360-1285(98)00016-1.
- Ahmed, S. F. and Mastorakos, E. (2006a) 'Spark ignition of lifted turbulent jet flames', *Combustion and Flame*, 146(1–2), pp. 215–231. doi: 10.1016/j.combustflame.2006.03.007.
- Ahmed, S. F. and Mastorakos, E. (2006b) 'Spark ignition of lifted turbulent jet flames', *Combustion and Flame*, 146(1–2), pp. 215–231.
- Albers, B. W. and Agrawal, A. K. (1999) 'Schlieren analysis of an oscillating gas-jet diffusion flame', *Combustion and Flame*, 119(1–2), pp. 84–94. doi: 10.1016/S0010-2180(99)00034-6.
- Allamandola, L. J., Tielens, A. G. G. M. and Barker, J. R. (1987) 'The IR Emission Features: Emission from PAH Molecules and Amorphous Carbon Particles', in *Polycyclic Aromatic Hydrocarbons and Astrophysics*. Dordrecht: Springer Netherlands, pp. 255–271. doi: 10.1007/978-94-009-4776-4_22.
- Ballal, D. R. and Lefebvre, A. H. (1979) 'Ignition and flame quenching of flowing heterogeneous fuel-air mixtures', *Combustion and Flame*, 35(C), pp. 155–168. doi: 10.1016/0010-2180(79)90019-1.

Baukal, C. E. (2013) *Oxygen-enhanced combustion*. CRC Press.

Baukal, C. E. and Gebhart, B. (1997) 'Surface condition effects on flame impingement heat transfer', *Experimental Thermal and Fluid Science*, 15(97), pp. 323–335. doi: 10.1016/S0894-1777(97)00036-8.

Baukal, C. E. and Gebhart, B. (1998) 'Heat transfer from oxygen-enhanced/natural gas flames impinging normal to a plane surface', *Experimental Thermal and Fluid Science*, 16(3), pp. 247–259. doi: 10.1016/S0894-1777(97)10023-1.

Bhatt, J. S. and Lindstedt, R. P. (2009) 'Analysis of the impact of agglomeration and surface chemistry models on soot formation and oxidation', *Proceedings of the Combustion Institute*, 32 I, pp. 713–720. doi: 10.1016/j.proci.2008.06.201.

Black body radiation and planck's radiation law (2017). Available at: <https://physicsabout.com/black-body-radiation/>.

Blunck, D. *et al.* (2009) 'Simultaneous water vapor concentration and temperature measurements in unsteady hydrogen flames', *Proceedings of the Combustion Institute*, 32 II, pp. 2527–2534. doi: 10.1016/j.proci.2008.05.046.

Böhm, H., Jander, H. and Tanke, D. (1998) 'PAH growth and soot formation in the pyrolysis of acetylene and benzene at high temperatures and pressures: Modeling and experiment', *Symposium (International) on Combustion*. Elsevier, 27(1), pp. 1605–1612. doi: 10.1016/S0082-0784(98)80570-5.

Bruhn, A., Weickert, J. and Schnörr, C. (2005) 'Lucas/Kanade meets Horn/Schunck: Combining local and global optic flow methods', *International Journal of Computer Vision*, 61(3), pp. 1–21. doi: 10.1023/B:VISI.0000045324.43199.43.

Cardani, D. (2001) 'Adventures in hsv space'.

Chander, S. and Ray, A. (2007a) 'Heat transfer characteristics of laminar methane/air flame impinging normal to a cylindrical surface', *Experimental Thermal and Fluid Science*, 32(2), pp. 707–721. doi: 10.1016/j.expthermflusci.2007.09.003.

Chander, S. and Ray, A. (2007b) 'Heat transfer characteristics of three interacting methane/air flame jets impinging on a flat surface', *International Journal of Heat and*

Mass Transfer, 50(3–4), pp. 640–653. doi: 10.1016/j.ijheatmasstransfer.2006.07.011.

Chander, S. and Ray, A. (2008) ‘An experimental and numerical study of stagnation point heat transfer for methane/air laminar flame impinging on a flat surface’, *International Journal of Heat and Mass Transfer*, 51(13–14), pp. 3595–3607. doi: 10.1016/j.ijheatmasstransfer.2007.10.018.

Chatterjee, P. *et al.* (2011) ‘A model for soot radiation in buoyant diffusion flames’, *Proceedings of the Combustion Institute*, 33(2), pp. 2665–2671. doi: 10.1016/j.proci.2010.06.112.

Chemiluminescence (2005). Available at: https://www.uni-due.de/ivg/rl/chemilumineszenz_en.php (Accessed: 17 March 2018).

Cherry Blossoms in Japan: All About Sakura and Hanami - LIVE JAPAN (2018).

Chloe, M. and Mcdaid, J. (2013) *Developing and Implementing Advanced Optical Diagnostics for the Investigation of Fuel and Flow Effects on Impinging Jet Flames*.

Cho, J. H. and Lieuwen, T. (2005) ‘Laminar premixed flame response to equivalence ratio oscillations’, *Combustion and Flame*, 140(1–2), pp. 116–129. doi: 10.1016/j.combustflame.2004.10.008.

Connelly, B. C. *et al.* (2009) ‘Computational and experimental investigation of the interaction of soot and NO in coflow diffusion flames’, *Proceedings of the Combustion Institute*, 32(1), pp. 777–784. doi: 10.1016/j.proci.2008.06.182.

Csele, M. (2004) ‘Light and Blackbody Emission’, *Fundamentals of Light Sources and Lasers*, pp. 1–20. doi: 10.1002/0471675210.ch1.

D’Anna, A. (2009) ‘Combustion-formed nanoparticles’, *Proceedings of the Combustion Institute*, 32, pp. 593–613.

Dong, L. L., Cheung, C. S. and Leung, C. W. (2002) ‘Heat transfer from an impinging premixed butane/air slot flame jet’, *International Journal of Heat and Mass Transfer*, 45(5), pp. 979–992. doi: 10.1016/S0017-9310(01)00215-0.

Dong, L. L., Leung, C. W. and Cheung, C. S. (2003) ‘Heat transfer of a row of three butane/air flame jets impinging on a flat plate’, *International Journal of Heat and*

- Mass Transfer*, 46(1), pp. 113–125. doi: 10.1016/S0017-9310(02)00225-9.
- Draine, B. T. (2011) ‘Astronomical Models of PAHs and Dust’, *EAS Publications Series*, 46, pp. 29–42. doi: 10.1051/eas/1146003.
- Drysdale, D. (2011) *An Introduction to Fire Dynamics: Third Edition, An Introduction to Fire Dynamics: Third Edition*. doi: 10.1002/9781119975465.
- Ebi, D. and Clemens, N. T. (2016) ‘Simultaneous high-speed 3D flame front detection and tomographic PIV’, *Measurement Science and Technology*. IOP Publishing, 27(3), p. 035303. doi: 10.1088/0957-0233/27/3/035303.
- Edwards, D. E. *et al.* (2014) ‘Pathways to Soot Oxidation: Reaction of OH with Phenanthrene Radicals’, *The Journal of Physical Chemistry A*. American Chemical Society, 118(37), pp. 8606–8613. doi: 10.1021/jp5033178.
- Edwards, H. and Vandenberghe, P. (2012) *Analytical Archaeometry: Selected Topics*. London, U.K.: Royal Society of Chemistry Publishing.
- El-Mahallawy, F. and Habik, S. E.-D. (2002) ‘Chapter 5 - Combustion, Heat Transfer, and Emission in Boilers and Furnaces’, *Fundamentals and Technology of Combustion*, pp. 499–746. doi: <http://dx.doi.org/10.1016/B978-008044106-1/50007-3>.
- Els Peeters (2002) *Polycyclic Aromatic Hydrocarbons*. Available at: http://www.astro.uwo.ca/~epeeters/research_new.shtml (Accessed: 18 March 2018).
- Elsinga, G. E. and Scarano, F. (2014) ‘Characterization of PIV systems’, *Measurement Science and Technology*. doi: 10.1088/0957-0233/25/8/080301.
- Fan, Y., Suzuki, Y. and Kasagi, N. (2011) ‘Quenching mechanism study of oscillating flame in micro channels using phase-locked OH-PLIF’, *Proceedings of the Combustion Institute*, 33(2), pp. 3267–3273. doi: 10.1016/j.proci.2010.05.041.
- Fijałkowski, A. J. (2011) *Combustion kept simple - OSC IB Blogs*. Available at: https://blogs.osc-ib.com/2011/03/ib-teacher-blogs/dp_chemistry/combustion-kept-simple/.
- Foat, T., Yap, K. P. and Zhang, Y. (2001) ‘The visualization and mapping of turbulent premixed impinging flames’, *Combustion and Flame*, 125(1–2), pp. 839–851. doi:

10.1016/S0010-2180(00)00238-8.

Fu, J. *et al.* (2013) ‘Study on laminar flame speed and flame structure of syngas with varied compositions using OH-PLIF and spectrograph’, *International Journal of Hydrogen Energy*, 38(3), pp. 1636–1643. doi: 10.1016/j.ijhydene.2012.11.023.

Fu, S. and Wu, Y. (2001) ‘Detection of velocity distribution of a flow field using sequences of Schlieren images’, *Optical Engineering*, 40(8), p. 1661.

Fun Optical Illusions (2015). Available at: <https://www.opticalspy.com/spy-blog/forced-perspective>.

Garo, A., Prado, G. and Lahaye, J. (1990) ‘Chemical aspects of soot particles oxidation in a laminar methane-air diffusion flame’, *Combustion and Flame*. Elsevier, 79(3–4), pp. 226–233. doi: 10.1016/0010-2180(90)90134-D.

Gaydon, A. G. (1941) ‘Applications of spectroscopy to combustion’, *Reports on Progress in Physics*, 8(1), pp. 50–70. doi: 10.1088/0034-4885/8/1/305.

Gaydon, A. G. (1974) *The spectroscopy of flames*. London, U.K.: Chapman and Hall.

Gaydon, A. G. and Wolfhard, H. G. (1953) ‘Mechanism of formation of CH, C₂, OH and HCO radicals in flames’, *Symposium (International) on Combustion*, 4(1), pp. 211–218. doi: 10.1016/S0082-0784(53)80027-5.

Gaydon, A. G. and Wolfhard, H. G. (1971) ‘Flames: Their structure, radiation and temperature’, *Physics Today*, 24(10), p. 54. doi: 10.1063/1.3022389.

Glassman, I. and Yetter, R. A. (2008) *Combustion, Combustion*. doi: 10.1016/B978-0-12-088573-2.X0001-2.

Glassman, I. and Yetter, R. A. (2008) *Combustion*. Academic Press.

Gnani, F. *et al.* (2015) ‘Shock Wave Diffraction Phenomena around Slotted Splitters’, *Aerospace*, 2(1), pp. 1–16. doi: 10.3390/aerospace2010001.

Griebel, P., Siewert, P. and Jansohn, P. (2007) ‘Flame characteristics of turbulent lean premixed methane/air flames at high pressure: Turbulent flame speed and flame brush thickness’, *Proceedings of the Combustion Institute*, 31 II, pp. 3083–3090. doi: 10.1016/j.proci.2006.07.042.

Gu, M., Chu, H. and Liu, F. (2016) 'Effects of simultaneous hydrogen enrichment and carbon dioxide dilution of fuel on soot formation in an axisymmetric coflow laminar ethylene/air diffusion flame', *Combustion and Flame*, 166, pp. 216–228. doi: 10.1016/j.combustflame.2016.01.023.

Gu, X. *et al.* (2012) 'Emission characteristics of a spark-ignition engine fuelled with gasoline-n-butanol blends in combination with EGR', *Fuel*. Elsevier Ltd, 93(x), pp. 611–617. doi: 10.1016/j.fuel.2011.11.040.

Guéret, C., Daroux, M. and Billaud, F. (1997) 'Methane pyrolysis: Thermodynamics', *Chemical Engineering Science*, 52(5), pp. 815–827. doi: 10.1016/S0009-2509(96)00444-7.

Guo, J. *et al.* (2015) 'Effect of ignition position on vented hydrogen-air explosions', *International Journal of Hydrogen Energy*. Elsevier Ltd, 40(45), pp. 15780–15788. doi: 10.1016/j.ijhydene.2015.09.038.

Guyot, D. *et al.* (2010) 'CH*/OH* Chemiluminescence Response of an Atmospheric Premixed Flame under Varying Operating Conditions', *Proceedings of ASME Turbo Expo 2010: Power for Land, Sea and Air*, (GT2010-23135), pp. 1–12. doi: <http://dx.doi.org/10.1115/GT2010-23135>.

Hardalupas, Y. *et al.* (2004) 'Chemiluminescence sensor for local equivalence ratio of reacting mixtures of fuel and air (FLAMESEEK)', in *Applied Thermal Engineering*, pp. 1619–1632. doi: 10.1016/j.applthermaleng.2003.10.028.

Hargather, M. J. and Settles, G. S. (2010) 'Natural-background-oriented schlieren imaging', *Experiments in Fluids*, 48(1), pp. 59–68. doi: 10.1007/s00348-009-0709-3.

El Hassan, M. *et al.* (2012) 'Experimental investigation of the wall shear stress and the vortex dynamics in a circular impinging jet', *Experiments in Fluids*, 52(6), pp. 1475–1489. doi: 10.1007/s00348-012-1269-5.

El Hassan, M. *et al.* (2013) 'Experimental investigation of the wall shear stress in a circular impinging jet', *Physics of Fluids*, 25(7). doi: 10.1063/1.4811172.

Holmen, A., Rokstad, O. A. and Solbakken, A. (1976) 'High-Temperature Pyrolysis of Hydrocarbons. 1. Methane to Acetylene', *Industrial & Engineering Chemistry*

Process Design and Development. American Chemical Society, 15(3), pp. 439–444. doi: 10.1021/i260059a017.

Horn, B. K. P. and Schunck, B. G. (1981) ‘Determining optical flow’, *Artificial Intelligence*, 17(1–3), pp. 185–203. doi: 10.1016/0004-3702(81)90024-2.

Hossain, M. M. *et al.* (2013) ‘Three-dimensional reconstruction of flame temperature and emissivity distribution using optical tomographic and two-colour pyrometric techniques’, *Measurement Science and Technology*. IOP Publishing, 24(7), p. 074010. doi: 10.1088/0957-0233/24/7/074010.

Hottel, H. C. and Hawthorne, W. R. (1948) ‘Diffusion in laminar flame jets’, *Symposium on Combustion and Flame, and Explosion Phenomena*. Elsevier, 3(1), pp. 254–266. doi: 10.1016/S1062-2896(49)80034-1.

Huang, H.-W. *et al.* (2008) ‘Flame colour characterization in the visible and infrared spectrum using a digital camera and image processing’, *Measurement Science and Technology*. IOP Publishing, 19(8), p. 085406. doi: 10.1088/0957-0233/19/8/085406.

Huang, H.-W. and Zhang, Y. (2008a) ‘Flame colour characterization in the visible and infrared spectrum using a digital camera and image processing’, *Measurement Science and Technology*, 19(8), p. 085406. doi: 10.1088/0957-0233/19/8/085406.

Huang, H.-W. and Zhang, Y. (2008b) ‘Flame colour characterization in the visible and infrared spectrum using a digital camera and image processing’, *Measurement Science and Technology*. IOP Publishing, 19(8), p. 085406. doi: 10.1088/0957-0233/19/8/085406.

Huang, H. W. *et al.* (2013) ‘Variation of hydrocarbon compositions and ignition locations on the radiative flame initiation characteristics through multi-dimensional DFCD incorporated image analysis’, in *Fuel*, pp. 334–346. doi: 10.1016/j.fuel.2012.04.046.

Huang, H. W. and Zhang, Y. (2011) ‘Analysis of the ignition process using a digital image and colour processing technique’, *Measurement Science and Technology*, 22(7). doi: 10.1088/0957-0233/22/7/075401.

Huang, H. W. and Zhang, Y. (2012) ‘Syngas combustion radiation profiling through

spectrometry and DFCD processing techniques’, *International Journal of Hydrogen Energy*, 37(6), pp. 5257–5267. doi: 10.1016/j.ijhydene.2011.12.048.

Huang, H. W. and Zhang, Y. (2013) ‘Imaging based chemiluminescence characterisation of partially premixed syngas flames through DFCD technique’, *International Journal of Hydrogen Energy*, 38(11), pp. 4839–4847. doi: 10.1016/j.ijhydene.2013.01.142.

Hult, J. *et al.* (2007) ‘Measurement of flame surface density for turbulent premixed flames using PLIF and DNS’, *Proceedings of the Combustion Institute*, 31 I, pp. 1319–1326. doi: 10.1016/j.proci.2006.07.188.

Incropera, F. P. *et al.* (2007) *Fundamentals of Heat and Mass Transfer, Water*. doi: 10.1016/j.applthermaleng.2011.03.022.

Kaminski, C. F. *et al.* (2000) ‘Spark ignition of turbulent methane/air mixtures revealed by time-resolved planar laser-induced fluorescence and direct numerical simulations’, *Proceedings of the Combustion Institute*, 28(1), pp. 399–405. doi: 10.1016/S0082-0784(00)80236-2.

Katti, V. and Prabhu, S. V. (2008) ‘Experimental study and theoretical analysis of local heat transfer distribution between smooth flat surface and impinging air jet from a circular straight pipe nozzle’, *International Journal of Heat and Mass Transfer*, 51(17–18), pp. 4480–4495. doi: 10.1016/j.ijheatmasstransfer.2007.12.024.

Kimura, I. and Kumagai, S. (1956) ‘Spark Ignition of Flowing Gases’, *Journal of the Physical Society of Japan*, 11(5), pp. 599–604. doi: 10.1143/JPSJ.11.599.

Kindracki, J. *et al.* (2007a) ‘Influence of ignition position and obstacles on explosion development in methane-air mixture in closed vessels’, *Journal of Loss Prevention in the Process Industries*. doi: 10.1016/j.jlp.2007.05.010.

Kindracki, J. *et al.* (2007b) ‘Influence of ignition position and obstacles on explosion development in methane-air mixture in closed vessels’, *Journal of Loss Prevention in the Process Industries*, 20(4–6), pp. 551–561. doi: 10.1016/j.jlp.2007.05.010.

Koched, A., Pavageau, M. and Aloui, F. (2011) ‘Vortex structure in the wall region of an impinging plane jet’, *Journal of Applied Fluid Mechanics*, 4(2), pp. 61–69.

- Kreith, F., Bohn, M. and Kirkpatrick, A. (1997) 'Principles of Heat Transfer', *Journal of Solar Energy Engineering*, 119(2), p. 187. doi: 10.1115/1.2887901.
- Krishnamachari, S. L. N. G. and Broida, H. P. (1961) 'Effect of molecular oxygen on the emission spectra of atomic oxygen-acetylene flames', *The Journal of Chemical Physics*, 34(5), pp. 1709–1711. doi: 10.1063/1.1701067.
- Lahaye, J. (1990) 'Mechanisms of soot formation', *Polymer Degradation and Stability*, 30(1), pp. 111–121. doi: 10.1016/0141-3910(90)90121-M.
- Law, C. K. and Sung, C. J. (2000) 'Structure, aerodynamics, and geometry of premixed flamelets', *Progress in Energy and Combustion Science*, 26(4), pp. 459–505. doi: 10.1016/S0360-1285(00)00018-6.
- Lawes, M. *et al.* (2012) 'The turbulent burning velocity of iso-octane/air mixtures', *Combustion and Flame*, 159(5), pp. 1949–1959. doi: 10.1016/j.combustflame.2011.12.023.
- Lee, T.-W., North, G. L. and Santavicca, D. A. (1993) 'Surface Properties of Turbulent Premixed Propane/Air Flames at Various Lewis Numbers', *Combustion and Flame*, 93, pp. 445–456.
- Lee, T. W. and Lee, S. J. (2003) 'Direct comparison of turbulent burning velocity and flame surface properties in turbulent premixed flames', *Combustion and Flame*, 132(3), pp. 492–502. doi: 10.1016/S0010-2180(02)00495-9.
- Léger, A. *et al.* (1989) 'Physics of IR emission by interstellar PAH molecules', *Astronomy and Astrophysics*, 216, pp. 148–164.
- Lerner, L. S. (1996) *Modern physics for scientists and engineers*. Jones and Bartlett Publishers.
- Li, H. B. *et al.* (2010) 'Effects of plate temperature on heat transfer and emissions of impinging flames', *International Journal of Heat and Mass Transfer*, 53(19–20), pp. 4176–4184. doi: 10.1016/j.ijheatmasstransfer.2010.05.040.
- Li, Z. and Wang, H. (2003) 'Drag force, diffusion coefficient, and electric mobility of small particles. I. Theory applicable to the free-molecule regime', *Physical Review E*

- *Statistical Physics, Plasmas, Fluids, and Related Interdisciplinary Topics*, 68(6). doi: 10.1103/PhysRevE.68.061206.

Lindecrantz, S. (2010) *Investigation of flame emission and absorption spectroscopy using the HITRAN/HITEMP database and simulations for concentration and temperature determination in combustion environments.*

Liu, F. *et al.* (2015) 'Numerical and experimental study of the influence of CO₂ and N₂ dilution on soot formation in laminar coflow C₂H₄/air diffusion flames at pressures between 5 and 20atm', *Combustion and Flame*, 162(5), pp. 2231–2247. doi: 10.1016/j.combustflame.2015.01.020.

Llowarch, W. (1964) 'Schlieren methods', *Contemporary Physics*, 5(5), pp. 394–397. doi: 10.1080/00107516408203101.

Lodgejr, J. (1996) 'Air quality guidelines. Global update 2005. Particulate matter, ozone, nitrogen dioxide and sulfur dioxide', *Environmental Science and Pollution Research*, 3(91), pp. 23–23. doi: 10.1007/BF02986808.

Luján, J. M. *et al.* (2015a) 'Influence of a low pressure EGR loop on a gasoline turbocharged direct injection engine', *Applied Thermal Engineering*, 89, pp. 432–443. doi: 10.1016/j.applthermaleng.2015.06.039.

Luján, J. M. *et al.* (2015b) 'Influence of a low pressure EGR loop on a gasoline turbocharged direct injection engine', *Applied Thermal Engineering*, 89, pp. 432–443. doi: 10.1016/j.applthermaleng.2015.06.039.

Ma, Z. *et al.* (2016) 'Measuring the Temperature of a Flame Propagating Through a Quartz Tube Using High Speed Colour Imaging and Thin SiC Filament Based Two Colour Method', in *12th International Conference on Heat Transfer, Fluid Mechanics and Thermodynamics*. At Costa del Sol, Spain.

Mahan, J. R. (2002) *Radiation heat transfer: a statistical approach*, John Wiley & Sons. New York, U.S.A.

Malalasekera, W. M. G., Versteeg, H. K. and Gilchrist, K. (1996) 'A review of research and an experimental study on the pulsation of buoyant diffusion flames and pool fires', *Fire and Materials*, 20(6).

- Malikov, G. K. *et al.* (2001) ‘Direct flame impingement heating for rapid thermal materials processing’, *International Journal of Heat and Mass Transfer*, 44(9), pp. 1751–1758. doi: 10.1016/S0017-9310(00)00204-0.
- Mansurov, Z. A. (2005a) ‘Soot formation in combustion processes (review)’, *Combustion, Explosion and Shock Waves*, 41(6), pp. 727–744. doi: 10.1007/s10573-005-0083-2.
- Mansurov, Z. A. (2005b) ‘Soot formation in combustion processes (review)’, *Combustion, Explosion and Shock Waves*, pp. 727–744. doi: 10.1007/s10573-005-0083-2.
- Mao, Q., van Duin, A. C. T. and Luo, K. H. (2017) ‘Formation of incipient soot particles from polycyclic aromatic hydrocarbons: A ReaxFF molecular dynamics study’, *Carbon*. Pergamon, 121, pp. 380–388. doi: 10.1016/J.CARBON.2017.06.009.
- Martins, C. A. *et al.* (2005) ‘CH and C2 radicals characterization in natural gas turbulent diffusion flames’, *Journal of the Brazilian Society of Mechanical Sciences and Engineering*, 27(2), pp. 110–117.
- Mastorakos, E. (2009) ‘Ignition of turbulent non-premixed flames’, *Progress in Energy and Combustion Science*. Elsevier Ltd, 35(1), pp. 57–97. doi: 10.1016/j.pecs.2008.07.002.
- Matalon, M. (2009) ‘Flame dynamics’, *Proceedings of the Combustion Institute*, 32 I, pp. 57–82. doi: 10.1016/j.proci.2008.08.002.
- Mattocchia, S. (2013) ‘Stereo Vision Algorithms for FPGAs’, in *2013 IEEE Conference on Computer Vision and Pattern Recognition Workshops*, pp. 636–641. doi: 10.1109/CVPRW.2013.96.
- Mattocchia, S. (2014) ‘Stereo vision algorithms suited to constrained FPGA cameras’, in *Advances in Computer Vision and Pattern Recognition*, pp. 109–134. doi: 10.1007/978-3-319-09387-1_5.
- Mazumdar, A. (2011) ‘Principles and Techniques of Schlieren Imaging’, *Columbia University*, pp. 1–16. Available at: <http://hdl.handle.net/10022/AC:P:20839>.

- McAllister, S., Chen, J.-Y. and Fernandez-Pello, A. C. (2011) ‘Non-premixed Flames (Diffusion Flames)’, in. Springer, New York, NY, pp. 139–154. doi: 10.1007/978-1-4419-7943-8_7.
- McDaid, C., Zhou, J. and Zhang, Y. (2013) ‘Experimental observations of complex flame propagations initiated at different locations of an impingement configuration’, *Fuel*. Elsevier Ltd, 103, pp. 783–791. doi: 10.1016/j.fuel.2012.06.079.
- Mckinnon, J. T., Meyer, E. and Howard, J. B. (1996) ‘Infrared analysis of flame-generated PAH samples’, *Combustion and Flame*, pp. 161–166.
- Medina, A. *et al.* (2014) *Quasi-dimensional simulation of spark ignition engines: From thermodynamic optimization to cyclic variability*, *Quasi-Dimensional Simulation of Spark Ignition Engines: From Thermodynamic Optimization to Cyclic Variability*. doi: 10.1007/978-1-4471-5289-7.
- Migliorini, F. *et al.* (2014) ‘Analysis of chemiluminescence measurements by grey-scale ICCD and colour digital cameras’, *Measurement Science and Technology*, 25(5). doi: 10.1088/0957-0233/25/5/055202.
- Mikofski, M. A. *et al.* (2007) ‘Structure of laminar sooting inverse diffusion flames’, *Combustion and Flame*, 149(4), pp. 463–478.
- Miller, J. H. (1991) ‘The kinetics of polynuclear aromatic hydrocarbon agglomeration in flames’, *Symposium (International) on Combustion*, 23(1), pp. 91–98. doi: 10.1016/S0082-0784(06)80246-8.
- Ming-wei, Y. O. U. (2012) ‘Premixed Flammable Gas Explosion in Containers Connected by Pipes with Different Lengths’.
- Mitchell, P. and Frenklach, M. (2003) ‘Particle aggregation with simultaneous surface growth’, *Physical Review E - Statistical Physics, Plasmas, Fluids, and Related Interdisciplinary Topics*, 67(6), p. 11. doi: 10.1103/PhysRevE.67.061407.
- Moldoveanu, S. C. (2010) ‘Chapter 7 Pyrolysis of Hydrocarbons’, *Techniques and Instrumentation in Analytical Chemistry*, pp. 131–229. doi: 10.1016/S0167-9244(09)02807-8.

- Molkov, V. and Saffers, J. B. (2013) ‘Hydrogen jet flames’, *International Journal of Hydrogen Energy*, 38(19), pp. 8141–8158. doi: 10.1016/j.ijhydene.2012.08.106.
- Muñiz, L. and Mungal, M. . (2001) ‘Effects of heat release and buoyancy on flow structure and entrainment in turbulent nonpremixed flames’, *Combustion and Flame*, 126(1–2), pp. 1402–1420. doi: 10.1016/S0010-2180(01)00253-X.
- Mze Ahmed, A. *et al.* (2016) ‘Experimental and numerical study on rich methane/hydrogen/air laminar premixed flames at atmospheric pressure: Effect of hydrogen addition to fuel on soot gaseous precursors’, in *International Journal of Hydrogen Energy*, pp. 6929–6942. doi: 10.1016/j.ijhydene.2015.11.148.
- Nishad, P. M. and Manicka Chezian, R. (2013) ‘Various Colour Spaces and Colour Space Conversion Algorithms’, *Journal of Global Research in Computer Science*.
- Nori, V. and Seitzman, J. (2007) ‘Chemiluminescence Measurements and Modeling in Syngas, Methane and Jet-A Fueled Combustors’, *45th AIAA Aerospace Sciences Meeting and Exhibit*, (January), pp. 1–14. doi: 10.2514/6.2007-466.
- Nye, D. . *et al.* (1996) ‘Flame stretch measurements during the interaction of premixed flames and Kármán vortex streets using PIV’, *Combustion and Flame*, 105(1–2), pp. 167–179. doi: 10.1016/0010-2180(95)00186-7.
- Onursal, B. and Gautam, S. (1997) *Vehicular air pollution : experiences from seven Latin American urban centers*. World Bank.
- Ota, N. (2015) ‘Asymmetric Polycyclic Aromatic Hydrocarbon as a Capable Source of Astronomically Observed Interstellar Infrared Spectrum’.
- Otsuka, T. and Wolanski, P. (2001) ‘Particle image velocimetry (PIV) analysis of flame structure’, *Journal of Loss Prevention in the Process Industries*, 14(6), pp. 503–507. doi: 10.1016/S0950-4230(01)00045-6.
- Park, D. J. and Lee, Y. S. (2012) ‘Experimental investigation of explosion pressures and flame propagations by wall obstruction ratios and ignition positions’, *Korean Journal of Chemical Engineering*, 29(2), pp. 139–144. doi: 10.1007/s11814-011-0159-5.

- Penttinen, P. *et al.* (2001) ‘Ultrafine particles in urban air and respiratory health among adult asthmatics’, *Eur Respir J*, 17, pp. 428–435.
- Petersson, P. *et al.* (2007) ‘Simultaneous PIV/OH-PLIF, Rayleigh thermometry/OH-PLIF and stereo PIV measurements in a low-swirl flame.’, *Applied Optics*, 46(19), pp. 3928–3936. doi: 10.1364/AO.46.003928.
- Phalnikar, K. A., Kumar, R. and Alvi, F. S. (2008) ‘Experiments on free and impinging supersonic microjets’, *Experiments in Fluids*, 44(5), pp. 819–830. doi: 10.1007/s00348-007-0438-4.
- Pick, S. and Lehmann, F. O. (2009) ‘Stereoscopic PIV on multiple color-coded light sheets and its application to axial flow in flapping robotic insect wings’, *Experiments in Fluids*, 47(6), pp. 1009–1023. doi: 10.1007/s00348-009-0687-5.
- Plyler, E. K. and Plyler, B. E. K. (1948) ‘Infrared Radiation From a Bunsen Flame 1’, *Research Paper RPL*, 40(February).
- Raffel, M. (2007) *Particle image velocimetry : a practical guide*. Springer.
- Raffel, M. (2015) ‘Background-oriented schlieren (BOS) techniques’, *Experiments in Fluids*, 56(3), pp. 1–17. doi: 10.1007/s00348-015-1927-5.
- Raghunandan, B. N., Oommen, C. and Sullerey, R. K. (2004) ‘Air Breathing Engines and Aerospace Propulsion’, in *Proceedings of NCABE*, p. 32.
- Richard, H. and Raffel, M. (2001) ‘Principle and applications of the background oriented schlieren (BOS) method’, *Measurement Science and Technology*, 12(9), pp. 1576–1585. doi: 10.1088/0957-0233/12/9/325.
- Richter, H. and Howard, J. B. (2000) ‘Formation of polycyclic aromatic hydrocarbons and their growth to soot—a review of chemical reaction pathways’.
- Rienitz, J. (1975) ‘Schlieren experiment 300 years ago’, *Nature*, 254(5498), pp. 293–295. doi: 10.1038/254293a0.
- Rosell, J. *et al.* (2017) ‘Multi-species PLIF study of the structures of turbulent premixed methane/air jet flames in the flamelet and thin-reaction zones regimes’, *Combustion and Flame*. Elsevier Inc., 182, pp. 324–338. doi:

- 10.1016/j.combustflame.2017.04.003.
- Ross, R. T. (1967) 'Some thermodynamics of photochemical systems', *The Journal of Chemical Physics*. doi: 10.1063/1.1840606.
- Roth, K. (2003) 'Alle Jahre wieder: die Chemie der Weihnachtskerze', *Chemie in unserer Zeit*. Wiley-Blackwell, 37(6), pp. 424–429. doi: 10.1002/ciuz.200390086.
- Ryerson, W. G. and Schwenk, K. (2012) 'A simple, inexpensive system for digital particle image velocimetry (DPIV) in biomechanics', *Journal of Experimental Zoology Part A: Ecological Genetics and Physiology*, 317 A(2), pp. 127–140. doi: 10.1002/jez.725.
- Salama, F. (2008) 'PAHs in Astronomy -A Review'. doi: 10.1017/S1743921308021960.
- San, J. Y. and Shiao, W. Z. (2006) 'Effects of jet plate size and plate spacing on the stagnation Nusselt number for a confined circular air jet impinging on a flat surface', *International Journal of Heat and Mass Transfer*, 49(19–20), pp. 3477–3486. doi: 10.1016/j.ijheatmasstransfer.2006.02.055.
- Sandford, S. A., Bernstein, M. P. and Materese, C. K. (2013) 'The Infrared Spectra of Polycyclic Aromatic Hydrocarbons with Excess Peripheral H Atoms (Hn-PAHs) and their Relation to the 3.4 and 6.9 μm PAH Emission Features.', *The Astrophysical Journal. Supplement series*. NIH Public Access, 205(1). doi: 10.1088/0067-0049/205/1/8.
- Sang-Joon, L., Jung-Ho, L. and Dae-Hee, L. (1994) 'Local heat transfer measurements from an elliptic jet impinging on a flat plate using liquid crystal', *International Journal of Heat and Mass Transfer*, 37(6), pp. 967–976. doi: 10.1016/0017-9310(94)90221-6.
- Santi, P. A. (2011) 'Light sheet fluorescence microscopy: A review', *Journal of Histochemistry and Cytochemistry*, pp. 129–138. doi: 10.1369/0022155410394857.
- Savage, P. E. (2000) 'Mechanisms and kinetics models for hydrocarbon pyrolysis', *Journal of Analytical and Applied Pyrolysis*, 54(1), pp. 109–126. doi: 10.1016/S0165-2370(99)00084-4.

- Schefer, R. W. *et al.* (2009) ‘Visible emission of hydrogen flames’, *Combustion and Flame*, 156(6), pp. 1234–1241. doi: 10.1016/j.combustflame.2009.01.011.
- Serway and Jewett (2006) *Physics for Scientists and Engineers, Journal of College Science Teaching*. doi: 013613923X.
- Settles, G. and Covert, E. (2002) ‘Schlieren and Shadowgraph Techniques: Visualizing Phenomena in Transport Media’, *Applied Mechanics Reviews*, 55(4), p. B76. doi: 10.1115/1.1483362.
- Settles, G. S. (1985) ‘Colour-coding schlieren techniques for the optical study of heat and fluid flow’, *International Journal of Heat and Fluid Flow*, 6(1), pp. 3–15. doi: 10.1016/0142-727X(85)90024-4.
- Shaddix, C. R. (1999) ‘Correcting thermocouple measurements for radiation loss: a critical review’, *Proceedings of the 33rd National Heat Transfer Conference*, pp. HTD99-282. doi: 10.1088/0957-0233/17/4/008.
- Shah, M. *et al.* (2014) ‘Gold nanoparticles: various methods of synthesis and antibacterial applications’, *Front Biosci (Landmark Ed)*, 19(May 2015), pp. 1320–1344.
- Shimura, M. *et al.* (2011) ‘Simultaneous dual-plane CH PLIF, single-plane OH PLIF and dual-plane stereoscopic PIV measurements in methane-air turbulent premixed flames’, *Proceedings of the Combustion Institute*. Elsevier Inc., 33(1), pp. 775–782. doi: 10.1016/j.proci.2010.05.026.
- Sjoholm, J. *et al.* (2013) ‘Simultaneous visualization of OH, CH, CH₂O and toluene PLIF in a methane jet flame with varying degrees of turbulence’, *Proceedings of the Combustion Institute*, 34(1), pp. 1475–1482. doi: 10.1016/j.proci.2012.05.037.
- Smith, G. P., Park, C. and Luque, J. (2005) ‘A note on chemiluminescence in low-pressure hydrogen and methane-nitrous oxide flames’, *Combustion and Flame*, 140(4), pp. 385–389. doi: 10.1016/j.combustflame.2004.11.011.
- Solberg, D. M., Pappas, J. A. and Skramstad, E. (1981) ‘Observations of flame instabilities in large scale vented gas explosions’, *Symposium (International) on Combustion*, 18(1), pp. 1607–1614. doi: 10.1016/S0082-0784(81)80164-6.

Solomon, C. and Breckon, T. (2013) *Fundamentals of digital image processing : a practical approach with examples in matlab*. Wiley.

Someya, T. (1993) *Advanced Combustion Science*. Springer Japan.

Stevenson, D. and Skews, B. (2015) ‘Quantitative colour schlieren development’, *Journal of Visualization*, 18(2), pp. 311–320. doi: 10.1007/s12650-014-0248-8.

Taylor, C. F. (1985) *The internal-combustion engine in theory and practice*. M.I.T. Press.

Teini, P. D., Karwat, D. M. A. and Atreya, A. (2012) ‘The effect of CO₂/H₂O on the formation of soot particles in the homogeneous environment of a rapid compression facility’, *Combustion and Flame*, 159(3), pp. 1090–1099. doi: 10.1016/j.combustflame.2011.10.002.

Terao, K. (2007) *Irreversible phenomena: Ignitions, combustion and detonation waves*, *Irreversible Phenomena: Ignitions, Combustion and Detonation Waves*. doi: 10.1007/978-3-540-49901-5.

Thangaraja, J. and Kannan, C. (2016a) ‘Effect of exhaust gas recirculation on advanced diesel combustion and alternate fuels - A review’, *Applied Energy*. Elsevier Ltd, 180, pp. 169–184. doi: 10.1016/j.apenergy.2016.07.096.

Thangaraja, J. and Kannan, C. (2016b) ‘Effect of exhaust gas recirculation on advanced diesel combustion and alternate fuels - A review’, *Applied Energy*. Elsevier Ltd, 180, pp. 169–184. doi: 10.1016/j.apenergy.2016.07.096.

Thomas Mckinnon, J. and Howard, J. B. (1992a) ‘The roles of pah and acetylene in soot nucleation and growth’, *Symposium (International) on Combustion*. Elsevier, 24(1), pp. 965–971. doi: 10.1016/S0082-0784(06)80114-1.

Thomas Mckinnon, J. and Howard, J. B. (1992b) ‘The roles of pah and acetylene in soot nucleation and growth’, *Symposium (International) on Combustion*, 24(1), pp. 965–971. doi: 10.1016/S0082-0784(06)80114-1.

Tian, K. *et al.* (2007) ‘Numerical simulation aided relative optical density analysis of TEM images for soot morphology determination’, *Proceedings of the Combustion*

Institute, 31 I, pp. 861–868. doi: 10.1016/j.proci.2006.07.064.

Tilley, R. J. D. (2010) ‘Colour due to Scattering’, in *Colour and the Optical Properties of Materials*, pp. 175–196.

Tinetti, G., Encrenaz, T. and Coustenis, A. (2013) ‘Spectroscopy of planetary atmospheres in our Galaxy’, *Astronomy and Astrophysics Review*. doi: 10.1007/s00159-013-0063-6.

Tokarev, M. P. *et al.* (2015) ‘3D velocity measurements in a premixed flame by tomographic PIV’, *Measurement Science and Technology*, 26(6). doi: 10.1088/0957-0233/26/6/064001.

Tombari, F. *et al.* (2008) ‘Classification and evaluation of cost aggregation methods for stereo correspondence’, in *26th IEEE Conference on Computer Vision and Pattern Recognition, CVPR*. doi: 10.1109/CVPR.2008.4587677.

Totton, T. S. *et al.* (2010) ‘Modelling the internal structure of nascent soot particles’, *Combustion and Flame*, 157(5), pp. 909–914.

Tummers, M. J., Jacobse, J. and Voorbrood, S. G. J. (2011) ‘Turbulent flow in the near field of a round impinging jet’, *International Journal of Heat and Mass Transfer*, 54(23–24), pp. 4939–4948. doi: 10.1016/j.ijheatmasstransfer.2011.07.007.

Turns, S. R. (2000) *An introduction to combustion: concepts and applications*. New York: McGraw-Hill Higher Education.

Viskanta, R. (1993) ‘Heat transfer to impinging isothermal gas and flame jets’, *Experimental Thermal and Fluid Science*, 6(2), pp. 111–134. doi: 10.1016/0894-1777(93)90022-B.

Wang, H. (2011a) ‘Formation of nascent soot and other condensed-phase materials in flames’, *Proceedings of the Combustion Institute*, 33(1), pp. 41–67.

Wang, H. (2011b) ‘Formation of nascent soot and other condensed-phase materials in flames’, *Proceedings of the Combustion Institute*. Elsevier, 33(1), pp. 41–67. doi: 10.1016/J.PROCI.2010.09.009.

Wang, Q. *et al.* (2012) ‘Vortex dynamics and structures of methane/air jet diffusion

- flames with air coflow', *Experimental Thermal and Fluid Science*, 37, pp. 84–90.
- Wang, Q. *et al.* (2013) 'Impinging flame ignition and propagation visualisation using Schlieren and colour-enhanced stereo imaging techniques', *Fuel*, 108, pp. 177–183. doi: 10.1016/j.fuel.2013.01.048.
- Wang, R. (2009) *Digital stereo imaging and reconstruction of flame dynamics*. University of Manchester.
- Wang, Y. *et al.* (2016) 'Investigation of ignition process from visible to infrared by a high speed colour camera', *Fuel*, 185, pp. 500–507.
- Weinkauff, J. *et al.* (2013) 'Tomographic PIV measurements in a turbulent lifted jet flame', *Experiments in Fluids*, 54(12). doi: 10.1007/s00348-013-1624-1.
- Wiley, J., Hepburn, K. and Levenspiel, O. (1964) *Chemical Reaction Engineering, Chemical Engineering Science*. doi: 10.1016/0009-2509(64)85017-X.
- Winder, S. (2002) *Bandpass filters*. doi: 10.1016/B978-075067547-5/50006-3.
- Won, S. H. *et al.* (2000) 'Lifted flame stabilization in developing and developed regions of coflow jets for highly diluted propane', *Proceedings of the Combustion Institute*, 28(2), pp. 2093–2099. doi: 10.1016/S0082-0784(00)80618-9.
- World Energy Council (2016) *World Energy Resources, World Energy Council*.
- Xiao, H. *et al.* (2014) 'An investigation of premixed flame propagation in a closed combustion duct with a 90° bend', *Applied Energy*. Elsevier Ltd, 134(16), pp. 248–256. doi: 10.1016/j.apenergy.2014.07.071.
- Xiong, Y., Cha, M. S. and Chung, S. H. (2015) 'AC electric field induced vortex in laminar coflow diffusion flames', *Proceedings of the Combustion Institute*, 35(3), pp. 3513–3520.
- Xu, H. J. *et al.* (2010) 'Ignition and combustion of diesel spray in premixed ethanol mixture with high temperature', *Neiranji Xuebao/Transactions of CSICE (Chinese Society for Internal Combustion Engines)*, 28(3), pp. 207–213.
- Yan, X. and Saniei, N. (1997) 'Heat transfer from an obliquely impinging circular, air jet to a flat plate', *International Journal of Heat and Fluid Flow*, 18(6), pp. 591–599.

doi: 10.1016/S0142-727X(97)00051-9.

Yang, C. H. (1962) 'Theory of ignition and auto-ignition', *Combustion and Flame*, 6, pp. 215–225. doi: 10.1016/0010-2180(62)90099-8.

Yang, J. *et al.* (2015) 'Oscillating flames in open tubes', *Proceedings of the Combustion Institute*. Elsevier, 35(2), pp. 2075–2082. doi: 10.1016/J.PROCI.2014.07.052.

Yang, J., Ma, Z. and Zhang, Y. (2015) 'A Novel Flame Chemiluminescence Measurement using a Digital Colour Camera', in *Proceedings of the 25th International Colloquium on the Dynamics of Explosions and Reactive Systems*. Leeds, UK, p. 199.

Yoo, D.-H., Hong, K. S. and Yang, H.-S. (2007) 'Study of thermal conductivity of nanofluids for the application of heat transfer fluids', *Thermochimica Acta*. doi: 10.1016/j.tca.2006.12.006.

Zhang, D. *et al.* (2013) 'Flow and heat transfer characteristics of single jet impinging on protrusioned surface', *International Journal of Heat and Mass Transfer*, 58(1–2), pp. 18–28. doi: 10.1016/j.ijheatmasstransfer.2012.11.019.

Zhang, Y. and Bray, K. N. C. (1999) 'Characterization of impinging jet flames', *Combustion and Flame*, 116(4), pp. 671–674. doi: 10.1016/S0010-2180(98)00084-4.